ABCM Series on Mechanical Sciences and Engineering

Henry França Meier
Amir Antônio Martins de Oliveira Junior
Jonathan Utzig *Editors*

Advances in Turbulence

Selected Papers from the XII Spring School on Transition and Turbulence

ABCM
Associação Brasileira de
Engenharia e Ciências Mecânicas

Springer

Lecture Notes in Mechanical Engineering

ABCM Series on Mechanical Sciences and Engineering

This series publishes selected papers as well as full proceedings of events organized and/or promoted by the Brazilian Society for Mechanical Sciences and Engineering (ABCM) on an international level. These include the International Congress of Mechanical Engineering (COBEM) and the International Symposium on Dynamic Problems of Mechanics (DINAME), among others.

Henry França Meier ·
Amir Antônio Martins de Oliveira Junior ·
Jonathan Utzig
Editors

Advances in Turbulence

Selected Papers from the XII Spring School on Transition and Turbulence

ABCM
Associação Brasileira de
Engenharia e Ciências Mecânicas

Springer

Editors
Henry França Meier
Chemical Engineering Department
University of Blumenau
Blumenau, Santa Catarina, Brazil

Amir Antônio Martins de Oliveira Junior
Department of Mechanical Engineering
Federal University of Santa Catarina
Florianópolis, Santa Catarina, Brazil

Jonathan Utzig
Chemical Engineering Department
University of Blumenau
Blumenau, Santa Catarina, Brazil

ISSN 2195-4356 ISSN 2195-4364 (electronic)
Lecture Notes in Mechanical Engineering
ISSN 2662-3021 ISSN 2662-303X (electronic)
ABCM Series on Mechanical Sciences and Engineering
ISBN 978-3-031-25989-0 ISBN 978-3-031-25990-6 (eBook)
https://doi.org/10.1007/978-3-031-25990-6

© The Editor(s) (if applicable) and The Author(s), under exclusive license to Springer Nature Switzerland AG 2023
This work is subject to copyright. All rights are solely and exclusively licensed by the Publisher, whether the whole or part of the material is concerned, specifically the rights of translation, reprinting, reuse of illustrations, recitation, broadcasting, reproduction on microfilms or in any other physical way, and transmission or information storage and retrieval, electronic adaptation, computer software, or by similar or dissimilar methodology now known or hereafter developed.
The use of general descriptive names, registered names, trademarks, service marks, etc. in this publication does not imply, even in the absence of a specific statement, that such names are exempt from the relevant protective laws and regulations and therefore free for general use.
The publisher, the authors, and the editors are safe to assume that the advice and information in this book are believed to be true and accurate at the date of publication. Neither the publisher nor the authors or the editors give a warranty, expressed or implied, with respect to the material contained herein or for any errors or omissions that may have been made. The publisher remains neutral with regard to jurisdictional claims in published maps and institutional affiliations.

This Springer imprint is published by the registered company Springer Nature Switzerland AG
The registered company address is: Gewerbestrasse 11, 6330 Cham, Switzerland

ABCM—Brazilian Society of Mechanical Sciences and Engineering

Board of Directors (Term 2021–2023)

President: Prof. Domingos Alves Rade, ITA
Vice-President: Prof. Amir Antônio Martins de Oliveira Jr., UFSC
Secretary-General: Prof. Aline Souza de Paula, UnB
Scientific Director: Prof. Francis Henrique Ramos França, UFRGS
Treasury Director: Prof. Fabio Toshio Kanizawa, UFF

ABCM Committee of Fluid Mechanics in 2022

Prof. Rigoberto E. M. Morales, UTFPR (Secretary)
Prof. Roney L. Thompson, UFF
Prof. Angela O. Nieckele, PUC-Rio
Prof. Daniel Dall'Onder dos Santos, UFU
Prof. Juliana Loureiro, UFRJ
Prof. Guilherme Fiorot, UFRGS
Prof. Marcelo Castro, UNICAMP
Prof. Marcello A. Faraco de Medeiros, USP/SC
Prof. Monica Naccache, PUC-Rio
Prof. Robson Leal da Silva, UFGD

EPTT 2020 Chairmen

Prof. Henry França Meier
Prof. Jonathan Utzig

Foreword

This book is the fourth volume of the ABCM Series on Mechanical Sciences and Engineering, and brings a compendium of works presented at EPTT 2022—Spring School of Transition and Turbulence, held in Blumenau, State of Santa Catarina, Brazil, from September 19 to September 23, 2022. Its organization was undertaken by the research groups of the Laboratory of Computational Fluid Dynamics and the Laboratory of Verification and Validation of the University of Blumenau, under the coordination of Profs. Henry França Meier and Jonathan Utzig.

The EPTT, whose first edition was held in 1998, is one of the scientific meetings promoted by the Brazilian Society of Mechanical Sciences and Engineering (ABCM), gathering students and experienced researchers to present and discuss relevant topics in the field of Transition and Turbulence in Fluid Mechanics. These topics have been intensively investigated lately by an increasing number of research groups worldwide, especially with the growing interest in turbulent multiphase, non-isothermal, and reactive flows.

The successful ABCM Series on Mechanical Sciences and Engineering results from an agreement set by Springer and ABCM and is regarded as an effective vehicle for the international diffusion of the best works presented in the meetings promoted by our society.

The ABCM Direction Board gratefully acknowledges the organizing committee of EPTT 2022, the Editors of the book series, Profs. Marcello A. Faraco de Medeiros, Marco Lucio Bittencourt, and Ricardo Diego Torres, the members of the Technical Committee of Fluid Mechanics of ABCM, and all those who contributed to the organization of EPTT 2022, especially authors, co-authors, and reviewers.

The ABCM Direction Board is also grateful to the University of Blumenau, the Federal Council of Engineering and Agronomy (CONFEA) and respective Regional Council of Santa Catarina (CREA-SC), the Coordination for the Improvement of Higher Education Personnel (CAPES) of the Brazilian Ministry of Education, the Santa Catarina State Foundation for the Support to Research and Innovation

(FAPESC) and the industrial sponsors for providing the indispensable logistic and financial support that made possible the successful organization of EPTT 2022.

Rio de Janeiro, RJ, Brazil
October 2022

Prof. Domingos A. Rade
President of ABCM, on behalf
of the ABCM Direction Board

Preface

The Spring School on Transition and Turbulence (EPTT) gathers students and researchers every 2 years in order to present, discuss, and debate relevant topics on Transition and Turbulence in Fluid Mechanics. These topics are extensively investigated by an increasing number of researchers around the world and, in the last years, these have attracted even more interest with the addition of turbulent multiphase, non-isothermal, and reactive flows.

The specific objectives of the EPTT were kept the same over the last 20 years. It aims to bring together professionals and students in the area to present lectures from national and international experts on fundamental concerns in transition and turbulence free of cost. It also has the intention of providing opportunity for students, researchers, and professors to expose their recent work to the community of transition and turbulence. Furthermore, this meeting encourages the discussion and exchange of experiences, promotes the interaction between the academic community and the industrial sector, proposes research and development projects, and contributes to the training of high-level human resources, preparing them for the development of fundamental and applied research.

The EPTT 2020 was held online by the Computational Fluid Dynamics and Verification and Validations Laboratories, University of Blumenau, Brazil. Throughout the event program, 59 technical works and 9 keynote lectures were presented. All papers were revised twice and the revisors were invited to select the 15 best papers to compose the present special edition, Advances in Turbulence: Selected Papers from the XII Spring School on Transition and Turbulence, part of the ABCM Series on Mechanical Sciences and Engineering.

As an EPTT tradition, the lectures were devoted to the education of young researchers and students, as well as to share the advanced topics in their fields. Some of these topics were multi-scale approach applied to turbulent flows, spray formation and dual-scale large eddy simulation of the atomization process, interfacial behavior of turbulent multiphase flows, disturbances in stability studies, and transition in aeronautics applications assessed by deep learning and metamodels.

The papers are organized in the following sections: Computational Fluid Dynamics, Aerodynamics, Multi-Phase Flow, and Instrumentations and Experiments.

Blumenau, Brazil	Henry França Meier
Florianópolis, Brazil	Amir Antônio Martins de Oliveira Junior
Blumenau, Brazil	Jonathan Utzig

Contents

Part I Computational Fluid Dynamics

Part II Aerodynamics

Part III Multi-Phase Flow

Part IV Instrumentation and Experiments

Contributors

Sarah Laysa Becker Federal University of Santa Catarina (UFSC), Florianopolis, SC, Brazil;
University of Blumenau, Blumenau, SC, Brazil

Matheus Maia Beraldo USP, EESC, São Paulo, SAA, Brazil

Donald J. Bergstrom Department of Mechanical Engineering, University of Saskatchewan, Saskatoon, SK, Canada

Bruna Iten Bittelbrunn University of Blumenau, Blumenau, SC, Brazil

Christine Fredel Boos Fluid Dynamics Laboratory, University of Blumenau, Blumenau, Santa Catarina, Brazil

Giovanni Belloni Fernandes Braga University of São Paulo-USP, São Paulo, Brazil

Christian Salaro Bresci USP, EESC, São Paulo, SAA, Brazil

Gabriel Narváez Campo Pontifícia Universidade Católica do Rio Grande do Sul, Porto Alegre, RS, Brazil

Luís Henrique da Silva Ignacio School of Mechanical Engineering, Federal University of Uberlândia, Uberlândia, Minas Gerais, Brazil

Barbara L. da Silva Department of Mechanical Engineering, University of Saskatchewan, Saskatoon, SK, Canada

Paula Trindade da Silva Process Engineering Department, School of Chemical Engineering, University of Campinas, Campinas, Brazil

Guilherme José de Castilho Process Engineering Department, School of Chemical Engineering, University of Campinas, Campinas, Brazil

Francisco José de Souza School of Mechanical Engineering, Federal University of Uberlândia, Uberlândia, Minas Gerais, Brazil

Rodrigo Koerich Decker Fluid Dynamics Laboratory, University of Blumenau, Blumenau, Santa Catarina, Brazil

Maicon Vinicius Ritter Deggeroni Programa de Pós-Graduação Em Engenharia Mecânica, Santa Catarina State University, Joinville, Brazil

Rodrigo de Lima Amaral NDF, Department of Mechanical Engineering, POLI, University of São Paulo, São Paulo, Brazil

Juan Pablo de Lima Costa Salazar Universidade Federal de Santa Catarina, Joinville, Brazil

Lucas Freitas de Lima e Freitas Process Engineering Department, School of Chemical Engineering, University of Campinas, Campinas, Brazil

Marcello Augusto Faraco de Medeiros University of São Paulo-USP, EESC, São Paulo, SAA, Brazil

Helder Lima de Moura Process Engineering Department, School of Chemical Engineering, University of Campinas, Campinas, Brazil

Igor Braga de Paula Department of Mechanical Engineering, Pontifical Catholic University of Rio de Janeiro, Gavea, RJ, Brazil

Ricardo Nava de Sousa Fluid Dynamics Laboratory, University of Blumenau, Blumenau, Santa Catarina, Brazil;
School of Mechanical Engineering, Federal University of Uberlândia, Uberlândia, Minas Gerais, Brazil

Carla Nayara Michels dos Santos University of Blumenau, Blumenau, SC, Brazil

Celso Murilo dos Santos University of Blumenau, Blumenau, SC, Brazil

Rubem Mário Figueiró Vargas Pontifícia Universidade Católica do Rio Grande do Sul, Porto Alegre, RS, Brazil

Livia S. Freire Instituto de Ciências Matemáticas e de Computação, University of São Paulo, São Carlos, Brazil

Omar Elias Horna Pinedo Department of Mechanical Engineering, Pontifical Catholic University of Rio de Janeiro, Gavea, RJ, Brazil

Luiz Adolfo Hegele Júnior Department of Petroleum Engineering, Santa Catarina State University, Balneário Camboriú, Brazil

Sylvain Laizet Department of Aeronautics, Imperial College London, London, UK

Guilherme Torres Marques Vidal Pontifícia Universidade Católica do Rio Grande do Sul, Porto Alegre, RS, Brazil

Waldir Pedro Martignoni University of Blumenau, Blumenau, SC, Brazil

Eckart Meiburg Department of Mechanical Engineering, University of California Santa Barbara, Santa Barbara, CA, USA

Henry França Meier Fluid Dynamics Laboratory, University of Blumenau, Blumenau, Santa Catarina, Brazil

Lucas de Souza Meira Federal University of Uberlândia, Uberlândia, MG, Brasil

José Roberto Nunhez Process Engineering Department, School of Chemical Engineering, University of Campinas, Campinas, Brazil

Natan Padoin Federal University of Santa Catarina (UFSC), Florianopolis, SC, Brazil

Harlley Henrique Parno University of Blumenau, Blumenau, SC, Brazil

Pedro Bruno Pereira Panisset Department of Mechanical Engineering, Pontifical Catholic University of Rio de Janeiro, Gavea, RJ, Brazil

Carlos Antonio Ribeiro Duarte Department of Engineering, Federal University of Catalão, Catalão, Goiás, Brazil

Sávio Brochini Rodrigues Federal University of São Carlos-UFSCar, São Carlos, Brazil

Vivien Rossbach Federal University of Santa Catarina (UFSC), Florianopolis, SC, Brazil;
University of Blumenau, Blumenau, SC, Brazil

Felipe Nornberg Schuch School of Technology, Pontifical Catholic University of Rio Grande do Sul, Porto Alegre, Brazil

Cristian Ricardo Schwatz Fluid Dynamics Laboratory, University of Blumenau, Blumenau, Santa Catarina, Brazil

Diogo Nardelli Siebert Universidade Federal de Santa Catarina, Joinville, Brazil

Jorge Hugo Silvestrini School of Technology, Pontifical Catholic University of Rio Grande do Sul, Porto Alegre, RS, Brazil

Cintia Soares Federal University of Santa Catarina (UFSC), Florianopolis, SC, Brazil

David Sumner Department of Mechanical Engineering, University of Saskatchewan, Saskatoon, SK, Canada

Jonathan Utzig Fluid Dynamics Laboratory, University of Blumenau, Blumenau, Santa Catarina, Brazil

Victor Barcelos Victorino USP, EESC, São Paulo, SAA, Brazil

Julia Volkmann Fluid Dynamics Laboratory, University of Blumenau, Blumenau, Santa Catarina, Brazil

Part I
Computational Fluid Dynamics

Chapter 1
Dynamic Flow Structures in the Wake of a Surface-Mounted Finite-Height Square Prism

Barbara L. da Silva, David Sumner, and Donald J. Bergstrom

Abstract The flow around surface-mounted finite-height square prisms is complex due to the strong three-dimensionality of the flow, especially for prisms of small aspect ratio AR = H/D (where D is the prism width and H is its height). Different flow models have been proposed in the literature to describe the dynamic flow structures in the wake of surface-mounted prisms, although gaps and inconsistencies remain—for instance, in explaining the origins of regions of high streamwise vorticity in the upper part of the wake. This study aims to explore the dynamic flow structures in the wake of a surface-mounted finite-height square prism of AR = 3 at a Reynolds number of Re = 500 based on the prism width, with a thin boundary layer on the ground plane. Large-eddy simulation results were analyzed using a phase-average approach to extract the dominant periodic features of the wake. The phase-averaged flow fields show the occurrence of alternating structures similar to half-loops, although the regions of highest streamwise vorticity take place outside the near-wake formation region and are associated with the downwash and with a large-scale motion of the wake in the transverse direction. The dynamic behavior of the wake reveals the alternate entrainment of fluid close to the ground plane. In contrast, the upper region of the wake is more symmetric.

Keywords Surface-mounted finite-height square prism · Turbulent wake · Bluff body · Large-eddy simulation · Phase average

---

B. L. da Silva (✉) · D. Sumner · D. J. Bergstrom
Department of Mechanical Engineering, University of Saskatchewan, 57 Campus Drive,
Saskatoon, SK S7N 5A9, Canada
e-mail: barbara.silva@usask.ca

D. Sumner
e-mail: david.sumner@usask.ca

D. J. Bergstrom
e-mail: don.bergstrom@usask.ca

H. F. Meier et al. (eds.), *Advances in Turbulence*, ABCM Series on Mechanical Sciences and Engineering, https://doi.org/10.1007/978-3-031-25990-6_1

1.1 Introduction

The flow around bluff bodies is found in many situations, including moving automobiles and trucks, the wind around buildings, chimneys and wind turbines, and the wind and ocean currents acting on offshore structures. In engineering applications, a common approach to facilitate the study of the flow field around complex obstacles is by approximating them to simpler geometries, such as a circular or square prism. For a prism of height H and characteristic length D, if the aspect ratio $\mathrm{AR} = H/D$ is very high, a two-dimensional or "infinite" assumption can be made so that the end effects of the prism are negligible. In this case, flow separation and subsequent vortex shedding are assumed to take place along the entire prism height.

The flow field and fluid forces for the infinite (two-dimensional) prism are reasonably well understood over a wide range of flow conditions (e.g., Igarashi 1984; Ozgoren 2006). However, for most applications, the end conditions of the prism change the flow significantly by introducing three-dimensional structures, which make the flow field and the fluid-obstacle interactions more complex. For the specific case of the cross-flow around a surface-mounted finite-height square prism, one of its ends (the junction) is attached to a ground surface, and the other end (the free end) is exposed to the flow and subject to flow separation. Some of the main flow structures of the time-averaged wake are illustrated in Fig. 1. They include the horseshoe vortex system, lateral and top recirculation regions due to the flow separation from the upstream edges of these surfaces, the top and base counter-rotating pairs of streamwise vortices (not shown in the figure), the corner vortices and a recirculation region downstream of the prism with downwash (Wang and Zhou 2009; Sumner et al. 2017; Zhang et al. 2017; da Silva et al. 2020). The presence of some of the flow structures in the wake may depend on the prism AR, the relative boundary layer thickness δ/D or δ/H, and the Reynolds number $\mathrm{Re} = U_\infty D/\nu$, where U_∞ is the freestream velocity and ν is the kinematic viscosity of the fluid. For example, the streamwise vorticity pair at the upper part of the wake is typically always present and associated with the downwash, whereas the base vortices are sometimes absent, especially for thin boundary layers (Hosseini et al. 2013). In this case, the wake is a dipole type. When the base vortices are present, they are usually accompanied by an upwash flow in the wake, and the wake is characterized as a quadrupole type.

Various flow models have been proposed to explain the instantaneous wake behavior of surface-mounted finite-height square prisms. The model of Sakamoto and Arie (1983) introduced a critical AR that subdivided the occurrence of different structures: above the critical AR, the near wake would present the antisymmetric von Kármán vortex shedding along the prism height, except for regions close to the free end or the prism-ground junction (Wang et al. 2004). Below the critical AR, an arch-type or hairpin vortex would prevail, which consists of two spanwise "legs" connected near the free end and shed in a contiguous manner from the top and lateral surfaces (Kawai et al. 2012; Sakamoto and Arie 1983). Instantaneous particle image velocimetry (PIV) measurements performed by Wang and Zhou (2009) resulted in the proposal of a different flow model, where the near-wake structure was described

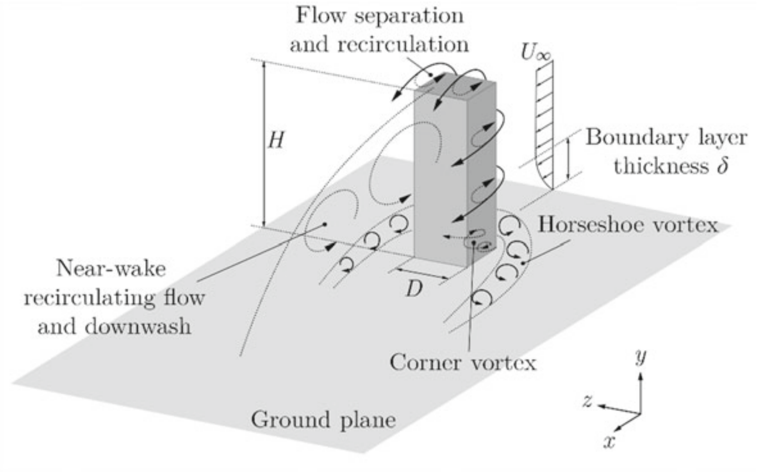

Fig. 1 Schematic of the flow around a surface-mounted finite-height square prism

as an arch vortex even above the critical AR. The arch vortex was found to be shed with symmetric and antisymmetric modes, with the symmetric mode being more frequent for lower AR.

One of the main points addressed in the model of Wang and Zhou (2009) was the source of the large streamwise vorticity regions. Earlier studies like Wang et al. (2004) attributed the streamwise vorticity in the upper part of the wake to independent structures that were formed from the corners of the tip of the prism—hence their common name, "tip vortices". Wang and Zhou (2009), on the other hand, found the streamwise vorticity to be associated with the projection of the vertically inclined arch vortices, and therefore to be a part of the overall wake structure.

A more recent interpretation of the structures in the near wake of a surface-mounted finite-height square prism was proposed by Bourgeois et al. (2011), based on a phase average analysis of the dipole wake of a prism with AR = 4, also using PIV. The authors observed an always antisymmetric shedding of half-loop structures in the wake of the prism. Each half-loop consisted of an approximately vertical leg at the ground surface, resembling a Kármán vortex, connected at its top to adjacent half-loops by a mostly streamwise strand. In the case of a quadrupole wake, full loops with additional connector strands at their bases were observed instead (Hosseini et al. 2013).

In this flow model, the time-averaged streamwise vorticity was associated with the averaging of the connector strands of the half-loops, argued to be generated from the combination of the two other vorticity components of the flow detaching from the top and sides of the prism. However, these streamwise strands are inclined downward and shown to be connected to the base of the next half-loop. Its proximity to the ground plane is, therefore, inconsistent with the location of the large time-averaged streamwise vorticity regions. da Silva et al. (2020) investigated the time-averaged wake of a surface-mounted finite-height square prism with AR = 3, and found the mean streamwise vorticity to be formed from the three-dimensional bending of the flow that encircles the near wake, caused by the downwash.

Other recent studies addressed different aspects of the dynamic wake of surface-mounted finite-height square prisms, which include the effects of the flow on wind load fluctuations (Zu and Lam 2018), the occurrence of symmetric and antisymmetric shedding modes (Sattari et al. 2012; Behera and Saha 2019), low-frequency instabilities near the free end (Kindree et al. 2018), the influence of the boundary layer thickness on the horseshoe vortex interaction with the wake (El Hassan et al. 2015) and the occurrence of cellular shedding, which is found mostly for larger AR (Porteous et al. 2017; Yauwenas et al. 2019). However, the dynamic wake of surface-mounted finite-height square prisms is not yet fully clarified and contradictions remain about the shape of these structures, the cause of the streamwise vorticity regions, and the overall mechanism of shedding for this type of bluff body. The present study aims to address this gap in the literature, using a surface-mounted finite-height square prism with AR = 3 and Re = 500 as a reference case. The dynamic features of the wake will be investigated based on the phase-averaged flow field around the prism.

1.2 Computational Models and Methods

A large-eddy simulation (LES) of the flow around a surface-mounted finite-height square prism was performed for the present analysis, with the dynamic Lagrangian subgrid-scale model of Meneveau et al. (1996). The prism had a width of $D = 0.02$ m and an aspect ratio of AR = 3. The computational domain, presented in Fig. 2a, extends $20D$ in the streamwise (x) direction, $15D$ in the transverse (y) direction, and $10D$ in the vertical (z) direction, with the inlet boundary located $3.5D$ upstream of the prism center. The origin of the computational domain is located at the center of the base of the prism.

A uniform speed of 0.375 m/s was prescribed for the inlet, which gave a Reynolds number Re = 500 and a relative boundary layer thickness of $\delta/D = 0.39$ (or $\delta/H = 0.13$) at the location of the prism, considered "thin" according to the criteria of

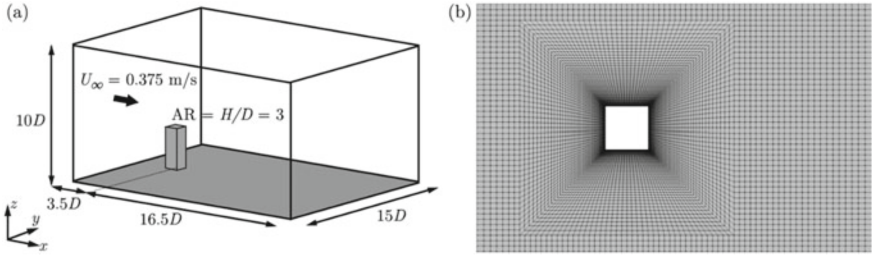

Fig. 2 **a** Computational domain and **b** section of the grid near the prism in an x–y plane

Sakamoto and Arie (1983). No-slip boundary conditions were used for the prism and ground plane surfaces, free-slip boundary conditions were used for the top and lateral boundaries and a convective outflow condition was imposed at the boundary downstream of the prism. The hexahedral grid had 2,110,336 elements, with 40 elements along each of the horizontal edges of the prism and 86 elements along its height. A slice of the grid normal to the z-axis is illustrated in Fig. 2b. The grid was refined near the prism and ground plane surfaces to ensure that the first wall-normal elements had $y^+ < 1$. In addition, adequate grid resolution was verified based on the ratio of the subgrid-scale viscosity and the fluid viscosity (ν_{SGS}/ν) and the ratio of the cubic root of the grid cell volume Δ and the estimated Kolmogorov length scale $\eta = (\nu^3/\varepsilon)^{1/4}$ (Pope 2000) (Δ/η). The maximum values found in the time-averaged wake were $\nu_{\mathrm{SGS}}/\nu = 0.4$ and $\Delta/\eta = 3.8$, confirming that the majority of the flow scales were resolved.

The simulation was carried out using the pisoFoam solver of OpenFOAM v6. The central-differencing scheme was used in the spatial discretization of both advective and gradient terms, and a second-order implicit scheme was used for time. The time step was fixed at 2×10^{-5} s, which kept the values of the Courant–Friedrichs–Lewy (CFL) number below 0.3. After the flow was observed to be fully developed, 1000 time samples or snapshots were collected for a period of approximately 20 vortex shedding cycles.

In addition to the time average, a phase average analysis was performed, based on the triple decomposition of Reynolds and Hussain (1972) for periodic flows. In this approach, a fluctuating signal or flow field u may be decomposed into a time average contribution U, a periodic fluctuation $\tilde{u}$ and a turbulent fluctuation u':

$$u = U + \tilde{u} + u'. \tag{1}$$

The phase-averaged field $\langle u \rangle$ is defined as the ensemble average over a large number of samples which have the same phase as a reference signal, or:

$$\langle u \rangle = U + \tilde{u}. \tag{2}$$

During the time averaging, the force coefficients of the prism were also recorded and the lift coefficient history was used as the reference signal to delimit the extent and phases of each vortex shedding period. Figure 3a presents the lift coefficient C_L versus the simulation flow time t normalized by the mean vortex shedding period $T = 1/f$, where f is the vortex shedding frequency. This frequency was obtained from the fast Fourier transform of the lift coefficient history (Fig. 3b), and it corresponds to a Strouhal number $\mathrm{St} = fD/U_\infty = 0.115$. Although other peaks with $\mathrm{St} = 0.025$ and 1.56 are present in the spectrum, the peak with $\mathrm{St} = 0.115$ agrees with the average value of 0.11 reported in the literature (Saha 2013; McClean and Sumner 2014; Zhang et al. 2017), and corresponds to the large-scale vortex shedding periodicity.

The periods in the lift coefficient history were identified based on the inflexion points in C_L, but only the ones that were close to the mean period T within a chosen tolerance of 30% were considered for the ensemble average. Each period was then

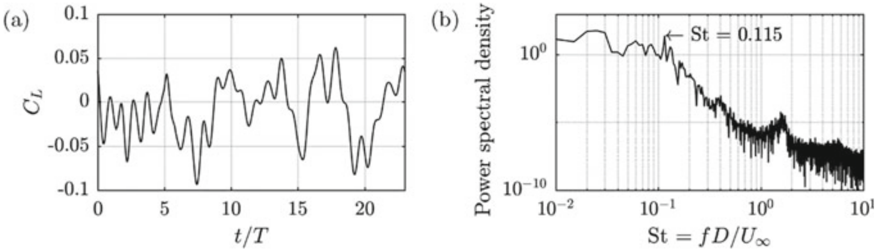

Fig. 3 **a** History and **b** spectrum of the lift coefficient of the surface-mounted finite-height square prism

discretized into 20 phase bins, following the procedure used by Bourgeois et al. (2011). The velocity field samples which occurred within the time intervals of a given phase bin were collected and ensemble-averaged for all periods, yielding 20 phase-averaged flow fields.

1.3 Results and Discussion

In this section, the mean flow field around the surface-mounted finite-height square prism will first be introduced, for comparison with the flow described in other studies under similar flow conditions. The phase-averaged features of the flow will then be addressed.

1.3.1 Mean Flow Field

Figure 4 presents mean velocity contours and streamlines in the x–z symmetry plane, where the region of reverse flow in the near wake and some of the critical points are highlighted. The flow field is very similar to the one obtained in the DNS of Zhang et al. (2017) for the same Re = 500 but for AR = 4. Vortices Bt and Nw, following the nomenclature of Sumner et al. (2017) and Krajnović (2011), are present in the upper and lower parts of the near wake, respectively. While vortex Bt is a common feature in the mean wake of surface-mounted finite-height square prisms, vortex Nw is present in the wake of prisms above the critical AR (Sumner et al. 2017). The horseshoe vortex can also be spotted upstream of the surface-mounted prism, at a similar location to Zhang et al. (2017) and da Silva et al. (2020).

The mid-height recirculation length, defined here as the distance between the center of the prism to the last point where the mean streamwise velocity component is equal to zero, is also illustrated in the figure. The present mean length of $L_r/D = 5.5$ is close to the ones obtained by Zhang et al. (2017) ($L_r/D \approx 6$, AR = 4, Re = 500) and Saha (2013) ($L_r/D \approx 6.5$, AR = 3, and Re = 250), but larger than the

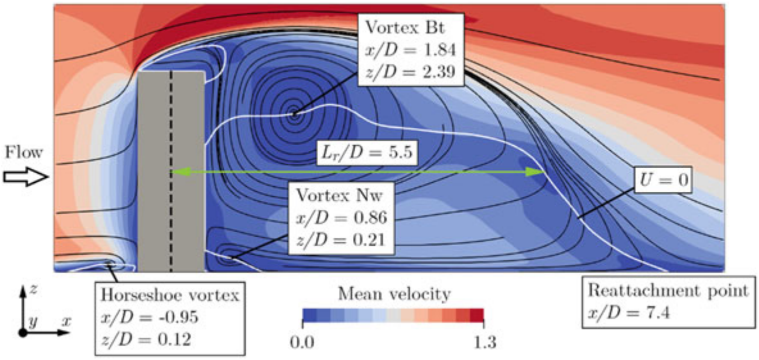

Fig. 4 Contours and streamlines of the mean flow velocity normalized by U_∞ in the x–z symmetry plane. The white contour line indicates where the mean streamwise velocity component U is equal to zero

recirculation length obtained in da Silva et al. (2020) ($L_r/D = 3.52$, AR = 3, and Re = 500), where a different subgrid-scale model was used. The maximum recirculation length, denoted by the reattachment point of the wake in Fig. 4, compares the same way with these other studies. The large reattachment length and the absence of a saddle point in the symmetry plane velocity streamlines are characteristics of a wake dominated by downwash, without an upwash region as obtained by Zhang et al. (2017) for smaller δ/D.

The mean streamwise vorticity $\omega_x D/U_\infty$ is shown in Fig. 5 in y–z planes located downstream of the prism at $x/D = 4$, 6.5, and 10, with the mean velocity vector field parallel to the planes included. Downwash is visible in the upper part of the wake for all planes, with a strength that correlates with the strength of the pair of streamwise vorticity regions. These vorticity regions show the typical counter-clockwise sense of rotation at the $+y$ side and clockwise sense of rotation at the $-y$ side of the wake. Although additional vorticity regions are present in the lower part of the wake, the flow upwash is not significant to generate stable “base vortices” and the wake is a dipole type. This is confirmed by the second invariant of the velocity gradient tensor $QD^2/U_\infty^2 = 0.01$ in Fig. 6, which shows prolonged tubes dominated by the streamwise vorticity that go into the far-wake region.

The shape and progression of the large mean streamwise vorticity regions in the x direction agree with the results of Zhang et al. (2017). They are positioned higher in the wake at $x/D = 4$, which is located inside the near-wake recirculation region, and have a side extension which was also reported by Kindree et al. (2018) for the high-Re wake of an AR = 4 prism. The large vorticity regions move downward downstream, increasing in size and reaching their highest magnitude at about $x/D = 6.5$, which is just outside the near-wake region in agreement with da Silva et al. (2020). Their size increases at $x/D = 10$, but the overall magnitude of the streamwise vorticity decreases.

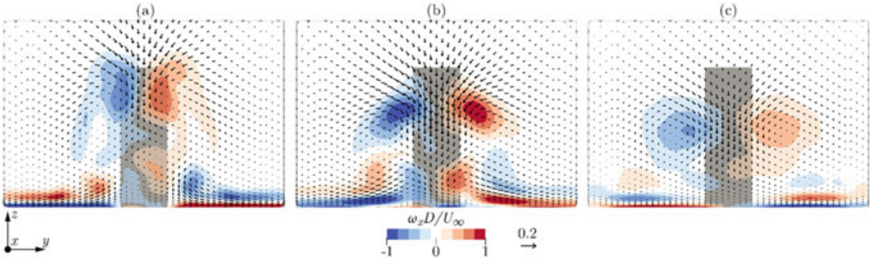

Fig. 5 Contours of the mean streamwise vorticity and mean velocity vector field parallel to y–z planes located at **a** $x/D = 4$, **b** $x/D = 6.5$, and **c** $x/D = 10$. Every third vector is shown in the y and z directions

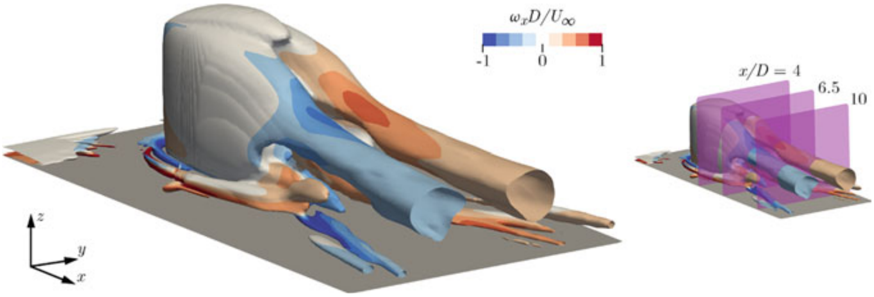

Fig. 6 Isosurface of the second invariant of the mean velocity gradient tensor $QD^2/U_\infty^2 = 0.01$ colored by the mean streamwise vorticity, and reference for the location of the planes in Fig. 5

The large upper vorticity regions originate from the bending of the flow that encircles the near wake by the downwash, as explained in da Silva et al. (2020), but the other streamwise vorticity regions in Fig. 5 have different sources. The very near-ground flow presents streamwise vorticity related to the inward flow in the near wake, and it transitions into an outward flow at $x/D = 6.5$ and 10 associated with the expansion of the mean wake in the y direction, downstream. Other streamwise vorticity regions of low magnitude are induced by this near-ground flow, but, at $x/D = 4$ and 6.5, there are minor regions of strong vorticity that are generated from the entrainment of fluid into the wake. This mechanism is related to the bottom section of the near wake described in da Silva et al. (2020). This flow was also observed in other studies for different aspect ratios and flow conditions (Shah and Ferziger 1997; Sau et al. 2003; El Hassan et al. 2015), with the entrainment mechanism closer to the prism having been attributed to the interaction between the wake and the horseshoe vortex. Note that the cores of the trailing arms of the horseshoe vortex are not observed in the y–z plane with $x/D = 4$ in Fig. 5a, which suggests that it has weakened significantly at this location possibly due to the thin boundary layer.

Overall, the time-averaged flow field presents a behavior consistent with the one reported in other studies, validating a qualitative analysis of the features of the phase-averaged flow.

1.3.2 Phase-Averaged Flow Field

The phase-averaged flow around the surface-mounted finite-height square prism is presented in Fig. 7 through isosurfaces of the second invariant of the phase-averaged velocity gradient tensor ($\langle Q\rangle D^2/U_\infty^2 = 0.1$), colored by the phase-averaged streamwise vorticity. The selected phases represent the progression of the phase-averaged flow for one half of the mean shedding period with St $= 0.115$.

The phase-averaged flow structures in Fig. 7 resemble the half-loops described by Bourgeois et al. (2011), but the vertical legs are only well defined in the near-wake region. The far wake is dominated by the streamwise strands of the structures, which are formed close to the middle of the wake and expand outward as they are convected downstream. Phases 1–11 show the shedding process of structure A with positive streamwise vorticity at the $+y$ side of the wake. Two additional structures which were "previously" shed are also visible: structure B with negative streamwise vorticity and structure C with positive streamwise vorticity, which corresponds to A in this phase-averaged period. At phase 11, structure D, which corresponds to B, is shed still with its vertical leg. More details about these vorticity distributions are presented in Fig. 8 in the y–z planes with $x/D = 4$, 6.5, and 10, which represent the near-wake, transition, and far-wake regions, respectively.

The large vorticity regions in the upper part of the wake in Fig. 8 follow the same patterns of the time-averaged vorticity in Fig. 5, regarding changes along x/D. The phases 1/20 and 11/20, which are opposite to each other, show that the vorticity

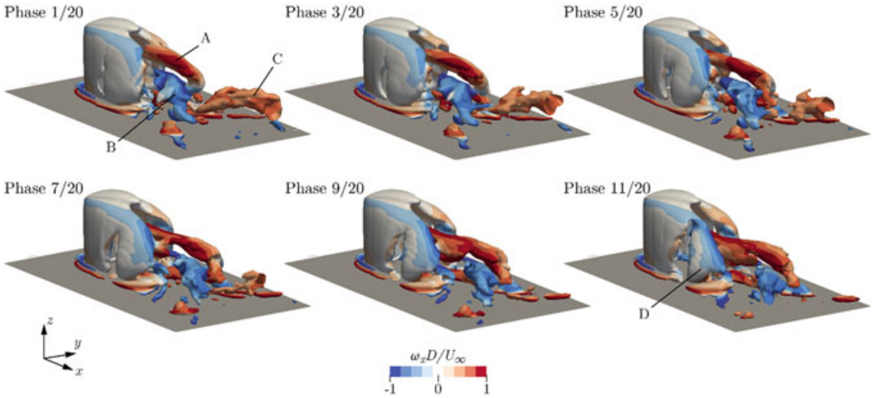

Fig. 7 Isosurface of the second invariant of the phase-averaged velocity gradient tensor $\langle Q\rangle D^2/U_\infty^2 = 0.1$ colored by the phase-averaged streamwise vorticity at selected phases

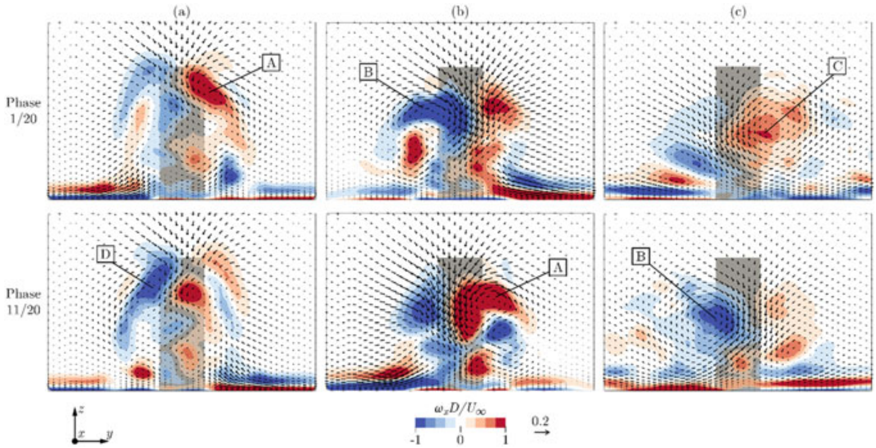

Fig. 8 Contours of the phase-averaged streamwise vorticity and velocity vector field parallel to y–z planes located at **a** $x/D = 4$, **b** $x/D = 6.5$, and **c** $x/D = 10$ for phases 1/20 and 11/20. Every third vector is shown in the y and z directions

alternates in strength between the sides of the wake following the structures of Fig. 7. For example, at $x/D = 6.5$ (Fig. 8b), structure B occupies the $-y$ side of the wake at phase 1/20, while structure A is stronger at the $+y$ side at phase 11/20. The fluid entrainment caused by the downwash follows this alternate behavior, as shown by the phased-averaged velocity vector fields. Streamlines of the phase-averaged velocity field are presented in Fig. 9a for the same phases as Fig. 8, located at the upper part of the wake (seed points at $x/D = -0.17$, $y/D = \pm 0.2$, $z/D = 0.67$–1). They confirm the association of the downwash-induced fluid entrainment with the structures' streamwise strands and reveal a large-scale motion of the phase-averaged wake in the transverse direction. In addition, the flow in the near wake by the top of the prism ($z/D = 3$) is shown to be more symmetric, in agreement with the reports of Wang and Zhou (2009), Sattari et al. (2012), and Behera and Saha (2019) and in contrast with the flow in the bottom section of the wake in Fig. 9b.

The phase-averaged flow in the bottom part of the wake has a more complex behavior. At $x/D = 4$ (Fig. 8a), an additional streamwise vorticity region of high intensity is found at the same side of the major upper vorticity, but with an opposite sense of rotation, near the ground plane. It resembles the base vortex of a full-loop structure (Hosseini et al. 2013), which is typically found for thicker boundary layers, and may be related to the presence of vortex Nw in Fig. 4. This vorticity distribution and the shape of the structures in Fig. 7 suggest that the shed structures have initially a full-loop shape, but they are molded into the streamwise strands downstream by the downwash and the surrounding flow.

At $x/D = 6.5$ (Fig. 8b), the streamwise vorticity distribution is connected to the alternate fluid entrainment mechanism close to the ground plane. The streamlines in Fig. 9b were seeded at $x/D = -0.17$, $y/D = \pm 0.25$, and $z/D = 0$–0.2 to illustrate this mechanism. Note that the main horseshoe vortex has significant strength only

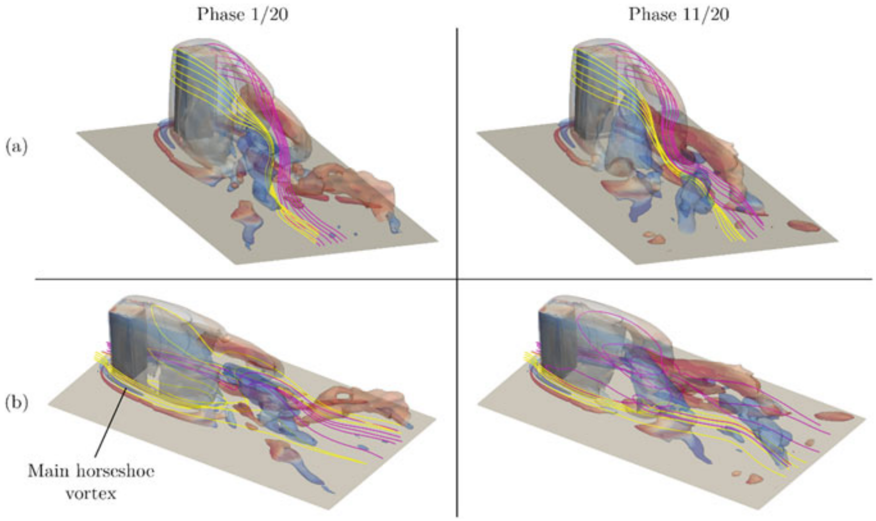

Fig. 9 Representative streamlines of the flow at the **a** top and **b** bottom sections of the phase-averaged wake, overlapped with the semi-transparent isosurfaces of Fig. 7 for phases 1/20 and 11/20. Streamlines originating at the $-y$ and $+y$ sides of the domain are colored yellow and magenta, respectively

in the very-near-wake region, but its induced vorticity of opposite sense of rotation extends into the near wake from the $-y$ side at phase 1/20, causing the strong positive (counter-clockwise) vorticity at this side which is also visible at $x/D = 4$ (Fig. 8a). Some of the streamlines ascend inside the near-wake region, following the same mechanism described in da Silva et al. (2020), while others encircle structures A and B. On the other side of the wake at phase 1/20, fluid entrainment still occurs but it is more subtle and bypasses the near-wake recirculation region. At phase 11/20, the described mechanisms shift sides, causing stronger vorticity concentrations near the ground plane at the $+y$ side of the wake.

The upper phase-averaged streamwise vorticity regions are, overall, less intense at $x/D = 10$ (Fig. 8c) due to the dissipation of the flow structures in the far wake. Additional low-magnitude vorticity regions are, still, alternately induced by the interaction of the vorticity near the ground plane and the flow structures, following the large-scale transverse movement of the wake.

1.4 Conclusions

The flow around a surface-mounted finite-height square prism with AR $= 3$, Re $=$ 500, and $\delta/D = 0.39$ was investigated based on large-eddy simulation results. An analysis of the time-averaged flow field served as a means to provide qualitative validation, by comparing several of its elements like the mean wake recirculation length and streamwise vorticity distribution with published studies of this type of flow.

The dynamic wake of the surface-mounted finite-height square prism was investigated based on the phase-averaged flow field. Alternate flow structures similar to the half-loops of Bourgeois et al. (2011) were found, but with two major differences for the present flow conditions. First, despite the thin boundary layer, the structures consisted more of full loops in their formation, with the base vorticity disappearing outside the near wake. Second, the far wake was dominated by the streamwise strands of these structures, due to the downwash-induced entrainment of the surrounding fluid in the upper region, which caused a large-scale alternating motion of the wake in the transverse direction.

The phase-averaged flow near the top of the prism in the near wake had a more symmetric behavior, but an antisymmetric fluid entrainment mechanism was found in the bottom section of the wake, near the ground plane. This mechanism was not caused directly by the main horseshoe vortex, but by the fluid nearby it. It took place simultaneously on both sides of the wake, although in different ways depending on the arrangement of the phase-averaged flow structures.

Acknowledgements Financial support from the National Sciences and Engineering Research Council of Canada (NSERC) Discovery Grants program and the University of Saskatchewan's Dean's Scholarship program is gratefully acknowledged.

References

Behera S, Saha AK (2019) Characteristics of the flow past a wall-mounted finite-length square cylinder at low Reynolds number with varying boundary layer thickness. J Fluids Eng 141:061204

Bourgeois JA, Sattari P, Martinuzzi RJ (2011) Alternating half-loop shedding in the turbulent wake of a finite surface-mounted square cylinder with a thin boundary layer. Phys Fluids 23:095101

da Silva BL, Chakravarty R, Sumner D, Bergstrom DJ (2020) Aerodynamic forces and three-dimensional flow structures in the mean wake of a surface-mounted finite-height square prism. Int J Heat Fluid Flow 83:108569

El Hassan M, Bourgeois J, Martinuzzi R (2015) Boundary layer effect on the vortex shedding of wall-mounted rectangular cylinder. Exp Fluids 56:33

Hosseini Z, Bourgeois JA, Martinuzzi RJ (2013) Large-scale structures in dipole and quadrupole wakes of a wall-mounted finite rectangular cylinder. Exp Fluids 54:1595

Igarashi T (1984) Characteristics of the flow around a square prism. Bull JSME 27:1858–1865

Kawai H, Okuda Y, Ohashi M (2012) Near wake structure behind a 3D square prism with the aspect ratio of 2.7 in a shallow boundary layer flow. J Wind Eng Ind Aerodyn 104–106:196–202

Kindree MG, Shahroodi M, Martinuzzi RJ (2018) Low-frequency dynamics in the turbulent wake of cantilevered square and circular cylinders protruding a thin laminar boundary layer. Exp Fluids 59:186

Krajnović S (2011) Flow around a tall finite cylinder explored by large eddy simulation. J Fluid Mech 676:294–317

McClean JF, Sumner D (2014) An experimental investigation of aspect ratio and incidence angle effects for the flow around surface-mounted finite-height square prisms. J Fluids Eng 136:081206

Meneveau C, Lund TS, Cabot WH (1996) A Lagrangian dynamic subgrid-scale model of turbulence. J Fluid Mech 319:353–385

Ozgoren M (2006) Flow structure in the downstream of square and circular cylinders. Flow Meas Instrum 17:225–235

Pope SB (2000) Turbulent flows. Cambridge University Press, Cambridge, UK

Porteous R, Moreau DJ, Doolan CJ (2017) The aeroacoustics of finite wall-mounted square cylinders. J Fluid Mech 832:287–328

Reynolds WC, Hussain AKMF (1972) The mechanics of an organized wave in turbulent shear flow. Part 3. Theoretical models and comparisons with experiments. J Fluid Mech 54:263–288

Saha AK (2013) Unsteady flow past a finite square cylinder mounted on a wall at low Reynolds number. Comput Fluids 88:599–615

Sakamoto H, Arie M (1983) Vortex shedding from a rectangular prism and a circular cylinder placed vertically in a turbulent boundary layer. J Fluid Mech 126:147–165

Sattari P, Bourgeois JA, Martinuzzi RJ (2012) On the vortex dynamics in the wake of a finite surface-mounted square cylinder. Exp Fluids 52:1149–1167

Sau A, Hwang RR, Sheu TWH, Yang WC (2003) Interaction of trailing vortices in the wake of a wall-mounted rectangular cylinder. Phys Rev E 68:056303

Shah KB, Ferziger JH (1997) A fluid mechanicians view of wind engineering: large eddy simulation of flow past a cubic obstacle. J Wind Eng Ind Aerodyn 67–68:211–224

Sumner D, Rostamy N, Bergstrom DJ, Bugg JD (2017) Influence of aspect ratio on the mean flow field of a surface-mounted finite-height square prism. Int J Heat Fluid Flow 65:1–20

Wang HF, Zhou Y, Chan CK, Wong WO, Lam KS (2004) Flow structure around a finite-length square prism. In: Proceedings of the 15th Australasian fluid mechanics conference, Sydney, Australia, 13–17 Dec 2004

Wang HF, Zhou Y (2009) The finite-length square cylinder near wake. J Fluid Mech 638:453–490

Yauwenas Y, Porteous R, Moreau DJ, Doolan CJ (2019) The effect of aspect ratio on the wake structure of finite wall-mounted square cylinders. J Fluid Mech 875:929–960

Zhang D, Cheng L, An H, Zhao M (2017) Direct numerical simulation of flow around a surface-mounted finite square cylinder at low Reynolds numbers. Phys Fluids 29:045101

Zu G, Lam KM (2018) Simultaneous measurement of wind velocity field and wind forces on a square tall building. Adv Struct Eng 21:2241–2258

Chapter 2
The Turbulence Damping Effect on the Slug Flow Modeling

Harlley Henrique Parno, Bruna Iten Bittelbrunn, Carla Nayara Michels dos Santos, Sarah Laysa Becker, Christine Fredel Boos, Celso Murilo dos Santos, Waldir Pedro Martignoni, and Henry França Meier

Abstract The slug flow is one of the most complex flow patterns due to the unstable behavior of phase distribution. This pattern occurs in a wide range of flow rates and therefore is observed in different industrial processes. The prediction and understanding of the hydrodynamic parameters of this flow regime have a significant engineering value. In this context, Computational Fluid Dynamics (CFD) has been shown to be an efficient tool for the prediction of this type of flow. However, to ensure the accuracy of the numerical solution, adequate modeling of interfacial properties transfer is necessary. One of the most important interface transfer phenomena is momentum transfer between phases. Therefore, it is necessary to use a robust approach to model the gas–liquid interface region. The aim of this study is to evaluate the effect of adding the damping of turbulent diffusion at the interface on flow modeling. For this, different cases of simulations were elaborated for a pipe with 2 m in length and 26 mm inner diameter. In all the cases, the multiphase approach used was the Volume of Fluid (VOF) with the Geo-Reconstruct scheme. The interface between the fluids was modeled with constant surface tension equal to 0.0728 N/m. The discontinuities present at the interface were treated in a "continuous surface stress" (CSS) manner. The turbulence was modeled using kω-SST with and without turbulence damping. The independence of the numerical solution in relation to the grid was evaluated by the Grid Convergence Index (GCI) method in which four levels of grid were used. Preliminary results showed that, in the cases with turbulence damping, a better representation of the flow pattern morphology was obtained. Regarding the quantitative parameters, the prominent frequency of the Power Spectral Density (PSD) of the pressure signal was under-predicted when the turbulence damping was not used.

H. H. Parno · B. I. Bittelbrunn · C. N. M. dos Santos · S. L. Becker · C. F. Boos · C. M. dos Santos · W. P. Martignoni · H. F. Meier (✉)
University of Blumenau, 3250 São Paulo Street, Blumenau, SC, Brazil
e-mail: meier@furb.br

H. H. Parno
e-mail: hparno@furb.br

C. F. Boos
e-mail: cfboos@furb.br

H. F. Meier et al. (eds.), *Advances in Turbulence*, ABCM Series on Mechanical Sciences and Engineering, https://doi.org/10.1007/978-3-031-25990-6_2

Keywords Slug flow · Interfacial modeling · Turbulence damping

2.1 Introduction

Two-phase flows are observed in numerous industrial and natural processes. Due to the surface tension force, an interface between the fluids is created and the fluids flow separately such as bubbles and droplets. Additionally, the gravity force segregates the flow by differences in density. As a result, horizontal two-phase flow is naturally stratified. However, the difference in fluid density also induces velocity and pressure gradients between phases. The instabilities generated by the gradients develop very small waves. Depending on operating conditions, the mass and momentum transfer between interfacial microwaves develop two-phase flow patterns.

Regarding the gas–liquid flow patterns, intermittent flow is one of the most observed in industrial processes. The slug and plug flows are characterized by a wave that closes the pipe cross-sectional area. The difference between plug and slug flows is the presence of gas bubbles in the liquid slug. Based on the gas quantity inside the liquid slug, the flow is subclassified in low- and high-aerated slugs. Slug flow is characterized by the occurrence of high pressure, velocity, and volume fraction oscillations. High slug frequency not only increases the pressure loss (drop) but also increases the material injury. Because of that, slug flow is undesirable in the majority part of industrial processes such as boilers, refrigeration systems, and several processes in the gas–oil industry. An exception is the two-phase flow in multichannel reactors, in which some authors related that the slug flow pattern increases the liquid–gas mixture in the reactor channels and the efficiency consequently also increased (Tonomura et al. 2018).

In the last century, several experimental studies have been conducted in order to understand the onset and development of the slug flow, mainly with flow studied in pipelines. Experimental studies commonly use volume fraction and pressure measurements to identify and classify the flow pattern. In addition, a flow visualization study helps to identify the pattern. Besides that, researchers developed charts to predict the gas–liquid flow patterns transition based on both phase-operating conditions (Baker 1953). One of the first explanations for slug formation was conducted by Taitel and Dukler (1976). They explain the formation of slug flow patterns due to the Kelvin–Helmholtz (KH) instabilities. Classical KH instabilities provide stability criteria of infinitesimal amplitude waves to be formed at the free surface.

Several authors have been conducted to propose empirical correlations to predict important parameters in two-phase flow such as frequency. This is one of the most important parameters due to the direct impact on pressure loss and material damage in industrial devices caused by the passage of slugs in the pipes. Empirical correlations based on non-dimensional numbers, such as the Strouhal and Froude numbers, were developed to predict the slug frequency. Gregory and Scott (1969) were the first authors to calculate the slug frequency based on non-dimensional slug frequency. Fossa et al. (2003) were the first author to propose an empirical correlation for slug frequency based on the Strouhal number. They proposed that the Strouhal number for slug flow is dominated by the gas velocity. Wang et al. (2007) modified the Strouhal number correlation considering the liquid velocity as well.

Recently, an empirical correlation for slug frequency was proposed by Thaker and Banerjee (2015). They assumed that the non-dimensional frequency is a product of Strouhal and Froude numbers. The non-dimensional frequency is obtained by an empirical correlation based on gas and liquid Reynolds numbers and the non-dimensional length. The empirical coefficients were obtained by linear regression of experimental measurements. The experiments were conducted in a wide range of Reynolds numbers for both phases (1400–18,500 for water and 390–7500 for air). The experimental data were obtained in a 25.4 mm pipe diameter and 8 m pipe length. The authors relate that the correlations prediction is in accordance with experimental observations such as the frequency decrease with the length.

Other experimental investigations were carried out in order to develop models to predict other important properties of slug flow, such as slug length, liquid holdup, pressure drop, velocity, and others (Barnea and Brauner 1985; Barnea and Taitel 1993; Cook and Behnia 2000; Gregory and Scott 1969; Greskovich and Shrier 1971; Nydal et al. 1992; Scott et al. 1989; Van Hout et al. 2002). Over time, several numerical strategies have been developed to predict the behavior of this flow pattern in a more detailed way.

For a better understanding of the phenomenon, computational fluid dynamics (CFD) have been used for decades to be able to predict the behavior of this type of flow. Although the one-dimensional (1D) numerical models are capable to predict pressure loss, they are not capable to predict the two-phase flow patterns. However interesting results are reported when a two-dimensional (2D) model is applied. One of the first studies involving two-phase flow 2D interfacial modeling was conducted by Lun et al. (1996). The researchers found a high dependence between numerical results and mesh quality. They showed that a very coarse mesh results in numerical oscillations called wiggles. Wiggles can result in false pressure and volume fraction oscillations and can be wrongly interpreted as a slug flow pattern. On the other hand, when the finest and high-quality mesh was applied, the wave flow pattern was predicted for equal operational conditions.

Regarding the tridimensional (3D) two-phase flow modeling, Vallée et al. (2008) conducted experimental and numerical experiments of gas–liquid flow in a horizontal channel with a rectangular cross section. Optical techniques were applied to measure the dynamic pressure and the results were synchronized with a high-speed camera system. The Euler–Euler two-phase model was applied using the ANSYS CFX code. The turbulence was modeled for each phase separately using the k-ω SST model, but turbulence damping was not considered. The numerical results showed a good qualitative agreement between experimental and numerical data. On the other hand, the slug flow was generated based on a variable liquid holdup for the inlet boundary condition, equal to the experimental measurements.

Self-generated slugs were modeled by Bartosiewicz et al. (2010). The 3D numerical simulations were carried out with different mathematical modeling and validated with experimental data. The first experimental slug generated was observed at 0.3–0.7 s and the onset of slug was at 1.5 m. The VOF approach was simulated with laminar, k-ε, k-ω, and k-ω SST, and the slug generation was not observed. The two-fluid model was applied with k-ω and a special turbulence damping function at the interface and a slug was obtained after 16.65 s at 3.5 m from the inlet. In addition, a 2D simulation was conducted using the multi-fluid VOF method and k-ε turbulence model with a Large Interface Model (LIM) for modeling the momentum transfer through the interface and the slug flow was initiated earlier at 1.6 s and 1.5 m from inlet. On the other hand, Shirodkar (2015) performed a 2D slug flow modeling using the multi-fluid VOF method, symmetric drag law, and k-ω with turbulence damping. It was reported as a reasonable match with the available experimental data in the literature, modeling the first slug at 0.87 s and 1.7 m from inlet.

Friedemann et al. (2019) conducted gas–liquid slug flow validation study in a concentric annulus geometry. Periodic boundary conditions were applied to alleviate the computational requirement. The VOF model was applied with a compressive method to reduce the numerical diffusion at the interface. The k-ω RANS model was used to solve the turbulence and no damping method was mentioned. The researchers concluded that the solution had a strong dependence on the mesh density and domain length.

Akhlaghi et al. (2019) conducted numerical simulations of the plug and slug flows regimes solving the VOF and multi-fluid VOF models. The k-ω SST model was applied to solve the turbulence, but no turbulence damping model was mentioned. The researchers reported that the multi-fluid VOF model provided a larger agreement with experimental data in comparison to the VOF model. On the other hand, the computational time requirement was increased 14 times.

Although a very fine mesh is recommendable to correctly simulate the two-phase interface, they are impracticable for industrial applications. Due to the high computational time requirement, industrial applications are normally conducted in coarse meshes. Because of that, the RANS turbulence models are applied, but additional equations are needed to model the turbulence near the interface. In a recent work, Frederix et al. (2018) presents the Egorov approach. The Egorov approach is a traditional method to model the turbulence damping. On the other hand, a high mesh dependence has been reported and Frederix et al. (2018) modified the turbulence damping model to be mesh independent and extended to the k-ε turbulence model. In addition, Höhne and Porombka (2018) improved the turbulence modeling by introducing a model for sub-grid size waves induced by Kelvin–Helmholtz instabilities.

The purpose of the present work is to simulate the turbulent two-phase flow in a high-aerated slug pattern in a horizontal pipe. This also involves a comparison between results with and without an additional equation to damp the turbulent at the gas–liquid interface. In addition, discretization errors were estimated, and numerical data was validated against experimental data available in the literature.

2.2 Mathematical Modeling

In the numerical studies carried out in this research, the fluids were assumed to be immiscible, and without phase change. The VOF (Hirt and Nichols 1981) approach is a classical method used to solve stratified flows. The VOF method tracks the interface between fluids by the solution of Eq. (1), which is the continuity equation for the volume fraction of one of the phases.

$$\frac{\partial}{\partial t}\left(\alpha_q \rho_q\right) + \mathbf{v} \cdot \nabla \alpha_q \rho_q = 0, \tag{1}$$

where α_q and ρ_q are the volumetric fraction and density for phase q, respectively, t is the time, and $\mathbf{v}$ is the average velocity vector.

In classical VOF, a single momentum equation is solved, Eq. (2), and the two fluids share the same transport equation. Recently, researchers have been using a multi-fluid VOF (Cerne et al. 2001) method to solve dispersed flows, but the authors emphasized the needed additional computational efforts.

$$\frac{\partial}{\partial t}(\rho \mathbf{v}) + \nabla \cdot (\rho \mathbf{v}\mathbf{v}) = -\nabla P + \nabla \cdot \left[(\mu + \mu_T)\left(\nabla \mathbf{v} + \nabla \mathbf{v}^T\right)\right] + \rho \mathbf{g} + \mathbf{F}, \tag{2}$$

where μ is the fluid viscosity, μ_T is the turbulent viscosity, P is the average static pressure, $\mathbf{F}$ is the surface tension, and ρ is density.

The fluid properties (density and viscosity, for example) were calculated by Eq. (3).

$$\phi = \sum \alpha_q \phi_q, \tag{3}$$

where ϕ is a generical mixture property.

Although density was treated as a constant, gas phase was assumed to be an ideal fluid. Thus, the energy transport equation, Eq. (4), must be solved.

$$\frac{\partial}{\partial t}(\rho E) + \nabla \cdot [\mathbf{v}(\rho E + p)] = \nabla \cdot (k_{\text{eff}} \nabla T), \tag{4}$$

where E stands for energy, which was calculated by Eq. (5), T is the temperature, and k_{eff} is the effective thermal conductivity.

$$E = \frac{\sum_{q=1}^{n} \alpha_q \rho_q E_q}{\sum_{q=1}^{n} \alpha_q \rho_q}, \tag{5}$$

where E_q is based on the specific heat of each phase and the shared temperature.

The turbulent viscosity was calculated by Eq. (6), using the two-equation model k-ω SST (Menter 1994).

$$\mu_T = \frac{\rho a_1 k}{\mathrm{Max}(a_1\omega;\ SF_2)}, \tag{6}$$

where k is the turbulent kinetic energy, which was calculated by Eq. (7), ω is the specific turbulence dissipation rate which was calculated by Eq. (8), F_2 is a weighting function that is one for boundary-layer flows and zero for free shear layers, S is the strain rate magnitude, and a_1 is a constant.

$$\frac{\partial}{\partial t}(\rho k) + \nabla \cdot (\rho \mathbf{v} k) = \nabla \cdot (\Gamma_k \nabla k) + G_k - Y_k, \tag{7}$$

where Γ_k is the effective diffusivity of k, G_k is the production of k, and Y_k is the dissipation of k due to turbulence.

$$\frac{\partial}{\partial t}(\rho \omega) + \nabla \cdot (\rho \mathbf{v} \omega) = \nabla \cdot (\Gamma_\omega \nabla \omega) + G_\omega - Y_\omega + D_\omega + S_\omega, \tag{8}$$

where Γ_ω is the effective diffusivity of ω, G_ω is the production of ω, Y_ω is the dissipation of ω due turbulence, D_ω is the cross-diffusion term, and S_ω is a source term.

Although this model has a good agreement for near and distant from the wall turbulence, an additional problem is observed in two-phase flow: the gas velocity near the interface reduces and a near-wall comportment was observed. Thus, a damping model was used to correctly compute the turbulence quantities at the interface region. The Egorov approch included the damping turbulence as a source term (S_ω) in the ω equation, calculated by Eq. (9)

$$S_\omega = A \Delta n \beta \rho \left(\frac{6B\mu}{\beta \rho \Delta n^2} \right)^2, \tag{9}$$

where A is the interfacial area, which was calculated by Eq. (10), Δn is the cell height normal to interface, β is a k-ω coefficient, and B is the damping factor

$$A = 2\alpha_q \left| \nabla \alpha_q \right|. \tag{10}$$

Additional models were necessary to solve the cells containing the interface. The Geo Reconstruct method, a piece-linear model, was used to solve the numerical diffusion and reconstruct the interface. The surface tension term was modeled in a continuous surface stress (CSS) manner instead of the continuous surface force (CSF), as described by Gueyffier et al. (1999).

2.3 Methods

The computational domain consisted of a pipe with an inner diameter of 26 mm and 2 m in length. Varying mesh densities were generated to evaluate the effect of the mesh resolution and quality on the numerical solution. Firstly, the cross section of pipe was divided into 320 face elements and the longitudinal divisions varied between 60 and 480, allowing to assess the impact of the aspect ratio on the solution. Based on mesh 04, coarse, fine, and extra fine meshes were generated varying all the tridimensional divisions with a constant ratio of approximately 1.3. Additionally, a special attention was paid to the first wall element length in order to solve the turbulence near the wall. A comparison between meshes is presented in Fig. 1 and the mesh information is summarized in Table 1.

The boundary conditions were set as no-slip at the wall and zero pressure at the outlet. The inlet face was horizontally divided into two equal, where air enters the upper part and water in the lower part. The superficial velocities were applied as boundary conditions at the entrance resulting in 9 m/s for air and 0.8 m/s for water phase. The simulation was initialized with a fully developed airflow. The time step was set as a variable with the maximum Courant number equal to 2 and the flow was simulated for 20 s, which was considered sufficient to observe a significant number of slugs. However, the first 2 s, correspondent to 4.9 residence times, were discarded to

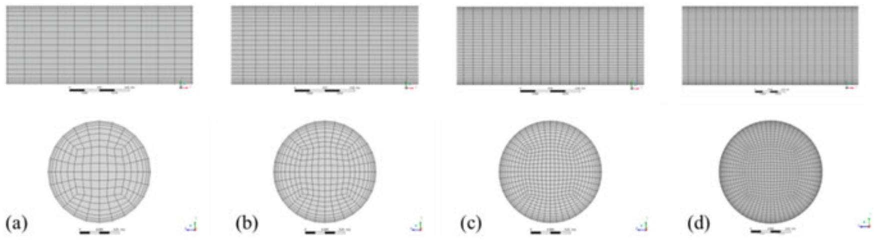

Fig. 1 Mesh. **a** Coarse mesh (mesh 05); **b** intermediate mesh (mesh 04); fine mesh (mesh 06); extra fine mesh (mesh 07)

Table 1 Mesh information

Mesh	Face elements	Longitudinal divisions	Total elements	First wall element
01	320	60	18,880	0.00020
02	320	120	38,080	0.00020
03	320	240	76,480	0.00020
04	320	480	153,280	0.00020
05	180	360	64,620	0.00030
06	672	625	419,328	0.00015
07	1216	815	989,824	0.00010

prevent the initial condition's influence on the analysis. The pressure was monitored at the center and along the pipe length, at 0, 0.5, 1.0, and 1.5 m.

The pressure measurements were analyzed in other to determine the slug frequency. An algorithm was implemented in the software MATLAB to calculate de PSD prominent frequency and realize a count of the pressure peaks. Also, the translational slug velocity was determined. These methods were widely described by Becker (2020).

2.4 Results and Discussion

The first results presented in this paper deal with the longitudinal mesh refinement influence on the slug frequency and onset. Figure 2 presents the results for slug frequency calculated as the normalized PSD for pressure oscillations at the pipe inlet. It can be observed that the slug frequency increases according to the longitudinal mesh refinement. Figure 3 shows the volume fraction contours at the plane normal to the gravity force and flow direction, showing a high influence of the longitudinal refinement on slug onset. Thus, it can be concluded that a large longitudinal element length postpones the onset of slug to the end of the pipe. A possible explanation for this is that large elements do not capture accurately the small oscillations that precede slug onset. Due to these preliminary analyses, it was clear that a high-quality mesh was necessary to accurately predict the slug flow, and the most longitudinal refined mesh was chosen as a base to the other meshes proposed.

Varying the global mesh refinement, a similar behavior on the slug frequency and its onset is also observed. Figure 4 shows the slug frequency calculated as the normalized PSD for pressure oscillations at the pipe inlet and Fig. 5 shows the passage of slugs in the contours of the volumetric fraction of liquid to meshes 05,

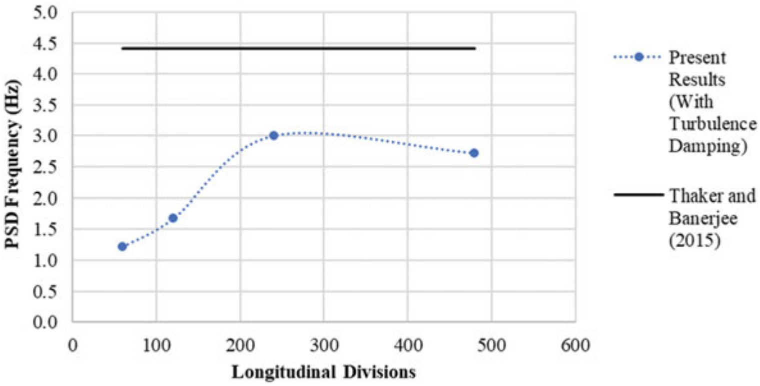

Fig. 2 Slug frequency (PSD) at the pipe inlet. Analysis considering longitudinal mesh refinement with turbulence damping

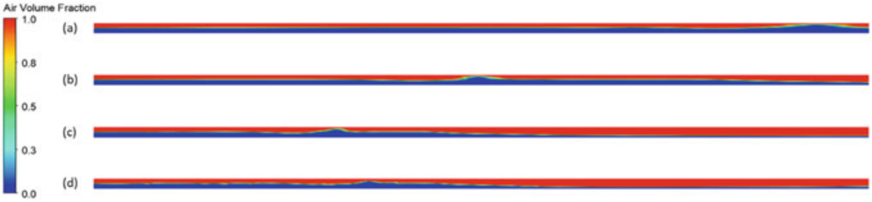

Fig. 3 Results for air volume fraction contours with turbulence damping. Comparison between the onset of slug. Analysis of the influence of longitudinal mesh refinement. **a** Mesh 01; **b** mesh 02; **c** mesh 03; **d** mesh 04

04, 06, and 07. According to mesh refinement, higher values of slug frequency were measured, but it appears that an asymptotic profile was reached, and this shows that the extra thin solution is close to being independent of the mesh. In addition, the grid index convergence was calculated, and it showed that the extra fine mesh result is close to the extrapolated mesh. The present results were compared to the empirical correlation predictions by Thaker and Banerjee (2015), and a difference of 9.3% was observed.

On the other hand, simulations were conducted using equal mesh refinement but without turbulence damping at the interface, and an interesting result is observed. Figure 6 shows the results for the counted slug frequency for simulations without turbulence damping. Results for coarse and intermediate meshes indicate that there is the formation of slugs and their frequency decreased with the refining of the mesh. However, when fine and extra fine meshes were used, slug flow was not observed, only wavy flow was observed. This observation is in opposite direction to the simulations with damping turbulence model and confirms the Lun et al. (1996) research, showing that when a poor-quality mesh is used, wiggles are generated. In this case, the numerical instabilities generated by the coarse mesh were confounded with real

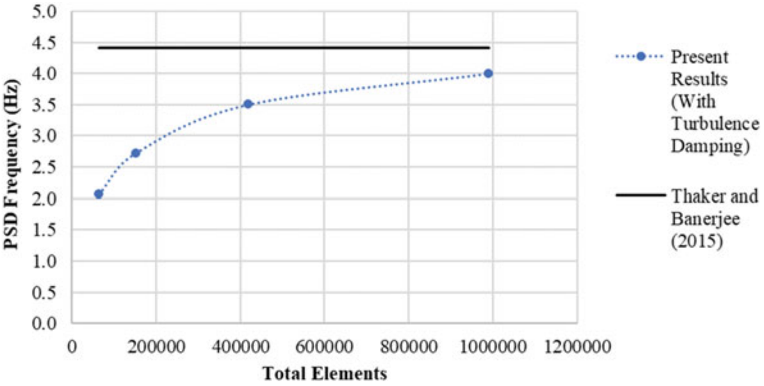

Fig. 4 Slug frequency (PSD) at the pipe inlet. Analysis for three-dimensional mesh refinement with turbulence damping

Fig. 5 Results for air volume fraction contours with turbulence damping. Comparison between the onset of slug. Analysis for tridimensional refinement influence. **a** Coarse mesh (mesh 05); **b** intermediate mesh (mesh 04); **c** fine mesh (mesh 06); **d** extra fine mesh (mesh 07)

slugs in the statistical analyses. Despite that, when a fine mesh was used, numerical instabilities decreased and, consequently, oscillations were not propagated.

Results obtained in the mesh analyses were presented in terms of static pressure oscillations at the pipe inlet. The pipe inlet analyses can represent the slug frequency as shown by Tonomura et al. (2018) with pressure measurements and visual observations. On the other hand, when other measured points along the pipe length are observed a different result is obtained, depending on the mesh refinement. Results for slug frequency along the pipe length are presented in Fig. 7, for simulations considering damping turbulence at the interface. These results showed that when a coarse and intermediate mesh were used a very similar result for slug frequency is calculated along the pipe. However, according to the mesh refinement, the slug frequency is damped along the pipe length and it corroborates with experimental observations related by Thaker and Banerjee (2015). It is important to add that this observation is valid for zero pressure at the pipe outlet, but when the pipe has a curve at the outlet, it can modify the flow characteristics (Santos 2019).

Another interesting result was obtained for the results with damping turbulence model and the finest mesh. In the last point, higher PSD frequencies are observed.

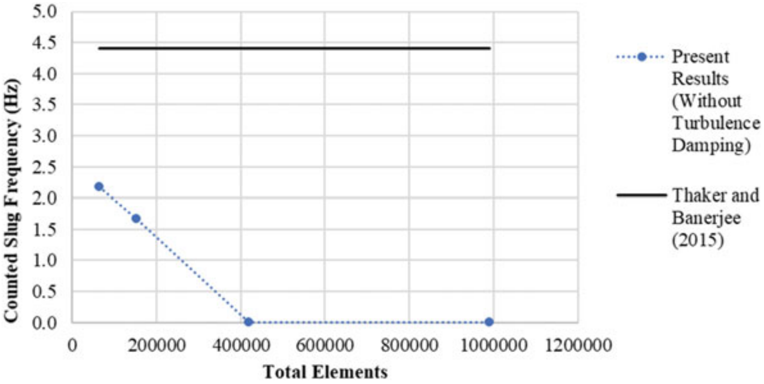

Fig. 6 Slug frequency (counted) at the pipe inlet. Analysis for three-dimensional mesh refinement without turbulence damping

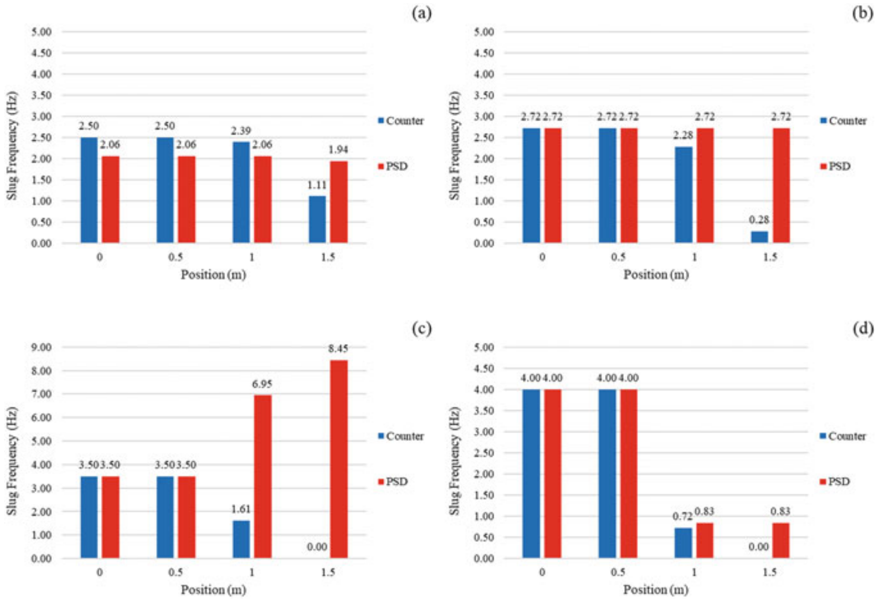

Fig. 7 Results for slug frequency at the pipe feed, simulations considering damping turbulence at the interface. Comparison between PSD prominent frequency and pressure peak counter. **a** Coarse mesh; **b** intermediate mesh; **c** fine mesh; **d** extra fine mesh

Contrary to the coarse mesh, PSD frequencies between 100 and 500 Hz are observed in the last measured point. It possibly means that a different flow pattern is occurring at the final tube region (Ujang et al. 2006). Although the VOF method used in this study is not indicated to model dispersed flow, it can be presumed that due to the mesh refinement, large bubbles and droplets are generated due to the slug break up and this explains the high-frequency oscillations. The results are shown in Fig. 8.

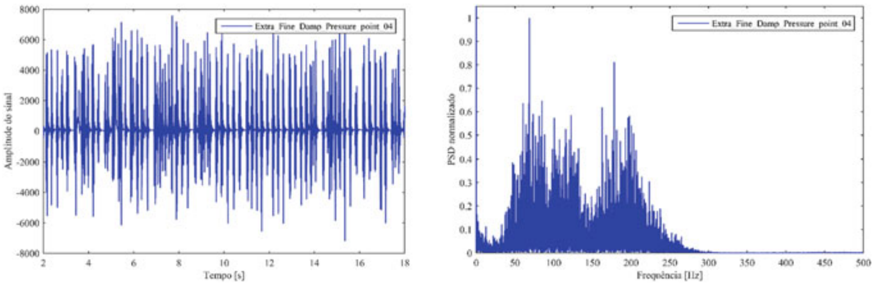

Fig. 8 Results for pressure oscillations (Pa) and PSD frequency at pipe position 1.5 m. Results for extra fine mesh

Table 2 Computational time requirement for simulations with turbulence damping

Mesh	Total elements	Number of processors	Time requirement (Days)
04	153,280	12	6.30
06	419,328	24	17.79
07	989,824	28	54.22

A comparison between the computational times required to obtain numerically 20 s of flow is presented in Table 2. The high computational time requirement for the extra fine mesh helps justify the choice of the VOF model to perform this study. After all, Akhlaghi et al. (2019) reported that the multi-fluid VOF model results in a 14 times larger computational time requirement in comparison to the VOF model, as mentioned earlier.

2.5 Conclusions

This study provided an analysis about mathematical modeling and solution methods applied to the intermittent two-phase flow patterns. It also included an overview about additional models involved in interfacial turbulence modeling. In addition, not only the spatial discretization independence was analyzed but also a validation study was conducted concerning the slug frequency. Both statistical methods used for the slug frequency analysis are shown to be useful.

Regarding mesh size uncertainty, the results showed that according to the longitudinal refinement, the frequency increased, and slugs were formed close to the pipe inlet. Moreover, high-frequency phenomena were modeled using the global mesh refinement.

An important conclusion provided by this research was that the flow was dependent on the interfacial turbulence model. The turbulence damping at the interface achieved better results, closer to the experimental observations (Thaker and Banerjee 2015). When this turbulence correction was not applied, the slug flow was not predicted.

The present results contradicted Bartosiewicz et al. (2010) ones, showing that the classical VOF method is a useful tool to predict the slug flow, even in high velocities. For this reason, the classical VOF method with turbulence damping at the interface is a viable method to be used industrially due to the lower computational cost obtained when compared with other models.

Investigating other turbulence models and the multi-fluid VOF method are suggestions for future work. Besides that, further studies should include the inlet geometry to ensure that the inlet condition does not influence the results.

Acknowledgements The authors are grateful for the financial support of PETROBRAS (research project grant number 5850.0103010.16.9), CAPES—financial code 001, and CNPq (processes 308714/2016-4).

References

Akhlaghi M, Mohammadi V, Nouri NM, Taherkhani M, Karimi M (2019) Multi-fluid VoF model assessment to simulate the horizontal air–water intermittent flow. Chem Eng Res Des 152:48–59. https://doi.org/10.1016/j.cherd.2019.09.031

Baker O (1953) Design of pipelines for the simultaneous flow of oil and gas. Pet. Branch, AIME

Barnea D, Brauner N (1985) Holdup of the liquid slug in two phase intermittent flow. Int J Multiph Flow 11:43–49. https://doi.org/10.1016/0301-9322(85)90004-7

Barnea D, Taitel Y (1993) A model for slug length distribution in gas-liquid slug flow. Int J Multiph Flow 19:829–838. https://doi.org/10.1016/0301-9322(93)90046-W

Bartosiewicz Y, Seynhaeve J, Vallée C, Höhne T, Laviéville J (2010) Modeling free surface flows relevant to a PTS scenario: comparison between experimental data and three RANS based CFD-codes. Comments on the CFD-experiment integration and best practice guideline. Nucl Eng Des 240:2375–2381. https://doi.org/10.1016/j.nucengdes.2010.04.032

Becker SL (2020) Estudo dos Efeitos das Propriedades Físicas do Líquido Sobre a Dinâmica do Escoamento Bifásico em Duto Horizontal. Master's dissertation, University of Blumenau, Blumenau

Cerne G, Petelin S, Tiselj I (2001) Coupling of the interface tracking and the two-fluid models for the simulation of incompressible two-phase flow. J Comput Phys 171:776–804. https://doi.org/10.1006/jcph.2001.6810

Cook M, Behnia M (2000) Slug length prediction in near horizontal gas–liquid intermittent flow. Chem Eng Sci 55:2009–2018. https://doi.org/10.1016/S0009-2509(99)00485-6

Fossa M, Guglielmini G, Marchitto A (2003) Intermittent flow parameters from void fraction analysis. Flow Meas Instrum 14:161–168. https://doi.org/10.1016/S0955-5986(03)00021-9

Frederix EMA, Mathur A, Dovizio D, Geurts BJ, Komen EMJ (2018) Reynolds-averaged modeling of turbulence damping near a large-scale interface in two-phase flow. Nucl Eng Des 333:122–130. https://doi.org/10.1016/j.nucengdes.2018.04.010

Friedemann C, Mortensen M, Nossen J (2019) Gas–liquid slug flow in a horizontal concentric annulus, a comparison of numerical simulations and experimental data. Int J Heat Fluid Flow 78:108437. https://doi.org/10.1016/j.ijheatfluidflow.2019.108437

Gregory GA, Scott DS (1969) Correlation of liquid slug velocity and frequency in horizontal cocurrent gas–liquid slug flow. AIChE J 15:933–935. https://doi.org/10.1002/aic.690150623

Greskovich EJ, Shrier AL (1971) Pressure drop and holdup in horizontal slug flow. AIChE J 17:1214–1219. https://doi.org/10.1002/aic.690170529

Gueyffier D, Li J, Nadim A, Scardovelli R, Zaleski S (1999) Volume-of-fluid interface tracking with smoothed surface stress methods for three-dimensional flows. J Comput Phys 152:423–456. https://doi.org/10.1006/jcph.1998.6168

Höhne T, Porombka P (2018) Modelling horizontal two-phase flows using generalized models. Ann Nucl Energy 111:311–316. https://doi.org/10.1016/j.anucene.2017.09.018

Hirt CW, Nichols BD (1981) Volume of fluid (VOF) method for the dynamics of free boundaries. J Comput Phys 39(1):201–225. https://doi.org/10.1016/0021-9991(81)90145-5

Lun I, Calay RK, Holdo AE (1996) Modelling two-phase flows using CFD. Appl Energy 53:299–314. https://doi.org/10.1016/0306-2619(95)00024-0

Menter FR (1994) Two-equation eddy-viscosity turbulence models for engineering applications. Am Inst Aeronaut Astronaut (AIAA) J 32:1598–1605

Nydal OJ, Pintus S, Andreussi P (1992) Statistical characterization of slug flow in horizontal pipes. Int J Multiph Flow 18:439–453. https://doi.org/10.1016/0301-9322(92)90027-E

Santos CNM (2019) Estudo Experimental e Numérico do Efeito do Duto de Saída Sobre a Dinâmica do Escoamento Bifásico em Duto Horizontal. Master's dissertation, University of Blumenau, Blumenau

Scott SL, Shoham O, Brill JP (1989) Prediction of slug length in horizontal, large-diameter pipes. SPE Prod Eng 4:335–340. https://doi.org/10.2118/15103-PA

Shirodkar V (2015) Slug flow modelling using blended drag law and interface turbulence damping. FMFP 2015 – Paper No. 332

Taitel Y, Dukler AE (1976) A model for predicting flow regime transitions in horizontal and near horizontal gas-liquid flow. AIChE J 22:47–55. https://doi.org/10.1002/aic.690220105

Thaker J, Banerjee J (2015) Characterization of two-phase slug flow sub-regimes using flow visualization. J Pet Sci Eng 135. https://doi.org/10.1016/j.petrol.2015.10.018

Tonomura O, Kobori R, Taniguchi S, Hasebe S, Matsuoka A (2018) Monitoring of two-phase slug flow in stacked multi-channel reactors based on analysis of feed pressure. Comput Aided Chem Eng. Elsevier Masson SAS. https://doi.org/10.1016/B978-0-444-64241-7.50397-9

Ujang PM, Lawrence CJ, Hale CP, Hewitt GF (2006) Slug initiation and evolution in two-phase horizontal flow. Int J Multiph Flow 32:527–552. https://doi.org/10.1016/j.ijmultiphaseflow.2005.11.005

Vallée C, Höhne T, Prasser HM, Sühnel T (2008) Experimental investigation and CFD simulation of horizontal stratified two-phase flow phenomena. Nucl Eng Des 238:637–646. https://doi.org/10.1016/j.nucengdes.2007.02.051

Van Hout R, Barnea D, Shemer L (2002) Translational velocities of elongated bubbles in continuous slug flow. Int J Multiph Flow 28:1333–1350. https://doi.org/10.1016/S0301-9322(02)00027-7

Wang X, Guo L, Zhang X (2007) An experimental study of the statistical parameters of gas–liquid two-phase slug flow in horizontal pipeline. 50:2439–2443. https://doi.org/10.1016/j.ijheatmasstransfer.2006.12.011

Chapter 3
Large-Eddy Simulation of Smooth Channel Flow with a Stochastic Wall Model

Livia S. Freire

Abstract Large Eddy Simulation (LES) is a useful tool in the study of smooth channel flows of high Reynolds number, but when the domain is large enough computational cost restricts the correct representation of the viscous sublayer. In this study, we test the use of a one-dimensional stochastic model (ODT) as an alternative to simulate the flow close to the wall within the LES. This approach comprises the use of one independent ODT (a vertical line) inside each LES grid close to the wall, driven by the LES at the top and providing the lower boundary condition to the LES (two-way coupling). Results of mean velocity and total stress for $\mathrm{Re}_\tau = 590$ and 5200 are similar to Direct Numerical Simulation, and they have the correct order of magnitude for velocity variances.

Keywords Large-eddy simulation · One-dimensional turbulence · Smooth channel flow

3.1 Introduction

Smooth, pressure-driven channel flows correspond to one of the classical problems highly studied in the field of turbulence. In addition to its relative simplicity in terms of dimensional analysis, combined with many interesting features due to the wall-blockage effect, channel flows are present in a diverse set of applications in the environment (e.g., rivers and the atmospheric boundary layer) and industry (e.g., rectangular ducts).

In this study, we consider a channel with no lateral walls and with a distance δ from the bottom wall to the free stream at the top. The flow is fully developed, stationary, and horizontally homogeneous, and the *mean* flow is parallel to the wall (in the streamwise direction x). Statistics of the flow change only in the vertical direction, y, and the bottom wall is smooth, i.e., the velocity vector $\overrightarrow{u} = \langle u, v, w \rangle$ goes to zero at $y = 0$ (u, v, and w correspond to streamwise, vertical, and spanwise

---

L. S. Freire (✉)
Instituto de Ciências Matemáticas e de Computação, University of São Paulo, São Carlos, Brazil
e-mail: liviafreire@usp.br

H. F. Meier et al. (eds.), *Advances in Turbulence*, ABCM Series on Mechanical Sciences and Engineering, https://doi.org/10.1007/978-3-031-25990-6_3

velocities, respectively). From the continuity and momentum equations, it can be shown that the total stress

$$\tau(y) \equiv \rho\nu\frac{d\overline{u}}{dy} - \rho\overline{u'v'} \tag{1}$$

varies linearly with y because $d\tau/dy$ is constant (Pope 2000). In Eq. (1) ρ and ν are the fluid density and kinematic viscosity, respectively (both assumed as constants), over bars correspond to Reynolds average, and primes are the fluctuating part. The total stress is the sum of the viscous stress (first term on the RHS of Eq. (1)) and the Reynolds stress (second term). Noting that $\tau(y = \delta) = 0$, due to the free stream condition with no stress (similarly if considered an axisymmetric flow with another wall at $y = 2\delta$), we have that

$$\tau(y) = \tau_w\left(1 - \frac{y}{\delta}\right), \tag{2}$$

were τ_w is the shear stress at the wall. Since at the wall $u = v = 0$, $\tau_w = \rho\nu(d\overline{u}/dy)|_{y=0}$. A velocity scale known as *friction velocity* can be defined from τ_w, namely $u_\tau \equiv (\tau_w/\rho)^{1/2}$, which allows the definition of a friction Reynolds number $\mathrm{Re}_\tau = u_\tau\delta/\nu$. In addition, u_τ and ν can be used as viscous (or wall) scales to define nondimensional variables such as $u^+ = \overline{u}/u_\tau$ and $y^+ = yu_\tau/\nu$.

Figure 1 shows the statistics of smooth channel flows from Direct Numerical Simulation (DNS, the numerical solution of the Navier–Stokes equation) with $\mathrm{Re}_\tau = 590$ (from Moser et al. 1999) and $\mathrm{Re}_\tau = 5200$ (from Lee and Moser 2015). Notice the linear behavior predicted by Eq. (2) for $\tau(y)$ in Fig. 1f (it goes from 1 to 0 when normalized by u_τ), which is a signature that all assumptions are met by the simulation, including the steady-state condition. In terms of dimensional analysis, the flow can be divided into two layers (Pope 2000): (i) the inner layer ($y/\delta < 0.1$), where u_τ and y^+ are the dominant scales (white background in Fig. 1a–c) and (ii) the outer layer ($y/\delta > 0.1$), where u_b and δ are the dominant scales (grey background in Fig. 1a–c). The inner layer can be further subdivided into three sublayers: (i) the viscous sublayer ($y^+ < 5$), where the viscous stress dominates over the Reynolds stress and $u^+ = y^+$; (ii) the logarithmic layer ($30 < y^+ < 200$) where the Reynolds stress dominates over the viscous stress and $u^+ = \log y^+/\kappa + B$; and (iii) the buffer sublayer where both viscous and Reynolds stresses are relevant (see Fig. 1c for the relative importance of each stress). These equations for the nondimensional mean streamwise velocity (u^+) come from dimensional analysis, and the values of the constants $\kappa = 0.4$ and $B = 5.2$ were obtained experimentally (Pope 2000).

The analysis and equations described above and corroborated by experiments and DNS set the overall picture of canonical channel flows. Some interesting features can be observed when increasing the Reynolds number of the flow: in wall units (y^+), the inner layer remains the same (same viscous stress in Fig. 1c) and the outer layer increases in length, presenting a region with higher streamwise velocity (Fig. 1a). Variances peak at the buffer or logarithmic sublayers, and their values increase with

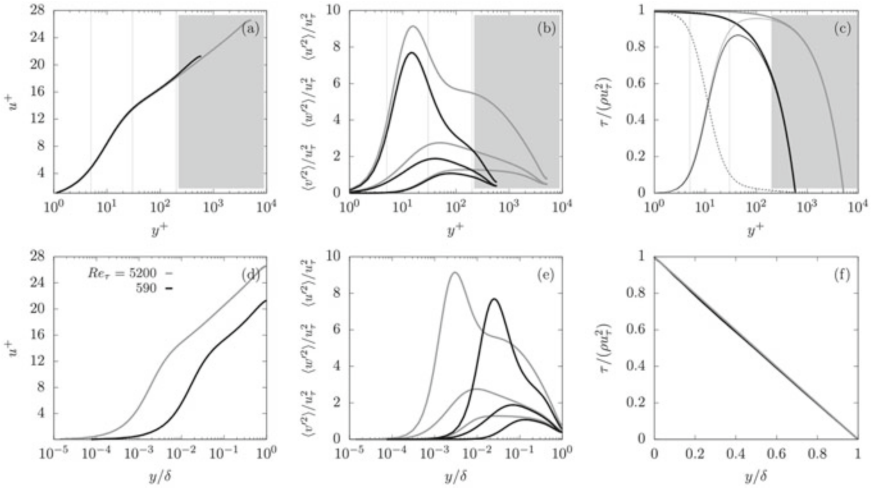

Fig. 1 Direct Numerical Simulation of smooth channel flows with $\mathrm{Re}_\tau = 590$ (black lines, from Moser et al. 1999) and $\mathrm{Re}_\tau = 5200$ (gray lines, from Lee and Moser 2015); **a** and **d**: mean streamwise velocity, **b** and **e**: variances of streamwise (upper lines), spanwise (middle lines) and vertical (lower lines) velocities, **c** and **f**: total (thick lines), viscous (dotted lines) and Reynolds (thin lines) stresses; **a**–**c** are displayed as a function of $y^+ = yu_\tau/\nu$, whereas **d**–**f** use y/δ. In **a**–**c** vertical lines separate the viscous, buffer, and logarithmic layers (from left to right); the outer layer corresponds to the gray area

Re_τ at all layers except the viscous sublayer (Fig. 1b). When looking at these statistics as a function of the distance from the wall (y/δ), the important feature to notice is that as Re_τ increases, the inner layer is "pushed" closer to the wall (Fig. 1d, e).

Simulation of $\mathrm{Re}_\tau = 5200$ from Lee and Moser (2015) already corresponds to one of the highest Re_τ values allowed by current computational capabilities for DNS, but some applications (such as the atmospheric boundary layer) require values of Re_τ one order of magnitude higher or more. In these situations, an alternative is to use another numerical tool known as Large-Eddy Simulation (LES), in which all variables are filtered for small-scale removal, significantly reducing the computational cost while maintaining most of the kinetic energy of the flow.

The governing equations of LES are obtained by filtering Navier–Stokes and continuity equations, which (for incompressible flow) corresponds to (Pope 2000)

$$\frac{\partial \tilde{u}_i}{\partial t} + \frac{\partial \widetilde{u_i u_j}}{\partial x_j} = -\frac{1}{\rho}\frac{\partial \tilde{p}}{\partial x_i} + \nu \frac{\partial^2 \tilde{u}_i}{\partial x_j \partial x_j} + F_i, \tag{3}$$

$$\frac{\partial \tilde{u}_i}{\partial x_i} = 0, \tag{4}$$

where $\tilde{u}_i$ is the filtered velocity field, $\tilde{p}$ is the filtered pressure field, and F_i is the mean streamwise pressure forcing (traditional index notation is used). In order to close this set of equations, the second term on the LHS of Eq. (3) needs to be rewritten as a function of the resolved velocity $\tilde{u}_i$ and pressure $\tilde{p}$. By defining the residual stress tensor and the residual kinetic energy as

$$\tau_{ij}^R \equiv \widetilde{u_i u_j} - \tilde{u}_i \tilde{u}_j, \tag{5}$$

$$e^R \equiv \frac{1}{2}\tau_{ii}^R, \tag{6}$$

it is possible to write

$$\widetilde{u_i u_j} = \tau_{ij} + \frac{2}{3}e^R \delta_{ij} + \tilde{u}_i \tilde{u}_j, \tag{7}$$

where τ_{ij} is the anisotropic part of the residual stress tensor ($\tau_{ij} = \tau_{ij}^R - 2e^R\delta_{ij}/3$), also known as subgrid-scale (SGS) stress tensor. The final Navier–Stokes equation for LES can be written as (Bou-Zeid et al. 2005)

$$\frac{\partial \tilde{u}_i}{\partial t} + \frac{\partial \tilde{u}_i \tilde{u}_j}{\partial x_j} = -\frac{1}{\rho}\frac{\partial \tilde{p}^*}{\partial x_i} + \frac{\partial \tau_{ij}}{\partial x_j} + F_i, \tag{8}$$

where $\tilde{p}^* = \tilde{p} + \frac{2}{3}\rho e^R$ is a modified pressure. Note that because molecular viscosity can be neglected in the resolved scales of high Reynolds number flows, it was removed from Eq. (8). The impact of the unsolved part of the flow on the resolved velocity field is represented by τ_{ij}, which is the term that needs to be parameterized as a function of the resolved velocity field. A diverse set of parameterizations, known as SGS models, has been developed for different applications and numerical approaches, most of them based on the eddy-viscosity and mixing-length assumptions.

When using LES to simulate smooth channel flows, it is possible to adopt a vertically stretched grid so that the first grid points are within the viscous sublayer, and a no-slip boundary condition can be enforced at the wall (e.g., Lund et al. 1998; Schlatter et al. 2010). This option, however, restricts the size of the domain, because the number of points to be used in the vertical direction is limited by the computational cost, the stretching function, and the assumptions of the SGS model used. Another option is to have the lowest LES grid points at the logarithmic region, and to use the log-law equation for the mean flow in this region ($u^+ = \log y^+/\kappa + B$) to relate the instantaneous streamwise velocity at the lowest grid point to the expected velocity gradient at the wall (used as a Neumann boundary condition). This is done through the value of u_τ, which carries the value of $d\overline{u}/dy|_{y=0}$ (see prior definitions of u^+, u_τ and τ_w). The main issue with this approach is that the log-law is true for the *mean* streamwise velocity $u^+ = \overline{u}/u_\tau$, but not for the instantaneous filtered velocity $\tilde{u}$ being resolved by the LES. Therefore, errors from this misuse of the log-law are present. Nevertheless, this method provides reasonable results, and it is widely used in cases in which the size of the domain is too large for the stretched grid approach (e.g., Bou-Zeid et al. 2005; Brasseur and Wei 2010).

An alternative to the use of the log-law when the first LES grid points are in the logarithmic sublayer was proposed by Schmidt et al. (2003). In this approach, a one-dimensional stochastic model is used to simulate the instantaneous flow field in the viscous and buffer sublayer, two-way coupled with the resolved flow field in the LES. In this study, we reproduce this method in a different LES code, comparing it again with DNS results of $\mathrm{Re}_\tau = 590$ by Moser et al. (1999) and performing a new comparison with the most recent DNS results of $\mathrm{Re}_\tau = 5200$ by Lee and Moser (2015). Positive and negative aspects of this method are discussed, and future applications for the model are envisioned.

3.2 Methods

3.2.1 One-Dimensional Stochastic Model

The one-dimensional stochastic model used in this study, known as ODT (One-Dimensional Turbulence model), was developed by Kerstein (1999) and successfully used as a stand-alone model to simulate different types of turbulent flows, including homogeneous turbulence, shear layers, buoyancy-driven flows (Kerstein 1999), mixing-layer and wakes (Kerstein et al. 2001), jet diffusion flames (Echekki et al. 2001), the stable atmospheric boundary layer (Kerstein and Wunsch 2006), particle dispersion in homogeneous flows (Sun et al. 2014) and flow through plant canopies (Freire and Chamecki 2018). The model corresponds to the one-dimensional diffusion equation of all variables of interest (which in this study are the three velocity components, but temperature, gas, and particle concentration can be included in the same way), i.e.,

$$\frac{\partial u_i}{\partial t} = \nu \frac{\partial^2 u_i}{\partial y^2} + F_i + stochastic\, eddies \tag{9}$$

where *stochastic eddies* correspond to the effect of three-dimensional turbulence in this one-dimensional field. The simulation is performed by evolving the diffusion equation in time, and at each time-step, a *stochastic eddy* is selected from a probability distribution of eddy size and location in the domain. When a *stochastic eddy* is selected, all variables at the position y within the eddy are replaced by the value of the same variable at the position $M(y)$. This mapping function is a model for advection, mixing the variables and creating small-scale fluctuations in such a way that mimics the energy cascade of turbulent flows. It is conservative (i.e., it preserves the total amount of the quantity being transported) and it does not introduce discontinuities. Mathematically, it is defined as

$$M(y) = y_b + \begin{cases} 3(y - y_b), & \text{if}\, y_b \leq y \leq (y_b + l/3), \\ 2l - 3(y - y_b), & \text{if}\, (y_b + l/3) \leq y \leq (y_b + 2l/3), \\ 3(y - y_b) - 2l, & \text{if}\, (y_b + 2l/3) \leq y \leq (y_b + l), \\ y - y_b, & \text{otherwise}, \end{cases} \tag{10}$$

where l and y_b are the size and bottom position of the eddy, respectively. As described by Kerstein and Wunsch (2006), the mapping function "takes a line segment, shrinks it to a third of its original length, and then places three copies on the original domain. The middle copy is reversed, which maintains continuity of advected fields and introduces the rotational folding effect of turbulent eddy motion." In addition to this mixing effect, when a *stochastic eddy* is selected, a second term creates redistribution of energy among velocity components, mimicking a pressure-induced tendency toward isotropy on the flow. The final model for the occurrence of *stochastic eddies* is

$$u_i(y) \rightarrow u_i(M(y)) + c_i(y - M(y)), \tag{11}$$

where c_i is the amplitude of the energy redistribution (calculated from the flow energy within the eddy). For more details on its calculation, see Kerstein (1999) and Kerstein et al. (2001).

The final piece of information needed for the ODT is the probability distribution of eddy size and location, $\lambda(l, y_b, t)$, which also evolves in time with the flow. It is calculated as proportional to the instantaneous amount of kinetic and potential energy in the flow (through dimensional analysis), adding another physical aspect to the stochastic model. For example, regions of high shear will have a higher probability of having *stochastic eddies*. A proportionality constant C_λ is used to regulate the number of eddies for a given amount of energy, effectively setting the turbulence intensity. Another constant, Z_λ, adjusts the damping effect of viscosity, because any eddy with a time scale longer than the viscous time scale should be prohibited. The values of C_λ and Z_λ are the only tunable parameters of the model, which are usually different for different types of flows, but they are not expected to vary with Re_τ. A detailed description of λ and its mathematical formulation can also be found in Kerstein (1999) and Kerstein et al. (2001).

When used as a bottom boundary condition for the LES, an independent ODT model is inserted inside each LES grid next to the wall. In this case, each ODT corresponds to a vertical line centered at the LES grid, refining the flow field in the vertical direction from the wall to the top of the grid. The LES velocity field provides a top boundary condition to the ODT, and the ODT provides the momentum flux across the first and second grid layers as a bottom boundary condition for the LES, which results in an instantaneous two-way coupling between the models.

Table 1 Simulation parameters for LES and ODT

	$\mathrm{Re}_\tau = 590$	$\mathrm{Re}_\tau = 5200$
Domain size ($X \times Y \times Z$)	$2\pi\delta \times \delta \times 2\pi\delta$	$2\pi\delta \times \delta \times 2\pi\delta$
Number of grid points ($N_x \times N_y \times N_z, N_{\mathrm{ODT}}$)	$32 \times 16 \times 32, 32$	$32 \times 32 \times 32, 96$
Mean pressure gradient force ($F_i = \langle (1/\rho)(d\overline{p}/dx), 0, 0\rangle$)	$\langle u_\tau^2/\delta, 0, 0\rangle$	$\langle u_\tau^2/\delta, 0, 0\rangle$
Simulation time step (Δt)	$0.0005\delta/u_\tau$	$0.0005\delta/u_\tau$
Number of simulation time steps (N_t)	$100,000$	$100,000$
Eddy rate distribution parameters (C_λ, Z_λ)	23, 15	23, 15

3.2.2 Large-Eddy Simulation Code

The LES code used in this study solves the filtered Navier–Stokes equation in a vertically-staggered grid with fixed size, in which the first grid points are located in the logarithmic sublayer. The numerical discretization combines a fully dealiased pseudo-spectral method in the horizontal directions and a second-order centered finite difference in the vertical direction. The fully explicit second-order Adams–Bashforth scheme is used for time integration. The SGS model is the planar averaging, scale-invariant dynamic model (Germano et al. 1991). More details of the code can be found in Bou-Zeid et al. (2005). A constant mean pressure gradient force is imposed in the streamwise direction and horizontal boundary conditions are periodic, while a stress-free boundary condition is applied at the top of the domain.

3.2.3 Simulation Setup

Two simulations are tested here, corresponding to $\mathrm{Re}_\tau = 590$ and 5200. Simulation parameters are listed in Table 1. Both simulations were run for 50 eddy turnover times (defined as δ/u_τ), and results presented in the next section correspond to the averaging of the last 15 eddy turnover times.

3.3 Results

Figure 2 shows the results of flow statistics for the two Re_τ tested. After the adjustment of the parameters C_λ and Z_λ (by trial and error), the mean flow is well represented by the model, with ODT providing the velocity field in the viscous and buffer sublayers in the $\mathrm{Re}_\tau = 590$ case (Fig. 2a), and in most of the inner layer in the case

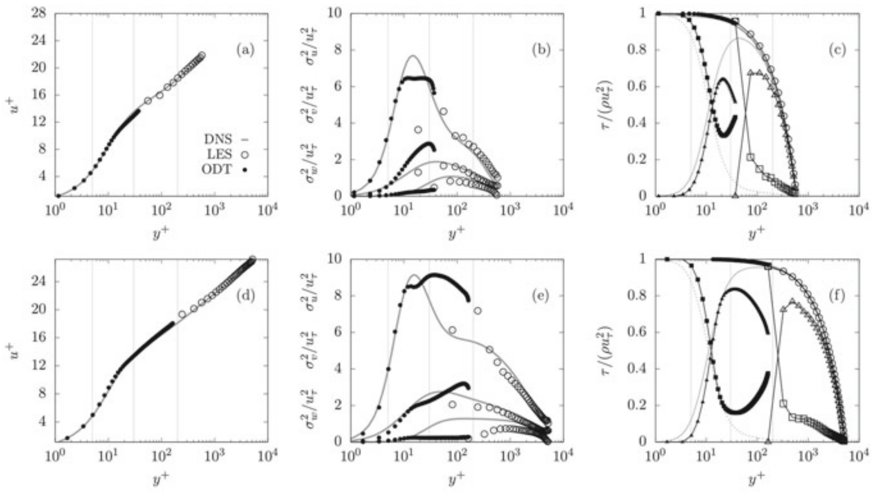

Fig. 2 Smooth channel flow simulation results from ODT-LES coupling for $\mathrm{Re}_\tau = 590$ (**a**–**c**) and $\mathrm{Re}_\tau = 5200$ (**d**–**f**); LES (ODT) results in empty (filled) symbols; gray lines correspond to DNS results; **a** and **d**: mean streamwise velocity, **b** and **e**: variances of streamwise (upper lines/symbols), spanwise (middle lines/symbols), and vertical (lower lines/symbols) velocities, **c** and **f**: total (circles), viscous and SGS (squares), and *stochastic eddies* and resolved (triangles) stresses

of $\mathrm{Re}_\tau = 5200$ (Fig. 2d). The fact that these tunable parameters do not change with Re_τ is useful in terms of the applicability of the model to different studies.

Overall, variances are well represented by the LES in the outer layer; this is also obtained when using wall models based on the log-law, and it is likely not significantly impacted by the use of the ODT. The variances at the viscous sublayer are also well represented by the ODT, but ODT results in the buffer and logarithmic sublayers show discrepancies when compared to DNS results (Fig. 2b, e). Even as a stand-alone model, variances from ODT are usually not correct, which has been consistently observed for different types of flows (Kerstein et al. 2001; Freire and Chamecki 2018). Nevertheless, having an estimate that has the correct order of magnitude can be useful in some applications where an instantaneous flow field close to the wall is needed.

Finally, stresses are well represented by the ODT-LES coupling. Note in Fig. 2c, f that the ODT viscous stress is similar to DNS values, and that the *stochastic eddies* emulate the Reynolds stress in the viscous and part of the buffer sublayers. The sum of them gives the correct total stress at these layers, and it provides the value of the stress in the second LES grid point (which enters as an SGS stress). The total stress in the LES is divided into SGS and resolved parts (both corresponding to the Reynolds stress), and no viscous stress exists as it is negligible in this part of the domain. As expected, the total stress matches the linear profile (from theory and DNS) in both ODT and LES parts, indicating a well-developed, steady-state simulation.

3.4 Conclusion

In this study, we tested the use of a one-dimensional stochastic model as an alternative to simulate, in LES, the lowest part of the inner layer of a smooth channel flow. This approach provides good results for mean velocity and total stress, in addition to reasonable results (in terms of order of magnitude) for the variances of the flow. Despite the errors in variances, this option is likely more robust than the use of the log-law as a wall model for the instantaneous resolved velocity, given that the latter is an equation defined for the *mean* flow. The trade-off of this correction, however, comes in a significant increase in the computational cost of the simulation. Perhaps the application in which the ODT-LES coupling will be most useful is when the information of the instantaneous flow field very close to the wall is needed in addition to a large domain (too large for the stretched grid approach), such as studies of particle transport at the surface of the atmospheric boundary layer under conditions of strong convective flows.

Acknowledgements LF was funded by São Paulo Research Foundation (FAPESP, Brazil) Grant No. 2018/24284-1. This research was carried out using the computational resources of the Center for Mathematical Sciences Applied to Industry (CeMEAI) also funded by FAPESP (Grant No. 2013/07375-0).

References

Bou-Zeid E, Meneveau C, Parlange M (2005) A scale-dependent Lagrangian dynamic model for large eddy simulation of complex turbulent flows. Phys Fluids 17(2):025105

Brasseur JG, Wei T (2010) Designing large-eddy simulation of the turbulent boundary layer to capture law-of-the-wall scaling. Phys Fluids 22(2):021303

Echekki T, Kerstein AR, Dreeben TD, Chen JY (2001) One-dimensional turbulence simulation of turbulent jet diffusion flames: model formulation and illustrative applications. Combust Flame 125(3):1083–1105

Freire LS, Chamecki M (2018) A one-dimensional stochastic model of turbulence within and above plant canopies. Agric For Meteorol 250–251:9–23

Germano M, Piomelli U, Moin P, Cabot WH (1991) A dynamic subgrid-scale eddy viscosity model. Phys Fluids A 3(7):1760–1765

Kerstein AR (1999) One-dimensional turbulence: model formulation and application to homogeneous turbulence, shear flows, and buoyant stratified flows. J Fluid Mech 392:277–334

Kerstein AR, Wunsch S (2006) Simulation of a stably stratified atmospheric boundary layer using one-dimensional turbulence. Bound-Layer Meteorol 118(2):325–356

Kerstein A, Ashurst WT, Wunsch S, Nilsen V (2001) One-dimensional turbulence: vector formulation and application to free shear flows. J Fluid Mech 447:85–109

Lee M, Moser RD (2015) Direct numerical simulation of turbulent channel flow up to $Re_\tau \approx 5200$. J Fluid Mech 774:395–415

Lund TS, Wu X, Squires KD (1998) Generation of turbulent inflow data for spatially-developing boundary layer simulations. J Comput Phys 140(2):233–258

Moser RD, Kim J, Mansour NN (1999) Direct numerical simulation of turbulent channel flow up to $Re_\tau = 590$. Phys Fluids 11(4):943–945

Pope SB (2000) Turbulent flows. Cambridge University Press

Schlatter P, Li Q, Brethouwer G, Johansson AV, Henningson DS (2010) Simulations of spatially evolving turbulent boundary layers up to $\mathrm{Re}_\theta = 4300$. Int J Heat Fluid Flow 31(3):251–261

Schmidt RC, Kerstein AR, Wunsch S, Nilsen V (2003) Near-wall LES closure based on one-dimensional turbulence modeling. J Comput Phys 186(1):317–355

Sun G, Lignell DO, Hewson JC, Gin CR (2014) Particle dispersion in homogeneous turbulence using the one-dimensional turbulence model. Phys Fluids 26(10):103301

Chapter 4
The Plunging of Hyperpycnal Plumes on Tilted Bed by Three-Dimensional Large-Eddy Simulations

Felipe Nornberg Schuch, Jorge Hugo Silvestrini, Eckart Meiburg, and Sylvain Laizet

Abstract Theoretical and experimental interest in transport and deposition of sediments from rivers to oceans has increased rapidly over the last two decades. The marine ecosystem is strongly affected by mixing at river mouths, with, for instance, anthropogenic actions like pollutant spreading. Particle-laden flows entering a lighter ambient fluid (hyperpycnal flows) can plunge at a sufficient depth, and their deposits might preserve a remarkable record across a variety of climatic and tectonic settings. Numerical simulations play an essential role in this context since they provide information on all flow variables for any point of time and space. This work offers valuable spatio-temporal information generated by turbulence-resolving 3D simulations of poly-disperse hyperpycnal plumes over a tilted bed. The simulations are performed with the high-order flow solver Xcompact3d, which solves the incompressible Navier–Stokes equations on a Cartesian mesh using high-order finite-difference schemes. Five cases are presented, with different values for flow discharge and sediment concentration at the inlet. A detailed comparison with experimental data and analytical models is already available in the literature. The main objective of this work is to present a new dataset that shows the entire three-dimensional spatio-temporal evolution of the plunge phenomenon and all the relevant quantities of interest.

Keywords Turbidity current · Plunging flow · Computational fluid dynamics · Large-eddy simulation · Xcompact3d

---

F. N. Schuch (✉) · J. H. Silvestrini
School of Technology, Pontifical Catholic University of Rio Grande do Sul, Porto Alegre, Brazil
e-mail: felipe.schuch@edu.pucrs.br

J. H. Silvestrini
e-mail: jorgehs@pucrs.br

E. Meiburg
Department of Mechanical Engineering, University of California Santa Barbara, Santa Barbara, CA, USA
e-mail: meiburg@engineering.ucsb.edu

S. Laizet
Department of Aeronautics, Imperial College London, London SW7 2AZ, UK
e-mail: s.laizet@imperial.ac.uk

H. F. Meier et al. (eds.), *Advances in Turbulence*, ABCM Series on Mechanical Sciences and Engineering, https://doi.org/10.1007/978-3-031-25990-6_4

4.1 Introduction

Hyperpycnal plumes are produced when the density of a fluid entering a quiescent basin is higher than that in the ambient fluid. They are observed in nature when a river transports enough suspended sediment to be denser than the environment where it flows into, such as channels, lakes, reservoirs, or the ocean (Mulder et al. 2003; Lamb and Mohrig 2009). When the inflow momentum decreases, it eventually plunges under the ambient fluid and flows along the bed as an underflow density current, as illustrated in Fig. 1. The inflow can be characterized by its initial depth $\tilde{h}_0$ (where $\tilde{\cdot}$ corresponds to dimensional quantities), volumetric discharge per unit width $\tilde{Q}_0$ and freshwater density plus an excess due to suspended sediments $\tilde{\rho}_w + \Delta\tilde{\rho}$. The plunging of the hyperpycnal flow can be represented by three main regions. The depth-limited plume is a homogeneous flow region that occupies the complete channel depth, and it is dominated by inertial forces. At sufficient depth $\tilde{H}_p$, the flow collapses in the so-called plunge region. Downstream, a turbidity current is formed, dominated by buoyancy forces, and can be characterized by new values of depth $\tilde{H}_d$, discharge $\tilde{Q}_d$, and density $\tilde{\rho}_a + \Delta\tilde{\rho}_d$, due to continuous mixing between ambient fluid and the underflow (García 1996). Many authors express this increase in flow discharge through the incorporation of ambient fluid in the form of the initial mixture coefficient $\gamma = \tilde{Q}_d/\tilde{Q}_0 - 1$.

The understanding of the parameters and mechanisms that govern the flow transition in the plunge zone is relevant in terms of the health of ecosystems in river deltas regions (Horner-Devine et al. 2015), in the management and operation of dam reservoirs (Chamoun et al. 2016) and in the field of geology, since old sand deposits can preserve records of climatic and tectonic environments (Mulder et al. 2003), in addition to becoming important hydrocarbon reservoirs (Meiburg and Kneller 2010).

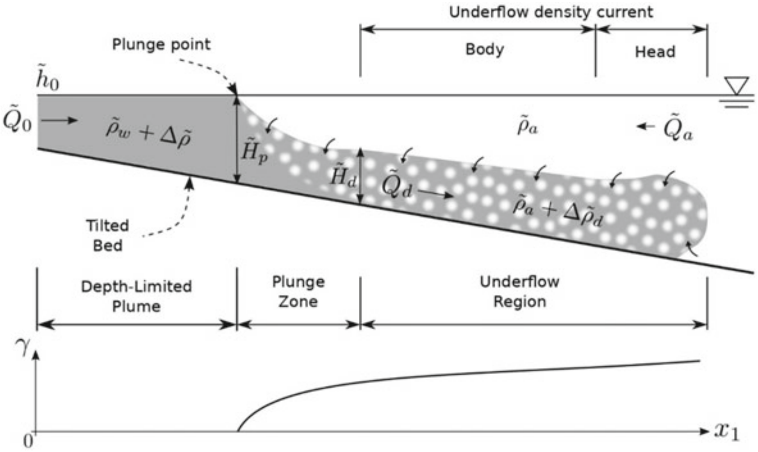

Fig. 1 Illustration of the plunging of an hyperpynal flow in a tilted channel. The mixing coefficient $\gamma = \tilde{Q}_d/\tilde{Q}_0 - 1$ is represented for reference. *Source* Modified from Schuch et al. (2018)

Many studies about this flow configuration are becoming available in the literature, including field observations (Wunderlich and Elder 1973; Ford and Johnson 1981; Best et al. 2005), analytical models (Akiyama and Stefan 1984; Parker and Toniolo 2007; Dai and García 2009), experiments (Singh and Shah 1971; Arita and Nakai 2008; Lamb et al. 2010) and numerical simulations (Farrell and Stefan 1986; Kassem and Imran 2001; Dai et al. 2007). In this context, numerical simulations unlike field observations and experiments can play an important role since they can provide information for all flow variables at any point in time and space. Schuch et al. (2018) presented a new numerical framework for the reproduction and analysis of the plunge phenomenon and its associated flow features, where the results of the three-dimensional turbulence-resolving simulations were compared with experimental data (Lamb et al. 2010) and analytical models (Parker and Toniolo 2007), and good agreement was found between them.

The main objective of this work is to present an original dataset that registers the entire spatio-temporal evolution of the plunge phenomenon and all relevant quantities. To generate this new dataset, the numerical methodology proposed by Schuch et al. (2018) was slightly modified, the simulated time is extended by 20%, the computational domain is six times wider and the flow variables are considered in a layer-averaged context. Additionally, the spatial–temporal data is available online,[1] in order to support future research.

4.2 Methodology

For the present study, N transport equations under the Boussinesq approximation can be used, in addition to the incompressible Navier–Stokes equations. They are written in their dimensionless form as

$$\frac{\partial u_j}{\partial x_j} = 0, \tag{1}$$

$$\frac{\partial u_i}{\partial t} = -u_j \frac{\partial u_i}{\partial x_j} - \frac{\partial p}{\partial x_i} + \frac{1}{\mathrm{Re}} \frac{\partial^2 u_i}{\partial x_j \partial x_j} + e_i^g \frac{1}{\mathrm{Fr}_0^2} \sum_{\updownarrow=1}^{N} c_{\updownarrow}, \tag{2}$$

$$\frac{\partial c_{\updownarrow}}{\partial t} = -\left(u_j + u_{s,\updownarrow} e_j^g\right) \frac{\partial c_{\updownarrow}}{\partial x_j} + \frac{1}{\mathrm{ReSc}} \frac{\partial^2 c_{\updownarrow}}{\partial x_j \partial x_j}, \updownarrow = 1, \ldots, N, \tag{3}$$

where u_i, p, and c correspond to velocity, pressure, and suspeded particle concentration, respectively, together with the coordinate system x_i (see Fig. 2), time t, unit vector pointing in gravity direction $e^g = [0, 1, 0]$ and the particle's settling velocity u_s. It is related to the particle diameter by the Stokes settling velocity law (Julien

---

[1] Available at https://doi.org/10.5281/zenodo.3968993 and https://github.com/fschuch/the-plunging-flow-by-3D-LES.

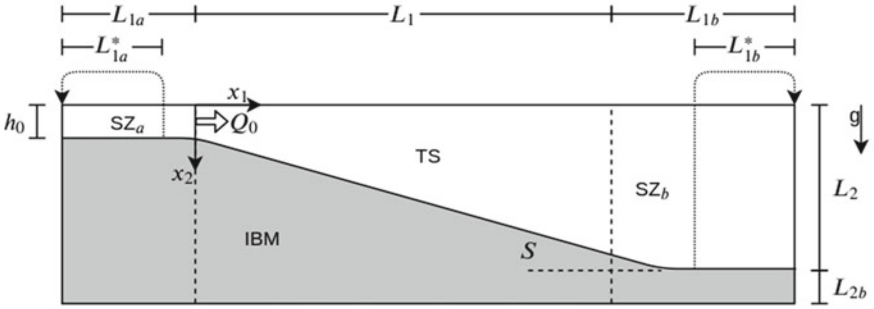

Fig. 2 Schematic representation of the computational domain (not to scale). Spanwise coordinate x_3 is perpendicular to the plane. In gray, the tilted bed is inserted by immersed boundary method (IBM); TS represents the test section, where the flow is analyzed; SZ$_a$ and SZ$_b$ represent the sponge zones. *Source* Modified from Schuch (2020)

1998) which assumes that the dominant flow force on an individual particle is the Stokes drag. The Reynolds, Schmidt, and initial densimetric Froude numbers at the inlet, besides the Stokes settling velocity, are the four dimensionless parameters that describe the problem, they are defined as follows:

$$\text{Re} = \frac{\tilde{Q}_0}{\tilde{\nu}}, \tag{4}$$

$$\text{Sc} = \frac{\tilde{\nu}}{\tilde{D}}, \tag{5}$$

$$\text{Fr}_0 = \frac{\tilde{Q}_0}{\sqrt{R\tilde{C}_0\tilde{g}\tilde{h}^3}}, \tag{6}$$

$$u_{s,\updownarrow} = \frac{\tilde{u}_{s,\updownarrow}\tilde{h}_0}{\tilde{Q}_0} = \frac{\tilde{d}^2_{s,\updownarrow}R\tilde{g}\tilde{h}_0}{18\tilde{\nu}\tilde{Q}_0}, \updownarrow = 1, \ldots, N, \tag{7}$$

where $\tilde{Q}_0$ and $\tilde{C}_0$ are the volumetric discharge per unit width and volumetric sediment concentration at the inlet of the channel, respectively. The kinematic viscosity is $\tilde{\nu}$, the fresh water and sediment densities are $\tilde{\rho}_w$, $\tilde{\rho}_s$, with R defined as $(\tilde{\rho}_s - \tilde{\rho}_w)/\tilde{\rho}_w$. The gravity acceleration is $\tilde{g}$, the diffusivity of particle concentration is $\tilde{D}$ and the grain size is $\tilde{d}_s$. All parameters and variables are made dimensionless using the influx velocity $\tilde{U}_0$, depth $\tilde{h}_0$ and sediment concentration $\tilde{C}_0$.

The computational setup (see Fig. 2) is based on the experimental channel configuration of Lamb et al. (2010) and the numerical study of Schuch et al. (2018). The test section (TS) is the region where the flow is analyzed, whose dimensions are $(L_1, L_2, L_3) = (250.0h_0, 16.875h_0, 24.0h_0)$. Notice that the dimensionless initial depth is $h_0 = 1$. The bed slope $S = 5\%$ is included in the computational domain via an immersed boundary method (IBM), following the alternating direction forcing strategy proposed by Gautier et al. (2014). Two sponge zones are employed for different reasons. Firstly, SZ_a provides the particle-laden flow upstream of the test section, with a recycling technique in order to generate a turbulent inflow condition. Secondly, SZ_b applies an intrinsic profile for the stream-wise velocity u_1 near the outflow boundary, in order to reduce the turbulence level to zero. The horizontal extension of the sponge zones is $(L_{1a}, L_{1b}) = (25.0, 62.5)$. The entire computational domain is discretized using $(n_1, n_2, n_3) = (1081, 121, 90)$ mesh points. A time step of $\Delta t = 0.0125$ is employed for a total of 4.8×10^5 iterations. In comparison with the previous study of Schuch et al. (2018), the numerical channel in this study is now six times wider, in a dimension compatible with the experimental reference if an initial depth of $\tilde{h}_0 = 10\,\mathrm{mm}$ is considered, and the simulated time is extended from 5,000 to 6,000 dimensionless units, an increase of 20%. A nondeformable water surface is imposed as top boundary condition (where $x_2 = 0$), which is described by Nasr-Azadani et al. (2013) as a free-slip condition for velocity and no-flux condition for the concentration field. The bottom boundary condition (at the solid/fluid interface) is no-slip for velocity and one-dimensional convective outflow for concentration, as functions of the settling velocity u_s (Necker et al. 2002). Inflow and outflow conditions are handled by both sponges zones and periodic boundary condition is employed in the spanwise direction (x_3). For the initial condition, the domain is filled with freshwater at rest ($u_i = c_{\updownarrow} = 0$). For more details about the computational setup see Schuch (2020).

The numerical simulations were carried out by the high-order Navier–Stokes solver Xcompact3d,[2] an open-source tool based on the Boussinesq system for incompressible fluids, designed for High-Performance Computing (Laizet and Lamballais 2009; Laizet and Li 2011; Bartholomew et al. 2020). The governing equations (2) are solved under an implicit Large-Eddy Simulations approach, in which only the largest and energy-containing flow structures are resolved. On the other hand, the small scales are not resolved, instead, they are modeled via an artificial dissipation that takes place when computing the viscous term (Sagaut 2006; Grinstein et al. 2007; Lamballais et al. 2011; Dairay et al. 2017).

Seven experiments were carried out by Lamb et al. (2010), and five of them are reproduced in this study, as shown in Table 1. The experimental grain-size distribution (crushed silica $\tilde{\rho}_s = 2{,}650\,\mathrm{kg/m^3}$) is modeled by three diameters ($\tilde{d}_{s,1} = 3\,\mu\mathrm{m}$, $\tilde{d}_{s,2} = 21\,\mu\mathrm{m}$, and $\tilde{d}_{s,3} = 43\,\mu\mathrm{m}$) in a distribution of about one third for each grain size. The Schmidt number Sc is equal to 1 in the present study. Notice that cases 2, 6, and 7 have the same flow discharge $\tilde{Q}_0$ and increasing sediment concentration $\tilde{C}_0$, while cases 4, 5, and 6 have the same sediment concentration $\tilde{C}_0$ and increasing flow discharge $\tilde{Q}_0$. The validation of the numerical framework employed here for the problem illustrated in Fig. 1 is out of the scope of this study, since a complete comparison between numerical, experimental, and analytical models is already available in Schuch et al. (2018).

---

[2] The code is available at https://github.com/xcompact3d/Incompact3d.

Table 1 Volumetric discharge per unit width $\tilde{Q}_0$ and volumetric sediment concentration $\tilde{C}_0$ recorded at the inlet from the experiments of Lamb et al. (2010), in addition to the respective Reynolds number Re, initial densimetric Froude number Fr_0 and Stokes settling velocity $u_{s,\updownarrow}$ for each granulometric fraction

Simulations	2	4	5	6	7
$\tilde{Q}_0$ (m^2/s)	0.0043	0.0025	0.0033	0.0043	0.0043
$\tilde{C}_0$ (%)	0.36	0.54	0.54	0.54	1.00
Re	4,300	2,500	3,300	4,300	4,300
Fr_0	17.81	8.45	11.16	14.54	10.68
$u_{s,1} \times 10^{-5}$	1.9	3.2	2.5	1.9	1.9
$u_{s,2} \times 10^{-3}$	0.9	1.6	1.2	0.9	0.9
$u_{s,3} \times 10^{-3}$	3.9	6.7	5.0	3.9	3.9

Source Modified from Lamb et al. (2010)

4.3 Results

A sample of the tridimensional plunging flow is shown in Fig. 3, represented by a snapshot of the total concentration field ($c_t = c_1 + c_2 + c_3$) for case 4 at dimensionless time equals to $t = 1{,}000$. In this figure, the plunge line is visible near $x_1 = 120$, as well as the body and head of the underflow turbidity current downstream plunging, including the lobes and clefts structures at the front. The dimensionless total concentration is one (red color) right at the inlet of the test section, and then decays due to sedimentation with the stream-wise coordinate x_1. Besides that, the turbulent mixing between the turbidity current and the ambient fluid is evidenced by the dark blue color, which corresponds to low concentration levels.

The complete spatio-temporal analysis of the relevant quantities is possible in a layer-averaged context per width unit, that is computed following Ellison and Turner (1959) according to the equations:

$$Uh(x_1, t) = \frac{1}{L_3} \int_0^{L_3} \int_{x_{2r}}^{x_{2i}} u_1(x_1, x_2, x_3, t) dx_2 dx_3, \tag{8}$$

$$U^2h(x_1, t) = \frac{1}{L_3} \int_0^{L_3} \int_{x_{2r}}^{x_{2i}} (u_1(x_1, x_2, x_3, t))^2 dx_2 dx_3, \tag{9}$$

$$UCh(x_1, t) = \frac{1}{L_3} \int_0^{L_3} \int_{x_{2r}}^{x_{2i}} u_1(x_1, x_2, x_3, t) c_t(x_1, x_2, x_3, t) dx_2 dx_3. \tag{10}$$

For the vertical integration, x_{2r} represents the bed position and x_{2i} represents the interface between the underflow turbidity current and the ambient fluid, considered in this work as the position where $u_1 \times c_t = 0.005$. Finally, the layer-averaged velocity U, flow depth H, flow discharge Q, concentration C, and local densimetric Froude number Fr are obtained, respectively, as

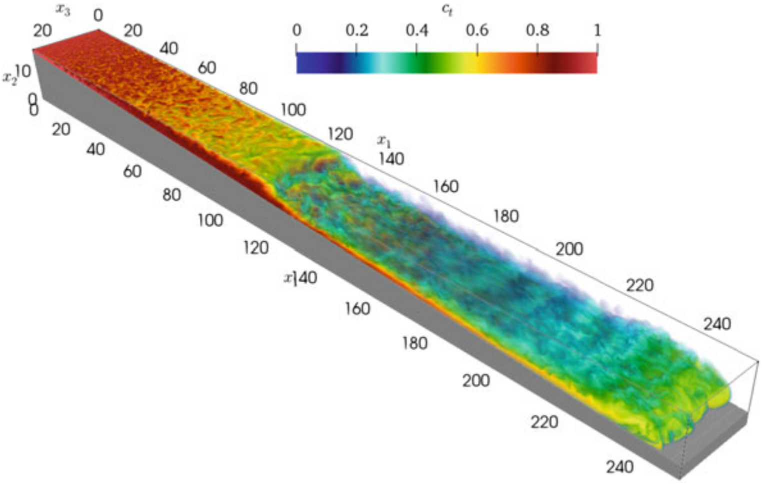

Fig. 3 Instantaneous volumetric visualization of the total concentration field c_t for case 4 at t = 1,000

$$U(x_1, t) = U^2h/Uh, \tag{11}$$

$$H(x_1, t) = (Uh)^2/U^2h, \tag{12}$$

$$Q(x_1, t) = Uh, \tag{13}$$

$$C(x_1, t) = UCh/Uh, \tag{14}$$

$$\mathrm{Fr}(x_1, t) = \frac{Q(x_1, t)}{\sqrt{C(x_1, t)(H(x_1, t))^3}}\mathrm{Fr}_0. \tag{15}$$

The spatio-temporal evolution of the quantities described above for case 4 are shown in Fig. 4, in addition to the spanwise-averaged total concentration field c_t for dimensionless time equals to 250, 500, 1,000, 2,000, and 6,000, from (a) to (e), respectively. All the features of the plunging flow in a tilted bed (see Fig. 1) can be seen. The plunge point is visible since early times (a and b) and moves downstream, for more advanced time (e) it tends to a quasi-stationary position at around $x_1 = 150$, the same position found experimentally in Lamb et al. (2010). Upstream plunging is located at the depth-limited flow region, where the inflowing turbidity current has enough momentum to push the ambient fluid downstream. Due to the tilted bed, the flow's depth increases with the streamwise coordinate (x_1) and progressively reduces its velocity until a critical point, the plunge zone, where the flow collapses, accelerates, and turns into a density current, governed now by the buoyance forces. This behavior reflects on the layer-averaged velocity U (f), where the maximum value is noticeable at the inflow boundary ($x_1 = 0$) and decreases until its minimum value at the plunge point, where the flow accelerates. Besides that, the incorporation of ambient fluid into the submerged turbidity current (entrainment) increases the flow velocity downstream plunging. The layer-averaged concentration C (g) decays with x_1 due to the sedimentation, and the mixing with the ambient fluid reduces concentration even more downstream plunging. Besides that, C works as an indicator for the temporal evolution of the front position x_f, which is obtained as the highest value of x_1 where the concentration is non-zero. The densimetric Froude number Fr (h) expresses the ratio between inertial and buoyance forces, that are dominant upstream and downstream plunging, respectively. In this way, Fr is directly related to the stable plunge position, in fact, the Froude value at plunge point observed in Fig. 4h is very close to $\mathrm{Fr}_p = 0.45$, a value reported in previous works (Parker and Toniolo 2007; Lamb et al. 2010; Schuch et al. 2018). The densimetric Froude number is also used to track the temporal evolution of the plunge point position x_p, since it is observed at the absolute minimum value for Fr.

If the flow is sufficiently intense, the turbidity currents can resuspend part of the material previously deposited, or even erode the bed over which it flows, as commented by Necker et al. (2002). Even though the numerical configuration of this work does not consider resuspension, a further analysis based on the simulated data can indicate places where the flow is more likely to present such phenomena. For that, the bed shear velocity u_τ has a fundamental role, and can be calculated according to the equation:

$$u_\tau = \sqrt{\tau_w}, \text{with} \tau_w = \frac{1}{\mathrm{Re}} \sqrt{\left(\frac{\partial \widehat{u}_1}{\partial \widehat{x}_2} \right)^2 + \left(\frac{\partial \widehat{u}_3}{\partial \widehat{x}_2} \right)^2} \Bigg|_{x_2 = x_{2i}} . \tag{16}$$

The notation $(\hat{\cdot})$ represents a rotation in the coordinate system, so that $\widehat{x}_1$ still points in the preferred flow direction, but is now parallel to the bed, and $\widehat{x}_2$ is normal to the bed, while x_{2i} corresponds to the position of the solid–fluid interface. In this way, the velocities required for the calculation are given by

$$\widehat{u}_1 = \cos(\theta) u_1 - \sin(\theta) u_2, \tag{17}$$

$$\widehat{u}_3 = u_3, \tag{18}$$

while the derivative normal to the bed is computed as

$$\frac{\partial}{\partial \widehat{x}_2} = \sin(\theta) \frac{\partial}{\partial x_1} + \cos(\theta) \frac{\partial}{\partial x_2}. \tag{19}$$

The bed shear velocity u_τ can be observed in Fig. 4i. It has a behavior very similar to that observed for the layer-averaged velocity U, being maximum at the entrance of the channel and then decreases. The minimum value for u_τ is reached exactly

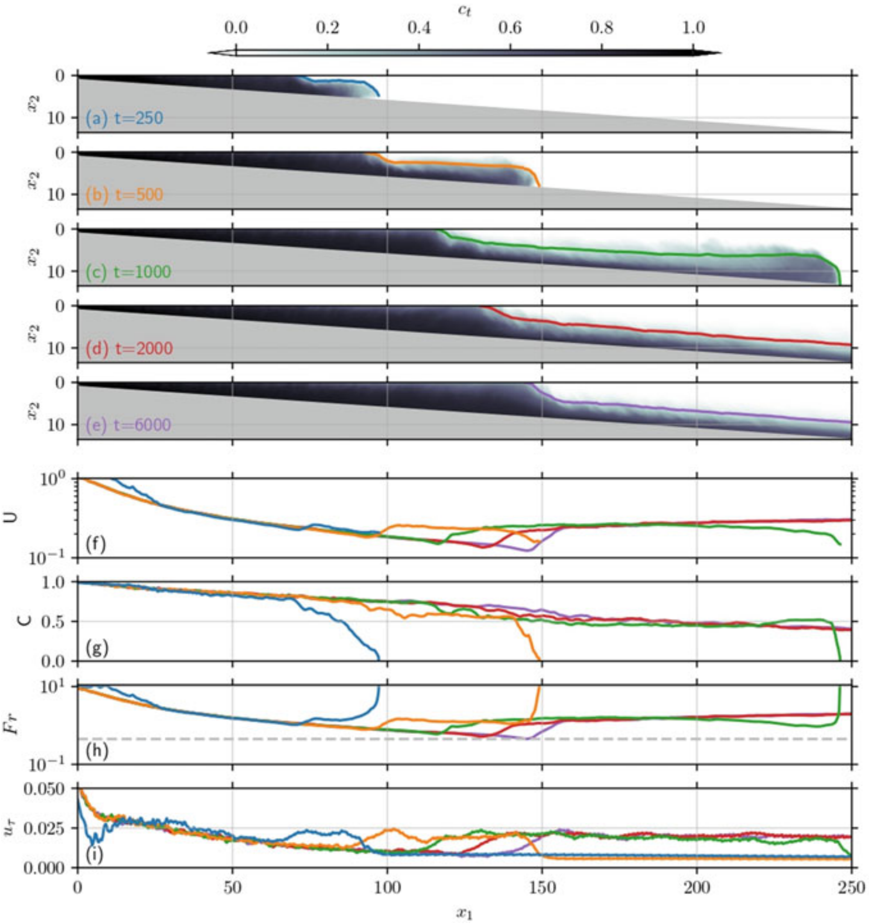

Fig. 4 Case 4 spanwise-averaged total concentration field c_t for dimensionless time equals to 250, 500, 1,000, 2,000, and 6,000 from (**a**) to (**e**), respectively. In addition to layer-averaged flow depth H (colored lines from **a** to **e**), streamwise velocity U (**f**), concentration C (**g**), and local densimetric Froude number Fr (**h**), $\mathrm{Fr}_p = 0.45$ is shown in dashed line for reference, computed according to Eq. (4), besides the spanwise-averaged bed shear velocity u_τ (**i**), expressed by Eq. (16)

where the reduction in flow's depth occurs, seen solid lines from (a) to (e), there is a local maximum immediately at the plunge point, where Fr is minimum, and then the value stabilizes in the body region, being slightly larger at the head. It indicates that the channel's entrance is the region with the greatest erosive potential, followed by the plunging point and then the head of the turbidity current.

The spanwise-averaged total concentration field c_t for all cases at dimensionless time $t = 1{,}000$ is shown in Fig. 5, from (a) to (e). Both flow head and plunging zone are well defined for all cases, however, their position is affected by the parameters of each case. In comparison, a plunging upstream accelerates the turbidity current earlier and impulsionates its body and head, as shown in the layer-averaged velocity U (f). The layer-averaged concentration C (g) is very similar for all cases upstream plunging, however, the value downstream differs due to differences in flow depth and mixing with the ambient fluid. The densimetric Froude number Fr is shown in Fig. 5h. At $t = 1{,}000$, the plunging for all cases is still in the transient phase, so the Froude value observed at plunge point is higher than the reference of $\mathrm{Fr}_p = 0.45$, on the other hand, the Fr value measured at underflow's head of around a unity is in agreement with previous studies (Sequeiros 2012; Sequeiros et al. 2018). Figure 5i shows the bed shear velocity for the different cases. In general, the maximum value for u_τ is where $x_1 = 0$, followed by underflow's head and body, and the minimum value is observed at the plunge point. The magnitude of u_τ is function of the flow velocity, that in turn depends on the plunge point location, therefore, cases with the plunging upstream produce higher bed shear velocity u_τ. The animated versions of the flow visualization are presented in Figs. 3, 4, and 5 are available as supplementary materials.

Figure 6a shows the temporal evolution of the plunge point position x_p. Cases 2, 6, and 7 have the same flow discharge and increasing sediment concentration, which moves the plunge point downstream. Additionally, cases 4, 5, and 6 have the same sediment concentration and increasing flow discharge, which also moves the plunge downstream. Both parameters can be combined into the initial densimetric Froude number Fr_0, where a higher Fr_0 demands more distance for plunging and more runtime to eventually reach an asymptotic state. It is evident that for case 2, with the highest initial Froude number, the plunge zone left the computational test section at around $t = 4{,}000$. Notice that the depth at plunge point is recovered by the linear equation $h_p = 1 + Sx_p$. Figure 6b shows the temporal evolution of the front position x_f, while Fig. 6c shows the front velocity $u_f = dx_f/dt$, where a moving average in time is employed in order to smooth the signal. Notice that both curves are just defined while the front is inside the test section ($x_f \leq 250$). As discussed previously, the front velocity is strongly affected by the plunge point position, once it impulsions the underflow's body and head. In this way, a higher front velocity is observed according to the same parameters that move the plunge point upstream, i.e., lower initial densimetric Froude number Fr_0, lower initial flow discharge Q_0 or higher initial sediment concentration C_0. Finally, Fig. 6d shows the time evolution of the densimetric Froude number at plunge position Fr_p, where a convergence to $\mathrm{Fr}_p = 0.45$ is noticeable, in good agreement with previous studies (Parker and Toniolo 2007; Lamb et al. 2010; Schuch et al. 2018). The averaged Froude number at plunge point measured is $\mathrm{Fr}_p = 0.438 \pm 0.027$, taking an average in time ($4{,}000 \leq t \leq 6{,}000$) and between cases (excluding case 2, that left the computational test section). This value depends on the bed roughness, suspended grain size, and bed slope, according to Sequeiros (2012). Besides, Fr_p can be useful in the development of new methodologies for the prediction of depth for plunging, or plunging criteria (Schuch 2020; Schuch et al. 2021).

Figure 7 shows the flow quantities under investigation as a function of time t and the streamwise coordinate x_1, are they: Flow depth H, layer-averaged concentration C and densimetric Froude number Fr, computed according to Eq. (4), in

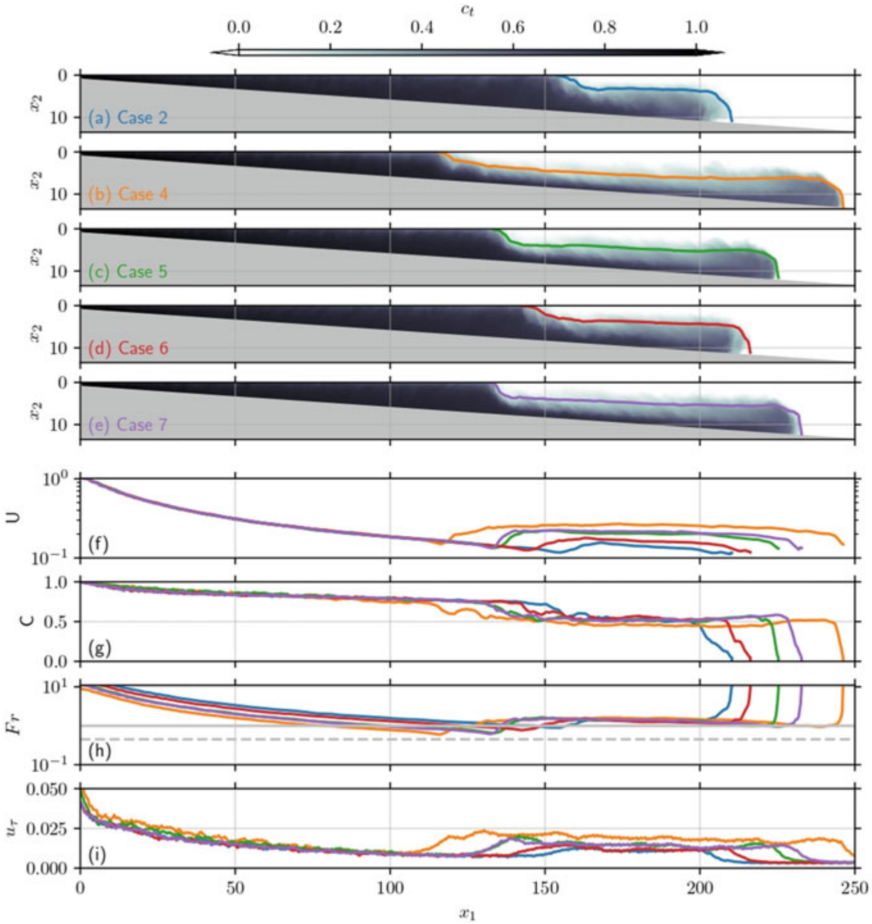

Fig. 5 Spanwise-averaged total concentration field c_t for all cases from (**a**) to (**e**) at $t = 1{,}000$. In addition to layer-averaged flow depth H (colored lines from **a** to **e**), streamwise velocity U (**f**), concentration C (**g**), and local densimetric Froude number Fr (**h**), 1.0 and 0.45 are shown in solid and dashed lines for reference, computed according to Eq. (4), besides the spanwise-averaged bed shear velocity u_τ (**i**), expressed by Eq. (16)

addition to the mixing coefficient $\gamma = Q/Q_0 - 1$ and the bed shear velocity u_τ (16), from top to bottom, respectively. The positions for plunge point x_p (solid lines) and front x_f (dashed lines) are presented for reference. The five simulated cases are arranged horizontally. The entire spatio-temporal evolution is shown, where some topics discussed previously in Figs. 4 and 5 are visible in details. The maximum flow depth H (Fig. 7a–e) occurs at plunge point, where the flow collapses and accelerates. The plunge point for case 2 left the test section (where $x_1 = 250$), its high initial Froude number demands a deeper domain in order to have a stable plunging position. The concentration C (Fig. 7f–j) decays due to sedimentation, and the mixing with the

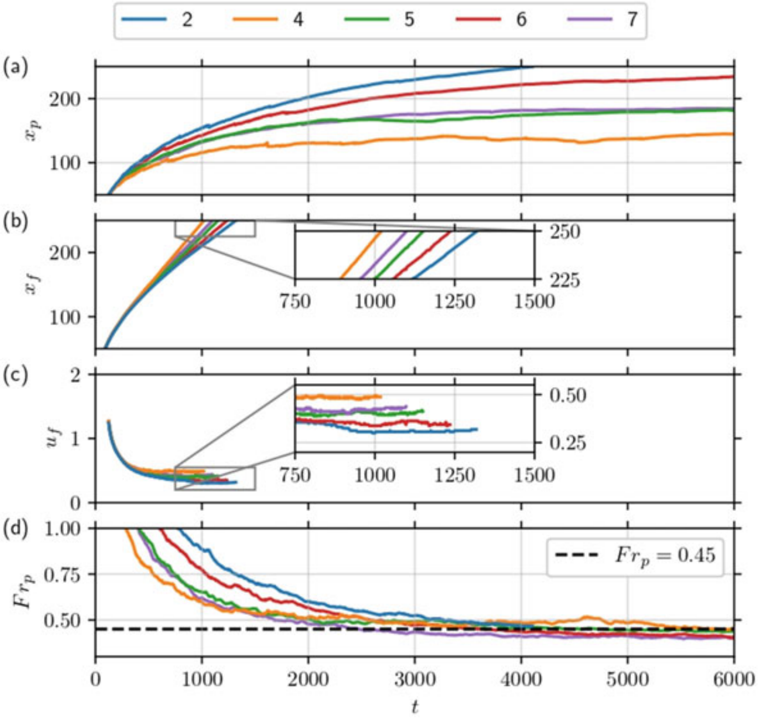

Fig. 6 Time evolution of **a** distance for plunging x_p, **b** front position x_f, **c** front velocity u_f and **d** densimetric Froude number at plunging point Fr_p, where $\mathrm{Fr}_p = 0.45$ is shown for reference

ambient fluid downstream plunging is another process that reduces sediment concentration. The densimetric Froude number Fr (Fig. 7f–j) decreases with the streamwise coordinate x_1, because the flow depth increases, until the minimum value at plunge zone. The acceleration at plunge zone increases Fr downstream plunging, as well as the increase in flow discharge due to entrainment. The densimetric Froude number measured downstream plunging Fr_d (at the end of the test section, where $x_1 = 250$) is equal to 1.93 ± 0.043, 1.722 ± 0.044, 1.385 ± 0.113 and 1.648 ± 0.047 for cases 4 to 7, respectively, all greater than one (e.g., supercritical), which is expected once the head has passed away in bed slopes steeper than about 1% according to Sequeiros (2012). Figure 7p–t show the spanwise-averaged bed shear velocity u_τ, the highest value is observed for case 4 (Fig. 7q), with the shortest distance for plunging and higher underflow velocity. Figure 7u–y shows the mixing coefficient $\gamma = Q/Q_0 - 1$, that represents the increase in the submerged flow discharge due to entrainment of ambient fluid into the turbidity current. Cases that have plunged early present more distance for entrainment, so the highest value is observed for case 4 (Fig. 7v), followed by case 7 (Fig. 7y) and case 5 (Fig. 7w). The plunging point for case 2 (Fig. 7u) left the computational test section, so the mixing coefficient is negligible for $t > 4{,}000$. On the other hand, this case has a negative mixing value

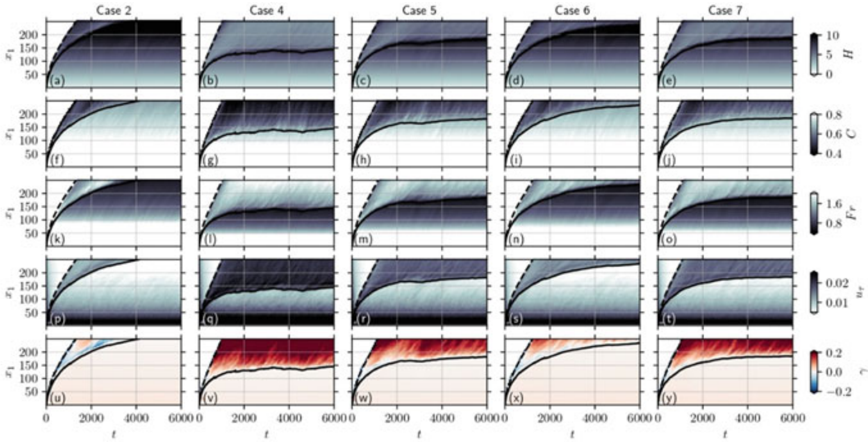

Fig. 7 Spatio-temporal evolution of flow depth H, layer-averaged concentration C, densimetric Froude number Fr, spanwise-averaged bed shear velocity u_τ and mixing coefficient, from top to bottom, respectively. Cases 2, 4, 5, 6, and 7 are arranged from left to right. Plunging point x_p (solid lines) and front x_f (dashed lines) positions are shown for reference. Horizontal and vertical axes represent time t and stream-wise coordinate x_1, respectively

(blue color) downstream plunging during the transient phase ($t < 4{,}000$), indicating that the submerged turbidity current loses its volume to the ambient in a detrainment process. Notice that a pulsing phenomenon is observed for all cases, even though the variables are evaluated in a spanwise-averaged context and the input flow is kept steady, this phenomenon is investigated in details in Best et al. (2005) and Kostaschuk et al. (2018).

4.4 Conclusions

Numerical simulations play an essential role in many different research fields, since they can provide information on all variables for any point of time and space. Lab experiments are very often not able to provide such information, with data only available in a plane and/or locally. In this study, a new dataset is presented, covering the entire spatio-temporal evolution of the plunge phenomenon and all quantities related to it using the layer-averaged context. Such database can be used to analyze the parameters and mechanisms that govern the flow transition in the plunge zone and support future research, it is available at https://doi.org/10.5281/zenodo.3968993 and https://github.com/fschuch/the-plunging-flow-by-3D-LES.

Acknowledgements This study was supported by Petrobras S.A. and financed in part by the Coordenação de Aperfeiçoamento de Pessoal de Nível Superior—Brazil (CAPES)—Finance Codes

88887.154060/2017-00 and 88881.187490/2018-01. Computing time was provided by the high-performance facility LAD-PUCRS at the Pontifical Catholic University of Rio Grande do Sul, in Porto Alegre, Brazil.

References

Akiyama J, Stefan HG (1984) Plunging flow into a reservoir: theory. J Hydraul Eng 110(4):484–499. ISSN 0733-9429. https://doi.org/10.1061/(ASCE)0733-9429(1984)110:4(484)

Arita M, Nakai M (2008) Plunging conditions of two-dimensional negative buoyant surface jets released on a sloping bottom. J Hydraul Res 46(3):301–306

Bartholomew P, Deskos G, Frantz RA, Schuch FN, Lamballais E, Laizet S (2020) Xcompact3d: an open-source framework for solving turbulence problems on a Cartesian mesh. SoftwareX 12:100550

Best JL, Kostaschuk RA, Peakall J, Villard PV, Franklin M (2005) Whole flow field dynamics and velocity pulsing within natural sediment-laden underflows. Geology 33(10):765–768

Chamoun S, De Cesare G, Schleiss AJ (2016) Managing reservoir sedimentation by venting turbidity currents: a review. Int J Sedim Res 31(3):195–204

Dai A, Cantero MI, García MH (2007) Plunging of two-dimensional gravity currents. In: Proceedings of the 5th international symposium on environmental hydraulics, IAHR, Temp, Ariz

Dai A, García MH (2009) Discussion of “note on the analysis of plunging of density flows” by Gary Parker and Horacio Toniolo. J Hydraul Eng 135(6):532–533

Dairay T, Lamballais E, Laizet S, Vassilicos JC (2017) Numerical dissipation vs. subgrid-scale modelling for large eddy simulation. J Comput Phys 337:252–274

Ellison T, Turner J (1959) Turbulent entrainment in stratified flows. J Fluid Mech 6(3):423–448

Farrell G, Stefan H (1986) Buoyancy induced plunging flow into reservoirs and coastal regions, project report, no. 241, st. Anthony Falls Hydr. Lab., University of Minnesota

Ford DE, Johnson MC (1981) Field observations of density currents in impoundments. In: Surface water impoundments. ASCE, pp 1239–1248

García M (1996) Hidrodinamica ambiental. Colección Ciencia y técnica, Universidad Nacional del Litoral

Gautier R, Laizet S, Lamballais E (2014) A DNS study of jet control with microjets using an immersed boundary method. Int J Comput Fluid Dyn 28(6–10):393–410

Grinstein FF, Margolin LG, Rider WJ (2007) Implicit large eddy simulation: computing turbulent fluid dynamics. Cambridge University Press

Horner-Devine AR, Hetland RD, MacDonald DG (2015) Mixing and transport in coastal river plumes. Annu Rev Fluid Mech 569–594

Julien PY (1998) Erosion and sedimentation. Cambridge University Press, Cambrige, Reino Unido

Kassem A, Imran J (2001) Simulation of turbid underflows generated by the plunging of a river. Geology 29(7):655–658

Kostaschuk R, Nasr-Azadani MM, Meiburg E, Wei T, Chen Z, Negretti ME, Best J, Peakall J, Parsons DR (2018) On the causes of pulsing in continuous turbidity currents. J Geophys Res Earth Surf 123(11):2827–2843

Laizet S, Lamballais E (2009) High-order compact schemes for incompressible flows: a simple and efficient method with quasi-spectral accuracy. J Comput Phys 228(16):5989–6015

Laizet S, Li N (2011) Incompact3d: a powerful tool to tackle turbulence problems with up to $O(105)$ computational cores. Int J Numer Methods Fluids 67(11):1735–1757

Lamb MP, McElroy B, Kopriva B, Shaw J, Mohrig D (2010) Linking river-flood dynamics to hyperpycnalplume deposits: experiments, theory, and geological implications. Geol Soc Am Bull 122(9–10):1389–1400

Lamb MP, Mohrig D (2009) Do hyperpycnal-flow deposits record river-flood dynamics? Geology 37(12):1067–1070

Lamballais E, Fortuné V, Laizet S (2011) Straightforward high-order numerical dissipation via the viscous term for direct and large eddy simulation. J Comput Phys 230(9):3270–3275

Meiburg E, Kneller B (2010) Turbidity currents and their deposits. Annu Rev Fluid Mech 42:135–156

Mulder T, Syvitski JPM, Migeon S, Faugeres JC, Savoye B (2003) Marine hyperpycnal flows: initiation, behavior and related deposits. A review. Mar Pet Geol 20(6):861–882

Nasr-Azadani M, Hall B, Meiburg E (2013) Polydisperse turbidity currents propagating over complex topography: comparison of experimental and depth-resolved simulation results. Comput Geosci 53:141–153

Necker F, Härtel C, Kleiser L, Meiburg E (2002) High-resolution simulations of particle-driven gravity currents. Int J Multiph Flow 28(2):279–300

Parker G, Toniolo H (2007) Note on the analysis of plunging of density flows. J Hydraul Eng

Sagaut P (2006) Large eddy simulation for incompressible flows: an introduction. Springer Science & Business Media

Schuch FN, Meiburg E, Silvestrini JH (2021) Plunging condition for particle-laden flows over sloping bottoms: three-dimensional turbulence-resolving simulations. Comput Geosci 156(2021):104880

Schuch FN, Pinto LC, Silvestrini JH, Laizet S (2018) Three-dimensional turbulence-resolving simulations of the plunge phenomenon in a tilted channel. J Geophys Res: Oceans 123:1–13

Schuch FN (2020) Análise do Mergulho de Escoamentos Hiperpicnais em Canal Inclinado por Meio de Simulação Numérica de Grandes Escalas. Ph.D. thesis, Programa de Pós-Graduação em Engenharia e Tecnologia de Materiais, Escola Politécnica, PUCRS

Sequeiros OE (2012) Estimating turbidity current conditions from channel morphology: a froude number approach. J Geophys Res: Oceans 117(C4)

Sequeiros OE, Mosquera R, Pedocchi F (2018) Internal structure of a self-accelerating turbidity current. J Geophys Res: Oceans 123(9):6260–6276

Singh B, Shah C (1971) Plunging phenomenon of density currents in reservoirs. La Houille Blanche 1:59–64

Wunderlich WO, Elder RA (1973) Mechanics of flow through man-made lakes. In: Washington DC American Geophysical Union Geophysical Monograph Series, vol 17, pp 300–310

Chapter 5
Numerical Investigation of the Flow-Induced Noise in a Turbulent Flow Inside an HVAC Duct

Lucas de Souza Meira and Francisco José de Souza

Abstract The present work aims to investigate the flow-induced noise generation in a turbulent pipe flow by means of Computational Fluid Dynamics. The flow behavior and noise production at a high Reynolds number internal flow are analyzed in a heating ventilation air conditioning (HVAC) system. In order to develop the present analysis and to find the most accurate approach for this application, we evaluated different advective discretization schemes in the context of DES simulations. Comparisons are established with experimental data of benchmark cases, for which gauge pressure in specific regions, sound pressure level, and velocity fields are evaluated. Simulations are performed using an in-house code, i.e., UNSCYFL3D, which was developed at the Federal University of Uberlândia and has been validated in several internal and external flows. By means of this work, we were able to find the most accurate setup parameters for such a problem. Reynolds Averaged Navier–Stokes turbulence models did not yield satisfactory results, whereas the Detached Eddy Simulation (DES) was found to produce much more accurate results, obviously at a higher computational cost. It is concluded that DES, along with the central difference scheme for the advection, is a viable approach for computational aeroacoustics for HVAC ducts.

Keywords Flow-induced noise · DES · HVAC system · Turbulence · Internal flow

5.1 Introduction

Over the last decades, researchers and engineers concentrated their efforts in the search of solutions for many industrial demands such as reduction of fuel consumption and pollutant generation, among others. Of no less importance, the environmental and comfort concerns have also been the object of many investigations. For

---

L. de S. Meira · F. J. de Souza (✉)
Federal University of Uberlândia, Av. João Naves de Ávila 2121, Uberlândia, MG, Brasil
e-mail: francisco.souza@ufu.br

L. de S. Meira
e-mail: lucas.meira@ufu.br

H. F. Meier et al. (eds.), *Advances in Turbulence*, ABCM Series on Mechanical Sciences and Engineering, https://doi.org/10.1007/978-3-031-25990-6_5

instance, the development of more silent vehicles and other devices represents a new requirement in the consumption standards.

The new age of jet-powered aircraft required more comprehension of the noise genesis, properties, and its relationship with the fluid mechanics. The fluid flow instabilities are able to create rapid short pressure waves, originating sound according to Howe (2003). The most advanced theories used to predict aerodynamic sound are based in the initial studies of Lighthill (1952, 1956). Quantitatively, one of the main difficulties in predicting aeroacoustics is that only a small parcel of the kinetic energy present in turbulent flows produces oscillations in the pressure field, creating acoustic noise.

Basically, there are three techniques to investigate aeroacoustics, experimental, analytical, or numerical approaches. The first one provides benchmark results or data related to complex geometries and designs; however, it is associated to the high cost of equipment and measurement systems. The second one produces fast and effective solutions, by means of the Lighthill's acoustic analogy, for instance, however its applications are extremely limited, only in cases related to finite regions of rotational and unbounded turbulent flow, such as downstream of a turbulent nozzle (Howe 2003). On the other hand, CFD (computational fluid dynamics) simulations are usually introduced as a project initial step for simplifying complexities found in experimental campaigns, reducing product development costs and increasing the possibilities of analysis.

Earlier scientific works had the purpose of creating samples to analyze the noise sources, such as bay doors and cavities in missile bays under transonic conditions (Henshaw 2000). Allen et al. (2005) simulated this bay with different models and correlated them with modes of tonal noise. In automobile industry, the main concern, beyond external flow-induced noise, is the internal noise. Heating ventilation and air conditioning (HVAC) systems are capable of producing an amount of noise, as demonstrated by Jäger et al. (2008) experimentally and numerically. Sunroof buffeting phenomenon and its contribution to the noise generation is presented, experimentally, by Islam et al. (2008).

This work aims to simulate experimental cases carried out by Jäger et al. (2008), whereas the main geometry is based on a simplified HVAC duct. The duct has a square cross section with a 90° bend. This angle causes a pressure-driven flow separation and a throttle flap is disposed downstream to the bend. Therefore, the simplified HVAC duct represents the main noise sources: flow separation and flow around an obstacle. Two different geometries are simulated in this work, one of them with the throttle flap and another one without the flap. An analysis of different discretization schemes for the advective term is presented throughout this paper, aiming to characterize the aerodynamic sound mechanisms and describe the best set and techniques to solve acoustics problems numerically.

5.2 Methodology

The methodology presented in this work consists of these basic steps: physical, mathematical, and numerical modeling and data processing. The first one deals with the experimental conditions, equipment, fluid properties, and sampling, among others. The second one is related to models and equations adopted to solve the problem. In the third, several assumptions and constraints were made to reduce computational costs. The latter considers a series of operations to process the output CFD data.

5.2.1 Physical Modeling

Jäger et al. (2008) conducted the experiment with a complex flow treatment upstream to the HVAC geometry. In his work, a series of devices, such as variable speed fan, mufflers, adapters with tripping wire, and a startup duct, were used to develop the turbulent flow avoiding the vibration and the fan blade pass frequency and analyze only the aeroacoustics of the HVAC duct. The HVAC system geometry and dimensions are represented in Fig. 1.

Assuming that the eddies, noise, and vibration were damped by upstream devices, a simplified domain was adopted. Figure 2a presents the domain that includes a boundary layer startup duct (3 m long), the HVAC, and a plenum volume for the flow discharge. Once that the turbulence properties are not described by Jäger et al. (2008), a uniform velocity profile (7.5 m/s) was imposed at the inlet boundary, resulting in a Reynolds number around 41,096. Therefore, a fully developed turbulent flow reaches

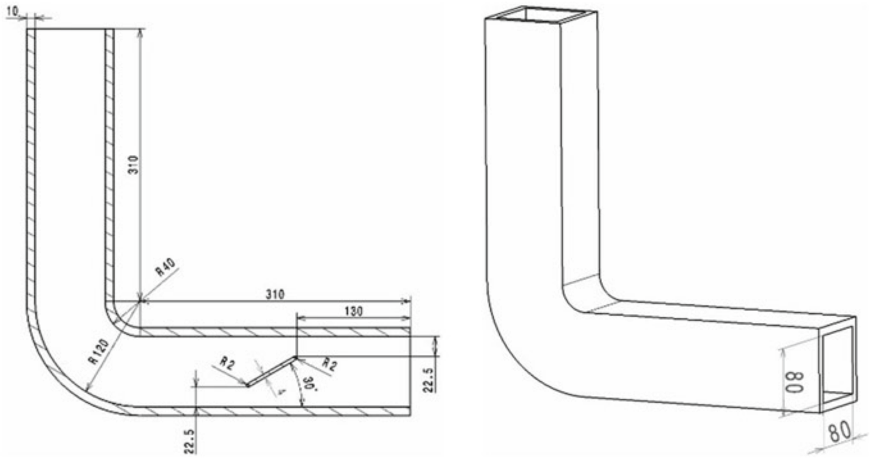

(a) **(b)**

Fig. 1 Dimensions of the HVAC duct: cut section (**a**) and isometric view (**b**) (Jäger et al. 2008)

Fig. 2 Geometry CAD model; total domain (**a**) and detailed HVAC with flap and probes position (**b**)

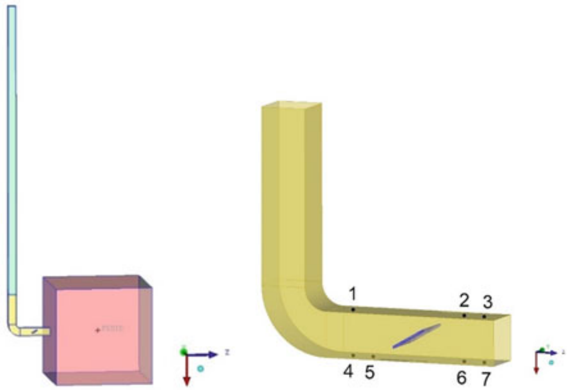

(a) **(b)**

the HVAC bend. To simulate mounted flush microphones, described in experimental work, seven probes were disposed near to the HVAC wall aiming to measure the gauge pressure value along calculations. Their positions are represented in Fig. 2b.

Other considerations and hypotheses were taken throughout this study. For example, the fluid was considered Newtonian and the flow was incompressible, due to the low Mach number of the experiments. The wall of the boundary layer startup duct, the 90° bend, and the flap were configured as non-slip surfaces. All faces of the plenum volume were set as pressure outlet boundaries, simulating an anechoic chamber to flow discharge.

5.2.2 *Mathematical Modeling*

The mathematical model includes the mass conservation equation, Eq. (1); the linear momentum equation, Eq. (2), in their filtered formulation for a Newtonian fluid with constant properties in incompressible flow.

$$\frac{\partial \widetilde{u}_j}{\partial x_j} = 0 \tag{1}$$

$$\frac{\partial \widetilde{u}_j}{\partial t} + \frac{\partial (\widetilde{u}_i \widetilde{u}_j)}{\partial x_j} = -\frac{1}{\rho}\frac{\partial \tilde{p}}{\partial x_i} + (\nu + \nu_t)\left(\frac{\partial^2 \widetilde{u}_i}{\partial x_j \partial x_j}\right) + g_i \tag{2}$$

where $\widetilde{u}_i$ is the filtered velocity component, ρ is the fluid density (1.225 kg/m^3), $\tilde{p}$ is the filtered pressure, g_i is the gravitational acceleration ($-9.81\ \text{m/s}^2$ aligned in Z-axis), and ν and ν_t are the kinematic molecular ($1.46 \times 10^{-5}\ \text{m}^2/\text{s}$) and eddy viscosities. Although gravity was included in the model, its effect is negligible under the conditions simulated.

Since the Reynolds number is high ($\mathrm{Re}_h = 41{,}096$), the flow can be characterized as turbulent and the turbulence effects must be taken into account. As near-wall effects, separated flow and adverse pressure gradient are important in this problem, as suggested by Silveira Neto (2020), the RANS closure model used in this work is the SST (shear stress transport), proposed by Menter (1994). The SST model is described in Eqs. (3) and (4).

$$\frac{\partial k}{\partial t} + \frac{\partial(\widetilde{u_i}\, k)}{\partial x_i} = P_k - \beta^* k \omega F_{\mathrm{DES}} + \frac{\partial}{\partial x_i}\left[(\nu + \sigma_k \nu_t)\frac{\partial k}{\partial x_i}\right] \tag{3}$$

$$\frac{\partial \omega}{\partial t} + \frac{\partial(\widetilde{u_i}\, \omega)}{\partial x_i} = \alpha \frac{P_k}{\nu_t} - \beta \omega^2 + \frac{\partial}{\partial x_i}\left[(\nu + \sigma_\omega \nu_t)\frac{\partial \omega}{\partial x_i}\right] + 2(1 - F_1)\sigma_{\omega 2}\frac{1}{\omega}\frac{\partial k}{\partial x_i}\frac{\partial \omega}{\partial x_i} \tag{4}$$

where k is the turbulent kinetic energy, ω is the characteristic frequency of turbulence, and P_k and $\beta^* k\omega$ are the production and transformation terms of k, respectively.

However, in aeroacoustics problems, pressure fluctuations are typically of a very low amplitude, and can be damped by the numerical viscosity of URANS models. Hence, an LES or DNS would be more suitable because of their low numerical diffusion. A DNS would demand tremendous computational resources and is ruled out. Although the cost of an LES would be a fraction of the DNS, it would still require considerable CPU time. So, the current simulations do not use a pure LES approach. By combining LES and URANS, a DES (detached eddy simulation) approach is adopted. This function (F_{DES}) is presented in Eq. (5):

$$F_{\mathrm{DES}} = \max\left\{\tfrac{L_{k-\omega}}{C_{\mathrm{DES}}\Delta}(1 - F_s),\, 1\right\},\ F_S = 0,\, F_1;\, F_2,\ \Delta = \max\{\Delta x, \Delta y, \Delta z\} \tag{5}$$

where Δ corresponds to the element mesh dimension (spatial filter). For that reason, the length scales are weighted for modeling in SST closure model. In regions where the grid spacing is small enough to solve for the local scales, the model behaves as a two-equation LES model. On the other hand, in regions where mesh spacing is large, such as close to walls, the URANS SST model is recovered. A compromise between accuracy and cost is then achieved, in which the LES requirements for mesh resolution are relaxed, especially in boundary layer regions.

5.2.3 Numerical Modeling

The solution of the mathematical model is performed by the Finite Volume Method (FVM) technique implemented in the in-house code UNSCYFL3D. The SIMPLE segregated pressure–velocity coupling algorithm and the collocated arrangement for all variables were used.

For this work, two different schemes were evaluated for advection, namely, the SOU (second-order upwind) and the CDS (central difference scheme). The bi-conjugate gradient and the algebraic multi-grid methods are used to solve the linear systems. Figure 3 is used to demonstrate the analyzed schemes in a simple adjacent cells in FVM approach. The SOU and CDS schemes are, respectively, described in Eqs. (6) and (7) and both present a second-order precision, according to Maliska (2010) and Ferziger and Peric (2012).

$$\phi_f = \phi_L + (\text{grad}\phi)_{rL}.\overrightarrow{d}\, r_L \tag{6}$$

$$\phi_f = \frac{1}{2}(\phi_L + (\text{grad}\phi)_{rL}.\overrightarrow{d}\, r_L + \phi_R + (\text{grad}\phi)_{rR}.\overrightarrow{d}\, r_R) \tag{7}$$

where ϕ is a transported information (such as concentration, temperature, or velocity components) across the volume face between the neighbor cells (L and R). The Gauss divergence theorem is applied:

$$(\text{grad}\phi)_r = \frac{1}{\Delta V}\sum_f (\overline{\phi}_f \overrightarrow{A}_f) \tag{8}$$

where $\overline{\phi}_f$ is an arithmetical average of ϕ property between cells that share the same face f, Eq. (9); $\overrightarrow{A}_f$ is the face area vector; and $\overrightarrow{d}_r$ is the distance vector from the cell node to the face f.

$$\overline{\phi}_f = \frac{\phi_R + \phi_L}{2} \tag{9}$$

The ICEM-CFD software was used for creating the mesh with the block-structured technique. Regions near the wall and around and downstream of the throttle flap were refined to meet the requirement for solving the boundary layer ($y^+ \approx 1$). Both meshes are presented in Fig. 4 with detailed bend HVAC. The mesh count for the

Fig. 3 Schematic of neighbor volumes in discretization of the balance equations (Souza 2012)

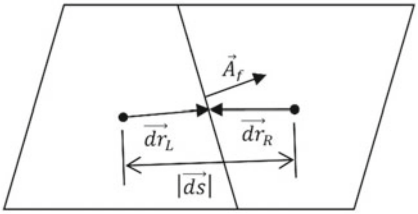

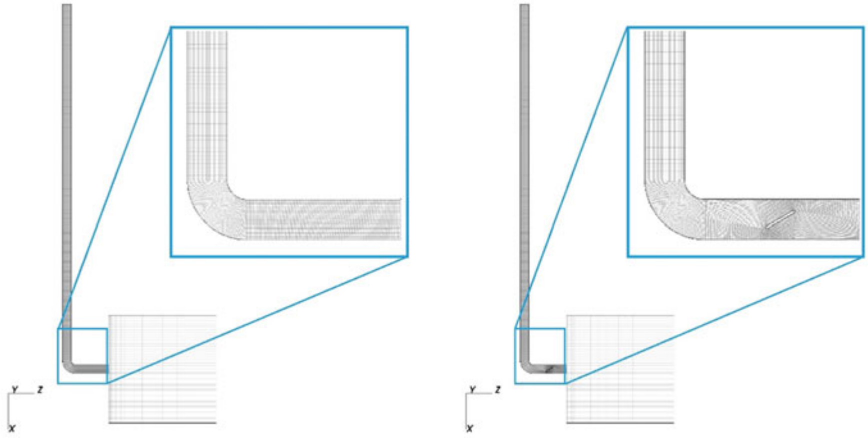

(a) (b)

Fig. 4 Geometry meshes of total domain and details: HVAC without flap (**a**) and HVAC with flap (**b**)

HVAC with flap was 2.9 million of hexahedra and, for the HVAC without flap, 2.7 million volumes.

5.2.4 Post-processing Data

The unsteady gauge pressure measurements are inherently noisy in DES simulation results. The gauge pressure was evaluated in short time intervals to ensure a high-frequency resolution and avoiding spectral leakage. To compare different unsteady signals, they must be analyzed in the frequency spectrum domain. The Fast Fourier Transform (FFT) is used to extract the amplitude by frequency from the time domain data. These data are, subsequently, transformed in the sound pressure level values (SPL) relative to an audible threshold pressure ($P_0 = 20\,\mu\text{Pa}$), according to Eq. (10), as mentioned by (Gerges 2000).

$$\text{SPL} = 20\log\frac{P}{P_0} \tag{10}$$

Smoothing is achieved by combining 164 windows of experimental data, according to Jäger et al. (2008). Therefore, a few windows were used to average SPL numerical results and they are summarized in Table 1 as well as other parameters adopted throughout this study.

Table 1 Comparison between the Jäger et al. (2008) experiment and the present work parameters

	HVAC with flap			HVAC without flap		
	Jäger et al. (2008)	CDS[a]	SOU[a]	Jäger et al. (2008)	CDS[a]	SOU[a]
Physical time (s)	20.80	2.0	2.1	20.80	1.4	1.7
Time step (s)	1.95e − 4	4.00e − 5		1.95e − 4	4.00e − 5	
Signal analysis	FFT	FFT	FFT	FFT	FFT	FFT
Averaged windows	164	5	5	164	6	6

[a] Present work

5.3 Results and Discussion

After setting the previously described cases, they were performed by UNSCYFL3D solver in a workstation totaling 1500 CPU.h in an Intel i7 processor for each case.

It was observed that a pure SST closure model in URANS approach produced unfeasible solutions. Due to the natural diffusion in URANS closure models, in preliminary tests, the results presented a non-physical response to the flow pattern and to the oscillations in a wideband frequency. The SPL diagrams for URANS solutions presented an extremely damped amplitude for wideband noise. Only low frequencies were predicted in the URANS SST case. This was somehow expected from this approach, once it embeds several assumptions from the homogeneous isotropic turbulence and all length scales are fully modeled.

To perform the DES simulation cases, the solutions were initialized from a steady flow field calculation (RANS with SST closure model). The gauge pressure results of the DES unsteady solution were acquired and cropped obeying the criterion of the statistically permanent turbulent flow. As depicted in Fig. 5, it is noticed that in the no-flap HVAC (a) the flow develops and fluctuations settle around 0.2 s, whereas in the flap-mounted HVAC (b) this occurs at around 0.9 s. This is as a result of the massive vortex shedding by the flap in the second case. This configuration presents a more chaotic flow pattern due to the obstacle.

The pressure signals in DES simulations results are inherently noisy and permeated by many frequency components, due to the turbulence of the problem. It is noticed that in the no-flap configuration, according to the gauge pressure signal at probe 1 (Fig. 5a), the values of pressure are lower than the two and six probes. This happens due to the pressure drop caused by the bend geometry. On the other hand, in the HVAC with flap (Fig. 5b), probe 1 presents higher values than the other probes, due to the flow blocking caused by the throttle flap, which induces a rising pressure upstream to the obstacle.

The flow patterns in certain regions were observed and compared to the averaged experimental Jäger et al. (2008) PIV. Figure 6 presents the comparison between experimental PIV, SOU, and CDS numerical results for a no-flap HVAC. In general, the flow behavior due to the bend follows the expected trend. However, in the numerical field, the bend inner wall presents a recirculating zone that does not totally agree with the experimental one. The recirculating zone is more restricted in the numerical

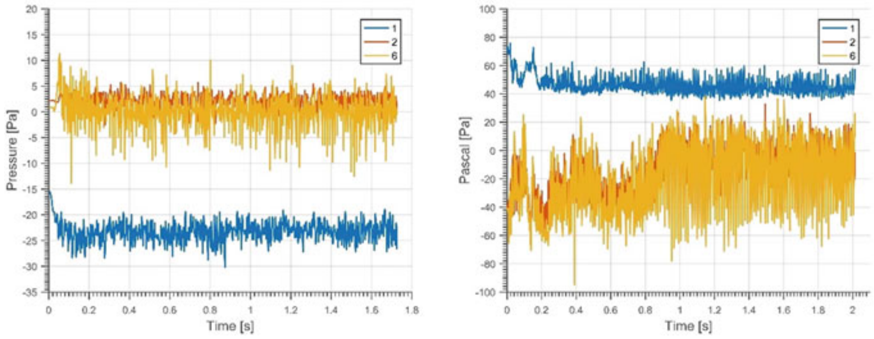

(a) (b)

Fig. 5 Pressure-gauged signals in probes 1, 2, and 6: without flap (**a**) and with flap configuration (**b**)

fields than in the experimental ones, very likely due to the uniformity on the sizes of the mesh cells in this region. The switching filter between the DES model and the URANS model forces the modeling of several scales and may damp the pressure gradients due to the coarse mesh in this region and limitations of SST for high frequencies.

In the flap-mounted HVAC cases, the velocity U component displays a good agreement with the experimental data, as can be seen from Fig. 7a. However, in W component (Fig. 7b), the wake downstream to the throttle flap is characterized with more fidelity in the CDS case. The time-averaged wake of the flap presents an oscillatory shape according to experimental and CDS numerical results. The recirculating region after the 90° bend is not well characterized, as in the HVAC without flap cases, and this probably occurs due to the spatial filtering caused by a uniform and coarse volume discretization. It should also be emphasized that the DES model has

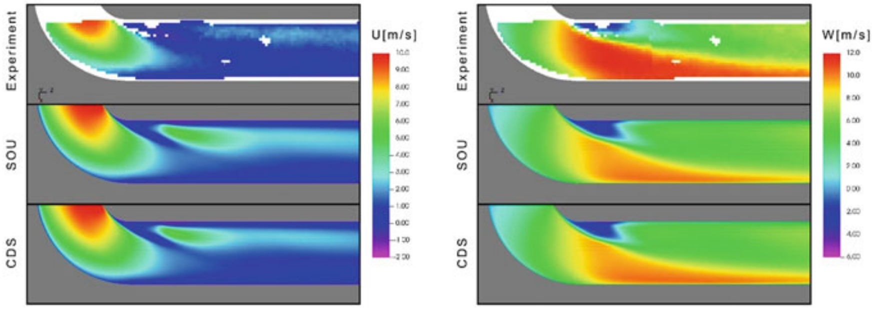

(a) (b)

Fig. 6 Comparison between experimental data (Jäger et al. 2008) and numerical simulations for configuration without flap in $y = 0$ section. Time-averaged U component (**a**) and time-averaged W component (**b**)

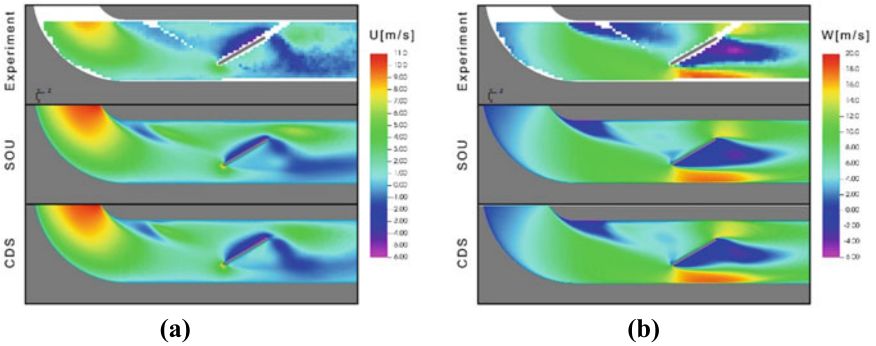

(a) **(b)**

Fig. 7 Comparison between experimental data (Jäger et al. 2008) and numerical simulations for configuration with flap in $y = 0$ section. Time-averaged U component (**a**) and time-averaged W component (**b**)

its own limitations, mainly in massive detached flow regions. Further investigation is ongoing to understand this underprediction.

After the statistical treatment of the instantaneous pressure signals in probes 1, 2, and 6, the FFT (fast Fourier transform) was used to obtain the amplitude and frequency of pressure oscillations. The pressure amplitude was used to compute the SPL (in dB) by frequency (in Hz), according to Eq. (10). The numerical gauge pressure data were divided into a few samples and averaged to smooth spurious noise, following the procedure carried out by experimental setting (Table 1). The sound pressure level diagrams for the HVAC without flap are presented in Fig. 8. It is observed that the CDS cases predict the wideband noise (200–1000 Hz) with more accuracy than in the SOU schemes. In probe 1, the prediction of the low-frequency noise is more accurate with the CDS scheme. The differences between the CDS and the experiment are less than 7 dB for a lower frequency range (probes 1 and 2). In the experiments, probe 6 presents a small range (30–70 dB) of high-amplitude frequency, which is not characterized as a tonal noise. This local increase in the experimental SPL is noticed in probe 2, however more attenuated than in the probe 6.

Differently, in the flap-mounted configuration (Fig. 9), the numerical SPL results predicted with good agreement the tonal noise present in frequencies around 80 Hz in probes 2 and 6. This tonal noise is produced by the intensive vortex emission due to the throttle flap. In probe 2, another peak was observed between 100 and 200 Hz. This peak is probably related to the small number of averaged samples in post-processing data, however it reveals a smoothed peak in the experimental data for the same range. In probe 1, the wideband noise was over-predicted if compared with experimental data. The low-frequency noise presented a more correct fitting with CDS scheme for the probes 1 and 2. The SOU results presented underprediction for probes 2 and 6 in wideband noise, due to its numerical diffusion.

In general, all results with the CDS discretization scheme presented a more correct prediction for the SPL in the flap-mounted HVAC. It suggests that the predominant sound generation mechanism for this case, i.e., flow around an obstacle, was more

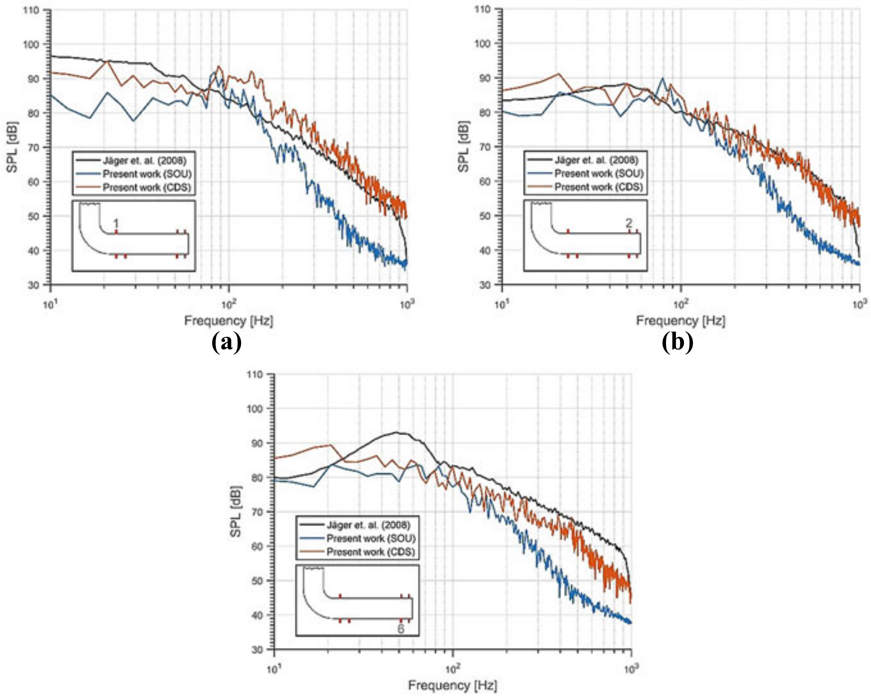

(a) (b)

(c)

Fig. 8 SPL at probe positions for the HVAC without flap. Comparison between experimental data (Jäger et al. 2008) and numerical simulations

accurately represented, as observed downstream of the flap probes, 2 and 6 (Fig. 9). The difficulty to obtain more accurate results for the probe 1 in the HVAC with flap and the low-frequency range for the probe 6 in the HVAC without flap (Fig. 8) is probably related to the poor characterization of the pressure-driven separation mechanism. Probe 6 suffers the influences due to the instabilities that originate in the bend, in the no-flap HVAC duct.

5.4 Conclusions

This study has been performed to investigate the flow-induced noise phenomenon in a simplified HVAC system. Although second-order schemes in numerical fluid flow solutions are the workhorse in science and engineering, it is not trivial to use them to characterize fluid dynamics noise production. This work presents approaches that should be used in preliminary geometries analysis.

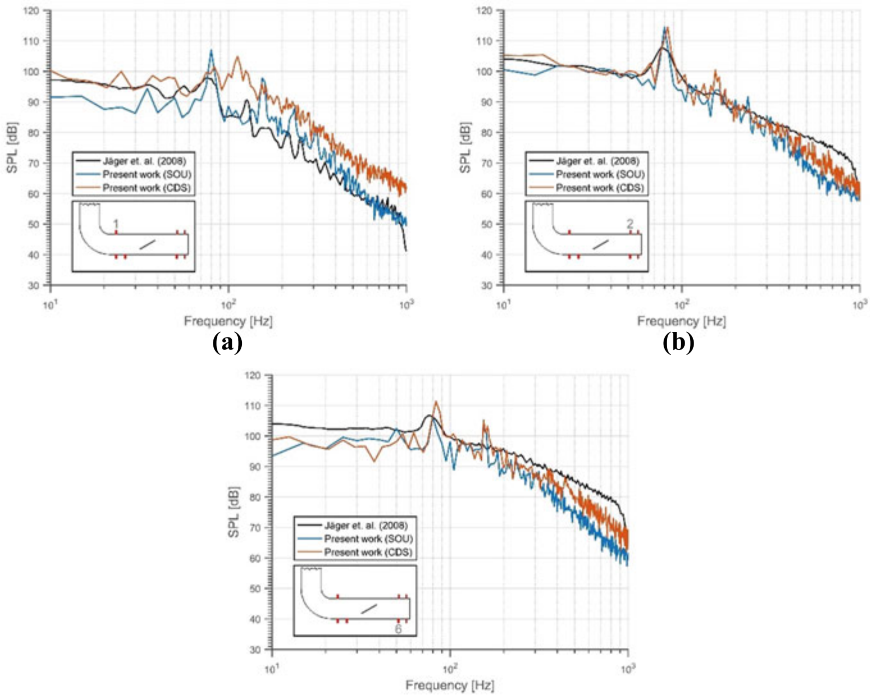

(a)

(b)

(c)

Fig. 9 SPL at probe positions for the HVAC with flap. Comparison between experimental data (Jäger et al. 2008) and numerical simulations

The good accuracy of Detached Eddy Simulation (DES) has to predict the unsteady fluid dynamics and noise production is demonstrated, with lower computational costs if compared to the LES approach. However, the discretization schemes of the advection term affect directly the SPL results. Once that the pressure variable propagates elliptically on the incompressible subsonic flow, the numerical diffusion of the SOU scheme disturbs directly the pressure oscillations in high frequency, as expected in wideband noise, causing a damping in the SPL amplitude in high frequencies. On the other hand, the CDS scheme is able to preserve the pressure information along the fluid flow.

Another important observation is the domain discretization criterion. The main noise sources in this HVAC system are related to flow around obstacles and a pressure-driven flow separation, and in these specific regions, the flow presents expressive velocity, pressure, and vorticity gradients. Based on it, the mesh around these regions must be carefully refined with particular attention to orthogonality and quality. Further analysis must account for this in future works on the flow-induced noise.

Acknowledgements The authors of this paper regard all those who contributed directly or indirectly to the results presented here. Special acknowledgment to Federal University of Uberlândia, CNPq, Petrobras S.A. and MFLab's professionals (professors, students, and technicians).

References

Allen R, Mendonca F, Kirkham D (2005) RANS and DES turbulence model predictions of noise on the M219 cavity at M=0.85. Int J Aeroacoust 4:135–151

Ferziger J, Peric M (2012) Computational methods for fluid dynamics. Springer Berlin Heidelberg. ISBN 9783642560262. https://books.google.com.br/books?id=BZnvCAAAQBAJ

Gerges SNY (2000) Ruído: fundamentos e controle, 2nd edn. NR Editora, Florianópolis

Henshaw MJdC (2000) M219 cavity case in verification and validation data for computational unsteady aerodynamics. RTO-TR-26, AC/323(AVT)TP/19, pp 473–480

Howe MS (2003) Theory of vortex sound. University Cambridge Press, United Kingdom

Islam M, Decker F, Hartmann M, Jäger A, Lemke T, Ocker J, Schwarz V, Ullrich F, Shröder A, Heider A (2008) Investigations of sunroof bufieting in an idealised generic vehicle model—part I: experimental results. In: AIAA/CEAS aeroacoustics conference (29th AIAA aeroacoustics conference), vol 14, pp 1–21

Jäger A, Decker F, Hartmann M, Islam M, Lemke T, Ocker J, Schmarz V, Ullrich F, Crouse B, Balasubramanian G, Mendonca F, Drobietz R (2008) Numerical and experimental investigations of the noise generated by a flap in a simplified HVAC duct. In: AIAA/CEAS aeroacoustics conference (29th AIAA aeroacoustics conference), vol 14, p 17

Lighthill MJ (1952) On sound generated aerodynamically—part 1: general theory. Proc R Soc Lond 564–587

Lighthill MJ (1956) Viscosity effects in sound waves of finite amplitude. In: Batchelor GK, Davies RM (eds) Surveys in mechanics. Cambridge University Press

Maliska CR (2010) Transferência de Calor e Mecânica dos Fluidos Computacional, 2nd edn. LTC Editora, Rio de Janeiro

Menter FR (1994) Two-equation eddy-viscosity turbulence models for engineering applications. AIAA J 32:1598–1605

Silveira Neto A (2020) Escoamentos Turbulentos: Análise Física e Modelagem Teórica, 1st edn. Universidade Federal de Uberlândia

Souza FJ (2012) UNSCYFL3D Versão 2.0—Manual Teórico. Federal University of Uberlândia, MFLab - Fluid Mechanics Laboratory

Chapter 6
Simex Implementation on a DNS Code

Giovanni Belloni Fernandes Braga, Marcello Augusto Faraco de Medeiros, and Sávio Brochini Rodrigues

Abstract This study is dedicated to the implementation, verification, and measurement of execution speed, using the method of manufactured solutions, of a new temporal integration method of the implicit–explicit kind, the Stepwise-IMEX or SIMEX, in the Aeroacoustics, Transition and Turbulence Group's (GATT) Direct Numerical Simulation (DNS) code. In simulations where Ma ≈ 0.1, or less, SIMEX should be able to reduce the explicit fourth-order Runge–Kutta's (ERK) execution time, which is currently used. A pilot program was created, in Python, with the Burgers' 1D equation, using fourth-order compact finite differences, to test from second- to fifth-order SIMEX methods and the mentioned explicit method. Indeed, in these preliminary tests, SIMEX proved to be faster than ERK only with linear Burgers' equation and only after a certain stiffness level. However, there are indications that some characteristics of the DNS, such as the y-axis' greater refinement, not found in the pilot are favorable to SIMEX. Both the decomposition of the ODE and the iterative method for implicit systems and the chosen tableaus pair have a huge impact on the SIMEX efficiency and will be targeted in next stage of DNS code implementation.

Keywords IMEX · SIMEX · Runge–Kutta · Temporal integration

G. B. F. Braga · M. A. F. de Medeiros (✉)
University of São Paulo-USP, São Paulo, Brazil
e-mail: marcello@sc.usp.br

G. B. F. Braga
e-mail: gbelloni@usp.br

S. B. Rodrigues
Federal University of São Carlos-UFSCar, São Carlos, Brazil
e-mail: savio.rodrigues@ufscar.br

H. F. Meier et al. (eds.), *Advances in Turbulence*, ABCM Series on Mechanical Sciences and Engineering, https://doi.org/10.1007/978-3-031-25990-6_6

6.1 Introduction

The current group's (Turbulence, Transition and Aeroacoustic Group—GATT) Direct Numerical Simulation (DNS) code is a reorganization of the previous versions (Mathias 2017). Details about its use and validation can be found (Silva et al. 2010; Bergamo 2014; Bergamo et al. 2015; Martinez and Medeiros 2016; Martinez 2016; Mathias 2017). In this code, the acoustic phenomena are always resolved which allows aeroacoustic analysis for every subsonic Mach number. At low Mach numbers, say $0 < Ma \approx 0.1$, the velocity fields are much slower then the acoustic waves, which in pratice makes the system stiff, thus imposing time-step restrictions for the simulations with explicit integration methods.

Fully implicit methods build up complexity and CPU cost proportionally to the integrated equation's complexity. So it is quite clear that Navier–Stokes equations are not very well suited for these kind of methods at first glance. But, because different terms contribute distinctly to the stiffness, implicit–explicit methods can offer some advantage. This class of methods decomposes the equation into two parts, the part with the stiff terms is integrated implicitly and the remaining part is integrated explicitly. Bigger stable time steps may reduce execution time as consequence of this approach. The trade-off to be managed is the necessity of keeping the implicit equation simple to solve against the possibility of using bigger time steps.

The use of implicit and explicit methods in an ODE system dates back to the 1970s. Early studies are Hofer (1976), Crouzeix (1980), and Cooper and Sayfy (1980). A comprehensive review can be found in Kennedy (2001) and Kennedy and Carpenter (2003). IMEX methods have been studied with a variety of time-stepping schemes. Here we use singly diagonally implicit Runge–Kutta with explicit first stage (ESDIRK) schemes (Ascher et al. 1997; Ghosh and Constantinescu 2016; Kennedy 2018; Wang et al. 2015). A comprehensive review of ESDIRK schemes can be found in Kennedy (2016).

Recently, IMEX methods have been used in compressible fluids simulations such as in atmospheric studies, where the stiffness is associated with terms that generate acoustic waves (Bispen et al. 2017; Colavolpe et al. 2017; Durran and Blossey 2012; Gardner et al. 2018; Ghosh and Constantinescu 2016; Restelli and Giraldo 2009; Vogl et al. 2019; Weller et al. 2013; Zhang et al. 2016a, b), which imposes strong time-step restrictions and are not relevant for climate phenomena, for example.

Within this scenario, SIMEX is a modification of the IMEX method. The advantage in this new class of methods is the absence of the need to iterate the implicit equation until a really low residue level. The residue that remains from the implicit equation is integrated along with the explicit part of the decomposition, thus keeping the method's precision. Due to the possibility of using less iterations, SIMEX has the potential to obtain precise solutions, as in IMEX, but faster (Rodrigues 2017).

In this work, SIMEX method is applied to Burgers' 1D equation as a preliminary test and the results are compared with the ones obtained from the classical fourth-order explicit Runge–Kutta. The spatial discretization is done by a compact finite difference method (Lele 1992), as in the GATT's DNS. Solution's quality and method's formal order of convergence are verified by means of a manufactured solution. All the implementation and data analysis was done in Python. In the next step of this project, SIMEX will be implemented in the GATT's DNS code which is written in FORTRAN 90.

6.2 Methodology

6.2.1 1D Burgers' Equation

Burgers' equation is an advection–diffusion PDE which is often used as a simplification for the Navier–Stokes equation, and it is expressed as follows:

$$\frac{\partial u}{\partial t} + f(u)\frac{\partial u}{\partial x} = \gamma \frac{\partial^2 u}{\partial x^2} + \Psi(x, t), \tag{1}$$

where γ is a positive real constant; Ψ is a source term; and $f(u)$ defines the advection speed, which here assumes two different profiles in order to get a linear or a nonlinear equation. The former one is obtained with $f(u) = u$ and the last one with a constant profile $f(u) = c$.

6.2.2 Manufactured Solutions

In the present work, the method of manufactured solutions is used for code verification. It consists of formulating an analytical solution by adding a source term to the original equation so that the numerical solution can be compared with the analytical one. For the one-dimensional PDE problem, the chosen analytical function is given by

$$U_{man}(x, t) = e^{\sin(\alpha x - at)}. \tag{2}$$

where α and a represent the wave number and angular frequency, respectively. This solution is chosen so that U_{man} is always positive, has infinite derivatives, and oscillates in space and time.

The source term Ψ is easily calculated by

$$\Psi(x, t) = U_t + f(U)U_x - \gamma U_{xx}, \tag{3}$$

where the subscript stands for the derivative with respect to that variable and the man subscript was suppressed to simplify notation.

6.2.3 Compact Finite Differences

Spatial derivatives are calculated with a spectral-like compact finite differences method described by Lele (1992), where centered stencil is defined as follows:

$$\begin{aligned}\beta\left(u'_{i+2}+u'_{i-2}\right)+\alpha\left(u'_{i+1}+u'_{i-1}\right)+u'_i &= a\frac{u_{i+1}-u_{i-1}}{2h}\\ +b\frac{u_{i+2}-u_{i-2}}{4h}+c\frac{u_{i+3}-u_{i-3}}{6h},\end{aligned} \tag{4}$$

where h is the mesh spacing. The correspondent modified wavenumber w' is

$$\omega'(\omega)=\frac{a\sin(\omega)+(b/2)\sin(2\omega)+(c/3)\sin(3\omega)}{1+2\alpha\cos(\omega)+2\beta\cos(2\omega)}. \tag{5}$$

Close to the boundaries, the stencil is shifted and coefficients are adjusted accordingly, as an example, the first derivative at the boundary can be calculated from the following relation:

$$u'_1+\alpha u'_2=\frac{1}{h}(au_1+bu_2+cu_3+du_4). \tag{6}$$

This system may be represented as

$$Au'=Bu, \tag{7}$$

where A and B are $N \times N$ square matrices with N being the number of grid points. The entries of B are proportional to h^{-1}.

Its worth mentioning that matrices A and B are narrowband diagonal matrices. By choosing $\beta = c = 0$ in Eq. 4 it is possible to obtain up to a sixth-order tridiagonal scheme whose coefficients are determined by matching Taylor series. This work uses a fourth-order tridiagonal scheme with $w = 1.8$. When necessary, we will formally write

$$u'=A^{-1}Bu, \tag{8}$$

although Eq. 7 is used for computational purposes.

6.2.4 ESDIRK-IMEX

IMEX is a class of methods that combines an explicit with an implicit integrator and to do so it decomposes the right-hand side of the ODE as the sum of two functions:

$$\frac{d\mathbf{u}}{dt} = \mathbf{f}(t, \mathbf{y}) + \mathbf{g}(t, \mathbf{y}), \tag{9}$$

where f is the explicit part of the decomposition and g is the implicit part. This allows stiff terms to be handled implicitly while non-stiff terms are placed in the explicit part. For IMEX methods, it is imperative to solve the implicit equation up to a given precision level in order to avoid introducing errors. This task is done by an iterative method that will iterate until the precision requirement is fulfilled or the maximum iteration number is reached, here we call this a Solver.

Explicit-first-stage singly diagonally implicit Runge–Kutta (ESDIRK) is a particular case of the DIRK class of implicit methods, for which an extensive review can be found in (Kennedy 2016). The ESDIRK-IMEX implicit equation for the ith stage has the following form:

$$\tilde{\mathbf{y}}_i - h\gamma\mathbf{g}(t_n + c_i h, \tilde{\mathbf{y}}_i) = \mathbf{y}_n + h\sum_{j=1}^{i-1}\Big(a_{i,j}\mathbf{k}_j + \tilde{a}_{i,j}\tilde{\mathbf{k}}_j\Big), i = 2, \ldots, \nu, \tag{10}$$

where $\mathbf{y}_n$ is the current approximation for $\mathbf{y}(t_n)$, h is the step-size, and γ is the *tableau* diagonal's value. $\overset{\sim}{\mathbf{y}}_i$ is the current stage approximation, which is obtained by a Solver $\mathbb{S}$ within some predefined residue tolerance. Finally, the next step approximation $\mathbf{y}_{n+1}$ is computed as follows:

$$\mathbf{y}_{n+1} = \mathbf{y}_n + h\sum_{j=1}^{\nu} b_j(\mathbf{k}_j + \overset{\sim}{\mathbf{k}}_j). \tag{11}$$

6.2.5 IMEX Decompositions

Having in mind that the advective term is the stiffness source to this problem, it should now be clear that this is the one to be placed in the implicit part of the decomposition. To avoid solving a non-linear system of equations, a linarization of the advective term can be made. Here four decompositions are presented, three for the non-linear Burgers' equation and one for the linear case (Table 1).

Here the independent variables are the space x and temporal t dimensions and $u \equiv u(x, t)$ is the dependent variable. In this work, g and f are functions of u, its first and second derivatives and also x and t.

Table 1 IMEX decompositions for the linear and non-linear Burgers' equation

	$g(u', u, x, t)$	$f(u'', u', u, x, t)$
Decomposition 1	$-u\frac{\partial u}{\partial x}$	$\gamma\frac{\partial^2 u}{\partial x^2} + \Psi(x, t)$
Decomposition 2	$-c\frac{\partial u}{\partial x}$	$-(u-c)\frac{\partial u}{\partial x} + \gamma\frac{\partial^2 u}{\partial x^2} + \Psi(x, t)$
Decomposition 3	$-u_0\frac{\partial u}{\partial x}$	$-(u-u_0)\frac{\partial u}{\partial x} + \gamma\frac{\partial^2 u}{\partial x^2} + \Psi(x, t)$
Decomposition 4	$-c\frac{\partial u}{\partial x}$	$\gamma\frac{\partial^2 u}{\partial x^2} + \Psi(x, t)$

6.2.6 ESDIRK-Stepwise-IMEX

SIMEX (Rodrigues 2017) is a new implicit–explicit integration method that can be seen as an improved IMEX, where a within-step decomposition adjustment is proposed with the intent of removing the need of getting precise solutions for the implicit equations. This new decomposition is named Residual Balanced Decomposition (RBD) and it is directly related to the traditional IMEX decomposition, Eq. 12. The job once done by a Solver is now done by a *implicit step filter*, or *Filter* for short, which is defined as a predefined successive iterations of one or more iterative methods. For example, one can define a Filter as two Newton iterations. Thus, solvers and filters are distinguished because neither precision nor convergence are required from a filter.

$$\frac{d\mathbf{y}}{dt} = \mathbf{f}(t, \mathbf{y}) + \mathbf{g}(t, \mathbf{y}) = \mathbf{f}^{rbd}(t, \mathbf{y}) + \mathbf{g}^{rbd}(t, \mathbf{y}). \tag{12}$$

The implicit equation that has to be solved at each SIMEX implicit step is exactly the same as the one for IMEX, Eq. 10. After that, the remaining residue has to be managed properly and that's what motivates the following definition for the RBD decomposition:

$$\mathbf{g}^{rbd}(t, \mathbf{y}) = \frac{\mathbf{y} - \mathbf{y}_n - \mathcal{F}^{-1}(\mathbf{y} - \mathbf{y}_n, t)}{h\gamma}, \tag{13}$$

where $\mathcal{F}^{-1}$ is the inverse filter $\mathcal{F}$ and

$$\mathbf{f}^{rbd}(t, \mathbf{y}) = \mathbf{f}(t, \mathbf{y}) + \mathbf{g}(t, \mathbf{y}) - \mathbf{g}^{rbd}(t, \mathbf{y}). \tag{14}$$

Now the question that arises is how to calculate the inverse filter, but even when possible it is certainly not a quick job. Altough its existence being important for the theoretical justification of the method, fortunately, there's a practical way to evaluate $\mathbf{g}^{rbd}$ and $\mathbf{f}^{rbd}$ without the need of computing $\mathcal{F}^{-1}$. So, let the value returned by the filter, Eq. 15, be the exact answer for the implicit equation, Eq. 10, when the function $\mathbf{g}$ is replaced by $\mathbf{g}^{rbd}$, Eq. 16. Mathematically,

$$\widetilde{\mathbf{y}}_{i,rbd} = \mathcal{F}(\mathbf{rhs}, t) \tag{15}$$

such that

$$\widetilde{\mathbf{y}}_{i,rbd} - h\gamma \mathbf{g}^{rbd}(t_n + c_i h, \widetilde{\mathbf{y}}_{i,rbd}) = \mathbf{rhs}, \tag{16}$$

where $\mathbf{rhs} = \mathbf{y}_n + h\sum_{j=1}^{i-1}(a_{i,j}\mathbf{k}_j + \tilde{a}_{i,j}\widetilde{\mathbf{k}}_j)$. Hence, solving for $\mathbf{g}^{rbd}$,

$$\mathbf{g}^{rbd}(t_n + c_i h, \widetilde{\mathbf{y}}_{i,rbd}) = \frac{\widetilde{\mathbf{y}}_{i,rbd} - \mathbf{rhs}}{h\gamma}. \tag{17}$$

And now $\mathbf{f}^{rbd}$ is completely determined by Eq. 14. After the calculations for the RBD decomposition, the only thing missing is the variable update which is done exactly in the same way as in IMEX, Eq. 11.

The ESDIRK–SIMEX algorithm for a single step of size h starting from $t = t_n$ with step approximation $\mathbf{y}_n$ is presented below:

Algorithm 1 ESDIRK-SIMEX algorithm

```
$k_1 = g(t_n, y_n)$
$\tilde{k}_1 = f(t_n, y_n)$
for $i = 2;\quad i <= \nu;\quad i++$ do
    rhs $= y_n + h\sum_{j=1}^{i-1}(a_{i,j}k_j + \tilde{a}_{i,j}\tilde{k}_j)$
    $\tilde{y}_{i,rbd} = \mathcal{F}$
    $k_i = (\tilde{y}_{i,rbd} - \mathrm{rhs})/h\gamma$
    $\tilde{k}_i = f(t_n + c_i h, \tilde{y}_{i,rbd}) + g(t_n + c_i h, \tilde{y}_{i,rbd}) - k_i$
end for
$y_{n+1} = y_n + h\sum_{j=1}^{\nu} b_j(k_j + \tilde{k}_j)$
```

An important but not so obvious observation that has to be made is about how to interpret this stepwise adjustment of the decomposition. Taking the filter's answer, Eq. 15, and putting it inside Eq. 10, it yields the following result:

$$\mathbf{g}(t_n + c_i h, \widetilde{\mathbf{y}}_{i,rbd}) = \frac{\widetilde{\mathbf{y}}_{i,rbd} - \mathbf{rhs} + \mathbf{res}}{h\gamma}, \tag{18}$$

where **res** is the implicit equation residue. So,

$$\mathbf{g} - \mathbf{g}^{rbd} = \frac{\widetilde{\mathbf{y}}_{i,rbd} - \mathbf{rhs} + \mathbf{res}}{h\gamma} - \frac{\widetilde{\mathbf{y}}_{i,rbd} - \mathbf{rhs}}{h\gamma} = \mathbf{res}/h\gamma. \tag{19}$$

And hence,

Table 2 Matrix-free Newton's step

	$\mathcal{A}$	$\mathcal{B}$
Decomposition 1	$A[1/(\theta\mathbf{u})][1+\theta\mathbf{u}_x]+B$	$A[1/(\theta\mathbf{u})](-F(\mathbf{u}))$
Decompositions 2 and 4	$A+\theta cB$	$-AF(\mathbf{u})$
Decomposition 3	$A[1/(\theta\mathbf{u}_0)]+B$	$-A[1/(\theta\mathbf{u}_0)]F(\mathbf{u})$

$$\mathbf{f}^{rbd}=\mathbf{f}+\mathbf{res}/h\gamma. \tag{20}$$

Therefore, it is possible to say that the implicit equation residue is integrated along with the explicit part.

6.2.7 Iterative Methods for Implicit Equations

Iterative methods for implicit equations play a big role in fully, or partially, implicit integration methods by affecting directly its computational efficiency. Thus, equating robustness and memory and processing costs is fundamental. In this work, we use Newton's step iteratios and to avoid the cost to compute and store the Jacobian matrix it is written in a way that there's no need of constructing the Jacobian matrix explicitly. This approach has the disadvantage of being customized for each case listed in Sect. 2.5. The spatial dimension is represented as a n point uniform grid, so the variable u is written as a vector $\mathbf{u}=(u_1,\ldots,u_n)$. We introduce the notation $[u]$ to represent a diagonal matrix with $\mathbf{u}$ as the diagonal entries. The first derivative will be written as in Eq. 8.

Starting from the IMEX implicit equation, Eq. 10, written for $\mathbf{u}$, the problem is rewritten in the shape below:

$$\mathbf{F}(\mathbf{u})=\mathbf{u}-\theta\mathbf{g}(\mathbf{u})-\mathbf{rhs}, \tag{21}$$

where $\theta=h\gamma$ and $\mathbf{rhs}=h\sum_{j=1}^{i-1}(a_{i,j}\mathbf{k}_j+\tilde{a}_{i,j}\tilde{\mathbf{k}}_j)$. Newton's step is obtained by the first-order approximation of $F(\mathbf{u}+\mathbf{d})$, where $\mathbf{d}$ is small compared to $\mathbf{u}$. Eventually, one would end up with a linear system for the Newton's step $\mathbf{d}$ that can be solved with very efficient methods as Thomas algorithm since $\mathcal{A}$ is band matrix (Table 2).

6.2.8 Butcher's Tableau for the Used Runge–Kutta

In this work, some tests are performed with explicit and implicit–explicit Runge–Kutta methods. The pure explicit one is the classical fourth-order four-stage ERK, also called as "RK4", which is used as reference of precision and execution time, the *tableau* is given in Eq. 22. Five ESDIRK–SIMEX pairs are used and they are listed below:

$$\begin{array}{ccccc} 0 & & & & \\ \frac{1}{2} & \frac{1}{2} & & & \\ \frac{1}{2} & 0 & \frac{1}{2} & & \\ 1 & 0 & 0 & 1 & \\ & \frac{1}{6} & \frac{2}{6} & \frac{2}{6} & \frac{1}{6} \end{array} \tag{22}$$

The pair "HCN" is a combination of Heun and Crank–Nicolson methods, which has two stages and a formal second-order convergence rate. Also with second order, but three stages, there is the pair "ARS222" proposed by (Ascher et al. 1997), using the choice of parameters $\gamma = 1 - \sqrt{2}/2$ and $\delta = 1 - 1/2\gamma$. The last three, which are proposed by Kennedy (2001) under the names "ARK3(2)4L[2]SA-(ERK and ESDIRK)", "ARK4(3)6L[2]SA-(ERK and ESDIRK)", and "ARK5(4)8L[2]SA-(ERK and ESDIRK)", pairs are, respectively, "ARK423", third-order three stages; "ARK634", fourth-order six stages; and "ARK845", fifth-order eight stages.

6.3 Preliminary Results

6.3.1 Maximum Stable CFL

Some tables are presented in this section, each of them containing the maximum stable CFL number, CFL per stage, and mean and maximum errors for each of the integration methods. Here the maximum CFL is defined as the highest CFL number that is possible to run the simulation without some kind of floating point error or with a resulting mean error below 10^{-2}. The uncertainty of these CFL numbers is smaller than 0.1. The results are grouped in each table by the IMEX decomposition. The simulation parameters are $n = 100$; $t = 6.5$ and $\alpha = \pi$. The last one is the manufactured solution wavenumber, the time is chosen to be long enough so the wave can travel at least one period across the spatial domain and the discretization is chosen in a way that it's not so refined but still far from coarse. There's a constant c that, when applicable, assumes the values 1.0, 0.5, and 6.0, in Tables 4, 5, and 7. Lastly, a variable time-steping is used in order to keep a constant CFL for the simulation.

These tests, Tables 3, 4, 5, 6 and 7, aim identifying which is the highest stable CFL number for each combination of method and decomposition. The error results are not suitable for a direct comparison, because even between methods with the same convergence order, the truncation errors are different.

The obtained result for the RK4 was pretty consistent, showing a maximum CFL number of 1.4 and 1.3 for the non-linear and linear case, respectively. All other tests were also consistent except for decomposition 2, where there was an increase

Table 3 Classical fourth-order ERK and SIMEX with different tableaus. $tmax = 6.5$; $n = 100$; $\alpha = \pi$. Decomposition 1

Method	Maximum CFL	CFL per stage	Mean error	Maximum error
RK4	1.4	0.35	2.12597336391e−08	5.53578647366e−08
ARS222	1.4	0.47	2.12597336391e−08	5.31696036359e−05
ARKHCN	0.8	0.40	5.31696036359e−05	5.33712707123e−05
ARK423	1.2	0.30	1.35042794817e−06	3.2319289156e−06
ARK634	1.8	0.30	3.87861306506e−08	1.10751743665e−07
ARK845	2.2	0.27	2.20427199615e−08	5.64687081539e−08

Table 4 Classical fourth-order ERK and SIMEX with different tableaus. $tmax = 6.5$; $n = 100$; $\alpha = \pi$; $c = 0.5$. Decomposition 2

Method	Maximum CFL	CFL per stage	Mean error	Maximum error
RK4	1.4	0.35	2.12597336391e−08	5.53578647366e−08
ARS222	0.5	0.17	6.92703387128e−07	1.63334577019e−06
ARKHCN	0.5	0.25	7.44611892022e−07	1.71130735405e−06
ARK423	1.9	0.47	9.53206692589e−08	1.75987866058e−07
ARK634	1.7	0.28	2.86721002751e−08	6.62538695018e−08
ARK845	1.4	0.17	2.38761007099e−08	5.51128892523e−08

Table 5 Classical fourth-order ERK and SIMEX with different tableaus. $tmax = 6.5$; $n = 100$; $\alpha = \pi$; $c = 1.0$. Decomposition 2

Method	Maximum CFL	CFL per stage	Mean error	Maximum error
RK4	1.4	0.35	2.12597336391e−08	5.53578647366e−08
ARS222	0.6	0.2	2.16166959997e−06	5.23954220011e−06
ARKHCN	0.7	0.25	3.8248342577e−06	8.73097576637e−06
ARK423	1.5	0.37	2.92057404881e−07	1.42896969668e−06
ARK634	1.65	0.27	1.58342790316e−06	1.37241348535e−05
ARK845	1.75	0.22	2.38639030237e−08	5.27925102523e−08

Table 6 Classical fourth-order ERK and SIMEX with different tableaus. $tmax = 6.5$; $n = 100$; $\alpha = \pi$. Decomposition 3

Method	Maximum CFL	CFL per stage	Mean error	Maximum error
RK4	1.4	0.35	2.12597336391e−08	5.53578647366e−08
ARS222	1.5	0.5	2.25566960148e−05	6.23677746594e−05
ARKHCN	0.9	0.45	2.45096164958e−05	6.6238264234e−05
ARK423	1.2	0.30	9.51473536619e−07	2.13228285784e−06
ARK634	1.8	0.30	3.21259124247e−08	8.22027608205e−08
ARK845	2.2	0.27	2.07414324993e−08	5.24803230872e−08

Table 7 Classical fourth-order ERK and SIMEX with different tableaus. $tmax = 6.5$; $n = 100$; $\alpha = \pi$; $c = 6.0$. Decomposition 4

Method	Maximum CFL	CFL per stage	Mean error	Maximum error
RK4	1.3	0.32	6.68213096799e−08	8.38123477287e−08
ARS222	1.6	0.53	1.11847720401e−05	2.87018115995e−05
ARKHCN	0.8	0.40	1.04666337489e−05	2.37316281639e−05
ARK423	1.2	0.30	6.9711260396e−07	1.16764736607e−05
ARK634	1.8	0.30	1.59663717008e−07	8.44560643687e−06
ARK845	2.3	0.29	4.36773949997e−07	3.15404632989e−05

of the maximum CFL number for ARK423 and a decrease for every other SIMEX *tableau*. It's not clear why this variations occurred, but the results were replicable even changing some parameters.

The highest CFL result was obtained for the ARK845, 2.3 in Table 7, as expected, due to its higher order. The smaller value for each test is always obtained for the one with the lowest order and less stages, which was also expected. Disconsidering the outlier results for decomposition 2, Tables 4 and 5, ARKHCN is always isolated with the worst CFL result. The pair ARS222 with only one more stage than ARKHCN was able to achieve up to 70%, even 100%, higher CFL numbers. Despite these differences in performance, both *tableau* pairs are strong candidates to beat the RK4's CPU time, due to its high maximum CFL numbers if taken in account the low number of stages. In the other hand, the pair ARK423 had a curious increase in stability at the decomposition 2 tests, what makes it a good candidate in this case.

6.3.2 CPU Time

In this section the CPU time for the simulations is measured, with the help of a Python's built-in function, and then plotted against the mean error, both in logarithmic scale. For the first four figures, the simulation parameters are the same as in the previous section and then the instance with best result is tested more deeply. Each method runs at their maximum CFL and at two close by values. No parallelization technique was employed.

In a broad sense, it can be observed that in three out of five instances, Figs. 1, 4, and 5, the second-order *tableau* pairs presented the lowest execution time among the SIMEX. Furthermore, the ARS222 consistently beats the ARKHCN. This shows that the cost of having one more stage is advantageous for ARS222. However, none of them was effectively faster than the RK4.

In the decomposition 2 cases, Figs. 2 and 3, the ARK423 was the quickest among the SIMEX, which confirms the expectation, but still a bit slower than the RK4. Another interesting thing that calls attention is that this third-order SIMEX gives a solution almost as precise as the one given by the RK4. Lastly, one must call the

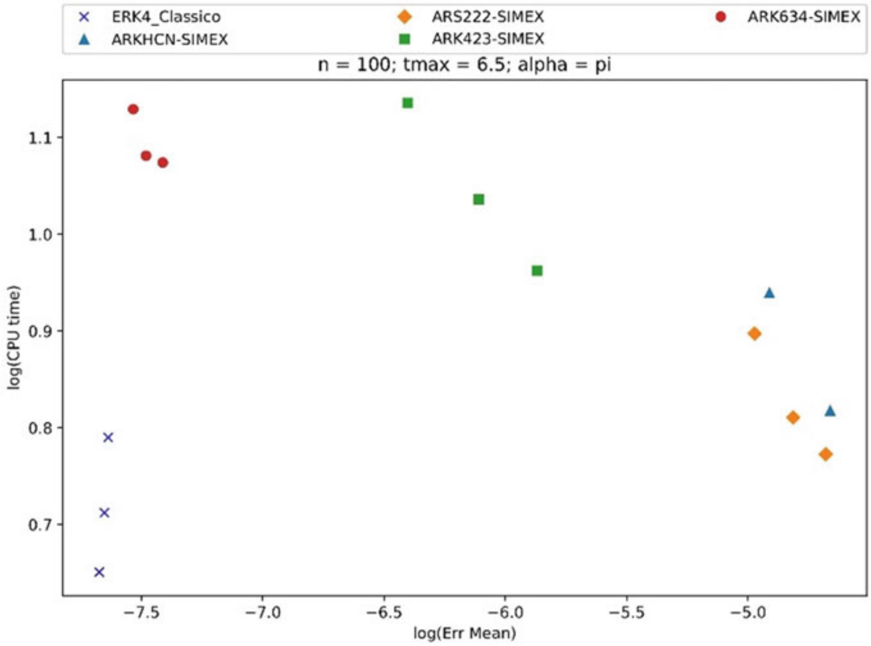

Fig. 1 CPU time versus mean error for classical fourth-order ERK and SIMEX with different tableaus. $tmax = 6.5$; $n = 100$; $\alpha = \pi$. Decomposition 1

attention to the second-order SIMEX methods which got a technical tie with the RK4 on the last test, Fig. 5. However, it came with a cost of a mean error three orders of magnitude greater.

Motivated by the results shown in Fig. 5 where the two second-order SIMEX basically equates the implicit steps' cost if compared to the reference explicit method, further investigation was made. Figure 5 shows that if the problem's stiffness is increased, SIMEX is more likely to be faster than the RK4. In this instance, three different advection speeds are used and the simulation total time was raised to $tmax = 30$ in order to let the execution time scale grow. Both ARKHCN and ARS222 were faster than the reference method, but the second was consistently the fastest. In Fig. 6, ARS222 decreased the RK4's CPU time by 10.5%; in Fig. 7 by 13.8% and in Fig. 8 by 13.6%. The bigger stiffness does favor SIMEX efficiency, but there's no clear growth relation between them.

6.4 Conclusions

A test case successfully developed where the SIMEX method was implemented in a simplified version of the GATT's DNS code and then it was possible to measure the

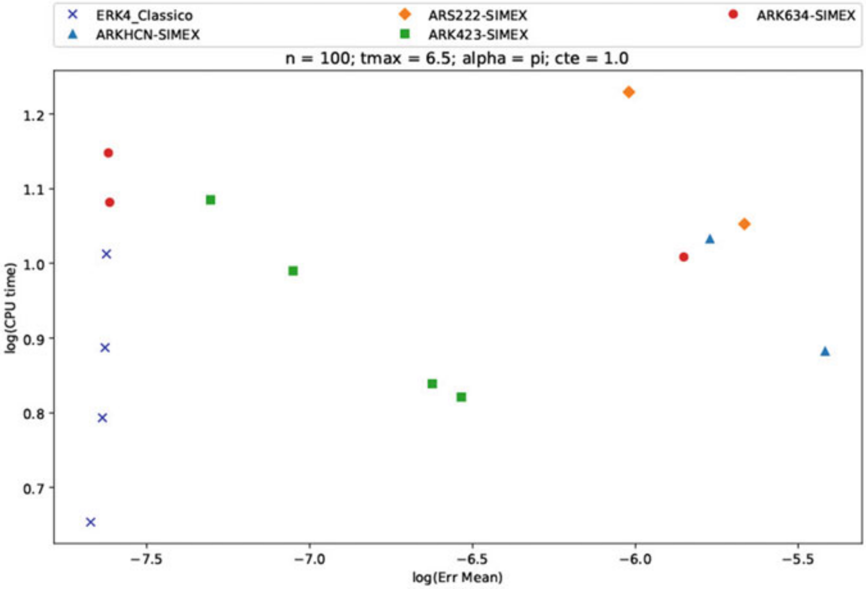

Fig. 2 CPU time versus mean error for classical fourth-order ERK and SIMEX with different tableaus. $tmax = 6.5$; $n = 100$; $\alpha = \pi$; $c = 1.0$. Decomposition 2

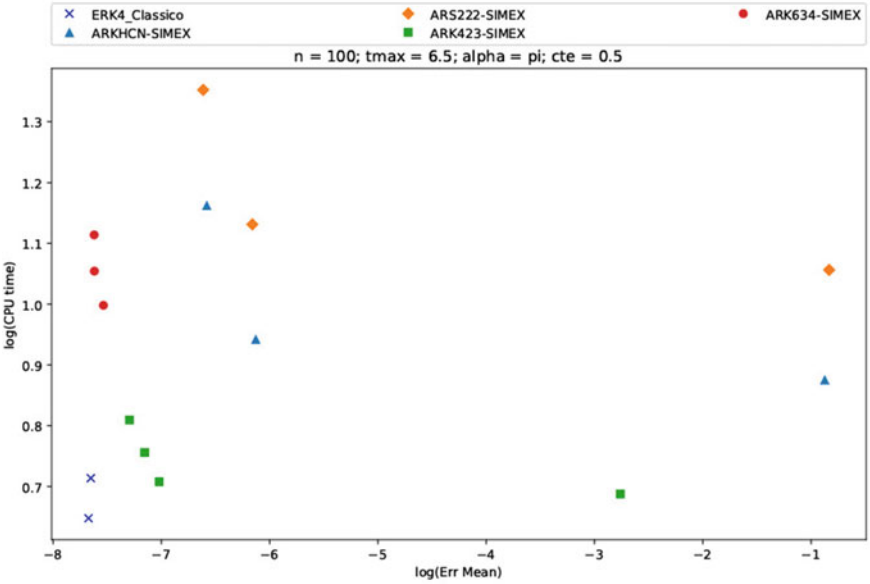

Fig. 3 CPU time versus mean error for classical fourth-order ERK and SIMEX with different tableaus. $tmax = 6.5$; $n = 100$; $\alpha = \pi$; $c = 0.5$. Decomposition 2

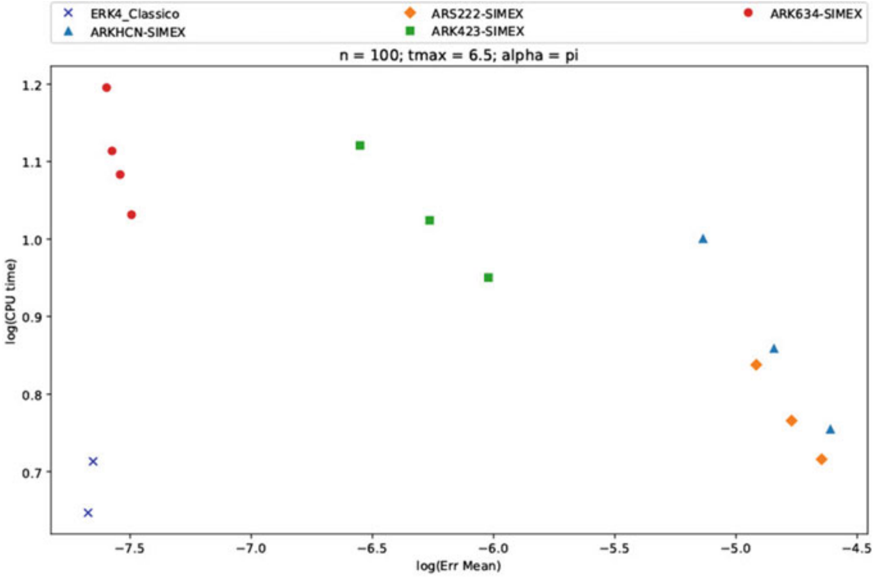

Fig. 4 CPU time versus mean error for classical fourth-order ERK and SIMEX with different tableaus. $tmax = 6.5$; $n = 100$; $\alpha = \pi$. Decomposition 3

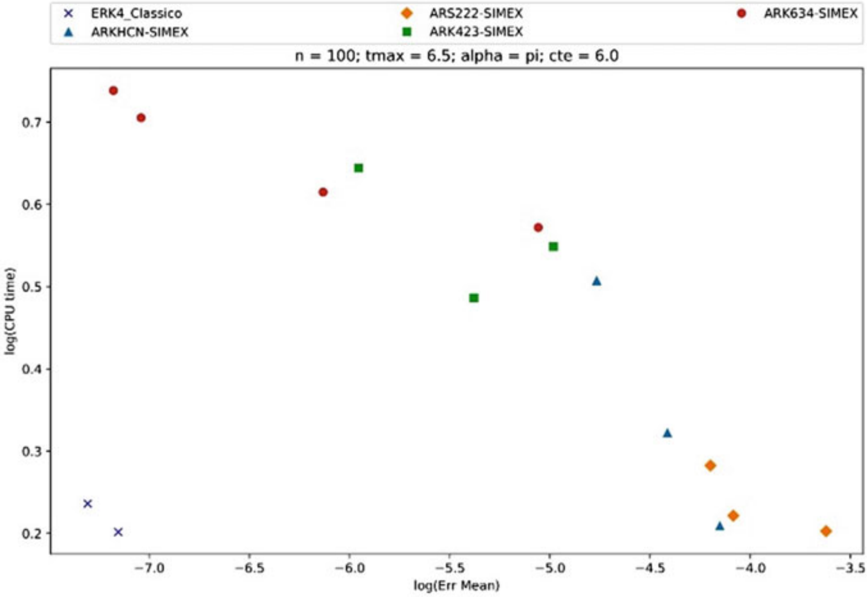

Fig. 5 CPU time versus mean error for classical fourth-order ERK and SIMEX with different tableaus. $tmax = 6.5$; $n = 100$; $\alpha = \pi$; $c = 6.0$. Decomposition 4

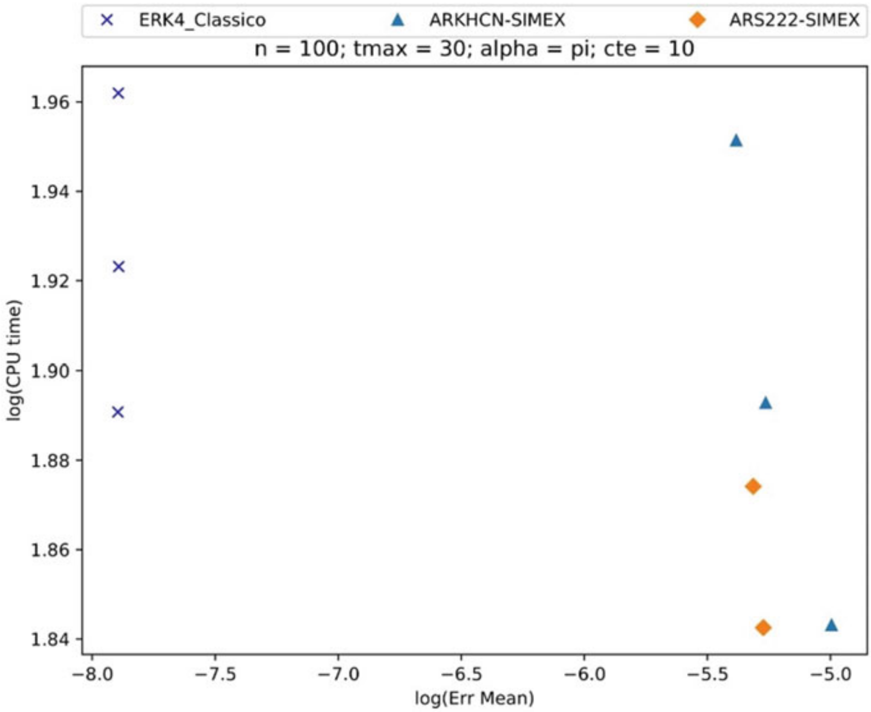

Fig. 6 CPU time versus mean error for classical fourth-order ERK and SIMEX with different tableaus. $tmax = 30$; $n = 100$; $\alpha = \pi$; $c = 10.0$. Decomposition 4

execution time and solution's quality and compare the results to the ones obtained with a classical fourth-order explicit Runge–Kutta. For such test, the 1D Burgers' equation was used.

Many *tableau* pairs were tested and they showed great impact on SIMEX efficiency but none of them was actually faster than the reference method for the nonlinear case. The results for the linear Burgers' equation were favorable for SIMEX only when the convection speed was above a certain value, namely, the stiffness. Additionally, this positive results were only observable for the two second-order *tableau* pairs. Despite the not so favorable results in these tests, it's not a bad sign for the SIMEX's performance with regard to future research, but the opposite. This conclusion is supported by a few things that need to be considered.

The model's stiffness is given by the convective term and when it is set in the implicit part the maximum step-size is now defined by the dissipative term; this doesn't happen in the DNS code. Considering the compressible Navier–Stokes equations, the terms related to convection and acoustic waves are the source of stiffness. At low Mach number flows, the propagation of acoustic waves imposes a much greater time-step restriction and a precise solution of this phenomena is not necessary unless one is studding aeroacoustics.

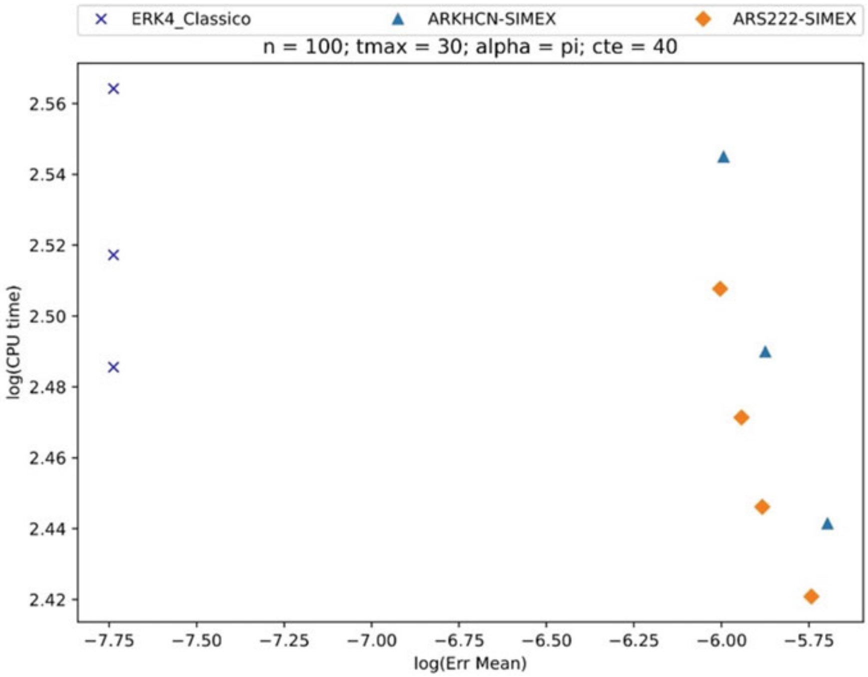

Fig. 7 CPU time versus mean error for classical fourth-order ERK and SIMEX with different tableaus. $tmax = 30$; $n = 100$; $\alpha = \pi$; $c = 40.0$. Decomposition 4

Besides, typical simulations use nonuniform meshes, where each spatial coordinate has a different refinement, which yields fairly different grid points density. Considering the standard 2D test case set in the DNS code, the grid points density is approximately one order of magnitude greater in the y-axis. In other words, the grid stiffness is considerably higher in this direction. This intense refinement in the vertical direction is due to the necessity to resolve precisely the boundary layer and it's related phenomena.

Lastly, the choice of the decomposition is crucial for implicit–explicit method's efficiency, always seeking the best relation between higher time-stepping and implicit equation's complexity. The iterative method for implicit systems and the *tableau* pair also have huge impact on the efficiency. As a work guideline, SIMEX should be faster than the reference ERK no matter what *tableau* is used. But, in the other hand, the ones with less stages gave better results. That's a good indicative of what to investigate.

The next section presents a draft for the work's next phase containing the DNS governing equations, proposed IMEX decompositions, and iterative methods.

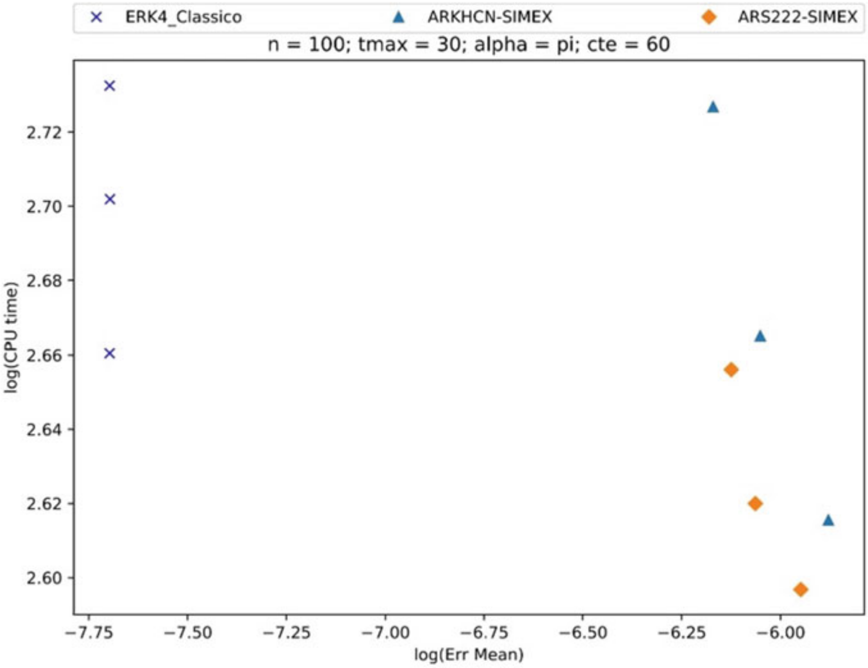

Fig. 8 CPU time versus mean error for classical fourth-order ERK and SIMEX with different tableaus. $tmax = 30$; $n = 100$; $\alpha = \pi$; $c = 60.0$. Decomposition 4

6.5 Next Steps

By the time the preliminary tests are ended, the next step is to implement the SIMEX method into the DNS code. A detailed explanation for the DNS code's structure is found in Mathias (2017).

The fluid's thermodynamic state is completely defined by the density (ρ), internal energy (e), and the three velocity components (u,v,w). Each variable depends on location (x,y,z) and time (t). The equations for the conservation of linear momentum, mass, and energy are written in the non-conservative form, which solves for each individual variable mentioned above, simplifying the boundary conditions. The pressure p is calculated assuming an ideal gas.

The first proposed IMEX implicit part is to be the source terms of acoustic wave propagation in the y-direction, due to refined grid in this direction. Hence, the implicit–explicit decomposition is defined as

$$g(\mathbf{y}) = \begin{pmatrix} -\rho_0 v_y \\ -\frac{\gamma-1}{\rho_0}(\rho_0 e_y + \rho_y e_0) \\ -\frac{p_0}{\rho_0} v_y \end{pmatrix} \; and \; f(\mathbf{y}) = \frac{d\mathbf{y}}{dt} - g(\mathbf{y}), \tag{23}$$

where the zero subscript as in ρ_0 represents the variable's value at the beginning of the integration step, which is kept constant through the entire step. The subscript y as in v_y denotes the derivative with respect to y, the constant γ, in the DNS context, is the thermodynamic relation c_p/c_v and

$$\mathbf{y} = \begin{pmatrix} \rho(y,t) \\ v(y,t) \\ e(y,t) \end{pmatrix}. \tag{24}$$

One good evidence that this proposed decomposition does group all the acoustic wave's source term that propagates in the y-direction is to be able to retrieve the wave equation starting from these terms, which is true, indeed.

The last item to be considered in this initial approach is the choice of an iterative method for the implicit system. Could be of great use a method that is simple to code and has a low processing cost as Gauss–Seidel and Gauss–Jacobi, so it'll be possible to have the first insights about the SIMEX's efficiency in the DNS. These iterations requires little computational effort and hopefully the increase in the time-step will more than compensate that cost. As the time-step becomes larger and larger, the off diagonal terms become larger, which makes the system more difficult to solve. Hence, it may be necessary to use more powerful methods.

Acknowledgements G.B.F.B. received funding from Coordination for the Improvement of Higher Education Personnel (CAPES/Brazil). M.A.F.M. is sponsored by CNPq/Brazil, grant no. 307956/2019-9.

References

Ascher UM, Ruuth SJ, Spiteri RJ (1997) Implicit-explicit runge-kutta methods for time-dependent partial differential equations. Appl Numer Math 25(2):151–167. https://doi.org/10.1016/S0168-9274(97)00056-1. ISSN 0168-9274. Special Issue on Time Integration

Bergamo LF, Gennaro EM, Theofilis V, Medeiros MA (2015) Compressible modes in a square lid-driven cavity. Aerosp Sci Technol 44:125–134. https://doi.org/10.1016/j.ast.2015.03.010. ISSN 12709638. https://linkinghub.elsevier.com/retrieve/pii/S1270963815001030

Bergamo LF (2014) Instabilidade hidrodinâmica linear do escoamento compressível em uma cavidade. Master thesis, Universidade de São Paulo, São Carlos. https://doi.org/10.11606/D.18.2014.tde-28052014-164324. http://www.teses.usp.br/teses/disponiveis/18/18148/tde-28052014-164324/

Bispen G, Luká˘cová-Medvid'ová M, Yelash L (2017) Asymptotic preserving imex finite volume schemes for low mach number euler equations with gravitation. J Comput Phys 335:222–248. https://doi.org/10.1016/j.jcp.2017.01.020. ISSN 0021-9991

Colavolpe C, Voitus F, Bénard P (2017) Rk-imex hevi schemes for fully compressible atmospheric models with advection: analyses and numerical testing. Q J R Meteorol Soc 143(704):1336–1350. https://doi.org/10.1002/qj.3008

Cooper G, Sayfy A (1980) Additive methods for the numerical solution of ordinary differential equations. Math Comput 35(152):1159–1172

Crouzeix M (1980) Une méthode multipas implicite-explicite pour l'approximation des équations d'évolution paraboliques. Numer Math 35(3):257–276

Durran DR, Blossey PN (2012) Implicit–explicit multistep methods for fast-wave–slow-wave problems. Mon Weather Rev 140(4):1307–1325

Gardner DJ, JEG, Hamon FP, Reynolds DR, Ullrich PA, Woodward CS (2018) Implicit–explicit (IMEX) Runge–Kutta methods for non-hydrostatic atmospheric models. Copernicus Publications on behalf of the European Geosciences Union

Ghosh D, Constantinescu EM (2016) Semi-implicit time integration of atmospheric flows with characteristicbased flux partitioning. SIAM J Sci Comput 38(3):A1848–A1875. https://doi.org/10.1137/15M1044369

Hofer E (1976) A partially implicit method for large stiff systems of odes with only few equations introducing small time-constants. SIAM J Numer Anal 13(5):645–663. https://doi.org/10.1137/0713054

Kennedy CA, Carpenter MH (2003) Additive runge–kutta schemes for convection–diffusion–reaction equations. Appl Numer Math 44(1):139–181. https://doi.org/10.1016/S0168-9274(02)00138-1. ISSN 0168-9274

Kennedy CA, MHC (2001) Additive Runge-Kutta schemes for convection-diffusion-reaction equations. Technical report, National Aeronautics and Space Administration, Virginia

Kennedy CA, MHC (2016) Diagonally implicit Runge-Kutta methods for ordinary differential equations. A review. National Aeronautics and Space Administration. https://ntrs.nasa.gov/search.jsp?R=201600059232020-03-22T21:22:55+00:00Z

Kennedy CA, MHC (2018) Higher-order additive Runge–Kutta schemes for ordinary differential equations. Appl Numer Math 183–205. https://doi.org/10.1016/j.apnum.2018.10.007

Lele SK (1992) Compact finite difference schemes with spectral-like resolution. J Comput Phys 103(1): 6–42. https://doi.org/10.1016/0021-9991(92)90324-R. ISSN 00219991

Martinez A (2016) Towards natural transition in compressible boundary layers. Phd. thesis, University of São Paulo

Martinez A, Medeiros MF (2016) Direct numerical simulation of a wavepacket in a boundary layer at Mach 0.9. In: 46th AIAA fluid dynamics conference. American Institute of Aeronautics and Astronautics, Reston, Virginia, vol 414, pp 1–33. ISBN 978-1-62410-436-7. ISSN 00221120. https://doi.org/10.2514/6.2016-3195. http://arc.aiaa.org/doi/10.2514/6.2016-3195

Mathias MS (2017) Instability analysis of compressible flows over open cavities by a Jacobian-free numerical method. Master thesis, University of São Paulo

Restelli M, Giraldo FX (2009) A conservative discontinuous galerkin semi-implicit formulation for the navier–stokes equations in nonhydrostatic mesoscale modeling. SIAM J Sci Comput 31(3):2231–2257

Rodrigues SB (2017) A shortcut for IMEX methods: integrate the residual explicitly. Vol 1705.04870. eprint arXiv. http://arxiv.org/abs/1705.04870

Silva HG, Souza LF, Medeiros MAF (2010) Verification of a mixed high-order accurate dns code for laminar turbulent transition by the method of manufactured solutions. Int J Numer Methods Fluids 64(3): 336–354. https://doi.org/10.1002/fld.2156. https://onlinelibrary.wiley.com/doi/abs/10.1002/fld.2156

Vogl CJ, AS, Reynolds DR, Ullrich PA , Woodward CS (2019) Evaluation of implicit-explicit additive Runge-Kutta Integrators for the HOMME-NH dynamical core. J Adv Model Earth Syst (JAMES)

Wang H, Shu CW, Zhang Q (2015) Stability and error estimates of local discontinuous galerkin methods with implicit-explicit time-marching for advection-diffusion problems. SIAM J Numer Anal 53(1):206–227. https://doi.org/10.1137/140956750

Weller H, Lock SJ, Wood N (2013) Runge–kutta imex schemes for the horizontally explicit/vertically implicit (hevi) solution of wave equations. J Comput Phys 252:365–381. https://doi.org/10.1016/j.jcp.2013.06.025. ISSN 0021-9991

Zhang H, Sandu A, Blaise S (2016a) High order implicit-explicit general linear methods with optimized stability regions. SIAM J Sci Comput 38(3):A1430–A1453. https://doi.org/10.1137/15M1018897

Chapter 7
Direct Numerical Simulation of Bi-Disperse Particle-Laden Gravity Currents on Lock-Exchange Configuration with Different Schmidt Number

Guilherme Torres Marques Vidal, Gabriel Narváez Campo, Rubem Mário Figueiró Vargas, and Jorge Hugo Silvestrini

Abstract We performed direct numerical simulations (DNS) of bi-disperse particle-laden gravity currents on a lock-exchange configuration with different values of Schmidt number (Sc) for each particle fraction, to investigate the impact of double mass diffusivity on flow dynamics and deposition. We used the high-order code Incompact3d to solve the incompressible Navier–Stokes equations and the scalar transport equation. We compared our results with previous physical and numerical experiments available in the bibliography, obtaining a good agreement. We simulated two cases: (i) $\mathrm{Sc} = 1$ for both particle fractions and (ii) $\mathrm{Sc} = 3$ and $\mathrm{Sc} = 1$, for coarse and fine fraction, respectively. Case (ii) shows higher reduction of the front velocity of current during the deceleration phase. For case (i), the current has higher amount of suspended fine particle during all the experiments, which could explain why the front velocity has lesser decreasing during the deceleration phase. The configuration of the final deposit profile shows that case (ii) has the highest deposit peak nearer to the lock-exchange gate than the case (i). We also calculated the temporal evolution of the energy budget of our simulations, and we find that the energy is conserved during all time of our simulations and the term related to turbulent dissipation is the principal responsible for energy loss.

Keywords Bi-disperse current · Particle-laden gravity current · Direct numerical simulation · High-order numerical simulation · Deposition of particles

---

G. T. Marques Vidal (✉) · G. N. Campo · R. M. Figueiró Vargas · J. H. Silvestrini
Pontifícia Universidade Católica do Rio Grande do Sul, Av. Ipiranga, Porto Alegre, RS 681, Brazil
e-mail: guilherme_torres@hotmail.com.br

R. M. Figueiró Vargas
e-mail: rvargas@pucrs.br

J. H. Silvestrini
e-mail: jorgehs@pucrs.br

H. F. Meier et al. (eds.), *Advances in Turbulence*, ABCM Series on Mechanical Sciences and Engineering, https://doi.org/10.1007/978-3-031-25990-6_7

7.1 Introduction

Gravity currents are created when there is a gradient of pressure between two fluids due to difference of density. When the main gradient is in horizontal direction, one fluid propagates horizontally through the other. The variation of density could be caused by a difference of temperature, salinity, or suspended particles in a fresh fluid. Gravity currents are formed in many different natural situations as well as human-made. Some examples of natural situations are thunderstorm outflows, sea-breeze fronts, airborne snow, sandstorms, powder snow avalanches, and pyroclastic flows. In the ocean, these flows are driven by salinity and temperature inhomogeneities, or like in turbidity currents whose density gradients are derived from suspended mud or silt. There are essential applications in different areas like aircraft safety; entomology and pest control; and in pollutants spreading into the atmosphere, lakes, and rivers. In a industry context, these flows can be observed in the manufacturing process of sheet glass. In an engineering context, these flows can destroy submarine pipes and cables (Simpson 1982).

The particle-laden gravity currents are an example of flow caused by the presence of suspended particles in a fresh fluid. This kind of current is considered non-conservative because particle sedimentation decreases the gradient of density between the flow and the surrounding fluid. This behavior is very different from conservative currents, where the gradient of density is created by temperature or salinity differences, and there is no sedimentation. In a geophysical context, particle-laden currents are essential mechanism for sediment transport from shallow to deep water. In the offshore environment, non-conservative currents of sand could form deposits with great potential of being hydrocarbon reservoirs as the oil reservoirs in the pre-salt layer, for instance (Meiburg and Kneller 2010; Lucchese 2018).

The behavior of gravity currents can be understood through physical experiments (Simpson 1972; Huppert and Simpson 1980; Manica 2009) or numerical simulation (Kubo 2004; Cantero et al. 2007). The studies of Winters et al. (1995), Necker et al. (2005), and Espath et al. (2014) develop a methodology to calculate the energy budget of the flow. They perform numerical simulation of mono-disperse gravity currents and demonstrate the relationship between each term involved in the energy budget and other global quantities like front position, suspended mass, and final deposit profile. The interaction of a particle-laden flows with three-dimensional topography was studied by Nasr-Azadani et al. (2016) through numerical simulations. Lucchese (2018) analyzed the influence of alteration of bottom topography for poly-disperse flows in a numerical context. In an experimental context, Gladstone et al. (1998) made experiments of poly-disperse flows to understand the impact of initial mixture of different particle fraction in current dynamics. They found that different initial concentrations had a strong impact on the features of the flow.

In a numerical context, Francisco et al. (2017) studied bi-dispersed particle-laden gravity in the lock-exchange configuration. Their work analyzed the impact of the initial concentration of different particle diameters in the main features of the flow. Their results show that high concentration of fine particles makes the current reach

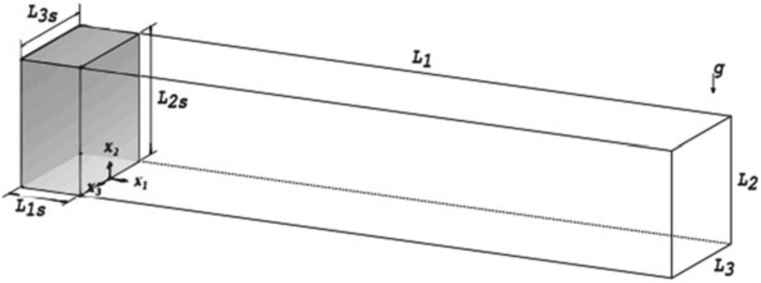

Fig. 1 Schematic view for the initial configuration of lock-exchange flow. The mixture of particles and fluid is initially in the lock, filled region. *Source* Francisco et al. (2017)

larger distances when comparing to flows with greater concentration of coarse particles. Their study used a unique unitary Schmidt number in all their simulations. In this paper, we want to extend their study by adding the effect of double mass diffusivity.

Our goal in this research is to understand the effect of different values of Schmidt number, for each particle fraction, on non-conservative and bi-disperse gravity currents, through the measurement of some flow and deposit variables as front position and velocity, suspended material, mass sedimentation rate, and deposit profile. We also compute the temporal evolution of the energy budget of the current. We use the in-house code *Incompact3d* to simulate (by *DNS*) bi-disperse and double diffusive particle-laden gravity currents in lock-exchange configuration (see Fig. 1), for a Reynolds number of 4000. We perform numerical experiments at the same initial concentration of coarse and fine fraction particle for unique and different values of Schmidt number. Our approach only considers the particle deposition, ignoring erosion and re-suspension. We compare our data with previous physical and numerical experiments presented in the literature.

7.2 Methodology

In this section, we describe the governing equations, the flow configuration as well as the treatment for the data post-processing.

7.2.1 Flow Configuration and Governing Equations

The lock-exchange flow configuration in a confined channel is used in this numerical study. This arrangement consists of a homogeneous mixing of sediment and fresh fluid which are trapped in an initial fraction of the dimension domain, separated from the clear fluid by a gate. When simulation begins, the gate is removed and the particle–fluid mixing flow due to the gravity action. Two mechanisms are responsible for motion: the first one is the transformation of potential energy into kinetic energy and the second one is the diffusive motion that is generated by the potential difference between heavy and clear fluid.

To evaluate the flow motion, we solve numerically the incompressible Navier–Stokes equations and the scalar (sediment) transport equation under the Boussinesq approximation. The dimensionless equations can be written as

$$\frac{\partial u_i}{\partial x_i} = 0, \tag{1}$$

$$\frac{\partial u_i}{\partial t} + u_j \frac{\partial u_i}{\partial x_j} = -\frac{\partial p}{\partial x_i} + \frac{1}{Re} \frac{\partial^2 u_i}{\partial x_j \partial x_j} + c_t e_i^g, \tag{2}$$

$$\frac{\partial c_l}{\partial t} + \left(u_j + u_l^s e_j^g\right) \frac{\partial c_l}{\partial x_j} = \frac{1}{Sc_l Re} \frac{\partial^2 c_l}{\partial x_j \partial x_j} \, l = 1, ..., N, \tag{3}$$

where u_i, p, and c_l are, respectively, velocity, pressure, and total particle concentration fields; c_t is the total particle concentration; i and j are the indexes for each spatial coordinate; $e_i^g = (0, -1, 0)$ is the unitary vector acting in the direction of the gravitational acceleration; u_l^s is the settling velocity of the particle fraction l related to its diameter; and N is the total number of particles fractions in the current, being each fraction characterized by a different diameter. As in this study, all our simulations were bi-disperse, then $N = 2$. The Reynolds and Schmidt numbers are, respectively, defined by

$$Re = \frac{\tilde{u}_b \tilde{h}}{\tilde{\nu}}, \tag{4}$$

$$Sc_l = \frac{\tilde{\nu}}{\tilde{k}_l}, \tag{5}$$

where $\tilde{u}_b$, $\tilde{h}$, and $\tilde{\nu}$ are the buoyancy velocity, the characteristic length scale (corresponding to the lock-exchange height), and the kinematic viscosity coefficient, respectively. Sc_l and $\tilde{k}_l$, respectively, are the Schmidt number and the mass diffusivity coefficient for the particle fraction l.

The total particle concentration is obtained by the sum of each particle fraction

$$c_t = \sum_{l=1}^{N} c_l \, l = 1, ..., N. \tag{6}$$

As the c_t is already normalized by the total initial concentration of the mixture, in the initial configuration (Fig. 1), the sum of all particle fractions is 1 in the lock region and 0 at the rest of the domain.

A Cartesian mesh with $n_1 \times n_2 \times n_3$ grid points is used in a domain of size $L_1 \times L_2 \times L_3$. For the velocity field, we apply no-slip boundary condition at the bottom of domain, periodic conditions at $x_3 = 0$ and $x_3 = L_3$, and free-slip conditions for the other boundaries. For the scalar field, we used null normal gradient boundary condition on $x_1 = 0$ and $x_1 = L_1$, periodic condition at $x_3 = 0$ and $x_3 = L_3$, and no-flux at $x_2 = L_2$. In order to take into account the particle's deposition in the vertical direction at the bottom of the domain, the following outflow boundary condition is used:

$$\frac{\partial c_l}{\partial t} + u_l^s e_2^g \frac{\partial c_l}{\partial x_2} = 0. \tag{7}$$

This condition allows to mimic the process of sediment leaving the computational domain when it touches the bottom wall. A perturbation on the velocity field at the interface between the two fluid is applied to simulate the effect of removing the gate. We use a white noise with 10% of the initial potential energy of the current with a initial perturbation.

In natural flows, as salt mixtures, the Schmidt number could be very high and computationally expensive to simulate. Moreover, for particle-laden flows, the mass diffussivity coefficient representative of the mixture is not well defined. To overcome this problem, we use an estimation based on the diffusivity coefficient for each particle fraction, considering the Einstein–Stokes equation:

$$k_l = \frac{k_B T}{6\pi \mu r_l}, \tag{8}$$

where k_B is Boltzmann's constant, T is the absolute temperature, μ is the dynamic viscosity coefficient, and r_l is the radius of each particle fraction l. Then, applying the ratio between the Schmidt number of the two particles and considering Eq. (8), we obtain a relation between the ratio of Schmidt number and the radius of each particle fraction:

$$\frac{Sc_1}{Sc_2} = \frac{k_2}{k_1} = \frac{r_1}{r_2}. \tag{9}$$

We propose in this paper to apply this ratio in a simulation, which means employing two Schmidt numbers, one for each particle fraction.

7.2.2 Software

We used the in-house code *Incompact3d* (www.incompact3d.com) to solve the incompressible Navier–Stokes equation and scalar transport equation presented above. This code employs a compact sixth-order finite difference scheme for spatial differentiation and a third-order Adams–Bashforth scheme for time integration. To apply the incompressibility condition, a fractional step method requires to solve a Poisson equation. This equation is fully solved in spectral space via the use of relevant 3D fast Fourier transforms. For more information about the numerical code and the parallel strategy used for *Incompact3d*, we recommend Laizet and Lamballais (2009) and Laizet and Li (2011).

7.2.3 Post-Processing

In order to quantify the impact of double mass diffusivity in the numerical experiments, we calculate the current front position and velocity, the suspended mass, the sedimentation rate, the deposit height, and the temporal evolution of energy budget of the flow. These quantities are computed at post-processing stage. Part of the post-processing step is embedded in the code *Incompact3d*, and the other part was carried out by using the programming language *Python* with some functions of libraries *Numpy* and *SciPy* for numerical integration. In this section, we are going to explain each method that we used in this step.

7.2.3.1 Evolution of Current Front Position and Velocity

To measure the current front position, x_f, we follow a procedure using a vertical and span-averaged total concentration defined as

$$\overline{c}_t(x_1, t) = \frac{1}{L_2 L_3} \int_0^{L_2} \int_0^{L_3} c_t dx_2 dx_3. \tag{10}$$

With this definition, the flow front position in our configuration is computed as the most forward point at x_1 where the averaged total concentration overcomes a threshold value which, in our calculations, is 0.1%. Usually, the flow front velocity, u_f, is measured by calculating the derivative of the front position. Unfortunately, the frequency that we save the data of our simulations introduces some noise, compromising the interpretation and reducing the accuracy when we apply this method. Because of that, we choose to use the recent method proposed by Farenzena (2020). This method determines the velocity of the front as the maximum point of an integral quantity. The reference velocity $\overline{u}$ in each point of the domain is defined as

$$\overline{u}(x_1, t) = \frac{\int_0^{L_3} \int_0^{L_2} \left(u_1 c_t - \sum_{l=1}^{N} \frac{1}{ReSc_l} \frac{\partial c_l}{\partial x_1} \right) dx_2 dx_3}{\int_0^{L_3} \int_0^{L_2} c_t dx_2 dx_3} \quad l = 1, ..., N. \tag{11}$$

The front velocity is estimated as the $\overline{u}$ maximum value inside the head flow:

$$u_f(t) = max\big[\overline{u}\big(-L_{head} < x_1 - x_f < 0, t\big)\big], \tag{12}$$

where L_{head} is the size of current head.

7.2.3.2 Suspended Mass and Sedimentation Rate

We also analyze the temporal evolution of the suspended material and the sedimentation rate. The suspended mass is computed as the volume integral of the total concentration in all domains, Ω, for each particle fraction,

$$m_{p_l}(t) = \int_{\Omega} c_l d\Omega \ l = 1, ..., N, \tag{13}$$

where m_{p_l} is the suspended mass for particle fraction l. The following equation gives the temporal evolution of sedimentation rate, $\dot{m}_{s_l}$, for the particle fraction l

$$\dot{m}_{s_l}(t) = \frac{1}{L_1 L_3}\int_0^{L_1}\int_0^{L_3} c_{w_l}(x_1, x_3, t) u_l^s dx_3 dx_1 \ l = 1, ..., N, \tag{14}$$

where c_{w_l} is the concentration at the bottom of the domain ($x_2 = 0$).

7.2.3.3 Deposit Mean Profile and Composition

In the numerical formulation, we impose at the bottom of the domain, the boundary condition defined in Eq. (7) to ensure that the sediments leave the computational domain throughout the simulation. Therefore, it is possible to calculate the mass deposited by the sedimentation process by integrating the mass flux through the bottom over time. The mass deposited profile, of particle fraction l, after a time t, is obtained by

$$D_l(x_1, t) = \int_0^t < c_{w_l(x_1,\tau)} >_{x_3} u_l^s d\tau \ l = 1, ..., N, \tag{15}$$

where $<.>_{x_3}$ operator denotes spanwise averaging. The profile of total mass deposited is expressed by

$$D_t(x_1, t) = \sum_{i=1}^{N} D_l(x_1, t) \ l = 1, ..., N. \tag{16}$$

In this equation, the contribution of each particle fraction to the deposit can be quantified by the ratio of D_l and D_t, as it follows:

$$P_l = \frac{D_l}{D_t} \; l = 1, ..., N, \tag{17}$$

where P_l is the portion of each particle fraction in the total deposit.

7.2.3.4 Energy Budget of the Flow

The potential energy inside the lock is turned into kinetic energy after the release of the gate. In the works of Winters et al. (1995) and Necker et al. (2005), methods to calculate the temporal evolution of energy budget of gravity currents were discussed. In this work, we follow the methodology used by Espath et al. (2014) to calculate the energy budget of the flow. This energy budget can be derived from the Navier–Stokes and scalar transport equations. The total energy can be split into kinetic and potential energy, and distinguish the dissipation associated to the strain rate in the macroscopic advective motion and the dissipation that occurs in the microscopic Stokes flows around the particles.

The kinetic energy, k, is computed by the inner product of velocity field integrated in the entire domain:

$$k(t) = \int_{\Omega} \frac{1}{2} u_i u_i d\Omega. \tag{18}$$

Differentiating Eq. (18) with respect to time and applying Eq. (2), we have

$$\frac{dk}{dt} = -\int_{\Omega} \frac{2}{Re} s_{ij} s_{ij} d\Omega - \sum_{l=1}^{N} \int_{\Omega} u_2 c_l d\Omega, \tag{19}$$

where s_{ij} is the strain rate tensor given by $s_{ij} = \frac{1}{2}\left(\frac{\partial u_i}{\partial x_j} + \frac{\partial u_j}{\partial x_i}\right)$.

The expression for total potential energy is given by

$$E_{p_t}(t) = \sum_{l=1}^{N} \int_{\Omega} c_l x_2 d\Omega. \tag{20}$$

Taking the derivative of this expression with respect to time and applying Eq. (3), we have

$$\frac{dE_{p_t}}{dt} = \sum_{l=1}^{N} \left[\int_{\Omega} \left(x_2 \frac{1}{Sc_l Re} \frac{\partial^2 c_l}{\partial x_2 \partial x_2} + x_2 u_l^s \frac{\partial c_l}{\partial x_2} \right) d\Omega + \int_{\Omega} u_2 c_l d\Omega \right]. \tag{21}$$

From Eqs. (19) and (21), we can derive an expression for the time variation of total mechanical energy

$$\frac{d(k+Ep_t)}{dt} = -\int\limits_{\Omega} \frac{2}{\mathrm{Re}} s_{ij}s_{ij}d\Omega$$
$$+\sum_{l=1}^{N}\left[\int\limits_{\Omega}\left(x_2\frac{1}{Sc_1\mathrm{Re}}\frac{\partial^2 c_1}{\partial x_2\partial x_2}+x_2u_t^s\frac{\partial c_1}{\partial x_2}\right)d\Omega\right] = -\epsilon-\epsilon_{st}, \quad (22)$$

where ϵ is associated to the turbulent dissipation rate and ϵ_{s_t} is the dissipation rate associated with loss of energy due to suspended particles. To compute the energy dissipated after a time t, we use

$$E_d(t) = \int_0^t \epsilon(\tau)d\tau, \quad (23)$$

$$E_{s_t}(t) = \sum_{l=1}^{N} E_{s_l}(t) = \sum_{i=1}^{N}\left[\int_0^t \epsilon_{s_l}(\tau)d\tau\right], \quad (24)$$

where E_{s_l} is the energy dissipated by effect of suspended particles. Finally, the complete energy equation is

$$k + E_{p_t} + E_d + E_{s_t} = E_{t_{0,}} \quad (25)$$

where E_{t_0} is the initial total energy, which can be obtained by calculating each term of the equation at $t = 0$.

7.2.4 Global Parameters

We performed numerical simulations of particle-laden gravity currents in a lock-exchange configuration with a fixed Reynolds number of 4000. We consider for the coarse and the fine particle fraction radii of 69 μm and 25 μm, respectively, which are the same values used in the study of Gladstone et al. (1998). We adopted the settling velocities of $u_1^s = 0.03$ and $u_2^s = 0.004$, for coarse and fine particle fractions, respectively. We use a computational domain size of $(L_1, L_2, L_3) = (30, 2, 0.1)$ with a number of grid points of $(n_1, n_2, n_3) = (2305, 325, 7)$. For all cases, the total simulation time was $t = 100$ with a time step of $\Delta t = 6.23 \times 10^{-4}$. For this paper, we choose two of our numerical experiments to compare with previous results presented in the literature, for the same initial concentration of coarse and fine particles of $\phi_1 = 50\%$ and $\phi_2 = 50\%$, respectively. For the first one (#1), the Schmidt number for both particle fractions was equal to 1. For the second (#2), the Schmidt numbers of coarse and fine fractions were $Sc_1 = 3$ and $Sc_2 = 1$. According to Eq. (9), we obtain a ratio of $\frac{Sc_1}{Sc_2} = 3$.

7.3 Results

In this section, we describe the results of our simulations in terms of front position and velocity, mass suspended, deposition rate, deposit profile (in mass), and energy budget.

7.3.1 Evolution of Current Front Position and Velocity

According to Huppert and Simpson (1980), the gravity currents can pass by three states after flow starts. The first occurs after the gate is removed and the fluid inside the lock flows toward the streamwise direction. At this phase, the ambient fluid creates a counter-flow to the current motion that retards its movement. During this so-called slumping phase, the current front moves with constant velocity. This regime may be followed by an inertial phase where the buoyancy forces are balanced by inertial forces. At this stage, the front velocity is no more constant and starts suffering deceleration. The final regime is the viscous phase, where the buoyancy forces are balanced by viscous forces.

In Fig. 2, the temporal evolution of the front position of the current is plotted, where the gate location is the initial position. We can observe a good agreement between our results and the reference for the initial time ($t < 20$). The difference for $t > 20$ related to Gladstone et al. (1998) is explained due to the higher Reynolds number ($Re \approx 24000$) in the experimental work. Moreover, there is possibility of re-suspension at this Re number. It should be pointed out that the reference for simulation #1 is the work of Francisco et al. (2017) which uses $Sc = 1$. On the other hand, up to $t \approx 18$, the front position of simulations #1 and #2 is very similar, suggesting no effect of double mass diffusivity on flow dynamics in this interval. After this period, the front velocity decreases, and a noticeable difference between these two simulations appears, being the front current of simulation #1 ahead when compared with simulation #2. This situation remains throughout the simulation.

Figure 3 shows the temporal evolution of front velocity for the two current simulations. Three phases (Cantero et al. 2007) are observed: (i) an initial almost constant regime; (ii) followed by a state in which the front velocity starts suffering deceleration, due to particle settling, at a rate of $\approx t^{-\frac{1}{3}}$; and (iii) a final regime where the velocity decreases with a rate of $\approx t^{-\frac{4}{5}}$. Both simulations show similar velocity until $t \approx 18$. When viscous effects start to be appreciable ($t > 18$), the deceleration phase starts, thus we can identify the effect of double mass diffusivity on flow dynamics, since simulation #2 seems to develop lower velocity (at least for a short period of time) than simulation #1 and this situation persists until $t \approx 35$. Looking back at Eq. (3), one reason this happens is the fact that increasing the Schmidt number reduces the effect of the diffusivity term in the flow and the convective term gains more importance being the only one promoting the current movement.

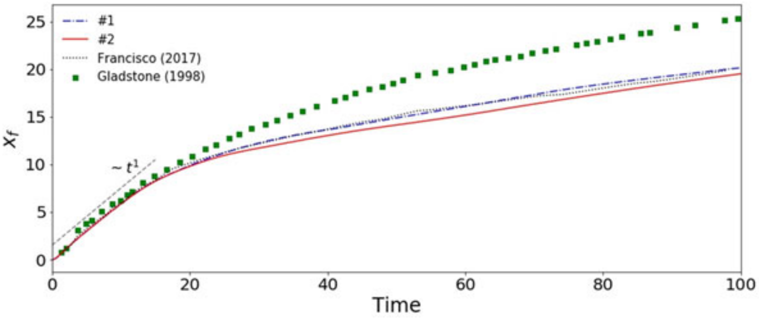

Fig. 2 Time evolution of the front position of the current for simulations #1 and #2 compared with the reference. The initial position is considered at the gate location

Fig. 3 Time evolution of the front velocity of the current for simulations #1 and #2

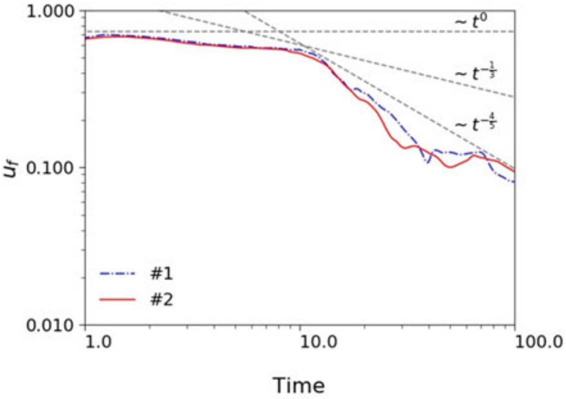

7.3.2 *Suspended Mass and Sedimentation Rate*

In Fig. 4, the temporal evolution of suspended mass for coarse $\left(m_{p1}\right)$ and fine $\left(m_{p2}\right)$ particle fractions is plotted. All curves are normalized by the initial material suspended $\left(m_{p0}\right)$. The suspended mass shows a good agreement with the reference. The suspended mass of *coarse particles* starts at the initial concentration of 50% followed by a quick drop reaching values less than 10% of m_{p_0} at $t \approx 20$ (Fig. 4a). Moreover, simulations #1 and #2 are very close until $t \approx 40$ from which simulation #2 shows a slightly higher amount of coarse particles suspended. For the suspended material of *fine particles*, the curves decrease slower when compared to coarse particles. The simulations are very similar until $t \approx 20$, at this point the curve for simulation #2 has a larger decrease when comparing against simulation #1, and remains lower for the rest of simulation. This suggests a slight impact of the double mass diffusivity in the amount and particle fraction of suspended mass. This behavior could help to explain the results on front position and velocity, since the fine particles are the most responsible for keeping the flow motion and reaching higher distances,

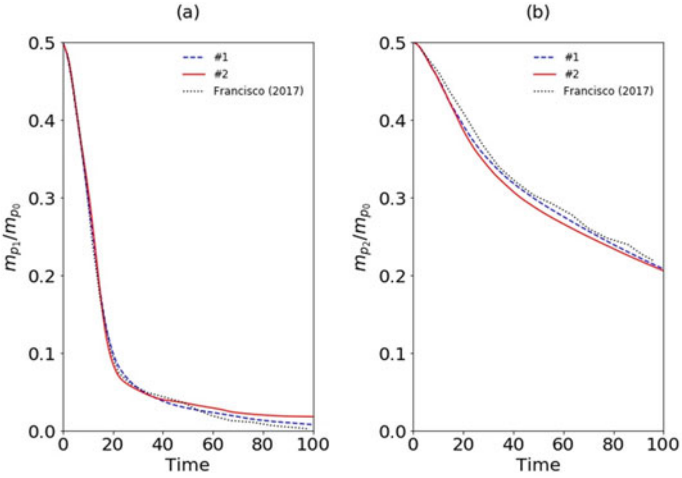

Fig. 4 Suspended particles as function of time: **a** coarse fraction and **b** fine fraction. All curves are normalized by the initial mass suspended

due to the coarse particles having a greater settling velocity depositing more quickly. This is because the fine particles remain for more time suspended, maintaining the density gradient. This has been demonstrated physically (Gladstone et al. 1998) as well as numerically (Francisco et al. 2017). Thus, as simulation #1 has more fine particles suspended during the experiment, it could explain why, after most of the coarse sediments are already deposited, the front position remains ahead if compared with the simulation #2.

The sedimentation rate gives the history of sediments that leave the computational domain at the bottom. Figure 5 shows the sedimentation rate for coarse and fine particle fraction as a function of time, showing a good agreement between our results and the reference. Two distinct phases (Francisco et al. 2017) can be identified: in the first phase, the curve increases proportionally to $\approx t^{0.4}$ until it reaches a maximum value around $t \approx 15$ (globally, the simulation #2 has higher sedimentation rate than simulation #1); in the following phase, the curve suffers a sharp decrease at a rate of $\approx t^{-3.25}$. In this last phase, both simulations are similar, but simulation #2 shows lower sedimentation rate in some instants. For the fine particle fraction, two phases can also be identified. However, the sedimentation rate grows proportionally to $\approx t^{0.75}$ and decreases at lower rate of $\approx t^{-1}$, after it reaches its peak at $t \approx 20$. Simulation #2 has substantially higher sediment rate in the interval between $t \approx 4$ and $t \approx 8$, and between $t \approx 15$ and $t \approx 50$. Both simulations show lower sediment rates when compared with the reference. For the moment, the only explanation for this difference is that the reference simulation is 2D.

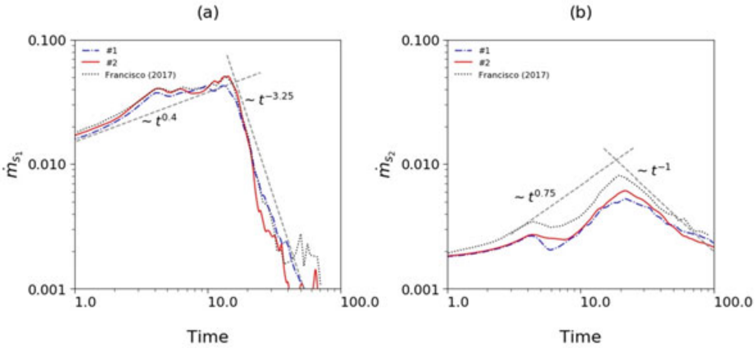

Fig. 5 Sedimentation rate as a function of time: **a** coarse fraction and **b** fine fraction

7.3.3 Deposit Mean Profile and Composition

In Fig. 6, the average profiles of deposit are plotted. The curves are normalized by final deposit at $t = 100$. There is a reasonable agreement between our results and the previous numerical and physical experiments. The peaks found in the deposit profile probably are related to the signature imposed by the strong Kelvin–Helmholtz vortexes mainly in quasi-2D simulations (Francisco et al. 2017). It was observed that the deposit was formed close to the gate, which is common for this kind of configuration.

Comparing the deposits of simulations #1 and #2, a difference in the configuration of the deposit, especially in the position of peaks, is identified. It could be a result of the difference in the temporal evolution of the front position between the two simulations and the impact of double mass diffusivity. There is no significant difference between the distance reached for the two deposits.

In Fig. 7, the temporal evolution of the deposit composition of each particle fraction for both simulations is plotted. Coarse particle concentration increases in the deposit during the beginning of the simulation, this situation persists until $t \approx 10$

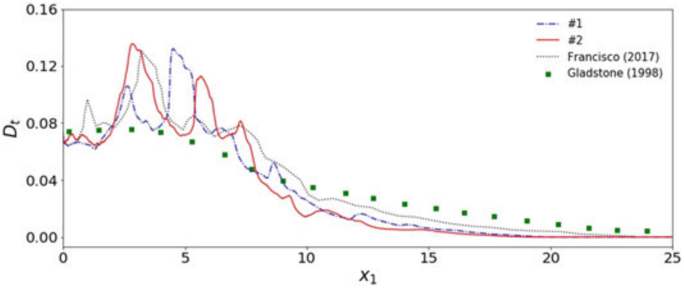

Fig. 6 Final deposit profile for bi-disperse lock-exchange. All curves are normalized with the total deposit at the final time

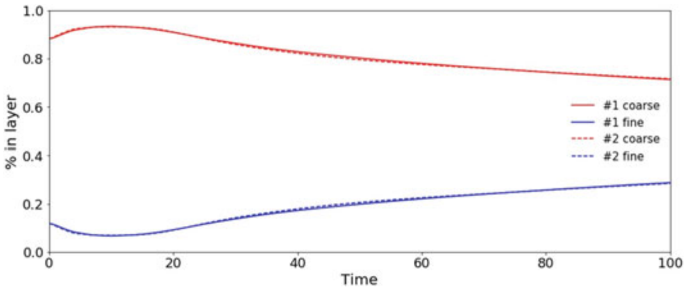

Fig. 7 Temporal evolution of deposit composition for each particle fraction of simulations #1 and #2

when the concentration of fine particle starts growing in the deposit composition. This phenomenon occurs because the particles with high settling velocity sediments faster while the fine particles remain suspended for more time. As a consequence of that, the coarse particles should reduce in the composition of deposit along the time (Lucchese 2018). At the end of the simulation time, the concentration of both particles approaches to the initial concentration in the lock, what could be reached if simulations were carried out for a very long time. Furthermore, the deposit composition of the two simulations is very similar for most of the time, which means that the double mass diffusivity does not impact the deposit composition, at least for the parameters used.

7.3.4 Energy Budget of the Flow

Figure 8 shows the evolution of energy budget flow, for simulations #1 and #2, normalized by the total energy at the beginning of the simulation, observing conservation of the total energy. At the beginning of the simulations, the potential energy is maximum and after the gate is released, it suffers a drop while the kinetic energy has a fast increase, reaching its peak around $t \approx 3$. The kinetic energy after $t \approx 3$ decreases even with the potential energy decreasing. This happens because the two mechanisms of dissipation, the associated to convection E_d and to drag around the particles E_{s_t}, grow in importance along with the time evolution. The kinetic energies at $t = 100$ for simulations #1 and #2, respectively, are 8.28% and 8.42%, and the values for potential energy are 12.64% and 14.09%, respectively.

Comparing the two mechanisms of dissipation we notice that E_d has more impact in the energy loss. For simulations #1 and #2, the values of E_d are, respectively, 43.59% and 41.60%, while for E_{s_t} are 35.35% and 35.76%. It seems that the double diffusivity (simulation #2) delays the conversion from potential to kinetic energy, since the respective curves only intercept at $t \approx 45$, in contrast to the unique difussitivity case where it occurs at $t \approx 25$.

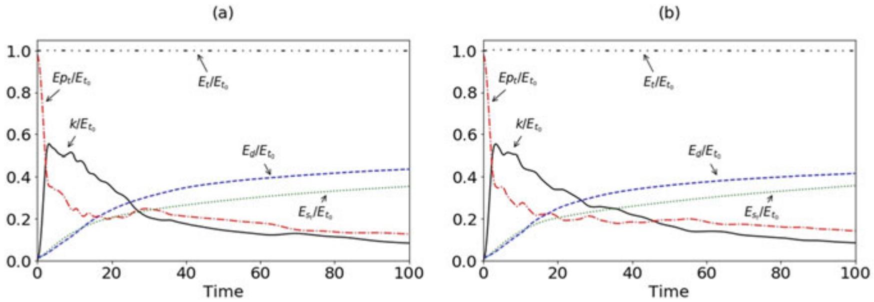

Fig. 8 Temporal evolution of the energy for simulations **a** #1 and **b** #2. All curves are normalized with total initial energy (E_{t_0})

7.4 Conclusion

We performed *DNS* of bi-disperse particle-laden gravity currents on a lock-exchange configuration with different values of Schmidt number for each particle fraction, to investigate the impact of double mass diffusivity on flow and deposit dynamics for a fixed Re number. Two simulations are considered in this study, the first one (#1) with a unique Schmidt number for the two particle fractions, $Sc = 1$, while the second (#2) possess the values $Sc = 3$ and $Sc = 1$ for coarse and fine particle fractions, respectively. We compared our results with physical and numerical experiments available in the literature, obtaining a fairly good agreement.

At the beginning of the simulation, the front position increases at a constant rate, with no effect of double mass diffusivity. At $t \approx 18$, when the streamwise movement is slowing down, a difference between the two simulations is identified, in which the flow with unique Schmidt number remains ahead when comparing with the other simulation. The time evolution of the front velocities for the two simulations is similar until $t \approx 18$, and after this time the current front velocity of simulation #1 is greater than the simulation #2 for most of the simulation time.

In terms of suspended material, the double mass diffusivity case shows lower fine particles suspended during the flow evolution. This impacts directly the flow movement because the fine particles are the most responsible for supporting the current motion. The final deposit agreed with the reference. The deposits have changed the configuration and position of the peaks for double mass diffusivity case. However, it seems that there is no perceptible effect of double diffusivity mass in the deposit composition. Finally, for the energy budget, it seems that in the double diffusive case the conversion from potential to kinetic energy is delayed, since the respective curves only intercept at $t \approx 45$, in contrast to the unique difussitivity case in which it occurs at $t \approx 25$.

Acknowledgements We would like to thank Petrobras S. A. for his financial support to this research through the program SINAPSE, co-operation term N ° 5900.0110995.19.9. We are to grateful to the CAPES—Coordenação de Aperfeiçoamento de Pessoal de Nível Superior—for his support through the program, PROSUP—Programa de Suporte à Pós-Graduação de Instituições de Ensino Particulares. Also, we are grateful to the Pontifical Catholic University of Rio Grande do Sul, PUCRS. Graduate Program in Materials Engineering and Technology—PGETEMA.

References

Cantero MI, Lee JR, Balanchandar S, Garcia MH (2007) On the front velocity of gravity currents. J Fluid Mech 586:1–39

Espath LFR, Pinto LC, Laizet S, Silvestrini JH (2014) Two- and three-dimensional direct numerical simulation of particle-laden gravity currents. Comput Geosci 63:9–16

Farenzena BA (2020) Simulação numérica de correntes de densidade hiperpicnais sob referencial móvel. Ph.D. thesis, Pontifícia Universidade Católica do Rio grande do Sul, Porto Alegre

Francisco EP, Espath LFR, Silvestrini JH (2017) Direct numerical simulation of bi-disperse particle-laden gravity currents in the channel configuration. Appl Math Model 49:739–752

Gladstone C, Phillips JC, Sparks RSJ (1998) Experiments on bidisperse, constant-volume gravity currents: propagation and sediment deposition. Sedimentology 45:833–843

Huppert HE, Simpson JE (1980) The slumping of gravity currents. J Fluid Mech 99:785–799

Kubo Y (2004) Experimental and numerical study of topographic effects on deposition from two-dimensional, particledriven density currents. Sed Geol 164:311–326

Laizet S, Lamballais E (2009) High-order compact schemes for incompressible flows: a simple and efficient method with quasi-spectral accuracy. J Comput Phys 228:5989–6015

Laizet S, Li N (2011) Incompact3d: a powerful tool to tackle turbulence problems with up to o (105) computational cores. Int J Numer Methods Fluids 67:1735–1757

Lucchese LV (2018) Estudo numérico da sedimentação em correntes de turbidez com evolução do relevo de fundo. Master's thesis, Universidade Federal do Rio Grande do Sul, Porto Alegre

Manica R (2009) Geração de Correntes de Turbidez de Alta Densidade: Condicionantes Hidráulicos e Deposicionais. Ph.D. thesis, Universidade Federal do Rio Grande do Sul

Meiburg E, Kneller B (2010) Turbidity currents and their deposits. Annu Rev Fluid Mech 42:135–156

Nasr-Azadani MM, Meiburg E, Kneller B (2016) Mixing dynamics of turbidity currents interacting with complex seafloor topography. Environ Fluid Mech

Necker F, Härtel C, Kleiser L, Meiburg E (2005) Mixing and dissipation in particle-driven gravity currents. J Fluid Mech 545:339–372. https://doi.org/10.1017/S0022112005006932. ISSN 00221120

Simpson JE (1972) Effects of the lower boundary on the head of a gravity current. Annu Rev Fluid Mech 53:759–768

Simpson JE (1982) Gravity currents in the laboratory, atmosphere, and ocean. Annu Rev Fluid Mech 14:213–234

Winters KB, Lombard PN, Riley JJ, D'Asaro EA (1995) Available potential energy and mixing in density stratified fluids. J Fluid Mech 189:115–128

Chapter 8
Turbulent Kinetic Energy Analysis in 2D Lid-Driven Cavity Flow at Re = 100,000

Maicon Vinicius Ritter Deggeroni, Juan Pablo de Lima Costa Salazar, Diogo Nardelli Siebert, and Luiz Adolfo Hegele Júnior

Abstract Simulation results based on the lattice Boltzmann method are shown for the turbulent lid-driven two-dimensional cavity flow at Reynold number 100,000. We use a boundary condition scheme that significantly improves stability for simulation of turbulent flows within the lattice Boltzmann method framework using a regularized form. Velocity profiles as well as explicit expressions for the turbulent kinetic energy budget are presented.

Keywords Budget of turbulent kinetic energy · Lattice Boltzmann method · Lid-driven cavity

8.1 Introduction

Turbulence is ubiquitous in nature and in industrial processes, and for many years has attracted interest as a fundamental problem for physics as well as mathematics and engineering (Chen et al. 2003; Landau and Lifshitz 1987). In many situations of practical interest, there is statistical non-homogeneity and anisotropy in the flow field, where highly nontrivial interactions between bulk flow and boundary layers emerge (Hegele Jr. et al. 2018). Computational fluid dynamics (CFD) in its current

---

M. V. R. Deggeroni
Programa de Pós-Graduação em Engenharia Mecânica, Santa Catarina State University, Joinville, Brazil

J. P. de Lima Costa Salazar (✉) · D. N. Siebert
Aerospace Engineering, Federal University of Santa Catarina, Joinville, Brazil
e-mail: juan.salazar@ufsc.br

D. N. Siebert
e-mail: diogo.siebert@ufsc.br

L. A. Hegele Júnior
Department of Petroleum Engineering, Santa Catarina State University, Balneário Camboriú, Brazil
e-mail: luiz.hegele@udesc.br

H. F. Meier et al. (eds.), *Advances in Turbulence*, ABCM Series on Mechanical Sciences and Engineering, https://doi.org/10.1007/978-3-031-25990-6_8

developmental stage offers a wide array of elaborate mathematical tools and numerical methods capable of solving the Reynolds-averaged or filtered Navier–Stokes equations in domains discretized with meshes of high geometrical complexity, over a large span of flow regimes, from low (subsonic) to high (hypersonic) Mach numbers. However, fundamental studies of turbulence rely on the full resolution of all the spatial and temporal scales present in the turbulent flow field. This is achieved through direct numerical simulation (DNS). The lid-driven cavity flow is a simple geometry commonly used to the study of multiple boundary layer interaction with the turbulent bulk flow. The flow is driven by a solid wall moving tangentially to a square hole, sealing off the cavity. Here we restrict our attention to the two-dimensional problem, which features fundamental differences with respect to three-dimensional turbulence, owing to the lack of the vortex-stretching term in the vorticity equation. We have used as numerical method the lattice Boltzmann method (LBM), a simulation technique based on a discretized form of the Boltzmann equation. The implementation of the LBM is shown to be equivalent to the macroscopic conservation equations—mass and momentum—besides having simple and efficient implementations. Hegele Jr. et al. (2018), on which this work is based on, introduce a novel implementation of boundary conditions in the regularized lattice Boltzmann method (LBM) and also show that, at increasing Reynolds number, complex flow dynamics emerge in the flow.

One of the fundamental quantities of interest is the budget of the turbulent kinetic energy (TKE). Despite the great interest in these equations, it is our goal to introduce and present as it is regarding the application for the two-dimensional lid-driven cavity flow.

The paper is divided as follows: Section 2 presents the lattice Boltzmann method, the boundary conditions, and the turbulent kinetic energy balance equation. The results are presented and discussed in Sect. 3. Section 4 concludes the paper.

8.2 Methodology

8.2.1 The Lattice Boltzmann Method

The lattice Boltzmann method solves the particle distribution function, $f_i\ (r, t)$, according to Eq. (1):

$$f_i(\mathbf{r}+\mathbf{c}_i, t+1) = f_i^{(eq)}(\mathbf{r}, t) + (1-\tau^{-1})\widehat{f}_i^{(neq)}(\mathbf{r}, t), \tag{1}$$

where $\mathbf{c}_i$ is related to microscopid velocity; $\mathbf{r}$ is position; and t is the time, in arbitrary units. There are velocity sets that are used to solve Navier–Stokes (N-S) equations, denoted by D d Q q, where d is the number of spatial dimensions and q is the number of microscopic velocities. Here we use the D3Q19 implementation (Krüger et al. 2017). The notation $f_i^{(eq)}$ is used for the equilibrium particle distribution, which is an expasion of the Maxwellian distribution function, $\widehat{f}_i^{(neq)}$ is the regularized non-equilibrium particle distribution, and τ is the relaxation time related to the viscosiy. The equilibrium depends on the local quantities density, ρ, and fluid velocity.

In order to regularize the particle distribution function, we use (Latt and Chopard 2006; Montessori et al. 2014)

$$\left\{\rho, \rho u_\alpha, \rho m_{\alpha\beta}^{(2)}\right\} = \sum_i f_i \left\{1, c_{i\alpha}, c_{i\alpha i\beta} - \delta_{\alpha\beta}/a_s^2\right\} = \sum_i \widehat{f}_i \left\{1, c_{i\alpha}, c_{i\alpha i\beta} - \delta_{\alpha\beta}/a_s^2\right\}, \tag{2}$$

Equation (2) gives the moments of the particle distribution function of zeroth order, ρ, first order, ρu_α, and second order, $\rho m_{\alpha\beta}^{(2)}$; $\delta_{\alpha\beta}$ is the Kronecker delta; and a_s is the scaling factor equal to $\sqrt{3}$.

The equilibrium particle distribution function $f^{(eq)}$ is expressed considering the second-order velocity expansion in the Hermite polynomials (Philippi et al. 2006; Shan et al. 2006):

$$f_i^{(eq)}(\mathbf{r}, t) = \rho w_i \left(1 + a_s^2 u_\alpha c_{i\alpha} + \frac{1}{2} a_s^4 u_\alpha u_\beta \mathcal{H}_{\alpha\beta,i}^{(2)}\right), \tag{3}$$

where w_i are the quadrature weights, which depend on the absolute value of the direction $\mathbf{c}_i$. The second-order moments are projected onto the velocity space, as we can see in Eq. (4):

$$\widehat{f}_i^{(neq)}(\mathbf{r}, t) = \frac{1}{2} \rho w_i a_s^4 \left[m_{\alpha\beta}^{(2)} - u_\alpha u_\beta\right] \mathcal{H}_{\alpha\beta,i}^{(2)}. \tag{4}$$

Finally, the regularization procedure is completed as given in Eq. (5) (Mattila et al. 2017; Coreixas et al. 2017):

$$\widehat{f_i}(\mathbf{r}, t) = f_i^{(eq)}(\mathbf{r}, t) + \widehat{f_i}^{(neq)}(\mathbf{r}, t). \tag{5}$$

The regularization procedure of LBM does not necessarily address boundary conditions (Hegele Jr. et al. 2018). Thus, from regularization procedure of particles distribution function, boundary conditions may be found turning possible the definition and characterization of the desired flow modeling (Latt et al. 2008; Malaspinas et al. 2011). With the sum of still unknown regularized particles at the boundary nodes, it is achievable to obtain the second-order particle momentum from Eq. (6), which is also expressed with regularized particles distribution function, as shown in Eq. (7).

$$\sum_{i \in I_s} f_i \mathcal{H}_{\alpha\beta,i}^{(2)} + \sum_{i \notin I_s} \widehat{f_i} \mathcal{H}_{\alpha\beta,i}^{(2)} = \rho m_{\alpha\beta}^{(2)}, \tag{6}$$

which is also expressed with regularized particles distribution function,

$$\sum_{i \in I_s} \widehat{f}_i \mathcal{H}^{(2)}_{\alpha\beta,i} + \sum_{i \notin I_s} \widehat{f}_i \mathcal{H}^{(2)}_{\alpha\beta,i} = \rho m^{(2)}_{\alpha\beta}. \tag{7}$$

In short, through second-order particle momentum decomposition to regularized particles distribution function (considering belonging and not belonging particles distribution to an incoming velocity set I_s) combined to Eq. (6), equivalence is established between the sum of f_i function (regularized and not-regularized), according to Eq. (8), leading to a set of six equations when using D3Q19 distribution.

$$\sum_{i \in I_s} f_i \mathcal{H}^{(2)}_{\alpha\beta,i} = \sum_{i \in I_s} \widehat{f}_i \mathcal{H}^{(2)}_{\alpha\beta,i}. \tag{8}$$

In a nutshell, LBM consists of collision and streaming. The collision is a local non-linear operator. After that, the resulting distribution of post-collision is linearly streamed to neighboring nodes (Krüger et al. 2017).

When considering Dirichlet boundaries, the velocity $\mathbf{u}$ is known, then, having mass conservation during the process of particles collision, the boundaries of each node can be found by

$$\sum_{i \in I_s} f_i(\mathbf{r}, t) = \sum_{i \in O_s} f_i(\mathbf{r} + \mathbf{c}_i, t+1) = (1 - \tau^{-1}) \sum_{i \in O_s} \widehat{f}_i(\mathbf{r}, t) + \tau^{-1} \sum_{i \in O_s} f_i^{(eq)}(\mathbf{r}, t). \tag{9}$$

8.2.2 Turbulent Kinetic Energy Budget

The following treatment will consider the three-dimensional form of the evolution equation for the sake of generality. The evolution of turbulent kinetic energy (TKE) is given by Pope (2000)

$$\partial_t k + U_\alpha \partial_\alpha k + \partial_\alpha T'_\alpha = \mathcal{P} - \epsilon, \tag{10}$$

where $k \equiv \frac{1}{2}\langle u'_\alpha u'_\alpha \rangle$ is the turbulent kinetic energy, $u'_\alpha \equiv u_\alpha - U_\alpha$ is the fluctuating velocity and $U_\alpha \equiv \langle u_\alpha \rangle$, T'_α is the turbulent transport term, and $\mathcal{P}$ and ϵ are production and dissipation of turbulence, respectively. We will apply to Eq. 10 the operator $\langle \cdot \rangle$, which is defined as

$$\langle \phi \rangle (x, y, z) \equiv \frac{1}{\delta_t} \int_{t_i}^{t_i + \delta_t} \phi(x, y, z, t) dt. \tag{11}$$

In this work, we are interested in the statistically stationary state, plus the incompressibility condition $\partial_\alpha u_\alpha = 0$. Under the statistically stationary state, the ensemble average of a property ϕ can be approximated as a time average over a interval of duration δ_t. Applying the above average definition to Eq. 10,

$$\partial_\alpha \langle U_\alpha k \rangle + \partial_\alpha \langle T'_\alpha \rangle = \langle \mathcal{P} \rangle - \langle \epsilon \rangle. \tag{12}$$

Since we are only interested in the statistical stationary state, the term $\partial_t k$ is null.

The statistical stationary average for the turbulent transport $\langle T'_\alpha \rangle$ is explicitly given by

$$\langle T'_\alpha \rangle = \frac{1}{2} \langle u'_\alpha u'_\beta u'_\beta \rangle + \langle u'_\alpha \frac{p^{'}}{\rho} \rangle - 2\nu \langle u'_\beta s_{\alpha\beta} \rangle, \tag{13}$$

and the production $\mathcal{P}$ is given by

$$\langle \mathcal{P} \rangle = \langle u'_\alpha u'_\beta \rangle \partial_\beta U_\alpha. \tag{14}$$

For the dissipation, $\langle \epsilon \rangle$, the explicit expression is given by

$$\langle \epsilon \rangle = 2\nu s_{\alpha\beta} s_{\alpha\beta}, \tag{15}$$

where $s_{\alpha\beta} = \frac{1}{2}\left(\partial_\alpha u'_\beta + \partial_\beta u'_\alpha \right)$ is the fluctuating rate of strain tensor and $p' = p - \langle p \rangle$ is the fluctuating (modified) pressure.

In the following equations, we write out all of the TKE terms explicitly; this will help the understanding of the energy budget.

8.2.2.1 Temporal and Convective Terms

The TKE can be written as

$$k \equiv \frac{1}{2} \langle u'_\alpha u'_\alpha \rangle = \frac{1}{2} \langle (u_\alpha - U_\alpha)(u_\alpha - U_\alpha) \rangle = \frac{1}{2} (\langle u_\alpha u_\alpha \rangle - 2\langle u_\alpha U_\alpha \rangle + \langle U_\alpha U_\alpha \rangle). \tag{16}$$

Since $\langle u_\alpha u_\alpha \rangle = \langle u^2 \rangle$, $\langle u_\alpha U_\alpha \rangle = \langle u_\alpha \rangle U_\alpha = U_\alpha U_\alpha$, and $\langle U_\alpha U_\alpha \rangle = U^2$, then Eq. (16) is written as

$$k = \frac{1}{2}\big(\langle u^2 \rangle - U^2 \big). \tag{17}$$

The term $\partial_\alpha \langle U_\alpha k \rangle$ is explicitly written as

$$\partial_\alpha \langle U_\alpha k \rangle = \partial_\alpha (U_\alpha \langle k \rangle) = \frac{\partial (U_x \langle k \rangle)}{\partial x} + \frac{\partial \big(U_y \langle k \rangle\big)}{\partial y} + \frac{\partial (U_z \langle k \rangle)}{\partial z}. \tag{18}$$

8.2.2.2 Turbulent Transport Term

For the turbulent transport term, $\langle T'_\alpha \rangle$ term, let us separate it in three terms, as

$$A_\alpha = \frac{1}{2} \langle u'_\alpha u'_\beta u'_\beta \rangle, \tag{19}$$

$$B_\alpha = \langle \frac{u'_\alpha p'}{\rho} \rangle, \tag{20}$$

and

$$C_\alpha = -2\nu \langle u'_\beta s_{\alpha\beta} \rangle, \tag{21}$$

where $\langle T'_\alpha \rangle = A_\alpha + B_\alpha + C_\alpha$.

Taking the term A_α, it is possible to express mathematically as

$$A_\alpha = \frac{1}{2} \langle (u_\alpha - U_\alpha)(u_\beta - U_\beta)(u_\beta - U_\beta) \rangle, \tag{22}$$

then

$$A_\alpha = \frac{1}{2} \langle u_\alpha u_\beta u_\beta + u_\alpha U_\beta U_\beta - 2 u_\alpha u_\beta U_\beta - u_\beta u_\beta U_\alpha - U_\alpha U_\beta U_\beta + 2 u_\beta U_\alpha U_\beta \rangle. \tag{23}$$

Using mathematical manipulations in an analogous way we have assumed before, the above equation is simplified as

$$A_\alpha = \frac{1}{2} \big(\langle u_\alpha u^2 \rangle - 2 \langle u_\alpha u_\beta \rangle U_\beta - U_\alpha \langle u^2 \rangle + 2 U_\alpha U^2 \big). \tag{24}$$

Considering now term B, it can be expressed as

$$B_\alpha = \langle \frac{(u_\alpha - U_\alpha)(p - \langle p \rangle)}{\rho} \rangle. \tag{25}$$

Since in the incompressible limit in the LBM the density is constant and $\rho = 1$, we have, after simplifications

$$B_\alpha = \langle u_\alpha p \rangle - U_\alpha \langle p \rangle. \tag{26}$$

Finally, for term C, we have

$$C_\alpha = -\nu \langle (u_\beta - U_\beta)\big(\partial_\alpha u'_\beta + \partial_\beta u'_\alpha\big)\rangle. \tag{27}$$

Then, applying the average operator to each term:

$$\begin{aligned} C_\alpha = -\nu\big(&\langle u_\beta \partial_\alpha u_\beta\rangle - \langle u_\beta \partial_\alpha U_\beta\rangle - \langle U_\beta \partial_\alpha u_\beta\rangle + \langle U_\beta \partial_\alpha U_\beta\rangle \\ &+\langle u_\beta \partial_\beta u_\alpha\rangle - \langle u_\beta \partial_\beta U_\alpha\rangle - \langle U_\beta \partial_\beta u_\alpha\rangle + \langle U_\beta \partial_\beta U_\alpha\rangle\big). \end{aligned} \tag{28}$$

If we use, in Eq. (28), the following identities:

$$\langle u_\beta \partial_\alpha u_\beta\rangle = \frac{1}{2}\partial_\alpha \langle u^2\rangle, \tag{29}$$

$$\langle u_\beta \partial_\alpha U_\beta\rangle = \langle U_\beta \partial_\alpha u_\beta\rangle = \langle U_\beta \partial_\alpha U_\beta\rangle = \frac{1}{2}\partial_\alpha U^2, \tag{30}$$

$$\langle u_\beta \partial_\beta u_\alpha\rangle = \partial_\beta \langle u_\beta u_\alpha\rangle, \tag{31}$$

$$\langle u_\beta \partial_\beta U_\alpha\rangle = \langle U_\beta \partial_\beta u_\alpha\rangle = \langle U_\beta \partial_\beta U_\alpha\rangle = U_\beta \partial_\beta U_\alpha, \tag{32}$$

then

$$C_\alpha = -\nu\left(\frac{1}{2}\partial_\alpha \langle u^2\rangle - \frac{1}{2}\partial_\alpha U^2 + \partial_\beta \langle u_\beta u_\alpha\rangle - U_\beta \partial_\beta U_\alpha\right). \tag{33}$$

8.2.3 *Production of Turbulence Term*

For the production term of turbulence, this is expressed as

$$\langle \mathcal{P}\rangle = \langle (u_\alpha - U_\alpha)(u_\beta - U_\beta)\rangle \partial_\beta U_\alpha, \tag{34}$$

then

$$\langle \mathcal{P}\rangle = (\langle u_\alpha u_\beta\rangle - U_\alpha U_\beta)\partial_\beta U_\alpha. \tag{35}$$

8.2.3.1 Dissipation of Turbulent Kinetic Energy Term

To express the dissipation term, Eq. (15) reads

$$\langle\epsilon\rangle = 2\nu\langle\frac{1}{2}\big[\partial_\alpha(u_\beta - U_\beta) + \partial_\beta(u_\alpha - U_\alpha)\big]\frac{1}{2}\big[\partial_\alpha(u_\beta - U_\beta) + \partial_\beta(u_\alpha - U_\alpha)\big]\rangle. \tag{36}$$

But the quantity $s_{\alpha\beta} = \frac{1}{2}\Big(\partial_\alpha u'_\beta + \partial_\beta u'_\alpha\Big)$ can be expressed as

$$s_{\alpha\beta} = S_{\alpha\beta} - \langle S_{\alpha\beta}\rangle, \tag{37}$$

where $S_{\alpha\beta} = \frac{1}{2}\big(\partial_\alpha u_\beta + \partial_\beta u_\alpha\big)$. In the lattice Boltzmann framework, this relevant quantity can be locally computed from the second-order tensor $m^{(2)}_{\alpha\beta}$ as

$$S_{\alpha\beta} = -\frac{a_s^2}{2\tau}\Big(u_\alpha u_\beta - m^{(2)}_{\alpha\beta}\Big). \tag{38}$$

Then, the dissipation can be written as

$$\epsilon = 2\nu\big(\langle S_{\alpha\beta}S_{\alpha\beta}\rangle - \langle S_{\alpha\beta}\rangle\langle S_{\alpha\beta}\rangle\big). \tag{39}$$

8.3 Results

Following Hegele Jr. et al. (2018), we set a constant tangential velocity equal to $\mathbf{u} = (u_L, 0, 0)$ applied at the top of the cubic cavity and on the other five faces of the cavity we set the velocity to zero. The spatial discretization is given by $N_x = N_z = 2049$ and $N_y = 1$. This allows for the implementation of a two-dimensional flow within the more general framework of a three-dimensional code. For the lid velocity, we consider $u_L = 0.1c_s$, where $c_s = 1/\sqrt{3}$ is the sound speed in the fluid, avoiding compressibility effects by keeping the Mach number low. The relaxation time is tuned to set the Reynolds number through the viscosity $\nu = (\tau - 1/2)/a_s^2$. The pressure p is given by$p = c_s^2\rho$. The flow Reynolds number is 100,000.

When the Reynolds number is low (laminar) the flow in the cavity remains steady. But as the Reynolds number increases, going through transition, the normal velocity traces (u along z and w along x) show that the center of the vortex created by the fluid moves toward the cavity center. which can be seen in Fig. 1. We note that there is already, even with 5×10^6 time steps, considerable turbulence in the cavity, owing to the high Reynolds number.

The average kinetic energy, $\frac{1}{2}u^2$, taken over the whole cavity, is steadily increasing as shown in Fig. 2. No sign of a statistically stationary state is seen for five million time steps. The evolution of the turbulent kinetic energy will depend on the relative magnitude of the terms in Eq. (16). Since there is no term associated with vortex-stretching in 2D turbulence, vorticity can only be generated along the solid boundaries, diffusing toward the bulk flow. A snapshot of the velocity field is shown

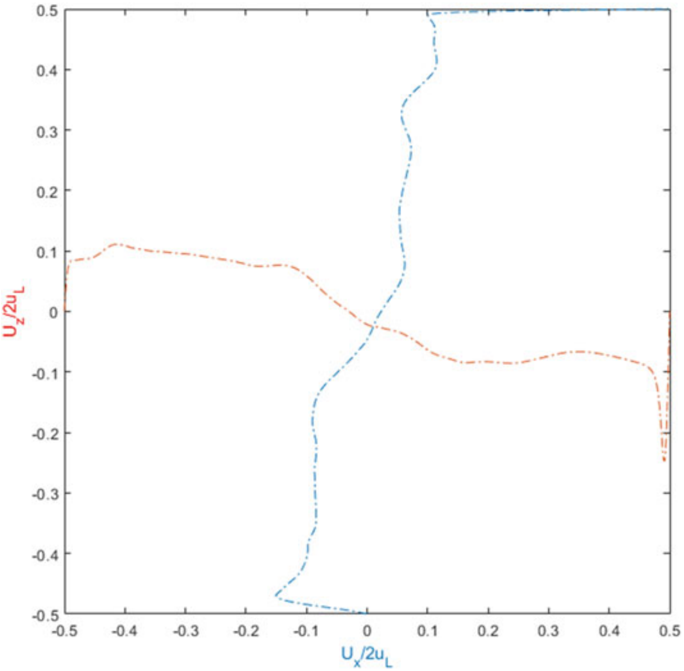

Fig. 1 Normal velocity traces along the centerlines of the x and z

in Fig. 3 after 5×10^6 time steps. The irregular pattern of many vortices in the cavity indicates the complex nature of turbulent flow.

8.4 Conclusions

We note that the LBM boundary condition implementation adopted in this simulation with $Re = 100,000$ is effectively stable, considering a large mesh resolution. In spite of the simulation having not reached a statistically stationary state, we estimate it will be achieved with an additional 10×10^6 simulation time steps.

For future works, after the statistically stationary state is reached, the evaluation of the budget of the TKE would be feasible, in order to check the consistency of the results, and also the analysis of other quantities, like enstrophy and palinstrophy.

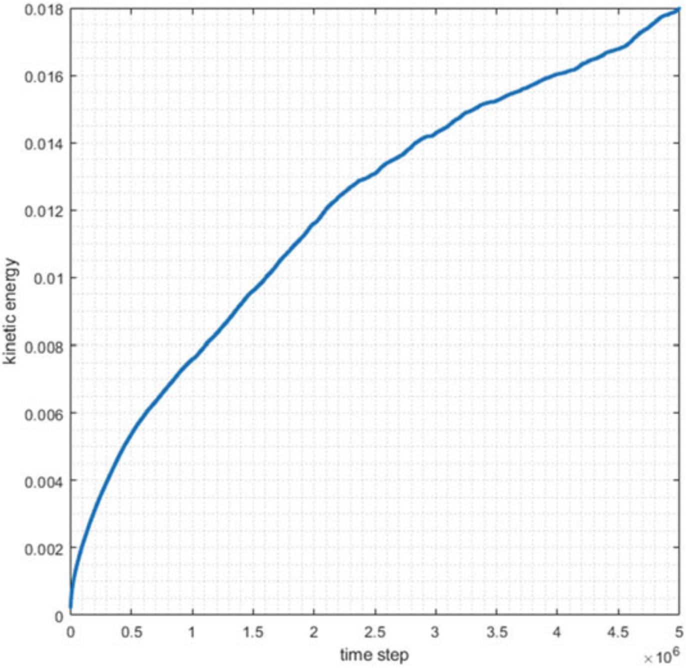

Fig. 2 Kinetic energy at 5 × 10^6 time steps

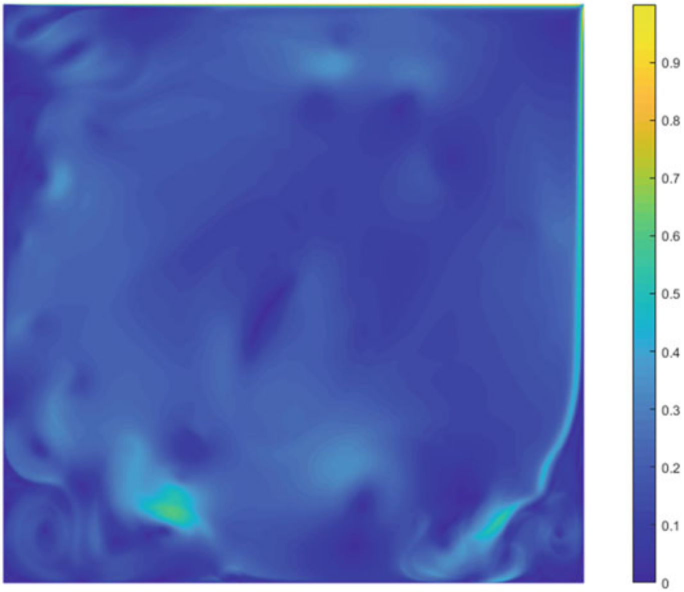

Fig. 3 Magnitude of the velocity field of the infinite span lid-driven cavity at 5 × 10^6 time steps

Acknowledgements The authors would like to acknowledge PROGRAMA UNIEDU/FUMDES PÓS-GRADUAÇÃO, for the financial support for this study.

References

Chen H, Kandasamy S, Orszag S, Shock R, Succi S, Yakhot V (2003) Extended boltzmann kinetic equation for turbulent flows. Science 301:633–636. https://doi.org/10.1126/science.1085048

Coreixas C, Wissocq G, Puigt G, Boussuge JF, Sagaut P (2017) Recursive regularization step for high-order lattice Boltzmann methods. Phys Rev E 96(9):033306. https://doi.org/10.1103/PhysRevE.96.033306

Hegele LA Jr, Scagliarini A, Mattila KK, Philippi PC, Puleri DF, Gounley J, Randles A (2018) High-Reynolds-number turbulent cavity flow using the lattice Boltzmann method. Phys Rev E 98(4):043302. https://doi.org/10.1103/PhysRevE.98.043302

Krüger T, Kusumaatmaja H, Kuzmin A, Shardt O, Silva G, Viggen EM (2017) The Lattice Boltzmann method: principles and practice. Springer, Berlin. ISBN 978-3-319-44647-9. https://doi.org/10.1007/978-3-319-44649-3_1

Landau LD, Lifshitz EM (1987) Fluid mechanics: Landau and Lifshitz: course of theoretical physics, Vol 6, 2nd edn. Butterworth-Heinemann, London. ISBN 978-0-750-62767-2

Latt J, Chopard B (2006) Lattice Boltzmann method with regularized pre-collision distribution functions. Math Comput Simul 72(2–6):165–168. https://doi.org/10.1016/j.matcom.2006.05.017

Latt J, Chopard B, Malaspinas O, Deville M, Michler A (2008) Straight velocity boundaries in the lattice Boltzmann method. Phys Rev E 77(5):056703. https://doi.org/10.1103/PhysRevE.77.056703

Malaspinas O, Chopard B, Latt J (2011) General regularized boudary condition for multi-speed lattice Boltzmann models. Comput Fluids 49(1):29–35. https://doi.org/10.1016/j.compfluid.2011.04.010

Mattila KK, Philippi PC, Hegele LA Jr (2017) High-order regularization in lattice-Boltzmann equations. Phys Fluids 29(4):046103. https://doi.org/10.1063/1.4981227

Montessori A, Falcucci G, Prestininzi P, La Rocca M, Succi S (2014) Regularized lattice Bhatnagar-Gross-Krook model for two-and three-dimensional cavity flow simulations. Phys Rev E 89(5):053317. https://doi.org/10.1103/PhysRevE.89.053317

Philippi PC, Hegele LA Jr, Dos Santos LOE, Surmas R (2006) From the continuous to the lattice Boltzmann equation: The discretization problem and termal models. Phys Rev E 73(5):056702. https://doi.org/10.1103/PhysRevE.73.056702

Pope SB (2000) Turbulent flows. Cambridge University Press, Cambridge. ISBN 978-0-521-59886-6. https://doi.org/10.1017/CBO9780511840531

Shan X, Yuan XF, Chen H (2006) Kinetic theory representation of hydrodynamics: a way beyond the Navier-Stokes equation. J Fluid Mech 550:413–441. https://doi.org/10.1017/s0022112005008153

Part II

Aerodynamics

Chapter 9
Investigation of Transient Regime in Laminar Separation Bubble Formation

Pedro Bruno Pereira Panisset, Omar Elias Horna Pinedo, and Igor Braga de Paula

Abstract The transient flow regime related with the formation of laminar separation bubbles (LSB) is examined by time-resolved measurements of the velocity field. The investigated scenario aims at studying the flow in multiple stage turbines, where the wake of airfoils in previous compression stages induces periodic variation of turbulence level in the subsequent airfoils. This can lead to periodic removal and formation of LSB. This process is simulated here by exciting controlled disturbances with a vibrating ribbon. Experiments are carried out in a laminar water channel at PUC-Rio. Longitudinal PIV measurements are performed on a flat plate subjected to an adverse pressure gradient. The pressure gradient is set by false walls with adjustable geometry. Suction is applied on the false wall, in order to avoid the boundary layer separation at this surface. Bubble topology and disturbance growth along the streamwise direction are measured during the transient of bubble formation. Results show spatial amplification over a narrow frequency bandwidth. Dominant non-dimensional frequencies ($St = f\delta^*_s/U$) at late stages of bubble formation are in close agreement with those reported in literature. During the transient the intensity of reverse flow is significantly changed, pointing out for possible changes on the stability mechanisms involved on the bubble reattachment.

Keywords Laminar separation bubble · Boundary layer transition · Hydrodynamic stability

9.1 Introduction

The performance of autonomous aircrafts and turbines, operating at low chord-based Reynold numbers (from 10^4 to 10^6), can be highly affected by the presence of laminar separation bubbles (LSB). The laminar separation bubble appears in this context as a combination of long extend of laminar flow over the airfoil surface and adverse pressure gradient. In this scenario, the transition to turbulent flow can occur in the

---

P. B. Pereira Panisset · O. E. Horna Pinedo · I. B. de Paula (✉)
Department of Mechanical Engineering, Pontifical Catholic University of Rio de Janeiro,
Rua Marques de São Vicente 225, Gavea, RJ 22451-041, Brazil
e-mail: igordepaula@puc-rio.br

H. F. Meier et al. (eds.), *Advances in Turbulence*, ABCM Series on Mechanical Sciences and Engineering, https://doi.org/10.1007/978-3-031-25990-6_9

separated boundary layer which further can cause a flow reattachment to the surface. This closed region formed between the separation point and the reattachment is known as LSB and its topology was detailed in the work of Tani (1964).

First works in the field showed that the presence of LSB creates a plateau on the pressure coefficient distribution in airfoils (Tani 1964, Mayle 1991; Gaster 1969). According to Tani (1964), the bubble can be classified as short bubble and long bubble. Short bubbles are more frequently observed near the suction peak of airfoils operating at low and moderate Reynolds numbers (Mayle 1991) and often do not have a strong influence on the airfoil performance. On the other hand, long bubbles can extend for a significant portion of the chord length and hence affect significantly drag and reduce lift. According to Gaster (1969), this type of bubble is very sensitive to flow conditions. Several parameters can affect the phenomenon including Reynolds number, freestream disturbances (turbulence and acoustic disturbance field), pressure gradient, surface roughness, and temperature gradient, among others (Akpolat et al. 2012). According to Swift (2009) and Yarusevych and Kotsonis (2017), combination of these effects can also influence the bubble dynamics. An important aspect related to LSBs is the occurrence at given flow conditions of the so-called "bubble bursting" events, characterized by a rapid switch between short and long bubble (Serna and Lázaro 2015a, b). This "bursting" can significantly affect the performance of airfoils and change its dynamics. Unfortunately, the phenomenon is not well predicted by current models (Serna and Lázaro 2015a, b). For a proper modeling of this problem, it is important to describe the physics underlying the bubble dynamics. Although several advances have been observed during last decades in the description of regimes of quasi-steady bubbles, very little is known about the bubbles in transient regimes (Yarusevych and Kotsonis 2017). Detailed characterization of bubbles in transient regimes can help to elucidate the dynamics of the bubble formation and the bubble "bursting".

The goal of current work is to shed further light on the description of the phenomenon by studying experimentally the formation of an LSB. To this end, controlled disturbances were introduced in the boundary layer by means of a vibrating ribbon. The disturbance source was located upstream of the separation region. Initially, the fluctuation amplitude was high enough to remove the bubble. The transient regime related with bubble formation was obtained by a sudden reduction in the level of fluctuations. Experiments were performed on a flat plate subjected to an adverse pressure gradient. Measurements were carried out in a low turbulence and close return water channel at PUC-Rio. The amplitude and frequency of disturbances were controlled by a magnetic actuator. Phase-locked planar and time-resolved PIV measurements were used for extraction of ensemble averaged velocity fields in the LSB region. The manuscript reports validate the apparatus and methods adopted by a comparison against benchmarks available in the literature. Thereafter, measurements performed during the transient regime are presented and discussed.

9.2 Experimental Methodology

The experimental campaign was carried out in a low turbulence level and close return water tunnel. With the aid of a frequency inverter ranging 0.1–20 Hz, an axial motor pump allows to achieve streamwise velocities within a range of 0.05–0.5 m/s. The tunnel is equipped with one honeycomb and four meshes to reduce turbulence in the test section. The contraction rate of the tunnel is 4:1 which is a typical value for quiet water tunnel facilities. It is interesting to mention that low turbulence wind tunnels have usually a much higher contraction rate of about 9:1. The measured turbulence level in the test section is estimated in about 0.25% within a bandwidth of 0.1 to 50 Hz, for velocities up to 0.15 m/s.

A flat plate 3000 mm long was inserted in the test section at 600 mm downstream from the test section inlet. The plate is made of transparent polycarbonate. The plate is equipped with a flap for adjustment of the stagnation point on the leading edge. Above the flat plate a false wall was built in order to create a variable pressure gradient on the plate. In the present configuration, the false wall created a convergent, divergent channel over the plate. The angle of divergent wall could be adjusted in order to provide a prescribed constant adverse pressure gradient. The throat height at the vertex of convergent–divergent channel was fixed in 200 mm. On the divergent part suction slots were machined on the false wall in order to avoid separation. Centrifugal pumps Sarlo2000 were used for boundary layer suction. The water was pumped to the tunnel corner downstream from the test section.

Controlled disturbances were created using a vibrating ribbon made of steel. The oscillation of the ribbon was provided by an electrical magnet with a controlled current. The magnet was placed in a sealed case that was flush mounted with the flat plate surface.

Time-resolved velocity fields were measured using a planar PIV system. High sampling frequency was achieved using a double cavity laser LITRON LDY-300, which provides 30 mJ/pulse at 2 kHz, and a Phantom Miro 341, which has a maximum resolution of 1600 × 2560 pixels and can run at frequencies up to 800 frames per second at the maximum resolution. Illumination and imaging systems were synchronized by a TSI 610036 synchronizer. For present measurements, the sampling frequency was set to 200 Hz. A set of spherical and cylindrical lens was used to create the illumination plan for PIV measurements. Polyamide particle tracers with diameters of about 20 μm and density of 1.03 kg/m^3 were used for flow seeding. Routines developed in LabView and MATLAB allowed to control the image acquisition and the PIV processing, respectively.

9.3 Results

The results obtained in this work are divided into two parts. First, the results regarding the quasi-steady bubble regime with the disturbance generator in the flow are presented. The results obtained in this regime are used for validation of measurement set-up and post-processing strategies. For this validation, the results of the separation bubble were compared with some results reported in the literature. After validation, results related with transient regime are reported. In this last regime, the actuator is used to introduce disturbances with high amplitude in the boundary layer, which removes completely the bubble. The disturbance source is then switched off and the transient regime until the bubble shows a quasi-steady behavior is captured.

9.3.1 Quasi-Steady Regime

One of the important parameters for laminar separation bubbles is the level of adverse pressure gradient. The pressure distribution of this work was estimated with the velocity fields measured with the PIV without the presence of the bubble. To this end, a trip was used to force the laminar-turbulent transition of the boundary layer upstream of the separation and remove the bubble. Thus, the free flow velocity fields were measured by moving the camera and the laser beam along the flat plate. The results are shown in Fig. 1 as a function of the pressure coefficient, assuming that the reference pressure is the static pressure at the last measurement station and that the flow is two dimensional. In the same figure, the vertical lines $L_p/\delta^*_s = 40$ e $L_p/\delta^*_s = 103$ indicate, respectively, the start and end positions of the measurement field ($x/\delta^*_s = 0$ and $x/\delta^*_s = 63$ in the speed contours, Fig. 4. The figure clearly shows the change in the pressure distribution on the plate, caused by the separation. In this case, the distribution presents a pressure plateau, typical of laminar separation bubbles, followed by a recovery. According to the work of Pinedo (2018), in the range where we have the bubble, the pressure gradient is approximately linear.

According to Dovgal et al. (1994), the velocity profile of the boundary layer at the separation point can be fitted by a modified hyperbolic tangent function. In Fig. 2, we have the velocity profile and its derivative very close to the separation location (lines $L_p/\delta^*_s \sim 55$). It is possible to observe that the obtained data are well represented by the function proposed by Dovgal et al. (1994). This function is

$$U(y) = \frac{\tanh(a(y-d)) + \tanh(ad)}{1 + \tanh(ad)} + b\sqrt{3}\eta \exp\left(-1.5\eta^2 + 0.5\right)$$

where $\eta = y/d$, b is a measure of the magnitude of the reverse flow, d is the dimensionless height of the inflection point, and a is treated like a free parameter. In this work, the height of the inflection point was used to scale y and d; consequently, the dimensionless height of the inflection was fixed at $d = 1$. In addition to the velocity

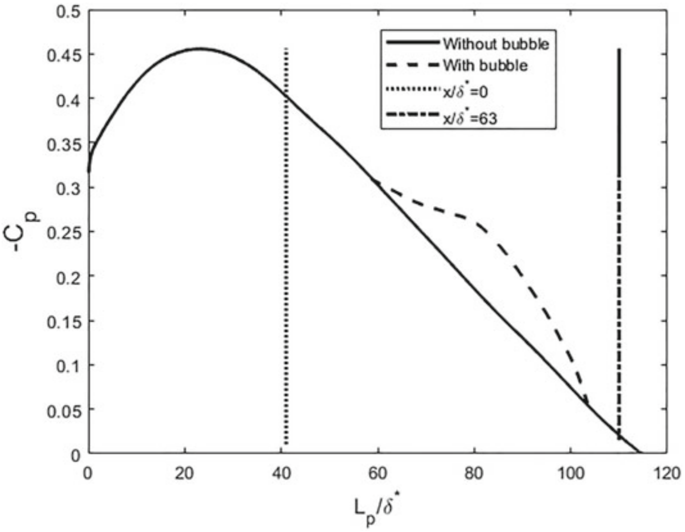

Fig. 1 Pressure distribution with and without the presence of the laminar separation bubble

Fig. 2 Velocity profile u(y) and shear stress τ(y) at the separation point. Blue circle: experimental data; solid line: modified Dovgal function

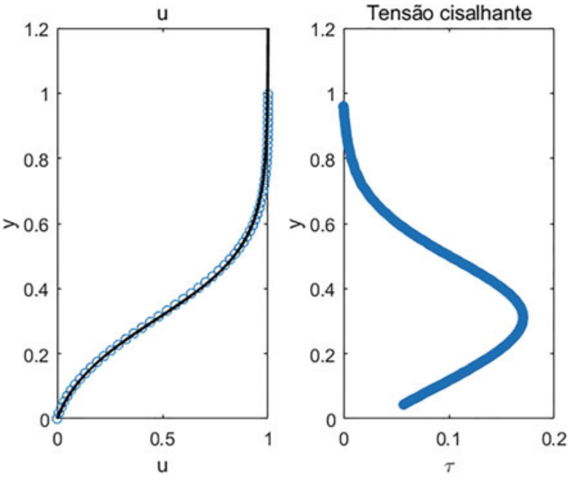

profile, the integral parameters of the boundary layer are important to describe the flow characteristics. These parameters are often reported in the literature and can be useful for validation of current results. In Fig. 3, we have the results of the distribution of δ^*, θ, and H measured experimentally. It can be observed that the evolution of the displacement thickness and, consequently, the form factor vary significantly along the flow, in the presence of the separation bubble. The increase in the displacement thickness and the form factor up to the maximum bubble height, as well as the maintenance of θ, follows the works reported in the literature (Hatman and Wang 1998; Hain et al. 2009).

In the present work, δ^*_s value was 0.0046 and θ_s was 0.0012. Since the study by Tani (1964), Re number values based on the displacement thickness and the momentum thickness at the point of separation ($Re_{\delta *s} = u0s\ \delta^*_s/\nu$, $Re_{\theta s} = u0s\ \theta s/\nu$, respectively) have been used as an indicator of the occurrence of the bursting process. In separation bubbles, the bursting process corresponds to its burst and abrupt growth. The respective $Re_{\delta *s}$ and $Re_{\theta s}$ values found based on the results obtained with the PIV were 1159 and 302. These values are consistent with the results found in the literature, $350 < Re_{\delta *s} < 1305$ and $150 < Re_{\theta s} < 450$ according to Mayle (1991), Michelis et al. (2017), Serna and Lázaro (2015b).

Figure 4 presents the result for the average velocity field U obtained under constant channel velocity conditions. The average velocity field was calculated by averaging

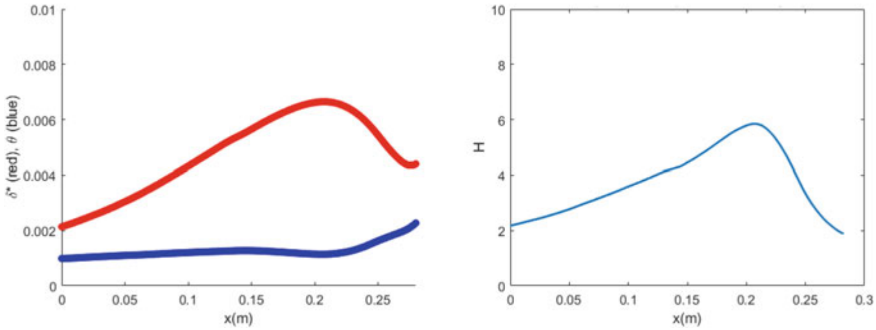

Fig. 3 Boundary layer integral parameters. Left: δ* (red), θ (blue); Right: shape factor H

Fig. 4 Contour of mean streamwise velocity field U. Dash-dotted line: δ*, dashed line: inflection points, solid line: stream line ψ = 0, dotted line: U = 0

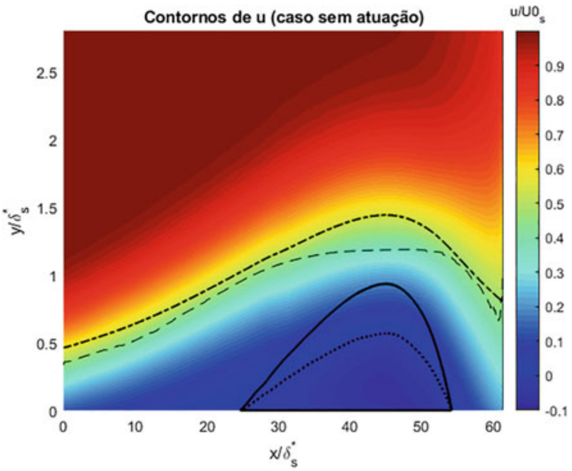

6737 instant fields. From this graph, it is possible to identify some characteristic dimensions of the bubble. For this, the streamline ($\psi = 0$) that divides the flow between the inner and outer regions of the bubble is used. It is worth mentioning that the zero velocity line maintains the same points of separation and reattachment of the streamline $\psi = 0$. Based on the results of the streamline, the total bubble length was approximately L = 140 mm ($L/\delta^*_s = 29$) and the maximum height was h = 4.3 mm ($h/\delta^*_s = 0.94$). Figure 5 show some u velocity profiles along the bubble. It is noticed as a profile close to the laminar profile in positions upstream of the separation. At the separation point, the velocity profile resembles the modified tanh (y)-type profile. Inside the bubble, we can observe the presence of reverse flow and the beginning of the formation of turbulent flow. Didactically, it is possible to separate the bubble length into two regions. The first goes from the separation point to the local of maximum bubble height. This region is called laminar L_I because the flow is still in the initial stages of transition. The second region, in turn, comprises the part that goes from the point of maximum height of the bubble to the reattachment (L_{II}), and is called turbulent due to the fact that the flow has already undergone the transition or is in the final stages of the transition. According to the data, from the experiments, the L_I region has 94 mm ($L_I/\delta^*_s = 20.4$), while the L_{II} region has 42 mm ($L_I/\delta^*_s = 8.6$). The relation between (L_I/L_{II}) obtained for the bubble was 2.24, this value is within the range (1.6–3) reported in the work of Marxen and Henningson (2011). Still on the topological characterization of the bubble, there is the divergence angle (α), another parameter that helps describe the phenomenon. This angle is obtained through the trigonometric relationship between the height (h) of the bubble and the length L_I. Thus, it has to be $\alpha = \tan^{-1}(h/L_I)$. In the present work, the value obtained was $\alpha = 0.046$ rad. Finally, the maximum reverse velocity was 6.2% of u0. This value is below the threshold for absolute instability proposed in the work of Rodríguez et al. (2013).

Fig. 5 Streamwise velocity profiles along the bubble. Just a few profiles are shown to illustrate the streamwise velocity profiles with the measurement region

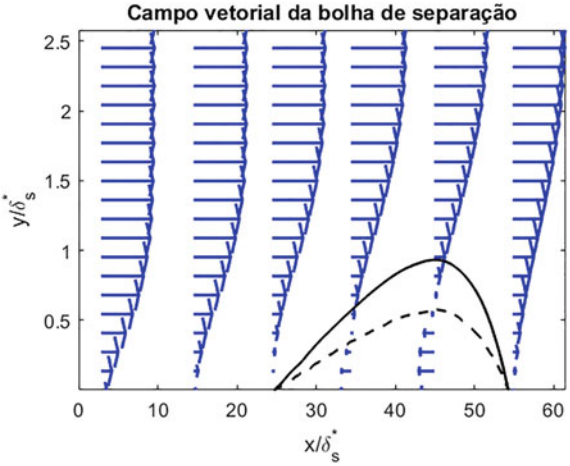

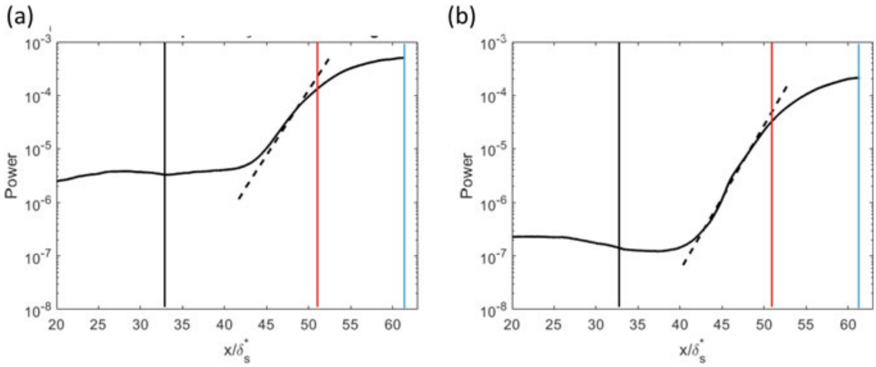

Fig. 6 Growth of the maximum velocity fluctuation (**a**) u' and (**b**) v'. Solid thick line: experimental data; dashed line: St-5/3; Vertical lines: separation (black), maximum height (red), and reattachment (blue) points

Figure 6a presents the results related to the velocity fluctuations u' distribution. In Fig. 6b, the velocity fluctuations v' are shown. The data in Fig. 6 was obtained along the inflection line in Fig. 4. Unlike the velocity fluctuations u', the fluctuations of v become relevant only close to the bubble maximum height location ($x/\delta^*_s \sim 45$). Only at the final stages, near the reattachment location, the two components reach values of the same order of magnitude. The growth of these velocity fluctuations corroborate, qualitatively, the results found in several works, for example, in Lengani et al. (2017). According to the figure, disturbances display a nearly exponential amplification (linear in log scale) in a narrow region from $40 < x/\delta^*_s < 50$. Further downstream the disturbances exhibit a saturation and quickly the flow becomes turbulent. In the growth of u', it is more difficult to visualize exponential behavior because, in this direction, there are small variations in the channel speed that make the signal noisy. Therefore, the analysis of flow fluctuations will focus on the v' component.

Figure 7 shows the contours of the spectral content of the disturbance v' along the flow direction (x). To this end, a Welch's periodogram was applied with a block of 512 points and a 50% overlap between blocks of the time series. The time series for each position (x) was collected at a height (y) corresponding to the inflection line of the base flow velocity profile. According to the figures, the highest energy of fluctuations is concentrated within the bubble reattachment region, where the flow is at final stages of the transition. Within this region the velocity fluctuations show variations of Strouhal number in the interval $0.01 < St < 0.05$. It is interesting to note that a similar range of Strouhal numbers was previously reported in the work of Michelis et al. (2017). In that work, the fluctuations were related with vortex ejection in the reattachment region.

Finally, Fig. 8 presents the power spectrum of v'. A traced line corresponding to Kolmogorov's energy cascade law is also included in the graph as a reference. The velocity fluctuations were obtained at a streamwise location (x) corresponding to the maximum bubble height (x/δ^*_s approx. 45). The spectrum shows higher energy in

Fig. 7 Contours of power spectrum of the velocity fluctuation v’ measured at the inflection points of base flow profiles

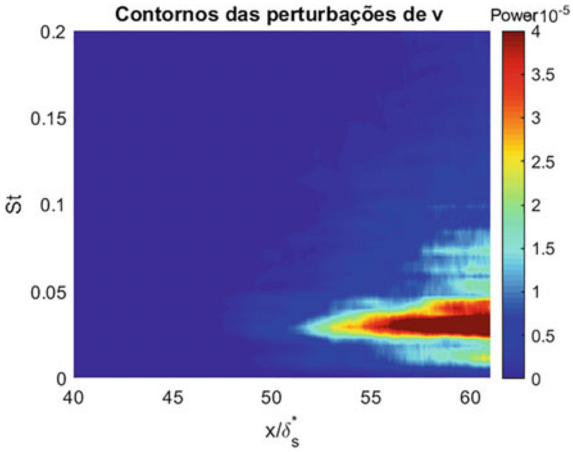

Strouhal numbers within the interval $0.01 < St < 0.05$. This is the range found in Fig. 7 for stations near and after the reattachment. This suggests a strong relation between most amplified disturbances near the bubble maximum height and those downstream of the reattachment. Indeed, this was previously reported in the work of Michelis et al. (2017), and it is related with generation of vortex in the reattachment region. It is also interesting to note that near the maximum bubble height the high frequencies in the spectrum do already exhibit some adherence with the Kolmogorov cascade ($f^{-5/3}$), even though the flow is not yet turbulent.

Fig. 8 Energy cascade of the wall normal velocity fluctuation v’ measured at maximum bubble height

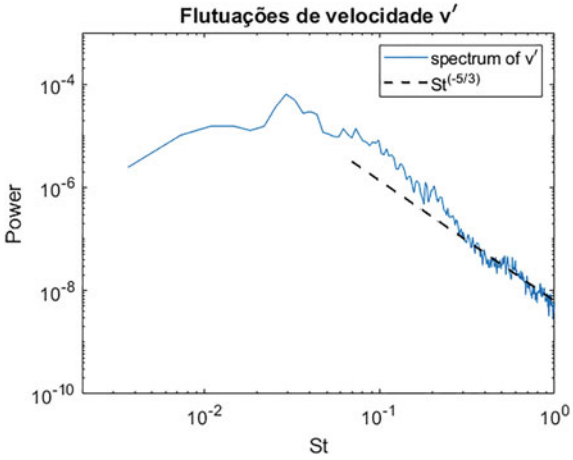

9.3.2 Transient Regime

The transient regime studied in current work covers the regime without boundary layer separation until the complete recovery of the separation bubble. To this end, the disturbance source was activated and suddenly switched OFF. During the period when the source was switched ON, the excitations were tonal with a frequency corresponding to those of most amplified disturbances observed in the quasi-steady regime ($St = 0.05$). The disturbance amplitude was set by adjusting the voltage source to the lowest possible voltage capable of removing the bubble. The bubble elimination was detected visually. After 15 s of actuation and the complete disappearance of the bubble, the system was suddenly turned OFF. A few seconds after the actuator was turned off, the bubble started to grow. This process of recovering the quasi-steady state of the bubble was repeated 30 times, and the results presented in this section represent the average of these 30 acquisitions. A time diagram representing the operation of the equipment during this transient period is illustrated in Fig. 9. The results shown in this section refer to that transient period until the bubble recovers.

Figure 10 shows the mean streamwise velocity fields, obtained with an average of 30 instants of time, for the initial (10a) and final (10b) instants of the transient regime. At first the flow does not present separation boundary layer and therefore there is no reverse flow. It is observed that after the transient, the bubble resembles the one found for the quasi-steady regime (see Fig. 4). The parameters related to the topology of the bubble that were obtained after its recovery are: $L = 140$ mm (L_I/δ^*_s

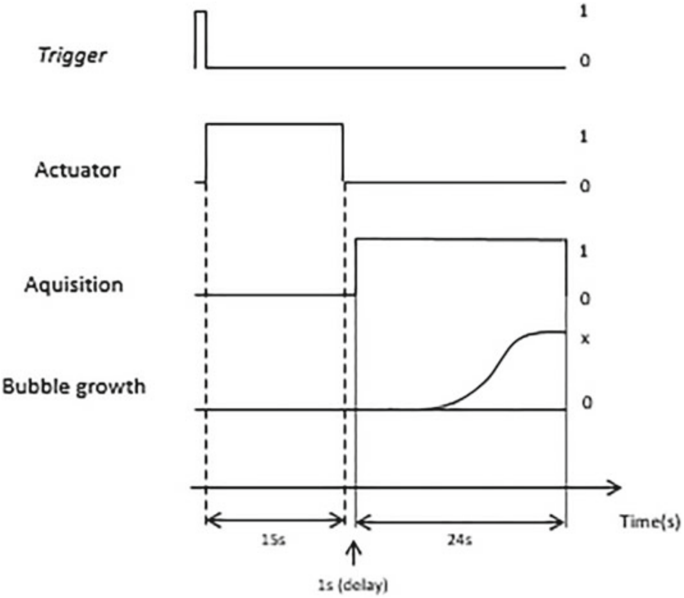

Fig. 9 Time diagram of the transient process data acquisition

= 30.4), h = 4.2 mm (h/δ^*_s = 0.91), L_I = 98 mm (L_I/δ^*_s = 21.3), L_{II} = 42 mm (L_{II} / δ^*_s = 9.1), = 0.043, L_I / L_{II} = 2.33, Re_{δ^*s} = 1333, $Re_{\theta s}$ = 310, and maximum reverse speed was 6.7%. Comparing these results with the case without disturbance actuation, it can be observed that such parameters are, in fact, similar and suggest full bubble recovery. Table 1 shows the summary comparative results between the transient case and the case without disturbing.

Velocity fluctuations were analyzed after its apparent recovery. The idea is to observe whether there is any apparent hysteresis in the bubble shortly after the transient. Figure 11a, b shows the amplification of streamwise and wall normal disturbances, respectively. Fluctuations exhibit a strong amplification close to maximum bubble height. This data was captured at y-position equal to the height of the inflection line. It is possible to identify an exponential growth of these disturbances at stations between 42 < x/δ^*_s < 50. The amplification of the disturbances measured without any forcing is in qualitative agreement with those measured after the bubble recovery in the transient regime. For a fair comparison, one should consider that these experiments have to be carried out in different days due to the long time required for

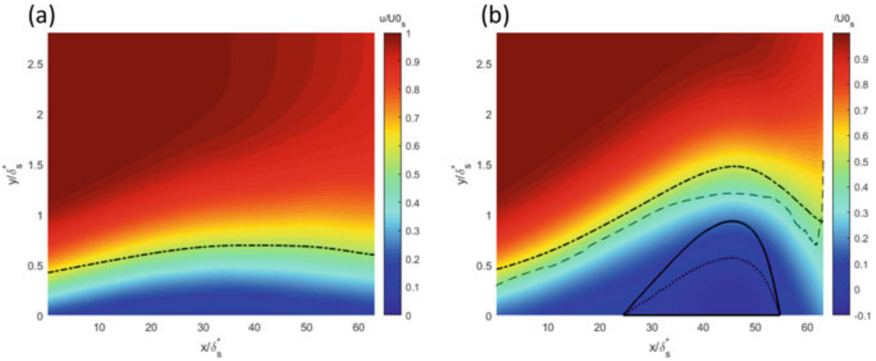

Fig. 10 Contours of mean streamwise velocity field at the beginning (**a**) and ending (**b**) of the transient process. Dash-dotted line: δ*, dashed line: inflection point, solid line: stream line $\psi = 0$, dotted line: U = 0

Table 1 Summary comparison of some parameter at the end of the transient and the quasi-steady state of the LSB

Parameters	End of transient	Quasi-steady state
L(mm)	140	136
h(mm)	4.2	4.3
L_I/L_{II}	2.33	2.24
α(rad)	0.043	0.046
$L_I/theta_s$	82	80
$Re_{\theta s}$	310	302
$Re_{\delta * s}$	1333	1159
$St_{\theta s}$	0.01–0.05	0.01–0.05

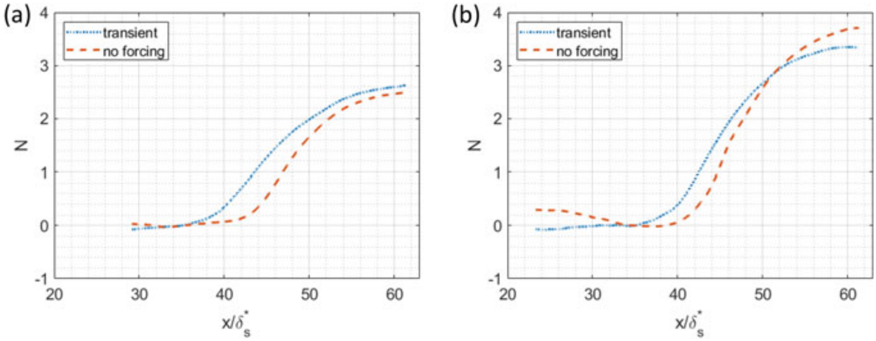

Fig. 11 N-factor of the maximum velocity fluctuations growth (**a**) u' and (**b**) v'. Blue dotted line: final instant of transient regime, light brown line: quasi-steady state

each campaign with 30 ensembles. Results suggest that the averaged bubble parameters were in close agreement. However, the growth of disturbances in the transient regime seems to be amplified slightly upstream in comparison to the case without excitation of disturbances. This might be related with residual disturbances near the wall which can remain in the flow for a long time. However, this conjecture demands further investigations.

The evolution of some bubble parameters during the transient period was also analyzed. The analysis includes bubble contour, shape factor H, separation angle (α), and separation and reattachment points. Figure 12a depicts bubble contours, corresponding to the streamline $\psi = 0$, during the transient. According to Michelis et al. (2017), at a certain instant during the transient, the bubble is extended beyond its quasi-steady length in quasi-steady regime. Here this was observed approximately at 12.8 s after the disturbance was switched off. Michelis et al. (2017) highlight some aspects of the phenomenon resemble those of bubble bursting process. It is interesting to note in Fig. 12a that despite the bubble parameters, such as length, height, and separation angle apparently undergo significant variations during the transient, the bubble shape appears to follow a regular pattern. In order to assess the general behavior of the phenomenon during this transient, the bubble dimensions are normalized by its instantaneous separation point (x_S), length (L), and the (h). Contours of normalized bubbles are illustrated in Fig. 12b. It is observed that in beginning of bubble formation the shape is different. However, after 3 s the overall bubble shape is not significantly affected during the transient, even though it exhibits significant changes on its parameters. Most remarkable differences are observed in the region of reattachment.

In Fig. 13a, the shape factor evolution is shown for different instants of time. The maximum in shape factor distributions present remarkable changes in the x-direction at the initial stages due to the fast bubble expansion. As the bubble approaches the quasi-steady topology, the shape factor tends to higher values. This is also in agreement with observations reported by Yarusevych and Kotsonis (2017). For a better comparison of the shape factors at the different instants, it was decided to subtract the

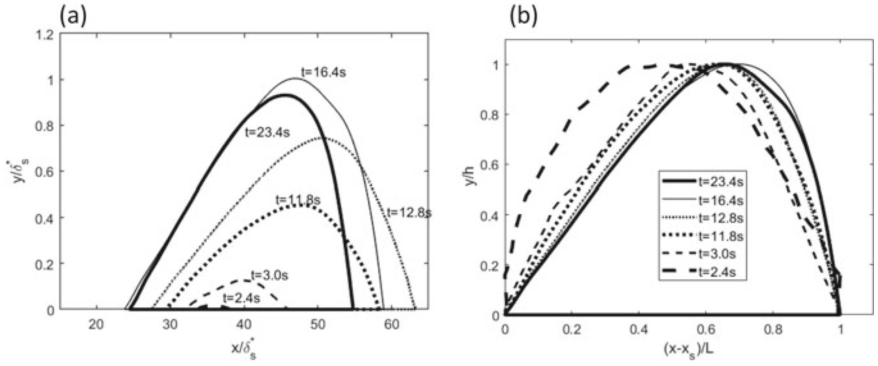

Fig. 12 Bubble streamline $\psi = 0$ for different time instants. **a** Non-normalized contour and **b** Normalized contour

position corresponding to the separation point x_s from the x-coordinates. Thus, the shape factor distributions of Fig. 13b are referenced to the separation point instead of a fixed reference. It is observed that the separation point in the transient regime occurs for a condition of H practically constant. This suggests that boundary layer separation is mostly dependent on local integral parameters. Therefore, separation criteria based on momentum thickness might be applicable also to transient regimes.

Figure 14 shows the transient locations of separation and reattachment points and also the position of maximum bubble heights. At the instant t = 2 s, there is the first identification of the boundary layer separation. From this time on, the bubble begins to grow until it stabilizes with characteristics similar to those of quasi-steady regime. At instants in the interval $2 < t < 5$ s, it is observed that the separation point moves continuously upstream, while x_h and x_r float around a single position. For times between 5 and 10 s, the bubble seems to assume a laminar length (L_I) very similar to the turbulent length (L_{II}). Near t = 11.8 s a sudden jump on the positions can be seen. This behavior can be linked to the ejection of a large vortex or to a discontinuity

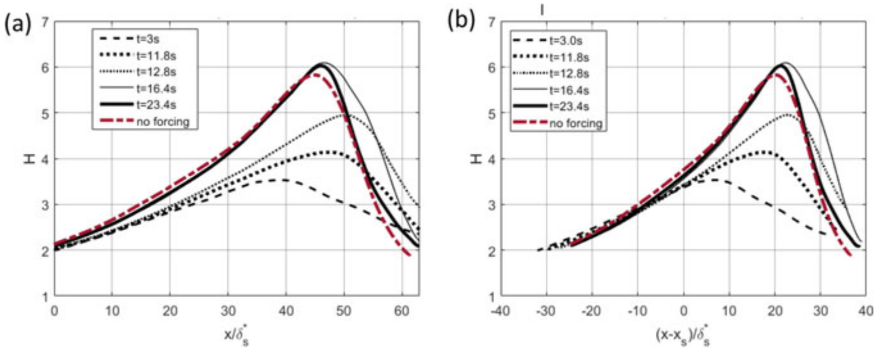

Fig. 13 Shape factor H at the transient regime. **a** Non-normalized H, **b** Normalized H

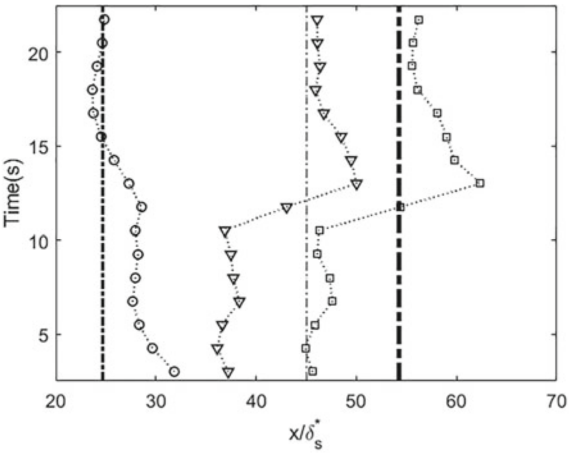

Fig. 14 Separation (circle), maximum height (triangle), and reattachment (square) points of the bubble at the transient process in the x-direction. Dashed-dotted line: separation, maximum height, and reattachment, respectively, at the quasi-steady state

in the sampling of the phenomenon due to the acquisition of two data series at two different moments. Due to the time needed for the bubble to recover, the acquisition of the transient regime had to be divided into two parts. In the first part, the instants $t_1 = 0$ to $t_{N/2} = 11.8$ s were measured; and in the second, the instants $t_{N/2+1} = 11.8$ s to $t_N = 24$ s. However, these measurements were made at a 1-day interval. Due to the high sensitivity of the bubble, some small change in the flow conditions in the channel may have occurred, causing a discontinuity of the data. Anyway, this does not refute the results presented so far, since their validation demonstrates that the recovered bubble has characteristics similar to the undisturbed case. Therefore, the variation may have caused some loss of information about the bubble evolution in the transient regime. However, it is still possible to identify the maximum bubble elongation near $t = 12.7$ s. From this moment, the three positions (x_s, x_h, x_r) move upstream again, this time showing a higher L_I/L_{II} ratio. At the end of the process ($t > 18$ s), the bubble stabilizes in the same positions of the case bubble without forcing.

The separation angle (α) evolution was evaluated in Fig. 15a. The average behavior seems to vary linearly until approximately $t = 16$ s. This parameter is less sensitive to changes in L_I and L_{II} lengths and maintains an approximately linear growth trend along the transient. Only when the bubble assumes the quasi-stationary topology does it stop growing. Regarding the behavior of the bubble height, we also observe a growth until close to $t = 16$ s (Fig. 15b). It is interesting to mention that the maximum bubble height is reached only after its maximum elongation. As well as α, h presented final values coinciding with those obtained for the bubble in the case without disturbance.

Information about the formation and ejection of the vortical structures was extracted by applying the λ_2 criterion. In Fig. 16, the formation of a vortex intensity in the region near the maximum bubble height can be seen, at time instants close to those of maximum bubble elongation. The vortex intensity grows as the bubble expands and does not seem to cause a noticeable bubble size reduction (Fig. 16a,

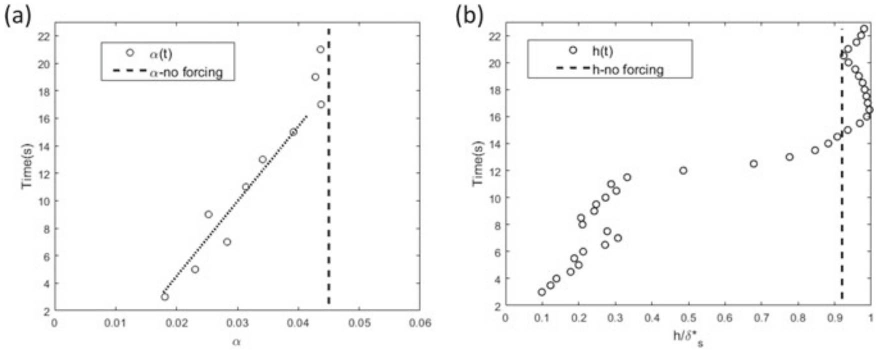

Fig. 15 **a** Separation angle and **b** bubble height evolution during the bubble growth. Circle: experimental data, dashed line: no forcing case

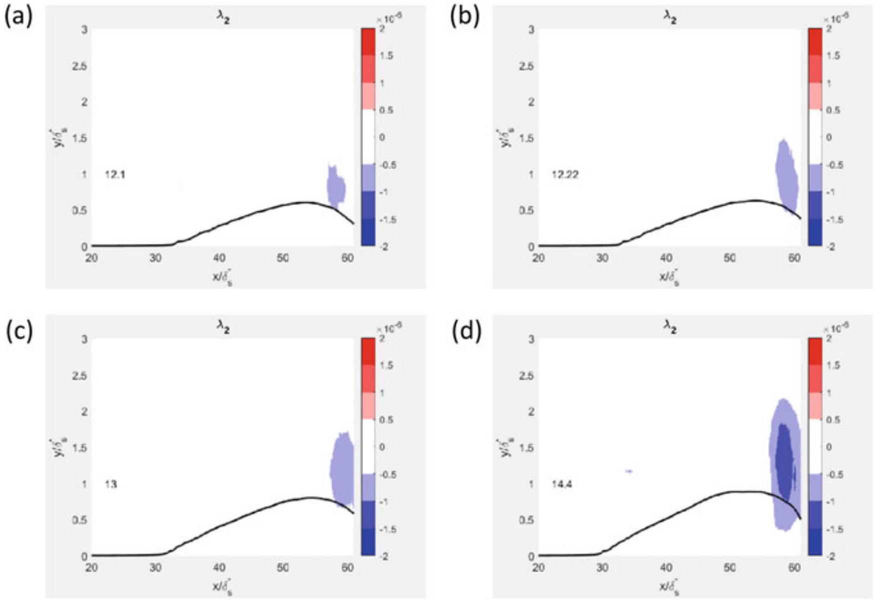

Fig. 16 λ2 contour for some instants at the transient regime during the maximum bubble expansion. Solid line: streamline $\psi = 0$

b, respectively). With the presence of the most elongated bubble the vortex slightly changes its core position and grows in intensity (Fig. 16c, d). The stronger vortex causes a greater mixture between the separated and the non-separated fluid. From this instant on the separation bubble starts to reduce its size. Besides acting on the bubble length, the presence of a large energy vortex excites the formation of a small vortex further upstream and a periodic vortex shedding starts. According to Fig. 17, the bubble shortening ceases around t = 18 s. In the quasi-stationary regime, a fusion

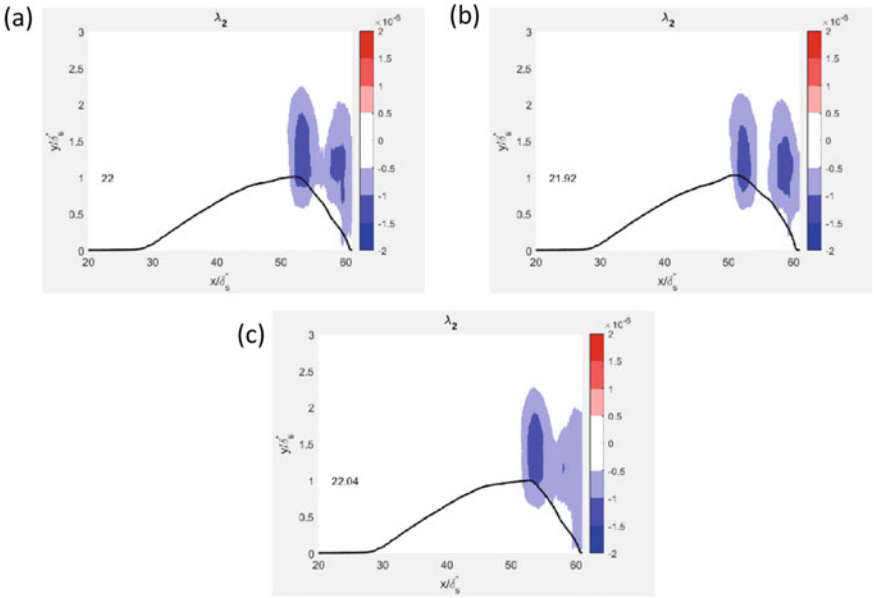

Fig. 17 λ2 for the final stages of the transient process. Solid line: streamline $\psi = 0$

between pair of vortices subsequently formed is also observed (Fig. 17a–c). These results suggest that this small change in the interaction between the bubble and the vortex ejection is capable of promoting significant changes in the phenomenon topology. This process may be associated with the phenomenon of bubble flapping or even bursting.

9.4 Conclusion

This work aimed at studying the behavior of a laminar separation bubble subjected to a sudden variation in the level of flow disturbances. Despite the practical relevance for turbines, wind generators, and UAVs, the problem was little addressed in the literature. The study was conducted in a low turbulence water channel. The pressure gradient required for the separation bubble formation was obtained with a convergent–divergent plate. Before the disturbance system installation, flow velocity fields were measured with the presence of a trip close to the leading edge of the flat plate and, consequently, without the presence of the bubble. The objective was to characterize the pressure gradient imposed on the flow with the convergent–divergent plate. At the second moment, without the presence of the trip, the separation bubble phenomenon was measured and validated by comparison with the results presented in the literature. A vibrating ribbon was used to introduce controlled disturbances in the flow and promotes the bubble elimination. After the bubble vanishes, the disturbance was turned off and the transient bubble recovery was measured using the PIV technique, with high temporal resolution. In this transient process, between the time when the flow is not separated and the moment when the bubble exhibits quasi-steady state, some topological parameters was analyzed, such as velocity contours; velocity profile at the separation point; separation point positions, reattachment, and maximum bubble height; separation angle; bubble height; and $Re_{\theta s}$.

According to the results, the momentum thickness Reynolds number and the shape factor at the separation point showed practically invariances in the transient regime. This differs from the results obtained for other parameters, such as the separation and reattachment points, the size and height of the bubble, and the separation angle. This behavior indicates that the boundary layer separation, in fact, is not much influenced by downstream flow dynamics. This result is interesting and unprecedented in the literature. Another interesting result was the analysis of the bubble topology during the transient. It was observed that there is little variation in the dimensionless form of the bubble. Significant differences in bubble shape were noted only in the instants very close to the beginning of the process. This suggests that in the case studied, the mechanism governing the shape of the separation bubble does not change significantly during the transient. Under the conditions of this study the bubble is close to the bursting, according to Gaster's criteria (1966). Indeed, in the undisturbed experiments, bubble reattachment oscillation was observed around a medium position. Under the transient regime, the bubble elongated to a greater length than that observed in the undisturbed case. Only after the ejection of the first high-intensity vortex the bubble reduced its size and moved to oscillate around the quasi-steady length. The association of the bubble length with vortex ejection had been reported in the work of Michelis et al. (2017). This behavior could be verified in detail due to the high temporal resolution in the measurement of the velocity fields.

After the transitional period, the bubble recovered completely the quasi-steady state. The recovery time was of the order of 20 s. This value is only an estimate, due to a discontinuity observed in the time series of the velocity fields. This discontinuity is probably associated with the data capture in two different moments. Although the problem has hindered the analysis of the temporal evolution of some bubble parameters, it does not compromise the observations and conclusions of the work. The results obtained contribute to characterize the complex dynamics of the transient regime of separation bubbles, providing new information about the phenomenon and supporting the development of tools for modeling the problem.

References

Akpolat T et al (2012) Low Reynolds number flows and transition. Low Reynolds Number Aerodynamics and Transition, Mustafa Serdar Genc, IntechOpen. https://doi.org/10.5772/31131

Diwan SS, Ramesh ON (2009) On the origin of the inflectional instability of a laminar separation bubble. J Fluid Mech 629:263–298

Dovgal A, Kozlov V, Michalke A (1994) Laminar boundary layer separation: instability and associated phenomena. Progr Aerosp Sci, Elsevier 30(1):61–94

Gaster M (1966) The structure and behavior of laminar separation bubbles. In: AGARD CP-4, pp 813–854

Gaster M (1969) The structure and behavior of laminar separation bubbles. Rep. Mem. No. 3595. Aeronautical Research Council

Hain R, Kahler C, Radespiel R (2009) Dynamics of laminar separation bubbles at low-reynolds-number aerofoils. J Fluid Mech, Cambridge University Press 630:129–153

Hatman A, Wang T (1998) Separated-flow transition. Part 2 – Experimental results. ASME Turbo Expo (98-GT- 462)

Lengani D et al (2017) Experimental investigation on the time–space evolution of a laminar separation bubble by proper orthogonal decomposition and dynamic mode decomposition. J Turbomach, Am Soc Mech Eng Digital Collect 139(3)

Mayle RE (1991) The role of laminar-turbulent transition in gas turbine. ASME J Turbomach 113:509–537

Marxen O, Henningson DS (2011) The effect of small-amplitude convective disturbances on the size and bursting of a laminar separation bubble. J Fluid Mech, Cambridge University Press 671:1–33

Michelis T, Yarusevych S, Kotsonis M (2017) Response of a laminar separation bubble to impulsive forcing. J Fluid Mech, Cambridge University Press 820:633–666

Pinedo OEO (2018) Projeto e Qualificação de um Aparato para o Estudo Experimental de Bolhas de Separação Laminar. Master Thesis, PUC-Rio

Rodríguez D, Gennaro EM, Juniper MP (2013) The two classes of primary modal instability in laminar separation bubbles. J Fluid Mech. Cambridge University Press 734

Serna J, Lázaro B (2015a) On the bursting condition for transitional separation bubbles. Aerosp Sci Technol, Elsevier 44:43–50

Serna J, Lázaro BJ (2015b) On the laminar region and initial stages of transition in transitional separation bubble. Eur J Mech B/Fluids 49:171–183

Swift K (2009) An experimental analysis of the laminar separation bubble at low Reynolds numbers. Master Thesis, University of Tennessee –Knoxville, Tennessee, EUA

Tani I (1964) Low speed flows involving separation bubbles. Prog Aeronaut Sci 5:70–103

Yarusevych S, Kotsonis M (2017) Steady and transient response of a laminar separation bubble to controlled disturbances. J Fluid Mech 813:955–990

Chapter 10
Simulation of Laminar-To-Turbulent Transitional Flow Over Airfoils

Luís Henrique da Silva Ignacio, Carlos Antonio Ribeiro Duarte, and Francisco José de Souza

Abstract In this work, the simulation of an airfoil with NACA 63-618 cross section was performed to obtain the curves of the lift and drag coefficients as a function of the angle of attack. The interest in this profile is its application in operational current turbines, such as SeaGen, which can harness the kinetic energy of the currents of rivers and seas. A two-dimensional model was used to simulate the airfoil with a chord of 0.23 m. The Reynolds number was $\mathrm{Re} = 5.3 \times 10^5$ and the angle of attack varied between $-5° < \alpha < 15°$. The values obtained were compared with experimental tests and other simulations. Several conventional RANS turbulence models have been applied, such as k-ε, optimized k-ε, SST and RSM, however none of them presented results that were in accordance with the literature. The Transition SST model showed better agreement with the experiments. It was demonstrated in the present study that the Transition SST model is fundamental in this specific case. This happens because there is a laminar-turbulent transition on the airfoil. Therefore, computational fluid dynamics (CFD) models accurately simulate provided appropriate numerical techniques are employed.

Keywords Airfoil · NACA 63-618 · Lift · Drag · Transition SST

L. H. da Silva Ignacio · F. J. de Souza (✉)
School of Mechanical Engineering, Federal University of Uberlândia, Av. João Naves de Ávila, 2121 Bloco 5P, Uberlândia, Minas Gerais, Brazil
e-mail: francisco.souza@ufu.br

L. H. da Silva Ignacio
e-mail: luis.henrique@ifgoiano.edu.br

C. A. Ribeiro Duarte
Department of Engineering, Federal University of Catalão, Av. Dr. Lamartine Pinto de Avelar, Catalão, Goiás 1120, Brazil
e-mail: carlosduarte@ufcat.edu.br

H. F. Meier et al. (eds.), *Advances in Turbulence*, ABCM Series on Mechanical Sciences and Engineering, https://doi.org/10.1007/978-3-031-25990-6_10

10.1 Introduction

More than 5000 years ago, in the Mediterranean region, has been documented that it was probably the first device that used the wind force: the sailing ships (Singer et al. 1954, 1956). Another mechanism that deserves mention is the windmill, which had its first mention around 400 B.C. and uses the kinetic energy of the wind to rotate a shaft in order to pump water or grind grains (Freese 1957).

However, these devices already captured the energy present in the winds, and the term wind turbine was not yet used. This nomenclature was only applied after the Scotsman James Blyth in 1887 built a device that extracted energy from the winds with the objective of generating electrical energy, storing it in accumulators, and using it to light lamps (Sørensen 2016). Blyth's wind turbine was improved with metallic materials in the structure and blades (Price 2005), whose better and bigger version was installed on the Montrose Lunatic Asylum (UoE 2018).

The 1930s in the United States, wind turbines produced by Jacobs Wind Electric Company were used to supply electricity to farms and to charge batteries. Later they fell into disuse because the energy generated by fuel has become economically more advantageous (Sørensen 2016).

Some decades ago, there was a new change in this concept (Luguang and Li 1997; Erdinc and Uzunoglu 2012). Many works aim to supply the need to find new sources of energy and to improve the efficiency of the existing ones, since the energy generation using only fossil fuels will not supply the global demand and its burning produces undesirable gases (greenhouse effect) (Ferreira et al. 2018; Jacobson et al. 2018). These characteristics of fossil fuels motivate studies to focus on clean and renewable energy sources. It is important to note that renewable energy is that generated from resources that are naturally replenished in a shorter period than the human life (Frewin 2020). Examples of renewable energy sources include sunlight, wind, biomass, and water currents (rivers, lakes, and ocean (Ng et al. 2013). As an example, it is estimated that the global tidal energy capacity is around 570 TWh/yr (Behrens et al. 2012). These sources can be exploited in different ways to extract their energy. Examples are the different wind turbine models, such as the horizontal axis wind turbines (HAWT) and vertical-axis wind turbines (VAWT).

The basic principle of wind turbines is the friction generated between the blades and air molecules that pass around them. Currently, the blades have aerodynamic profiles. Thus, when there is a flow, an aerodynamic force is generated that can be decomposed, in relation to the flow direction, in the parallel (drag) and perpendicular (lift) directions, as shown in Fig. 1.

Wind and current turbines are very similar because both convert the kinetic energy present in a fluid into electricity (Rahimian et al. 2017; Seng et al. 2009). Although they are quite similar and much of what has already been developed for a wind turbine can be applied to the current turbine, it is important and necessary to specifically study each type of turbine (Walker et al. 2014). It is essential to assess the performance of energy generation mechanisms for their development and improvement. In the case of these turbines, this assessment is usually modeled by means of

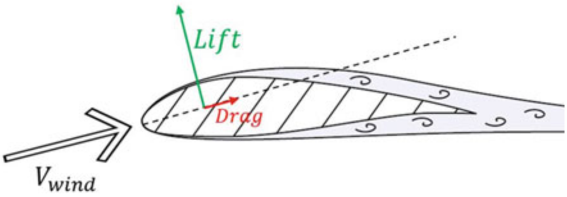

Fig. 1 Forces generated in an aerodynamic profile. (Branlard 2017)—adapted

computational fluid dynamics (CFD) or blade element momentum theory (BEM). CFD provides a greater level of detail of the interaction between the fluid (water, air) and the structure (turbine) which allows a more meticulous analysis, but involves a higher computational cost that has been mitigated with the computers progress (Rahimian et al. 2017; Noruzi et al. 2015; Hall 2012). On the other hand, BEM's main characteristic is that it is simpler to implement and use when compared to CFD (Sørensen 2016). This methodology is also suitable for wind and current turbines (Bedon et al. 2013; Baltazar and Campos 2011).

In any simulation, it is essential to reproduce what happens in practice. All details present in the CFD will only be valid if appropriate numerical techniques are applied. The same is valid for BEM, since one of the data required for the application of the technique is the curves of litf (C_L) and drag (C_D) coefficients as a function of the angle of attack (α). Such curves can be obtained experimentally or by CFD, and the simulation is generally the cheapest option. The choice of an appropriate turbulence model for the conditions to be simulated is essential to obtain good results.

In this study, some turbulence models have been selected to simulate of airfoil with NACA 63-618 cross section in order to determine the curves: $C_L \times \alpha$ and $C_D \times \alpha$. The results were compared with experimental data in the literature.

10.2 Methodology

The airfoil profile used in the simulations was a NACA 63-618, shown in Fig. 2. With this profile, the authors Walker et al. (2014) built and performed experimental tests on a turbine that is a 1:25 scale representation of the SeaGen turbine, justifying the role of this profile. The aerofoil coordinates were obtained from AirfoilTools (2020) and are presented in Fig. 3a. Figure 3b shows that for the leading and trailing edge regions more points were generated, as they are regions with more complex geometry and that could affect the mesh design and consequently the simulation results. The first point on the leading edge is placed at $x = 0$ and $y = 0$.

The two-dimensional mesh was generated in ICEM CFD 16.0. Its shape and all dimensions, which are based on the chord length (C) of the airfoil, are shown in Fig. 3a. It is worth noting that only the vertical line downstream of the airfoil was defined as outlet (pressure outlet), and all others were defined as inlet (velocity inlet). The airfoil chord is $C = 0.23$ m and the simulations were performed considering air

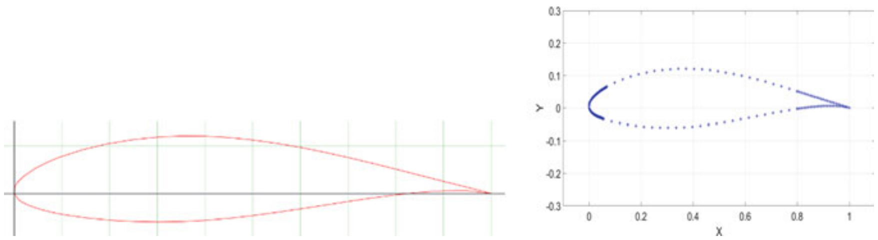

(a) Cross section (AirfoilTools, 2020). **(b) Points generated.**

Fig. 2 NACA 63-618

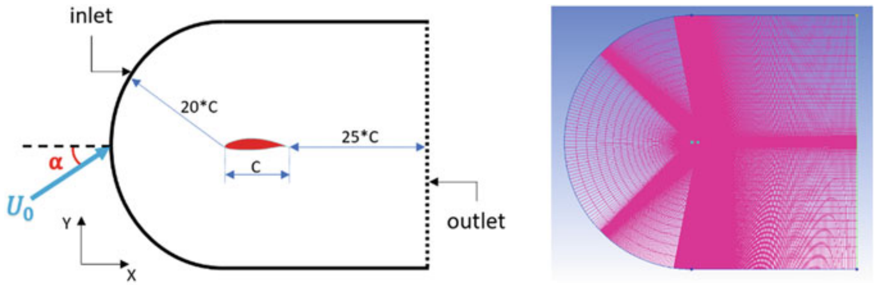

(a) Schematic representation. (b) Overview.

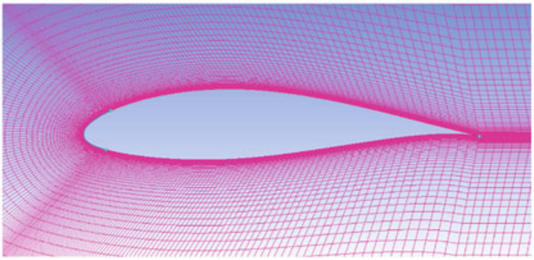

(c) Airfoil region.

Fig. 3 Two-dimensional mesh for NACA 63-618

as fluid ($\rho = 1.225\,\text{kg/m}^3$) with a Reynolds number of $Re_c = 5.3 \times 10^5$ in order to match the experiment of Walker et al. (2014). The mesh, shown in Fig. 3b, c, was developed with $y^+ = 1$ and has a total of 76, 725 elements. This number of elements provided mesh-independent results.

The main objective of the present study is to compute both lift and drag coefficients by varying the angles of attack from $-5° < \alpha < 15°$. For all the angles of attack, the freestream velocity $U_0 = 34.56522\,\text{m/s}$ was decomposed according to α instead of changing the position of the airfoil in the mesh (Stephens et al. 2017), as shown in Fig. 3a. The velocity components for each angle of attack are presented in Table 1.

Table 1 Velocity components as a function of angle of attack

α	$U_{0_x}\,[m/s]$	$U_{0_y}\,[m/s]$
−5°	34.43369	−3.01256
0°	34.56522	0.00000
5°	34.43368	3.01256
10°	34.04010	6.00219
15°	33.38744	8.94613

The simulations were performed using the Fluent 16.0 and the UNSCYFL3D code (Souza et al. 2012; Pereira et al. 2014). The forces F_x and F_y were oriented according to the coordinate axes shown in Fig. 3a. Therefore, to obtain drag and lift forces, we decomposed them to the parallel and perpendicular directions in relation to the flow direction, as shown in Fig. 1, applying the following expressions:

$$F_{Drag} = F_y \sin(\alpha) + F_x \cos(\alpha) \tag{1}$$

$$F_{Lift} = F_y \cos(\alpha) - F_x \sin(\alpha) \tag{2}$$

Once the drag and lift forces are obtained, the coefficients can then be calculated:

$$C_D = \frac{F_{Drag}}{(0.5 \rho V_0^2 C s)} \tag{3}$$

$$C_L = \frac{F_{Lift}}{(0.5 \rho V_0^2 C s)} \tag{4}$$

Since the model is two dimensional, the blade span (s) must be considered equal to the unit.

10.3 Results

In order to obtain the values of C_L and C_D for the NACA 63-618 profile with different angles of attack and $Re_c = 5.3 \times 10^5$, simulations were carried out in Fluent 16.0 software and USNCYFL3D code in steady-state and performing 5000 iterations. The angle of attack was varied by modifying the velocity components, as shown in Table 1. Note that for the same case, the results of the software and the code did not present a significant difference.

An important factor, which is the central point of discussion of this work, is the different turbulence models that can be applied in the simulations. In the present study, for $\alpha = 5°$ the conventional turbulence RANS (Reynolds Averaged Navier–Stokes) models were applied: k-ϵ, optimized k-ϵ, SST-DES (detached eddy simulation based

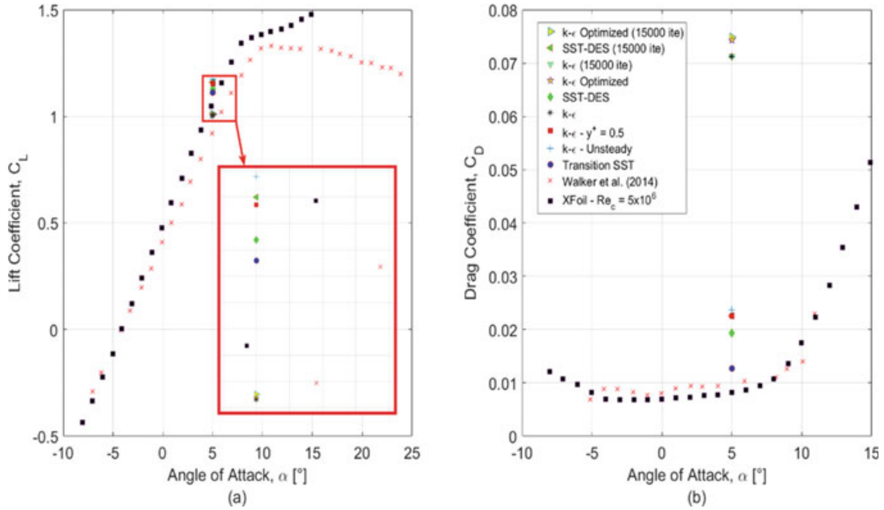

Fig. 4 Lift and drag coefficients applying different turbulence models (NACA 63-618, $\alpha = 5°$ and $Re_c = 5.3 \times 10^5$)

on shear stress transport), and RSM (Reynolds stress model). However, none of them presented results in accordance with the literature: experiment $Re_c = 5.3 \times 10^5$(Walker et al. 2014) and XFoil - $Re_c = 6 \times 10^6$ (Drela and Youngren 2006), as presented in Fig. 4. In some cases 15,000 iterations were also performed and the result for the RSM was not presented because it distorts the graph. Although the value of the Reynolds number for XFoil is higher, its results are valid for comparison, since C_L is independent of Re_c and C_D becomes independent when $Re_c \geq 5 \times 10^5$ (Walker et al. 2014).

Studying a NACA 64-618 profile with $Re_c = 6 \times 10^6$, whose profile is very similar to that considered in this study, Han et al. (2018) compared the results of its simulations with different turbulence models and those experimentally obtained by Abbott et al. (1945), as shown in Fig. 5. The authors noted that the results for the drag coefficient with completely turbulent models show significantly high errors. The SST k-ω transition model presents a good approximation with the wind tunnel data for most angles of attack and, consequently, was the turbulence model applied in the simulations, and the turbulent intensity was set as 0.01%.

Therefore, NACA 63-618 profile was performed in Fluent 16.0 for $\alpha = 5°$ and $Re_c = 5.3 \times 10^5$ using the Transition SST turbulence model and turbulent intensity equal to 0.01%. The coefficients C_L and C_D obtained were closer to the references, as shown in Fig. 4a, b, respectively (filled blue circle). In addition, the lift-drag ratio for this angle was also very close to the value obtained by Han et al. (2018), as presented in Fig. 5 (blue star).

Based on the difference in heat transfer coefficients by convection of laminar and turbulent flows, Ehrmann and White (2015) applied infrared thermography to determine the position of laminar-turbulent transition in a NACA 63–418 profile,

Fig. 5 Lift–drag ratios in various turbulence models for NACA 64–618 and $Re_c = 6 \times 10^6$. (Han et al. 2018)—adapted

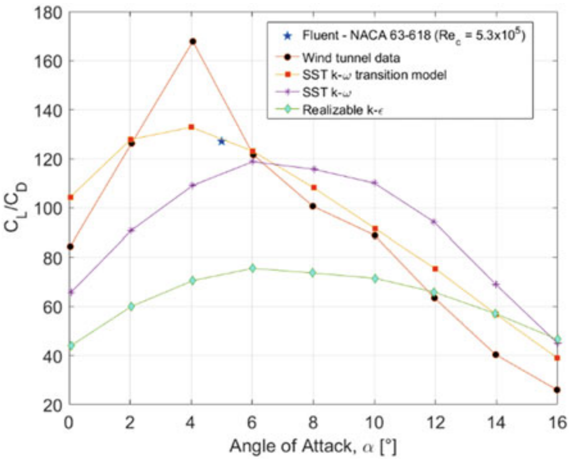

also very close to NACA 63-618, with Re_c ranging from 0.8×10^6 to 4.8×10^6. Figure 6 presents one of the results obtained by the authors, proving a laminar-turbulent transition on the airfoil. This laminar flow that occurs on NACA 6-series sections is one of the motivations for using them in turbines (Tangler and Somers 1995).

Finally, Fig. 7 presents the results obtained for the other angles of attack: $-5°, 0°, 10°$ and $15°$, using Fluent 16.0 and applying the Transition SST turbulence model and turbulent intensity equal to 0.01%. The results are very close to references. For $\alpha = 15°$ the C_L obtained was closer to the experimental than XFoil. The C_D is larger than the XFoil and there is no experimental data for this angle. However, Walker et al. (2014) show for $Re_c = 4.2 \times 10^5$ and $\alpha \approx 12°$ and $13°$ larger

Fig. 6 Red: transition front. Green: Mean (solid) and bound (dashed) locations. (Ehrmann and White, 2015)—adapted

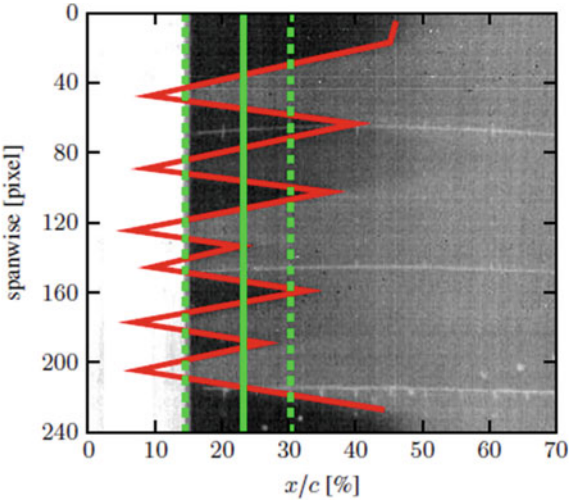

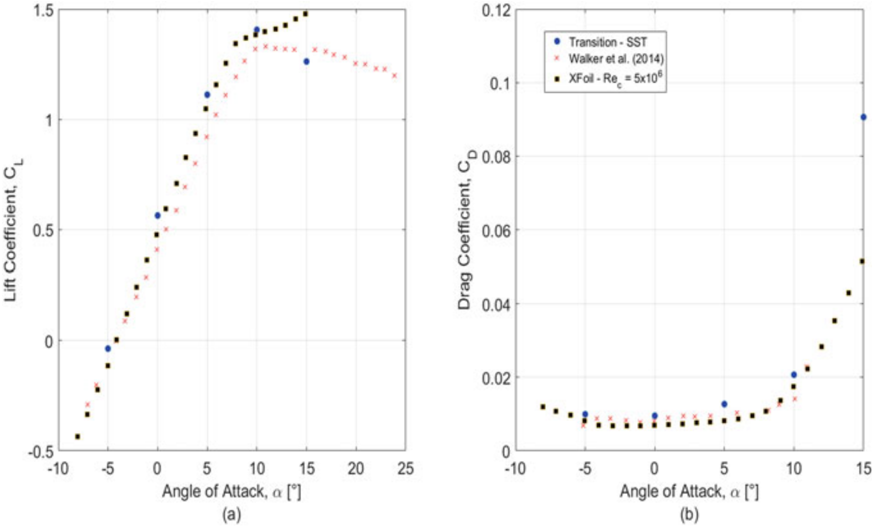

Fig. 7 Lift and drag coefficients as a function of the angle of attack for NACA 63-618, $Re_c = 5.3 \times 10^5$

values of C_D than those obtained using XFoil, suggesting that the result obtained is coherent.

10.4 Conclusion

The curves of lift and drag coefficients as a function of the angle of attack for an airfoil with NACA 63-618 cross section in the considered conditions were obtained and are in agreement with experimental values and other simulations. This result was obtained only when the Transition SST turbulence model was applied, being that the most remarkable point. Therefore, it is evident that in these conditions there is a laminar-transient transition on the airfoil.

Other studies carried out with 6-series sections also show this transition and that the use of completely turbulent models generates errors in the estimates related to the drag. As already discussed, results extracted from the CFD models will only be valid if numerical techniques are properly applied, being the turbulence model one of these techniques. Therefore, the importance of the analysis and choice of the turbulence model to be used in the simulations is highlighted, based on comparisons with experiments and simulations performed with the same or similar geometries.

Acknowledgements The authors are thankful to the Coordination for the Improvement of Higher Education Personnel (CAPES), Brazilian Research Council (CNPq), and the Foundation for Research Support at Minas Gerais State (FAPEMIG).

References

Abbott IH, von Doenhoff AE, Jr LSS (1945) Summary of airfoil data. Report No. 824, National Advisory Committee for Aeronautics, p 195

AirfoilTools (2020) Naca 63(3)-618. http://airfoiltools.com/airfoil/details?airfoil=naca633618-il

Baltazar J, Campos JFD (2011) Hydrodynamic analysis of a horizontal axis marine current turbine with a boundary element method. ASME J Offshore Mech Arct Eng 133:041304

Bedon G, Castelli MR, Benini E (2013) Optimization of a darrieus vertical-axis wind turbine using blade element - momentum theory and evolutionary algorithm. Renew Energy 59:184–192

Behrens S, Griffin D, Hayward J, Hemer M, Knight C, McGarry S, Osman P, Wright J (2012) Ocean renewable energy: 2015â€“2050, an analysis of ocean energy in Australia. www.csiro.au

Branlard E (2017) Wind turbine aerodynamics and vorticity-based methods, vol 7, 1st edn. Springer International Publishing

Drela M, Youngren H (2006) Xfoil 6.96. http://web.mit.edu/drela/Public/web/xfoil/

Ehrmann RS, White EB (2015) Effect of blade roughness on transition and wind turbine performance

Erdinc O, Uzunoglu M (2012) Optimum design of hybrid renewable energy systems: overview of different approaches. Renew Sustain Energy Rev 16:1412–1425

Ferreira A, Kun SS, Fagnani KC, Souza TA, Tonezer C, Santos GR, Coimbra-Araujo CH (2018) Economic overview of the use and production of photovoltaic solar energy in Brazil. Renew Sustain Energy Rev 81:181–191

Freese S (1957) Windmills and millwrighting, 1st edn. Cambridge University Press, Cambridge

Frewin C (2020) Renewable energy. https://www.studentenergy.org/topics/renewable-energy

Hall TJ (2012) Numerical simulation of a cross flow marine hydrokinetic turbine. Master's thesis, University of Washington, Washington

Han W, Kim J, Kim B (2018) Effects of contamination and erosion at the leading edge of blade tip airfoils on the annual energy production of wind turbines. Renew Energy 115:817–823

Jacobson MZ, Delucchi MA, Cameron MA, Mathiesen BV (2018) Matching demand with supply at low cost in 139 countries among 20 world regions with 100% intermittent wind, water, and sunlight (wws) for all purposes. Renew Energy 123:236–248

Luguang Y, Li K (1997) The present status and the future development of renewable energy in China. Renew Energy 10:319–322

Ng KW, Lam WH, Ng KC (2013) 2002â€“2012: 10 years of research progress in horizontal-axis marine current turbines. Energies 6:1497–1526

Noruzi R, Vahidzadeh M, Riasi A (2015) Design, analysis and predicting hydrokinetic performance of a horizontal marine current axial turbine by consideration of turbine installation depth. Ocean Eng 108:789–798

Pereira GC, Souza FJ, Martins DAM (2014) Numerical prediction of the erosion due to particles in elbows. Powder Technol 261:105–117

Price TJ (2005) James blyth-britain's first modern wind power pioneer. Wind Eng 29:191–200

Rahimian M, Walker J, Penesis I (2017) Numerical assessment of a horizontal axis marine current turbine performance. Int J Marine Energy 20:151–164

Sorensen JN (2016) General momentum theory for horizontal axis wind turbines, vol 4. Springer International Publishing, 1st edition

Seng Y, Koh LL, Koh SL (2009) Marine tidal current electric power generation: State of art and current status. Renewable Energy, InTech

Singer C, Holmyard EJ, Hall AR (1954 [1956]). A history of technology, vol 1, 2. Clarendon, London

Souza FJ, Salvo RV, Martins DAM (2012) Large eddy simulation of the gas-particle flow in cyclone separators. Sep Purif Technol 94:61–70

Stephens D, Jemcov A, Sideroff C (2017) Verification and validation of the caelus library: Incompressible turbulence models. ASME Fluids Engineering Division Summer Meeting

Tangler JL, Somers DM (1995) Nrel airfoil families for HAWTs. NREL/TP-442-7109 , National Renewable Energy Laboratory

UoE (2018) James blyth (1839 - 1906). University of Edinburgh - 30 October 2018 https://www.ed.ac.uk/alumni/services/notable-alumni/alumni-in-history/james-blyth

Walker JM, Flack KA, Lust EE, Schultz MP, Luznik L (2014) Experimental and numerical studies of blade roughness and fouling on marine current turbine performance. Renew Energy 66:257–267

Chapter 11
Tollmien-Schlichting Waves Artificially Inserted in Boundary Layer by Harmonic Point Source

Victor Barcelos Victorino, Christian Salaro Bresci, Matheus Maia Beraldo, and Marcello Augusto Faraco de Medeiros

Abstract The present work experimentally investigates the spatial evolution of controlled artificial disturbances inserted by a harmonic point source in a Blasius boundary layer over a flat plate. A small hole of 0.80 mm diameter is responsible to introduce a blowing and suction flow inside the boundary layer induced by an embedded loudspeaker. The model employed consists of a plexiglass plate with an 1800 mm chord, 1000 mm span, and 10 mm thickness, vertically assembled inside the test section of the Low Acoustic Noise and Turbulence (LANT) wind tunnel at EESC-USP. Aluminum leading edge, flap, and tab were attached to the model in order to promote a practically constant pressure distribution. Hot-Wire Anemometry was carried to measure base flow, turbulence level, and Tollmien-Schlichting profiles. Good agreement with Blasius was obtained in at least a 300 mm span range, on two different streamwise positions. Tollmien-Schlichting eigenfunction profiles were measured for different positions in a chordwise direction. The amplification region matches that predicted by Linear Stability Theory. Through spectral analysis, it was possible to identify the presence of fundamental and first harmonic oscillation, which led to the conclusion that the flow conditions corresponded to a weakly non-linear regime.

Keywords Tollmien-Schlichting wave · Harmonic point source · Transition in boundary layer · Flow Instability

11.1 Introduction

Flow instabilities and the onset of turbulence in the boundary layer are characterized by complex nature and chaotic motion. Such dynamics arise from, among several mechanisms, interactions of non-linear effects on oscillations present in

---

V. B. Victorino · C. S. Bresci · M. M. Beraldo · M. A. F. de Medeiros (✉)
USP, EESC, São Paulo, SAA 13566-590, Brazil
e-mail: marcello@sc.usp.br

V. B. Victorino
e-mail: barcelos.victorino@usp.br

H. F. Meier et al. (eds.), *Advances in Turbulence*, ABCM Series on Mechanical Sciences and Engineering, https://doi.org/10.1007/978-3-031-25990-6_11

the flow. Once a turbulent regime is reached, time-dependent motion promotes mass, momentum, and energy transference and as a consequence, losses become strongly affected. Therefore, engineering and physical sciences search for better understanding of the process.

First experimental evidence of flow turbulence was reported by Reynolds (1883). Following, Tollmien (1928) and Schlichting (1933) worked on the development of the Linear Stability Theory (LST), which is based on the stability of viscous laminar Blasius boundary layer to small amplitude disturbances. Nevertheless the validation of the LST was achieved only after experimental evidences was obtained by Schubauer (1948). The theory is derived from linearized Navier-Stokes equations (LNSE) applied on parallel flows, e.g., two-dimensional boundary layer. Variables are decomposed into time-invariant component (base flow) and time-dependent small amplitude harmonic oscillation. Non-linear terms are neglected, because it is assumed that the amplitude is small compared to the base flow magnitude. After manipulation and the application of normal modes analysis, the equation

$$(\alpha U - \omega)(\phi^{''} - \alpha^2\phi) - \alpha U^{''}\phi = -\frac{i}{Re_{\delta *}}(\phi^{''''} - 2\alpha^2\phi^{''} + \alpha^4\phi) \tag{1}$$

commonly referred to as Orr-Sommerfeld equation can be treated as an eigenvalue problem.

Originally, the LST treated the problem as temporal and once specified α and $Re_{\delta *}$, the complex eigenvalue, ω, is the solution. This variable represents temporal frequency and its imaginary part $\Im(\omega)$, called amplification factor. It determines whether the associated spatial wavenumber, α, at a specific $Re_{\delta *}$ is stable ($\Im(\omega) < 0$) or unstable ($\Im(\omega) > 0$). The eigenfunction, $\phi(y)$, describes the amplitude profile across the wall-normal direction (y), and the instability wave characterized by these parameters is named Tollmien-Schlichting (T-S) wave. After several calculations for different combinations of parameters, the instability locus can be mapped and it is usually plotted by means of the neutral stability curve diagram. The maximum Reynolds number based on displacement thickness, $Re_{\delta *}$, for which no amplification occurs is called critical Reynolds (Re_{crit}) and two branches bound the instability region. Such boundaries correspond to a region where $\Im(\omega) = 0$. It is important to point out the fact that the perturbations artificially imposed in the boundary layer at a fixed streamwise position consist of a spatial problem. Later, Gaster (1962) demonstrated through the Cauchy-Riemann relations that the spatial growth is related to temporal growth by the group velocity, $c_g = d\omega/d\alpha$.

Schubauer (1948) pointed out that the study of T-S waves produced by controlled artificial disturbances could be more beneficial than under natural circumstances, e.g., free-stream turbulence. Perturbation source devices of various kinds were explored and the vibrating ribbon was the most appropriate accordingly to the authors. Klebanoff et al. (1962) also performed experiments through this technique and remarkable contributions were achieved about the three-dimensional nature of T-S wave, characterized by spanwise pattern in wave amplitude. The authors stated that the actual breakdown of wave motion to turbulence occurs as a consequence of non-linear three-dimensional effects that lead to secondary instabilities by the formation of hairpin eddies. Afterward, this regime was named the K-type transition.

In addition, another laminar breakdown regime was observed by Kachanov et al. (1977), also reported by Kachanov and Levchenko (1984) and Kachanov (1994). In this type of transition, no turbulent spikes of unsteady velocity records were observed, as opposite to Schubauer (1948). The spectral analysis of this transition process leads to a subdivision of four stages. Initially, weakly linear development occurred as well as the growth of fundamental frequency harmonics of the perturbation imposed over the flow. The second stage is marked by the growth attenuation of these components and the appearance of low-frequency and sub-harmonic components in the spectrum. Subsequently, three-dimensional effects were reported followed by interaction among the low-frequency pulsation, fundamental mode, and its harmonics. Lastly, the process presents attenuation of harmonics and laminar breakdown. This kind of transition driven by three-dimensional resonance interactions was called N-type transition.

Gaster (1990) carried out experiments employing a harmonic point source to stimulate T-S waves in a Blasius boundary layer. The device selected as the source was a small loudspeaker buried in the plate. Transmission of disturbance to boundary layer flow was due to ring of small holes of 0.30 mm diameter in which a blowing and suction flow was induced by the loudspeaker. Three types of input signal were investigated: a periodic monochromatic sinusoidal wavetrain, a controlled broadband noise, with low amplitude relative to sinusoidal signal, and a composition of both. Despite no turbulence being reached through the regime employed, results exhibited a spectrum similar to those obtained by Kachanov and Levchenko (1984). The author concluded that large amplitude Tollmien-Schlichting waves are unstable to weak excitations at a subharmonic frequency and its multiples. The rate of amplification of the secondary motion was proportional to the square of the fundamental driving signal as expected based on weakly non-linear theory.

The non-linear evolution of a wavetrain emanating from a point source was also experimentally investigated by Medeiros (2004). The disturbance amplitude employed was sufficient to promote a weakly non-linear behavior. The results exhibited a three-dimensional mean flow distortion in the form of longitudinal streaks. Two distinct stages of the non-linear regime were reported. The first was characterized by a low spanwise wavenumber apparently associated with a pair of counter-rotating streamwise vortical regions. It was found that the phenomenon arise from the interaction between spanwise and wall-normal modes. The second stage presented more streaks and a higher spanwise wavenumber. The streamwise location of this stage onset was not influenced by the input amplitude, and appeared to be associated with the second branch of the neutral stability diagram.

Present work concerns the experimental study of the development of artificial Tollmien-Schlichting waves in a Blasius boundary layer. The disturbance source device employed was a small loudspeaker, like that used by Gaster (1990) and Medeiros (2004). Such disturbance is characterized by three-dimensional nature and depending on input amplitude, non-linear effects can become significant. The eigenfunction profile was measured and spectral analysis was employed. An attempt to identify some aspects related to previously cited references was carried out and LST calculations were applied in order to verify whether the experimental results match the predictions by theory.

11.2 Experimental Setup

The current work experiments were performed in the Low Acoustic Noise and Turbulence wind tunnel (LANT) located at EESC-USP. Such facility provides a good quality flow for transition study purposes, the free-stream turbulence intensity measured with an empty test section is 0.05%. The test section possesses a squared cross-sectional area of 1.00 m^2 and a length of 3.00 m. Figure 1 exhibits the floor plan of the wind tunnel facility, where the aforementioned devices are highlighted by colored schemes.

The model consists of a plexiglass flat plate (element number 2 in Fig. 2) with 1800 mm chordwise length, 1000 mm span, and 10 mm thickness, vertically installed inside the test section. An asymmetrical modified super-ellipse leading edge (element number 1 in Fig. 2) is attached at the frontal region of the plate, while at the trailing edge, a flap and tab set (elements number 3 and 4, respectively, in Fig. 2) are installed, all of them made of aluminum. This last apparatus is used to ensure a good pressure distribution, which is no significant pressure gradient along the experiment envelope region, and to position the stagnation line slightly at the work-side. The leading edge geometry was designed to prevent suction peak on work-side surface, and to promote reduced length where the pressure settles after the stagnation point (Hanson et al. 2012). The pressure distribution was measured through static pressure taps

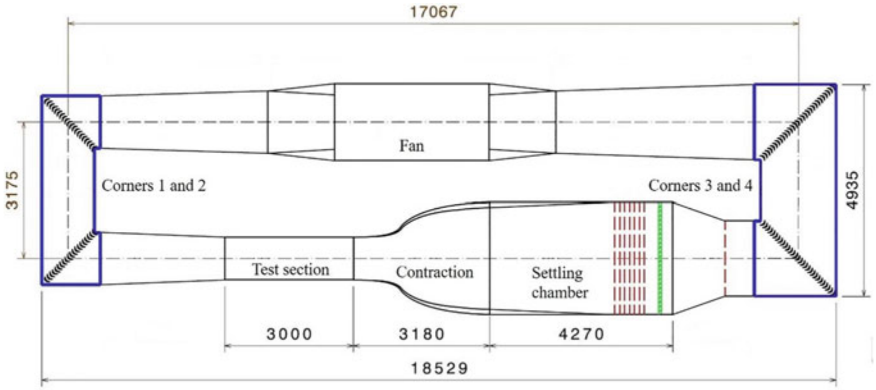

Fig. 1 Floor plan of LANT wind tunnel. The black C-shaped lines arrays indicate the corning vanes, blue boxes, the region coated by acoustic absorber foam, red dashed lines, the screens and green hatched strip, the honeycomb ducts. Air flows in clockwise direction. Dimensions in millimeters

distributed along the model and attached to an inclined U-tube manometer bank. Figure 2 exhibits the isometric view of the flat plate model, Fig. 3 displays the leading edge super-elliptical profile.

Located over the centerline, 200 mm distant from the flat plate leading edge, there is a small through-hole with 0.80 mm diameter connected to a cavity inside the plate. A loudspeaker was buried in the cavity and was responsible for the excitation of a controlled disturbance into the boundary layer flow. The loudspeaker diaphragm was flush to the entrance of the small diameter duct, and when driven by a signal input, vibration motion induced a blowing and suction flow. This flow was responsible for introducing a harmonic point source perturbation. The input signal was transmitted by an Agilent 33500B function generator. A sine-like monochromatic wave with 200 Hz frequency and 250 mV amplitude was chosen as input.

Hot-Wire Anemometry was the technique selected for velocity measurements. The constant temperature anemometer circuit model DISA 55D01 includes a DANTEC 55P05 tungsten probe with a filament diameter of 5 μm and length of 1 mm. The output signal was branched and transmitted to two acquisition devices. The first consists of 16-bit resolution National Instruments (NI) DAQ USB-6002 module, and

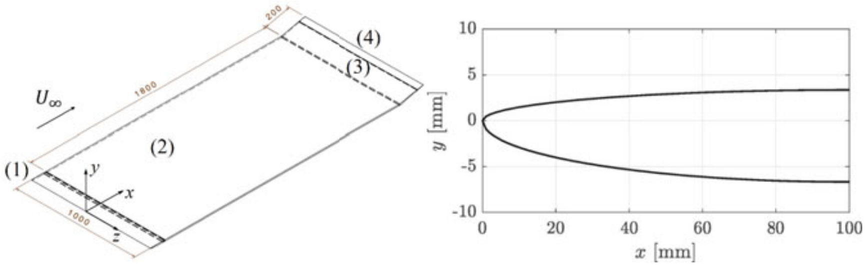

(a) Model.

(b) Leading edge.

Fig. 2 Isometric view of model and asymmetrical leading edge profile. Dimensions in millimeters

Fig. 3 Power spectral density of unsteady free-stream velocity component

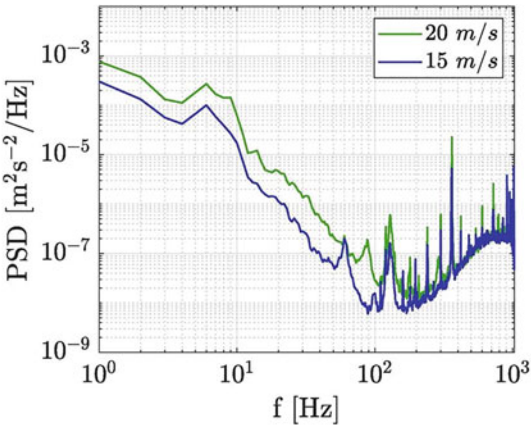

it was responsible for recording the DC voltage component. The second instrument, responsible for acquiring AC voltage component signal, was an acquisition board NI 4498, with 24-bit resolution and 114 dB dynamic range, connected to a NI PXI-1042Q chassis. Conditioning and manipulation of the signal were performed by MATLAB scripts. The position of the probe inside the test section was controlled by an in-house traverse mechanism. A calibration operation to convert voltage in velocity was done in situ. A script was able to fit the parameter values, through King's Law correlation between the velocity, measured by a static pitot tube placed inside the test section, and the output voltage of the anemometer. Environment conditions, such as atmospheric pressure, ambient and flow temperatures, were also employed. The traverse position, as well as data acquisition, were controlled by computer routines. The distance from the wall was obtained using the Blasius profiles as a reference.

11.3 Results

11.3.1 Preliminary Results

Preliminary experiments were conducted for base flow verification. Turbulence intensity was measured at position x = 400 mm, 150 mm distant from the flat plate work-side surface over the centerline. The signal was acquired at a rate of 2048 samples/s during 100 s, for two different free-stream velocities, $U_\infty = 15\ \text{ms}^{-1}$ and $U_\infty = 20\ \text{ms}^{-1}$. Two techniques were employed for signal conditioning and turbulence evaluation, respectively. Firstly, Welch's method (Cryer et al. 2010) was implemented in order to estimate the power spectral density (PSD). Such method reduces frequency resolution to improve the signal-to-noise ratio by reshaping the raw signal into 100 blocks, each one with 1 s time length, followed by the ensemble average of the PSD. The other technique, provided by Lindgren (2002), consists of applying a dynamic filter with a cut-off frequency given by $f_c = U_\infty/\lambda_c$. The parameter $\lambda_c = 2$ m was set based on twice the maximum reference length of the test section side. Turbulence intensity was calculated by $Tu = u_{rms}/U_\infty[\%]$ and root-mean-square (RMS) was calculated by the square root of PSD sum along the interval given by cut-off and Nyquist frequencies. Figure 3 shows the PSD of free-stream unsteady velocity component. The spectrum behaves as expected. It is possible to note high energy at low-frequency range of approximately 4–10 Hz, typical of closed-circuit wind tunnels and a region with energy decay in the range of 0–200 Hz. A smooth peak related to traverse vibration occurs around 140 Hz, however, such component did not interfere with the results. Sharp peaks associated with power line utility frequency ($f_{pl} = 60$ Hz) and its harmonics ($n \cdot f_{pl}; n = 1, 2, 3 \ldots$) are also noticed. For both velocities, the turbulence intensity measured was $Tu = 0.10\%$, which is suitable for current work.

The mean velocity boundary layer profile was measured and compared to Blasius' theory. Two sets of profiles were taken in two distinct streamwise positions, x =

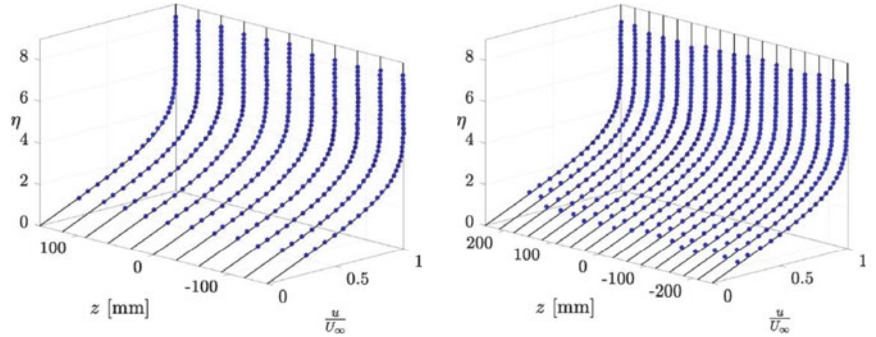

(a) x = 200 mm.

(b) x = 900 mm.

Fig. 4 Experimental mean velocity profile (blue dots) along span in comparison with Blasius (black solid lines) for two different chordwise positions

200 mm and x = 900 mm, both with the discretization of 30 mm, covering a span (z-axis) of 300 mm and 480 mm, respectively. The free-stream velocity was set constant near the velocity employed for T-S experiments ($\approx$17 ms^{-1}). The discretization in the wall-normal direction was set to 0.10 mm, at x = 200 mm, and 0.20 mm, at x = 900 mm. Wall distance of the measurement point closest to the model surface was estimated assuming the Blasius profile. Each profile was normalized by the boundary layer edge velocity, calculated by the mean velocity of the five most distant points from the model surface. The wall-normal direction (y-axis) is represented by the similarity parameter $\eta = y\sqrt{(U_\infty/\nu x)}$. Kinematic viscosity, $\nu = 1.76\times10^{-5}$ m^{2}s^{-1}, was calculated given mean flow temperature, and airflow density calculated by ideal gas relation for environmental conditions measured, $\rho = p_{atm}/RT_\infty$. Figure 4 shows the comparison between theoretical Blasius and experimental profiles. It is noted a good agreement with Blasius and high uniformity of boundary layer across the span covered.

11.3.2 Tollmien-Schlichting Waves

Six Tollmien-Schlichting amplitude profiles were measured in a streamwise (x-axis) range of 500–1000 mm, spaced by 100 mm. The free-stream velocity was set constant at $U_\infty = 17.3\,\text{ms}^{-1}$. The unsteady velocity records were taken along 31 s for each measurement point, with a sampling rate of 2000 samples/s. Welch's method was employed to increase the signal-to-noise ratio, by segmenting the raw signal into 35 blocks and taking the ensemble average to estimate the PSD. The profile amplitude of u' was given by the RMS of the unsteady record, which was calculated by the square root of PSD summed over a narrow interval centered at 200 Hz. Such range covered a $\pm2\Delta f$ wide span, where $\Delta f \approx 1.15$ Hz is the frequency resolution of the reshaped signal. The sum interval was chosen based on the PSD analysis, it was

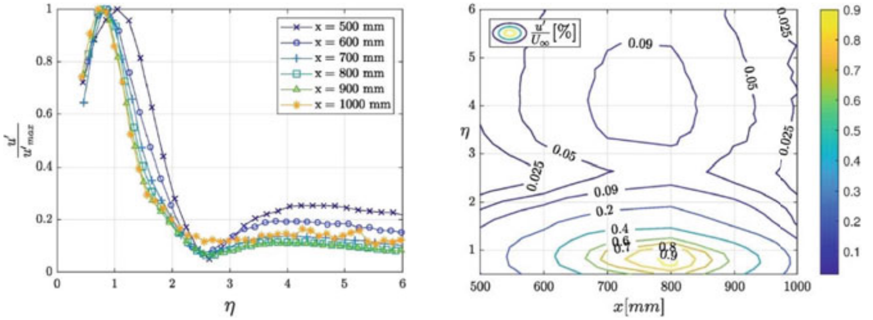

(a) Normalized TS profiles for different chordwise position.

(b) Contour of u'/U_∞ [%] amplitude on $x\eta$ plane.

Fig. 5 Experimentally measured Tollmien-Schlichting waves

necessary to include possible power leakage arising from Welch's method, although it should not include undesired energy of other frequency components.

Figure 5 (a) exhibits normalized profile for each x position, Fig. 5 (b) displays contours of percentage amplitude relative to free-stream velocity ($u'/U_\infty[\%]$) for the $x\eta$ plane. Analysis of Fig. 6 indicates that the T-S peak location becomes sharper as it evolves across a streamwise direction, which is expected since the non-normalized amplitude increases downstream within the instability region. Around the local maximum next to $\eta \approx 4$, one can note a decrease trend of the outer peak across the x-axis, and after the T-S reaches stability at x > 800 mm, a distortion seems to appear in amplitude profile. This is showed also in Fig. 5b.

The T-S inner peak spectrum was also investigated and it is shown in Fig. 6 by the dark blue solid lines. Several characteristics consistent with the flow instability are seen. Firstly, a bell-shaped amplitude value within a frequency band is present in the PSD plot of almost all x positions covered. This behavior is expected, since it exhibits the disturbances amplification of the unstable frequencies, which naturally arise inside the boundary layer. The light blue and yellow dash-dot lines displayed in Fig. 6 locate the dimensional frequency of branches I and II of the neutral curve stability diagram, respectively. Such values were obtained by in-house codes that solve Linear Stability Theory (LST) problem. In the range of 500 mm $\leq$ x $\leq$ 800 mm, the branch II frequency practically coincides with the maximum of those bell-shaped bulges, which is expected accordingly to LST. However, once the dominant forced perturbation with a frequency of 200 Hz is no longer unstable, the behavior of the remaining unstable frequencies apparently changes and the most amplified frequency appears close to the center of the unstable region delimited by the branches, around 100 Hz. A sharp peak at 200 Hz is highlighted by the green dashed line in Fig. 6a–f. As such frequency remains within the range of unstable frequencies, disturbance growth occurs.

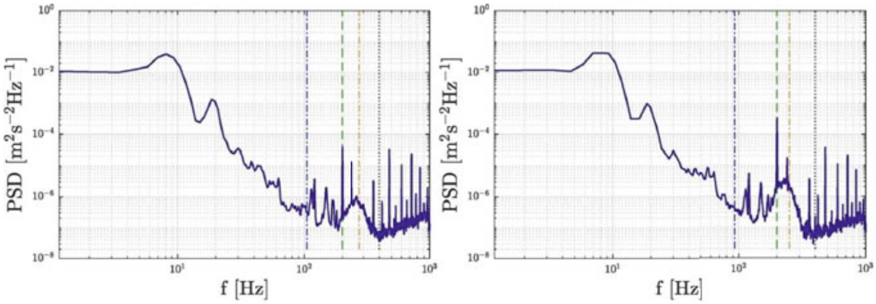

(a) x = 500 mm

(b) x = 600 mm

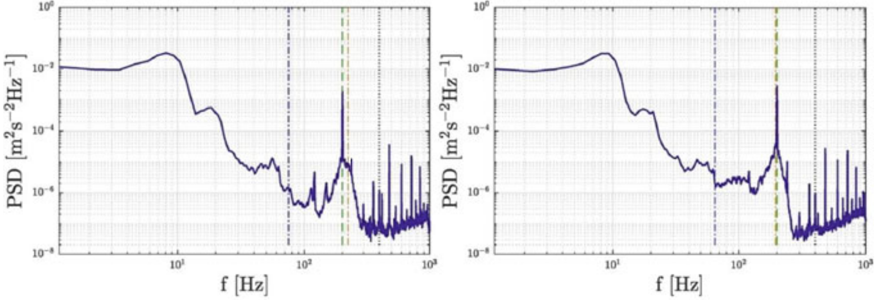

(c) x = 700 mm

(d) x = 800 mm

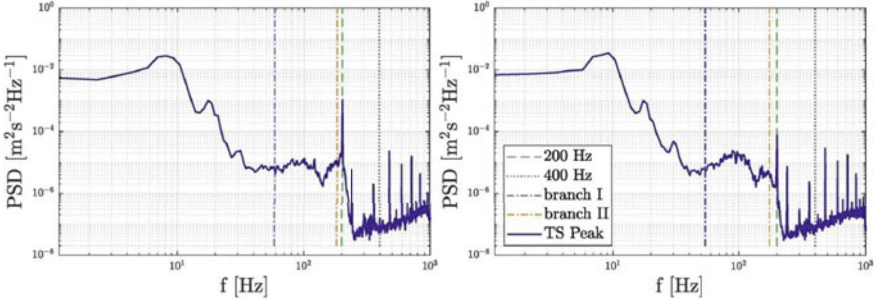

(e) x = 900 mm

(f) x = 1000 mm

Fig. 6 Power spectral density of T-S peak along the streamwise direction x

11.4 Concluding Remarks

Tollmien-Schlichting waves were artificially excited by a harmonic point source. The base flow over a flat plate with a virtual zero pressure gradient was characterized, including the free-stream turbulence intensity. A good agreement with Blasius was reached and a suitable level of turbulence was obtained. It was possible to measure the eigenfunction amplitude profile. Amplitude growth occurred inside the unstable region predicted by LST, as well as damping at positions downstream of branch II of the neutral curve. By analysis of PSD corresponding to the T-S peak location, it was possible to identify some aspects provided by Gaster (1990) and Kachanov et al.

(1977). Among which was possible to notice the presence of the first harmonic of fundamental disturbance (400 Hz). This component should not be amplified, once it is located in a stable locus of the stability diagram, however, growth was observed. Apparently, this component arises from non-linear interactions and its amplitude is related to the amplitude of fundamental disturbance (200 Hz). Low frequencies around the sub-harmonic (100 Hz) also presented amplification at downstream positions. As pointed out by Gaster (1990), this fact could be associated with the instability of relatively large amplitude T-S waves to small perturbations within frequencies close to sub-harmonic components.

Acknowledgements V.B.V. was funded by CNPq/Brazil, grant #134335/2018-0. C.S.B. was funded by CAPES/Brazil, under the CAPES/PROAP Social Demand program. M.M.B. was funded by CAPES/Brazil, grant #88882.379172/2019-1. M.A.F.M. thanks the National Council for Scientific and Technological Development (CNPq/Brazil) for grants 307956/2019-9 and the US Air Force Office of Scientific Research (AFOSR) for grant FA9550-18-1-0112, managed by Dr. Geoff Andersen from SOARD. The LANT wind-tunnel financial support was provided by FINEP/Brazil, grant #01.09.0334.04. The authors also thank FAPESP/Brazil for grant 2019/15366-7.

References

Cryer JD, Bendat JS, Piersol AG (2010) Random data—analysis and measurement procedures, 4th edn, vol 82. John Wiley & Sons, Inc. ISBN 9780470248775. https://doi.org/10.2307/2289430

Gaster M (1990) The nonlinear phase of wave growth leading to chaos and breakdown to turbulence in a boundary layer as an example of an open system. Proc R Soc Lond Ser A Math Phys Sci 430(1878):3–24. ISSN 0962-8444. https://doi.org/10.1098/rspa.1990.0078

Gaster M (1962) A note on the relation between temporally-increasing and spatially-increasing disturbances in hydrodynamic stability. J Fluid Mech 14(2):222–224. ISSN 14697645. https://doi.org/10.1017/S0022112062001184

Hanson RE, Buckley HP, Lavoie P (2012) Aerodynamic optimization of the flat-plate leading edge for experimental studies of laminar and transitional boundary layers. Exp Fluids 53(4):863–871. https://doi.org/10.1007/s00348-012-1324-2

Kachanov YS (1994) Physical mechanisms of laminar-boundary-layer transition. Annu Rev Fluid Mech 26:411–482

Kachanov YS, Kozlov VV, Levchenko VY (1977) Nonlinear development of a wave in a boundary layer. Fluid Dyn 12(3):383–390. ISSN 15738507. https://doi.org/10.1007/BF01050568

Kachanov YS, Levchenko VY (1984) The resonant interaction of disturbances at laminar-turbulent transition in a boundary layer. J Fluid Mech 138(1984):209–247. ISSN 14697645. https://doi.org/10.1017/S0022112084000100

Klebanoff PS, Tidstrom KD, Sargent LM (1962) The three-dimensional nature of boundary-layer instability. J Fluid Mech 12(1):1–34. ISSN 14697645. https://doi.org/10.1017/S0022112062000014

Lindgren B, Johansson AV (2002) Evaluation of the flow quality in the mtl wind-tunnel. Technical report, Royal Institute of Technology Department of Mechanics, SE-100 44 Stockholm, Swede. https://www.mech.kth.se/oso/papers/MTL_techrep.pdf

Medeiros MAF (2004) The nonlinear evolution of a wavetrain emanating from a point source in a boundary layer. J Fluid Mech 508:287–317. https://doi.org/10.1017/S0022112004009188

Reynolds O (1883) An experimental investigation of the circumstances which determine whether the motion of water shall be direct or sinuous, and of the law of resistance in parallel channels. Philos Trans R Soc Lond 35:84–99. ISSN 0261-0523. https://doi.org/10.1098/rstl.1883.0029

Schlichting H (1933) Laminare Strahlausbreitung. ZAMM. J Appl Math Mech/Zeitschrift für Angewandte Mathematik und Mechanik 13(4):260–263. ISSN 15214001. https://doi.org/10.1002/zamm.19330130403

Schubauer GB, Skramstad H (1948) Laminar-boundary-layer oscillations and transition on a flat plate. Technical Report 909, National Advisory Committee for Aeronautics, Washington, US. https://ntrs.nasa.gov/search.jsp?R=19930091976

Tollmien W (1928) Über die Entstehung der Turbulenz. 1. Mitteilung. Nachrichten von der Gesellschaft der Wissenschaften zu Göttingen, Mathematisch-Physikalische Klasse, vol 1929, pp 21–44. http://eudml.org/doc/59276

Part III
Multi-Phase Flow

Chapter 12
Investigation of Turbulent Gas-Solid Flow Multi-scale Dynamics in a Circulating Fluidized Bed Riser

Ricardo Nava de Sousa, Julia Volkmann, Cristian Ricardo Schwatz, Christine Fredel Boos, Rodrigo Koerich Decker, Jonathan Utzig, and Henry França Meier

Abstract Circulating Fluidized Bed (CFB) reactors have been extensively used for industrial applications such as mixing, drying, catalytic, and non-catalytic reactions. Due to the nonlinear and non-equilibrium gas-solid flow structures, the dynamic behaviors in a gas-solid multiphase flow remain far from being completely understood. In addition, considerable differences in the flow state occur under different operation conditions, resulting in different structures. These structures cause an impact on gas-solid momentum, mass, and heat transfer, affecting productivity. Pressure fluctuations are usually used to characterize dynamic behaviors of heterogeneous structures in fluidization. The signal of measured fluctuation contains the information about the multiscale flow characteristics and may also be associated with different phenomena. Identifying which scales of the flow are the most affected can help to reveal the dynamics of these different structures in gas-solid flow. The present work investigates pressure signals obtained through physical experiments at different experimental conditions in order to identify which scales were affected by the turbulent gas-solid flow. These signals were obtained in a CFB riser using glass beads particles, which were classified as group B of Geldart. Additionally, the gas velocity and mass flow were varied with the purpose of evaluating their influence over the turbulent scales. The obtained signals were investigated on the frequency and time-frequency domains. The power spectrum density (PSD) was applied to identify the dominant frequencies, as well the Wavelet transform was used as a mechanism to obtain the scales where its fluctuations were evaluated. The combination of such analyses resulted in the identification of the most affected scales, where it was observed

---

R. N. de Sousa · J. Volkmann · C. R. Schwatz · C. F. Boos · R. K. Decker · J. Utzig (✉) · H. F. Meier
Fluid Dynamics Laboratory, University of Blumenau, Rua São Paulo, 3250, I-204, Blumenau, Santa Catarina 89030-000, Brazil
e-mail: jutzig@furb.br

R. K. Decker
e-mail: rkdecker@furb.br

H. F. Meier
e-mail: meier@furb.br

H. F. Meier et al. (eds.), *Advances in Turbulence*, ABCM Series on Mechanical Sciences and Engineering, https://doi.org/10.1007/978-3-031-25990-6_12

that the mesoscales were attenuated with the addition of particles resulting in an increase in the fluctuation of the microscales.

Keywords CFB riser · Gas-solid flow · Turbulence modulation · Pressure signal · Wavelet transform

12.1 Introduction

Circulating Fluidized Bed (CFB) reactors are widely used in the petroleum, mineral, and energy industries. Several gas-solid flow phenomena present in this reactor are related to the turbulence of the fluid phase. When particles are inserted on the flow the turbulence is affected, this interaction can make turbulence completely govern the particles' behavior or the presence of particles can also influence the turbulence, which is known as turbulence modulation (Utzig et al. 2015). As a result of gas-solid interaction, several dissipative structures formation as clusters, particle segregation, and deposition of particles near to walls are observed. These structures are assigned to nonlinear and non-equilibrium interaction, which impacts gas-solid momentum, mass, and heat transfer, therefore, affecting CFB's productivity.

The dissipative behavior present in this multiphase flow shows a multiscale characteristic and a coupling of multi-sub-processes, scale-dependent behaviors, and the coupling between different mechanisms at different scales. There are three main approaches used to identify the scales: the first consists of tracking the movement of all individual particles, thus knowing the details of the particle-fluid interaction; the second involves analyzing the average of all parameters in a specific volume and the third approach involves analyzing the system in three basic scales. Those scales are the particle scale, cluster scale, and unit scale, which represent the micro, meso, and macro scales, respectively (Li 2000).

Recently, an increased interest in pressure signal fluctuations to characterize dynamic behaviors of heterogeneous structures has emerged (Verloop and Heertjes 1974; Kage et al. 1991; Musmarra et al. 1995; M'Chirgui et al. 1997; van der Schaaf et al. 1998; Bi 2007; Sasic et al. 2007). Pressure measurements are easy to obtain even under severe conditions, as seen in the industry, relatively cheaper, nonintrusive, and avoid distortion of the flow around the point of measurement. Despite this and even though the pressure fluctuations signal contains information about multiscale flow characteristics, the interpretation of pressure signals is not totally understood (van Ommen et al. 2011). Signals processes techniques are commonly used to obtain information about the gas-solid fluid dynamics. According to Johnsson et al. (2000) these methods include the time domain, frequency domain, time-frequency domain, and state space. Although there are extensive data available in the literature, the experimental data are rather controversial and there is no general agreement about which scales are most affected by the addition of particles in gas-solid flows.

Pressure fluctuation analysis has focused on the fluidized bed phenomena to characterize the flow regimes and transition velocities (Shou and Leu 2005), bubbling behavior (Wu et al. 2007), dynamic properties of clusters (Yang and Leu 2009) and investigation of multiscale structures dynamics (Chen et al. 2016). However, not too much attention has been paid to the scales' communication dynamics and the interaction effects between turbulence and particles.

This paper will focus on the experimental investigation of which scale is most affected by the addition of particles in a pilot-scale CFB riser. The experimental data was obtained through pressure transducers and were analyzed using standard deviation, Fast Fourier Transform (FFT), and Wavelet Transform. With this information, the homogeneity of signal, predominant frequencies, and the dynamic of scales were observed.

12.2 Mathematical Modeling

12.2.1 Statistic Analysis

According to van Ommen et al. (2011) most analysis methods involving standard deviation Eq. (1) in fluidized beds were applied in time domain analysis and used to determine the amplitude of the pressure signals. This application has often been used to identify a regime change, minimum fluidization velocity and to quantify the stability of different flow patterns. The standard deviation is defined mathematically as

$$\sigma = \sqrt{\frac{1}{n-1}\sum_{i=1}^{n}(x_i - \overline{x})^2} \tag{1}$$

where x_i indicates the measured datum within the acquisition duration, and its mean value $\overline{x}$ was calculated using Eq. (2):

$$\overline{x} = \frac{1}{n}\sum_{i=1}^{n} x_i \tag{2}$$

In the present paper, the standard deviation was used to observe the fluctuation of the signal by means of the original signal homogeneity in the time domain and the scales in time-frequency domain.

12.2.2 Frequency Domain

The Power spectral density (PSD) analysis estimated by the Fourier transform is a widely used tool in signal analysis. In this analysis, the time domain signal is decomposed in a set of sinusoids of different frequencies. The advantage of using this technique is to determine the characteristic frequencies and their amplitudes. In the turbulent gas-solid flow, the change of the dynamic behavior results in changes in power spectra, which results in a variation of the dominant frequency (Felipe and Rocha 2004). At the same time, when it is applied the temporal position of the information is lost, resulting in the knowledge of all the frequency components, but being impossible to know when they occur.

The discrete Fourier transform (DFT) used was deducted as Bendat and Piersol (1986). Starting from the Fourier Transform of a temporal function, Eq. (3):

$$X(f, T) = \int_{0}^{T} x(t) e^{-j2\pi f t} dt \tag{3}$$

Assuming that x(t) is sampled at N space points equally spaced at a distance of Δt, where Δt is selected to produce a sufficiently high Nyquist frequency. The time of sampling is tn = nΔt, but it is convenient to begin with n = 0, so:

$$x_n = x(n\Delta T) n = 0, 1, 2, \ldots, N - 1 \tag{4}$$

For the discrete version, to an arbitrary f:

$$X(f, T) = \Delta t \sum_{n=0}^{N-1} x_n e^{-j2\pi f n \Delta t}. \tag{5}$$

The usual selection of discrete frequency values for X(f, T) is.

$$f_k = \frac{k}{T} = \frac{k}{N\Delta t} k = 0, 1, 2, \ldots, N - 1. \tag{6}$$

At these frequencies, the transformed values give the Eq. (7), which is now a discrete Fourier transform (DFT):

$$X_k = \frac{X(f_k)}{\Delta t} = \sum_{n=0}^{N-1} x_n e^{-j\frac{2\pi k n}{N}} k = 0, 1, 2, \ldots, N - 1 \tag{7}$$

which is only valid for k = N/2 since the Nyquist frequency occurs at this point. From the discrete Fourier transform (DFT), the Power Spectrum Density (PSD) function Eq. (8) is defined as

$$PSD(f) = \frac{2|X_k|^2}{t_2 - t_1}. \tag{8}$$

where the PSD function is the magnitude of the FFT square divided by the period t_1 and t_2 (Cong et al. 2013). The shape of the power spectrum is subjective and depends on the number of samples (frequency of acquisition).

12.2.3 Time and Frequency Domain

To examine the chaotic characteristics of gas-solid interaction present in pressure signals and visualize the flow scales, the wavelet analysis was used to decoupling original pressure signals into different scales. The wavelet analysis transforms a signal in the time domain into the time-frequency domain. Initially, the continuous wavelet transformation is defined as Eq. (9)

$$f(a,b) = \langle f, \psi_{a,b} \rangle = \frac{1}{|a|^{1/2}} \int f(t)\psi^{*}\left(\frac{t-b}{a}\right)dt. \tag{9}$$

where ψ is the mother function, $1/|a|^{1/2}$ is a normalization factor, a represent the dilation parameter responsible for the localization in the frequency domain, and b the translation parameter that allows for the localization on the time domain (Sasic et al. 2006). As a result of non-periodicity of the signal, the dilatation and translation parameters are discretized:

$$a = a_0^m, b = n_l b_0 a_0^m \tag{10}$$

Thus, the discrete wavelet transform expression is obtained:

$$f(m, n_l) = \langle f, \psi_{m,n_l} \rangle = \frac{1}{|a_0|^{1/2}} \int f(t)\psi^{*}\left(a_0^{-m}t - n_l b_0\right)dt. \tag{11}$$

In essence, the discrete wavelet transform (DWT) is based on high-pass and low-pass filters, which decompose the signal into a low-frequency component A known as an approximation and a high frequency component known as D, called the detail (Mallat 1989):

$$f(t) = \sum_{i=1}^{k} A_k + D_j. \tag{12}$$

The decomposed signal known as bands or levels was grouped based on frequency, where each information bands represent information about a different frequency of original signal. This frequency can be related to the flow scale (microscales, mesoscales, and macroscales) and their respective phenomena. In the present paper, the wavelet decomposition was performed using a software coded in MATLAB © using the Daubechies 8 as the mother function to provide a multiresolution analysis.

12.3 Methodology

The experiments were run on the Pilot Unit of Riser and Cyclones, which can be seen in Fig. 1. This system consists of a riser made of acrylic with 12 m high and a T outlet. The internal diameter of the riser is 100 mm. Two cyclones placed at the exit of the riser returned the entrained solid to a reservoir. The solid used in the experiments as fluidized particles was glass beads with a mean diameter of 91 µm and particle density of 2450 kg/m^3, which were classified as Geldart group B. Atmospheric air was used as gas phase, and the relative humidity varied between 60 to 80%; the mean temperature was 25 °C and the pressure was 1 atm.

The system was operated in different experimental conditions. The mean gas velocity varied between 7 m/s and 10 m/s to provide information about how the increase of turbulence affects the flow scales. In order to identify the influence of the solid phase, different mass flow ($\dot{m}_s$) was used 0 kg/m^{2}s, 9.09 kg/m^{2}s, 20.23 kg/m^{2}s, 7.67 kg/m^{2}s and 15.80 kg/m^{2}s. These mass flow conditions were chosen to check the clean flow behavior and how the system variated with the addition of particles and the increase of the particles concentration.

The impact of the particles on the flow scales and their dynamics was measured through the acquisition of pressure signals obtained in the middle of the riser at 6 m from the particles feed, where the flow is developed. The data were collected using a differential pressure transducer with an output signal of 0–5000 Pa. The transducers were connected to the measurement points by small polyethylene tubes with an internal diameter of 5 mm and a length of 40 cm. A data acquisition system composed of a National Instruments USB-6000 board connected to a computer was responsible for receiving the pressure signals and transforming them into a digital signal. The frequency response used was 1000 Hz to be obtained in agreement with the Nyquist minimum frequency. The data was collected in 30 min and the first 10 s was analyzed, which resulted in 10,000 samples for each operational condition. The software created on the platform LabVIEW 2015 assisted in data visualization and acquisition, as well as in the reactor control system.

After the data acquisition, the processing was carried out with the aid of the MATLAB® software. Thereafter the PSD is calculated, the mother Wavelet function and the high-pass and low-pass filters are applied to the chosen levels, generating images of the details and approximation signals. Finally, the program stores and saves the data.

12.4 Results and Discussion

12.4.1 Frequency Domain

The power spectral density obtained for the experiments was used to analyze how frequencies behave in the different operation conditions. Figures 2 and 3 present

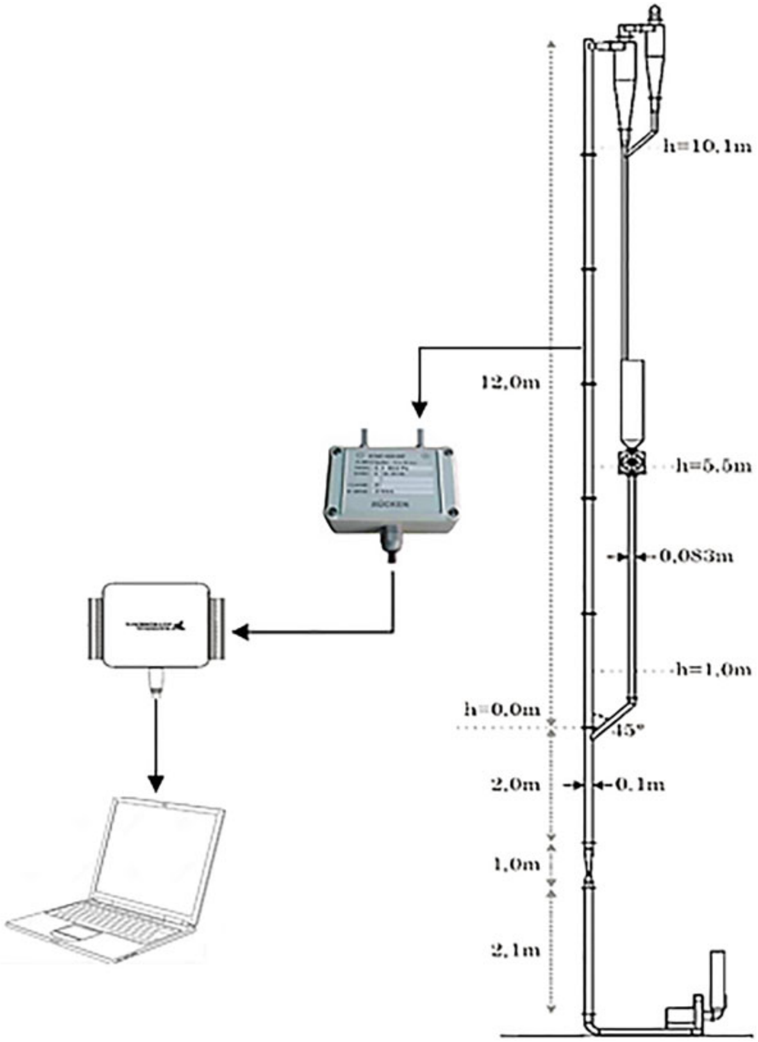

Fig. 1 Schematic of the experimental system: the pilot unit of riser and cyclones and the pressure acquisitions

the results for two gas phase velocities (v_g), 7 m/s and 10 m/s, respectively. It was observed in all cases several peaks across the spectrum with a frequency component of larger amplitude, almost always positioned at 30 Hz. According to Bi (2007), these highest intensity peaks are generally characterized as dominant frequencies, and these frequencies can correspond to different mechanisms.

When observing the predominant frequencies for the clean flow (Case A) at 7 m/s (Fig. 2), it is possible to see that the power peaks present in the high frequencies (70–300 Hz) were those that had the greatest variation, while the dominant frequency is

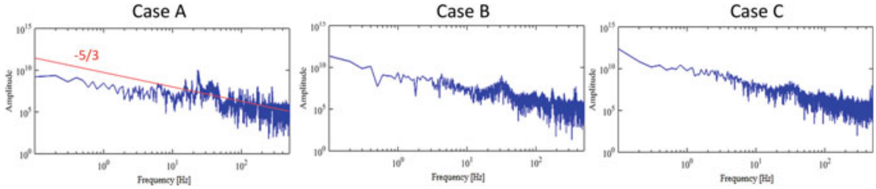

Fig. 2 Power spectral density, $v_g = 7\,\text{m/s}$: case A—clean flow; case B—$\dot{m}_s = 9.09\,\text{kg/m}^2\text{s}$; and case C—$\dot{m}_s = 20.23\,\text{kg/m}^2\text{s}$

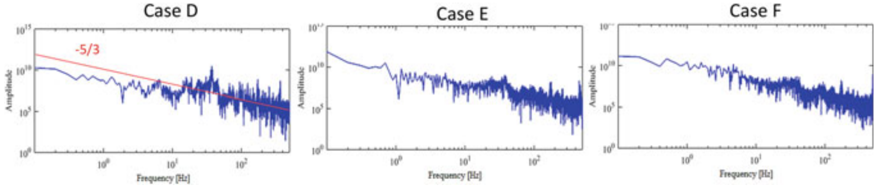

Fig. 3 Power spectral density, $v_g = 10\,\text{m/s}$: case D—clean flow; case E—$\dot{m}_s = 7.67\,\text{kg/m}^2\text{s}$; and case F—$\dot{m}_s = 15.80\,\text{kg/m}^2\text{s}$

25 Hz. When a flow of glass beads particles was fed (Case B), a low attenuation of the high frequencies amplitude is observed, the dominant peak moved to 30 Hz and a turbulent structure remains energized at 180 Hz. The increase of the solids flow (Case C), by its turn, results in stronger attenuation of the peaks around 100 Hz, except the one at 180 Hz. The increase in mean flow velocity to 10 m/s (Fig. 3) showed a shift to higher frequencies as a whole, even to the clean flow (Case D), where the dominant frequency changed to 35 Hz, this behavior was related to an increase in the energy of the system and consequently on turbulence. The solids mass flux is not the same compared to the lower flow velocity; however, there is a proximity between the ones of Cases B and E, C and F. Such comparison reveals that the energy intensity is nearly the same, although the frequency shifts an increase in peaks, the same characteristic of peaks attenuation with the addition of particles still was observed for all cases.

The results obtained show that the addition of solid particles impacts decreasing the power signals, which can be an indication of turbulence attenuation, while the increase in the gas phase velocity resulted in an elevation of the signal variation of the clean flow, as expected. On the other hand, the energized turbulent scales became the ones with higher frequency, those with smaller, more isotropic, and faster scales. The fact that the turbulent gas-solid flow is composed of multi-flow structures makes it difficult to determine the nature of the signal peaks. However, it was possible to observe that the 70–300 Hz frequencies were the most affected by particles.

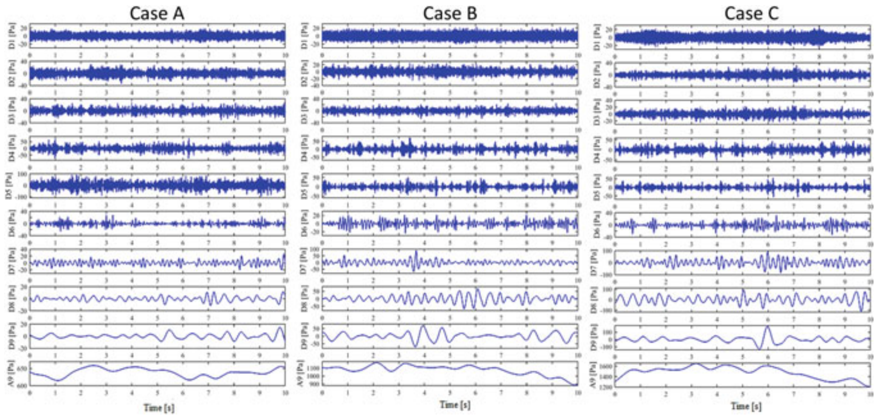

Fig. 4 Nine-level wavelet coefficients and one approximated coefficient of fluctuating pressure signal at the center of the riser ($v_g = 7\,\mathrm{m/s}$): case A—clean flow; case B—$\dot{m}_s = 9.09\,\mathrm{kg/m^2s}$; and case C—$\dot{m}_s = 20.23\,\mathrm{kg/m^2s}$

12.4.2 Time and Frequency Domain

In order to reveal features of the phase interactions in the gas-solid turbulent flow and verify which scales are most affected, the wavelet analysis was applied. The wall pressure fluctuations data collected was decomposed from wavelet levels 1 to 9, where each detail level represents a frequency range of the original signal. The 9 levels were the largest possible number of decompositions used for the 10 s time interval. Figures 4 and 5 provide an overview of all obtained fluctuation levels and are represented by the details D1, D2, …, D9 with the last approximation A9 at 7 m/s and 10 m/s, respectively. Both figures show the clean gas flow (Case A) and gas-solid flow cases with the increase of mass loadings (B and C).

Even though the results reflect the behavior of all scales, it is necessary to reveal the flow dynamics at different scales. As a result, the levels were separated to represent the flow scales based on the frequency. This division is illustrated in Table 1, where the phenomena of the main flow are presented based on each scale. As mentioned, the flow dynamics in fluidized beds systems is discussed at three levels of details. First, the microscale signals characterizing by phenomena with high frequency as gas turbulence, gas-solid and particle-particle interactions, were represented by components D1–D3. Then, the mesoscales that include frequency phenomena, localized at the medium range, as particles clusters and bubbles were characterized by components D4-D6. Lastly, the macroscales, which considers low-frequency phenomena, influenced by the effect of the fluidized bed unit geometry on the system behavior, have D7–D9 as representation components.

The homogeneity of the nine details was investigated using the standard deviation of each level and it is shown in Fig. 6. This statistical analysis makes it possible to

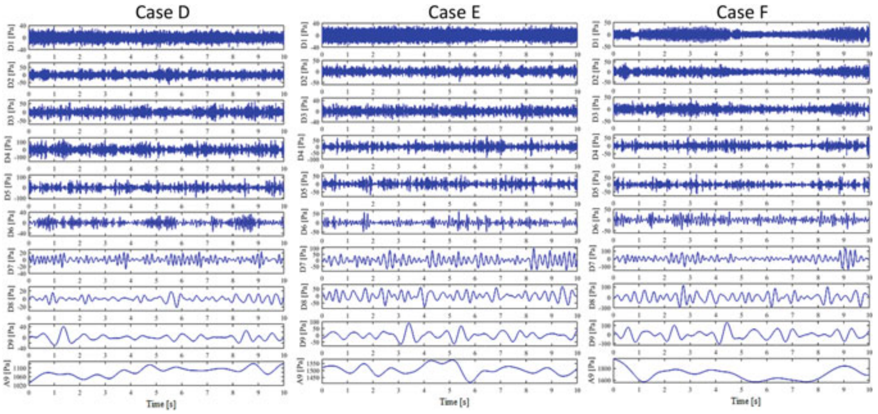

Fig. 5 Nine-level wavelet coefficients and one approximated coefficient of fluctuating pressure signal at the center of riser ($v_g = 10\,\text{m/s}$: case D—clean flow; case E—$\dot{m}_s = 7.67\,\text{kg/m}^2\text{s}$; and case F—$\dot{m}_s = 15.80\,\text{kg/m}^2\text{s}$

Table 1 Scale division, flow scales, and characteristics

Level j	Approximation A_j (Hz)	Detail D_j (Hz)	Flow scale	Flow characteristics
1	0–250	250–500	Microscale	Gas turbulence and particle-gas interaction
2	0–125	125–250		
3	0–62.5	62.5–125		
4	0–31.3	31.3–62.5	Mesoscale	Clusters
5	0–15.6	15.6–31.3		
6	0–7.81	7.81–15.6		
7	0–3.91	3.91–7.81	Macroscale	Unit scale phenomena
8	0–1.95	1.95–3.91		
9	0–0.977	0.977–1.95		

identify the levels with the greatest fluctuations by comparing these fluctuations between different experimental conditions.

For the clean flow (Cases A and D), the D5–D6 scales were the ones that achieved the greatest pressure fluctuation, thus it is estimated that the turbulent structures of the mesoscale were predominant in this flow. With the addition of particles with low solids mass fluxes (Cases B and E), the fluctuation of the mesoscales levels was attenuated, and the microscales D1–D3 were increased. As seen in Figs. 2 and 3, the energy intensity of the high frequency scales was attenuated, but the wavelet analysis shows that the fluctuation of these signals was increased with the solids flux. The pressure fluctuations of the turbulent flow scales between 125 and 150 Hz (D2) were increased 6 times from the $v_g = 10\,\text{m/s}$ clean flow to the dense flow ($\dot{m}_s = 15.80\,\text{kg/m}^2\text{s}$), while the 7.81–15.6 Hz scales were reduced 3 times in the same conditions. In the condition with the highest mass loadings (Cases C and F),

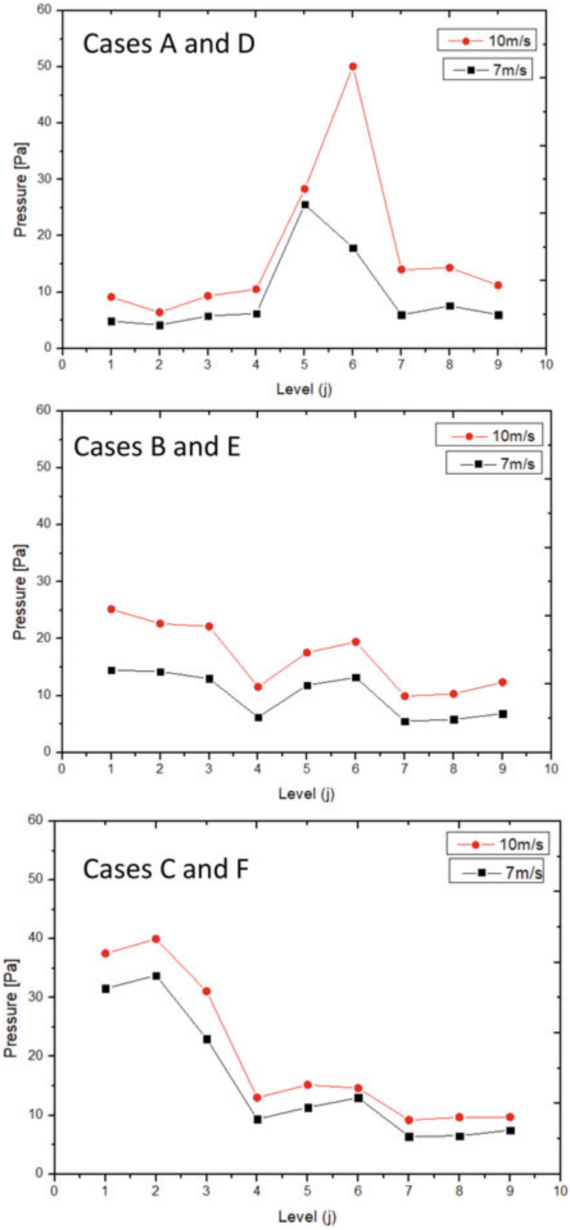

Fig. 6 Standard deviation of the pressure signals at each detail level: ($v_g = 7\,\mathrm{m/s}$): case A—clean flow; case B—$\dot{m}_s = 9.09\,\mathrm{kg/m^2s}$; and case C—$\dot{m}_s = 20.23\,\mathrm{kg/m^2s}$. . ($v_g = 10\,\mathrm{m/s}$): case D—clean flow; case E—$\dot{m}_s = 7.67\,\mathrm{kg/m^2s}$; and case F—$\dot{m}_s = 15.80\,\mathrm{kg/m^2s}$

the behavior observed in the Cases B and D was intensified at the microscales in a way much more relevant than at mesoscales. The increase of gas velocity resulted in the same behavior in all experiments, all scales pressure fluctuations were increased but they kept the same behavior. These results suggest that the addition of particles causes a dissipation of larger turbulent structures, at the same time two phenomena may be related to the increase in small scales. First, the particles split large structures assisting the dissipation process. Second, when the Kolmogorov length scales, which indicates that the smallest turbulent structures, are calculated to the clean flow as $\lambda_{K,7m/s} = 1.4 \times 10^{-4}\,\mathrm{m}$ and $\lambda_{K,10\,\mathrm{m/s}} = 1.1 \times 10^{-4}\,\mathrm{m}$, therefore, the smallest turbulent structures are of the same magnitude of particle size. Thus, the simple movement of particles can produce the smallest turbulent structures, or the particle-particle interaction can be responsible to increase the microscale fluctuation. These observations are similar to those obtained by Hussainov et al. (2000) and Utzig et al. (2015) for vertical flow.

Two objects of discussion were raised to explain the absence of structures in macroscales. The measurement point closer to the wall can influence the results, Gu et al. (2019) observed an action of the wall gradually appears and is restricted to medium-range fluctuations. Thus, this study did not consider the influence of the feeding and solids outlet. The observation time is another point of discussion, the short time of observation could be not enough to form structures with very low frequencies and large time and space scales.

12.5 Conclusions

Through the analysis of pressure signals wavelet transformation, the multiscale behavior contained in the turbulent gas-solid flow in the central region of a circulating fluidized bed riser was studied. The frequency and time-frequency domain were combined to observe the dominants frequencies and the most affected scales by particles. Relevant conclusions of this study were summarized as follows:

- The investigation of the predominant frequencies through the power spectral density, showed peaks along the entire frequency spectrum, where the greatest amplitude was observed at 20–30 Hz to the clean flows. With the addition of solids, these peaks were attenuated, such that the magnitude of this attenuation was directly related to the solids mass flow;
- The application of the Wavelet transform was performed for nine decomposition levels to the assessment of the most affected scales. The standard deviation of the detail levels revealed that at the single-phase flow the scales with the greatest fluctuation were as mesoscale classified. The addition of particles attenuated those scales, transferring energy to the microscales, which experienced greater fluctuations;

- The effect of the increase in gas phase velocity resulted in an increase in the flow scales intensity and the attenuation of mesoscales can be an indication of the influence of particles in the process of dissipating turbulent structures;
- The absence of well-defined macroscale structures was related to the short time of observation and the possible wall effect. Thus, for future work it is recommended to increase the investigation time and observe different radial measurement points as the effects of the entry and exit of solids. Measurements in these regions can supplement the information on the flow behavior;
- Lastly, the effects related to solid properties such as density and particle diameter used on the flow scales can add more information on the gas-solid interaction and turbulence modulation.

Acknowledgements The authors would like to acknowledge the support of Fundação de Amparo à Pesquisa e Inovação do Estado de Santa Catarina (Fapesc).

References

Bendat JS, Piersol AG (1986) Analysis and measurement procedures. John Wiley & Sons, New York

Bi HT (2007) A critical review of the complex pressure fluctuation phenomenon in gas–solids fluidized beds. Chem Eng Sci 62:3473–3493

Chen Y, Chen W, Grace JR, Zhao Y, Zhang J, Li Y (2016) Direct resolution of differential pressure fluctuations to characterize multi-scale dynamics in a gas fluidized bed. Int J Multiph Flow 85:380–394

Cong X, Guo X, Lu H, Gong X, Liu K, Sun X, Xie K (2013) Flow patterns of pulverized coal pneumatic conveying and time-series analysis of pressure fluctuations. Chem Eng Sci 101:303–314

Felipe CAS, Rocha SCS (2004) Time series analysis of pressure fluctuation in gas-solid fluidized beds. Braz J Chem Eng 21(3):497–507

Gu L, Zhang Y, Zhu J (2019) Wavelet denoising and nonlinear analysis of solids concentration signal in circulating fluidized bed riser. Particuology

Hussainov M, Kartushinsky A, Rudi Ü, Shcheglov I, Kohnen G, Sommerfeld M (2000) Experimental investigation of turbulence modulation by solid particles in a grid-generated vertical flow. Int J Heat Fluid Flow 21:365–373

Johnsson F, Zijerveld RC, Schouten JC, van den Bleek CM, Leckner B (2000) Characterization of fluidization regimes by time-series analysis of pressure fluctuations. Int J Multiph Flow 26:663

Kage H, Iwasaki N, Yamaguchi H, Matsuno Y (1991) Frequency analysis of pressure fluctuation in fluidized bed plenum. J Chem Eng Jpn 24:76–81

Li J (2000) Compromise and resolution—exploring the multi-scale nature of gas-solid fluidization. Powder Technol 111:50–59

Mallat SG (1989) A theory for multiresolution signal decomposition—the wavelet representation. IEEE Trans Pattern Anal Mach Intell 11:674–693

M'Chirgui A, Tadrist H, Tadrist L (1997) Experimental investigation of the instabilities in a fluidized bed origin of the pressure fluctuations. Phys Fluids 9:500–509

Musmarra D, Poletto M, Vaccaro S, Clift R (1995) Dynamic waves in fluidized beds. Powder Technol 82:255–268

Sasic S, Leckner B, Johnsson F (2006) Time–frequency investigation of different modes of bubble flow in a gas–solid fluidized bed. Chem Eng J 121(1):27–35

Sasic S, Leckner B, Johnsson F (2007) Characterization of fluid dynamics of fluidized beds by analysis of pressure fluctuations. Prog Energy Combust Sci 33:453–496

Shou M, Leu L (2005) Energy of power spectral density function and wavelet analysis of absolute pressure fluctuation measurements in fluidized beds. Chem Eng Res Des 83:478–491

Utzig J, Guerra HP, Decker RK, Souza FJ, Meier HF (2015) Gas-solid turbulence modulation: Wavelet MRA and euler/lagrange simulations. Chem Eng Trans 43:1675–1680

van Ommen JR, Sasic S, van der Schaaf J, Gheorghiu S, Johnsson F, Coppens MO (2011) Time-series analysis of pressure fluctuations in gas–solid fluidized beds—a review. Int J Multiph Flow 37:403–428

van der Schaaf J, Schouten JC, van den Bleek CM (1998) Origin, propagation and attenuation of pressure waves in gas–solid fluidized beds. Powder Technol 95:220–233

Verloop J, Heertjes PM (1974) Periodic pressure fluctuations in fluidized beds. Chem Eng Sci 29:1035–1042

Yang T, Leu L (2009) Multiresolution analysis on identification and dynamics of clusters in a circulating fluidized bed. Aiche J 55:612–629

Wu B, Kantzas A, Bellehumeur CT, He Z, Kryuchkov S (2007) Multiresolution analysis of pressure fluctuations in a gas–solids fluidized bed: application to glass beads and polyethylene powder systems. Chem Eng J 131(1–3):23–33

Chapter 13
Influence of Ultrasonic Waves and Airfoil-Shaped Ring Baffles on the Gas-Solid Dispersion in a CFB Riser

Vivien Rossbach, Sarah Laysa Becker, Natan Padoin, Henry França Meier, and Cintia Soares

Abstract Circulating fluidized beds (CFB) are used in several industrial applications, in which more homogeneous fluidization of solid particles is desired. In these devices, the core-annulus profile and the clusters of particles decrease the gas-solid contact. Two alternatives to improve solids dispersion are the use of aerodynamic ring-type baffles and ultrasonic waves. In this work, the influence of these devices on the solids dispersion in a lab-scale CFB riser was evaluated using Phase Doppler Anemometry (PDA) measurements. We used five airfoil-shaped ring baffles with 10 mm of thickness and 20 transducers with a frequency of 40 kHz and an input power of 10, respectively, above the riser inlet. The ring baffles increase the solid velocity near the wall and the ultrasound decreases it. With a velocity of 5.6 m/s, the solids distribution in the cross section improves with the rings and worsens with the influence of ultrasound, but with 8.3 m/s rings and ultrasound improve the solids distribution. The gas-solid dispersion improved by 18% with baffles at 8.3 m/s and 17% with ultrasound at 5.6 m/s. This study indicates that both the ring baffles and the ultrasonic field applied in the riser inlet region increase the gas-solid dispersion and contribute to reducing the concentration of particles near the riser walls and the development of clusters.

Keywords Circulating fluidized bed (CFB) · Airfoil-shaped ring baffles · Ultrasonic waves · Gas-solid dispersion

---

V. Rossbach · S. L. Becker · N. Padoin · C. Soares
Federal University of Santa Catarina (UFSC), Campus Universitário, s/n, Florianopolis, SC, Brazil
e-mail: natan.padoin@ufsc.br

C. Soares
e-mail: cintia.soares@ufsc.br

V. Rossbach · H. F. Meier (✉)
University of Blumenau, Rua São Paulo, Blumenau, SC 3250, Brazil
e-mail: meier@furb.br

H. F. Meier et al. (eds.), *Advances in Turbulence*, ABCM Series on Mechanical Sciences and Engineering, https://doi.org/10.1007/978-3-031-25990-6_13

13.1 Introduction

Circulating Fluidized Beds (CFB) are used in different industrial applications, as in the fluid catalytic cracking (FCC) process (Da Rosa et al. 2008), polymerization in the gaseous phase (Yan et al. 2012), ozone decomposition (Jiang et al. 1991) and oxy-coal combustion (Zhou et al. 2011). The gas-solid flow in a CFB riser is ascendant and the radial forces involved push solid particles into the riser wall, which leads to the formation of the core-annulus profile. A central dilute region with higher velocity and another region near the wall, with higher solids concentration and lower velocity, characterize this solids concentration profile (Ferschneider and Mège 2002). In processes that involve chemical reactions, as the FCC process, catalyst particles are the solids phase. Here, the first gas-solid contact occurs above the solids inlet region, and the reaction is completed rapidly. The presence of the core-annulus profile in this region decreases the contact between the catalyst particles and the gas phase containing reagents, reducing the yield of these reactions (Gan et al. 2011). In addition, a locally higher solids flux causes the particles to fall near the wall which produces back mixing and the over-cracking of products into light compounds (Namkung and Kim 1998).

Many alternatives were proposed to redistribute solid particles in the CFB riser and improve gas-solids contact in the inlet region. A viable alternative is the use of ring baffles with a variety of geometrical formats, like aerodynamic, wedged, trapezoidal, and squared baffles. These baffles are an intrusive technique that reduces the opening area and redirect solid particles from the wall to the center of a duct. Also, the use of acoustic waves is a non-intrusive way to improve gas-solids contact in the riser inlet region. Rossbach et al. (2016a, b,2019) used a set of airfoil-shaped ring-type baffles to improve solids distribution in the inlet region of a lab-scale CFB riser under dilute flow conditions. The authors studied numerically and experimentally the gas-solid flow behavior and used a statistical dispersion coefficient to evaluate the solids dispersion improvement due to the ring baffles. Four baffles with a thickness of 10 mm and an opening area of 80% were introduced below and above the solids inlet. The aerodynamic format of the baffles slows up the laminar boundary layer detachment from the surface and reduces back mixing. The solid particles were accelerated in the baffle region and redirected to the riser center. Rossbach et al. (2020) investigated the influence of ultrasonic waves on the solids dispersion in a lab-scale CFB riser. A design of experiments was conducted to find the best configuration for the ultrasonic device, including geometrical properties, sound frequency, and input power, under dilute flow conditions. As a result, the authors proposed the construction of a cylindrical device in which 20 transducers with a frequency of 40 kHz and a power of 10 W produce acoustic streaming transversally to the gas-solid flow direction. The acoustic energy increases gas turbulence and improves gas-solids mixing in the radial direction. Sufficient acoustic energy applied to the gas-solid flow can increase solids fluctuation to break up clusters of particles.

This study aims to compare the gas-solids dispersion in a lab-scale CFB riser using the ultrasonic device proposed by Rossbach et al. (2020) and the airfoil-shaped ring-type baffles of Rossbach et al. (2019). For that, experimental data of solid velocity and solid volume fraction of the two cases and the blank case were compared in the same operating conditions. We evaluated solids dispersion using the statistical dispersion coefficient proposed by Rossbach et al. (2016a) and the radial Péclet number correlation of Wei et al. (1998).

13.2 Material and Methods

This section presents the CFB experimental unit and the particle dispersion devices. The experimental methodology and the PDA technique used in the measurement of flow properties are also described.

13.2.1 Experimental Setup

The lab-scale CFB unit is presented in Fig. 1. Air at ambient conditions enters the riser base (1) when suctioned by an exhauster positioned at the riser outlet, while the solid particles are fed through the inclined duct (2), coming from a storage vessel (3), whose mass flow is controlled by a rotating valve. In this study, glass spheres with a specific mass of 2450 kg/m^3 and an average surface diameter of 80 μm were used as a solid phase. Air with solid particles exits on top of the riser, where a cyclone collects these particles and the air is directed to a bag filter. The riser outlet has an inclination of 12° relative to the solids inlet (2), as stated in Fig. 1a. the riser has a height of 2.667 m and an internal diameter of 0.104 m, as stated in Fig. 1c. The solids inlet has an internal diameter of 0.044 m, an inclination of 45° relative to the vertical line, and is positioned 40 cm above the gas inlet.

The ultrasonic device illustrated in Fig. 1b is positioned 70 cm above the gas inlet and has a total height of 0.092 m. In this device, 20 Manorshi MSO-P1640H12T transmitters with a width of 10 mm and an external diameter of 16 mm were arranged in 4 rows facing each other on the x and y axes shown in the figure. Each row has 5 transducers equally spaced for a vertical distance of 3 mm. The transducers have a frequency of 40 kHz, a sound pressure level of 115 dB, and individual electric power of 10 W. Taking into account the reference pressure of 20 μPa, it is considered that the set of transducers produces a sound pressure level of 128 dB in the internal flow to the riser. In this design, ultrasonic waves were generated on an Arduino UNO board using the code developed by Marzo et al. (2017). Square waves equivalent to sinusoidal waves with a frequency of 40 kHz are produced and delivered to an H-L298n bridge. The H-L298n bridge amplifies the power of the wave and delivers it to the transmitters, where these electrical signals are converted into acoustic signals. If the distance between two transducers arranged opposite each other is equal to

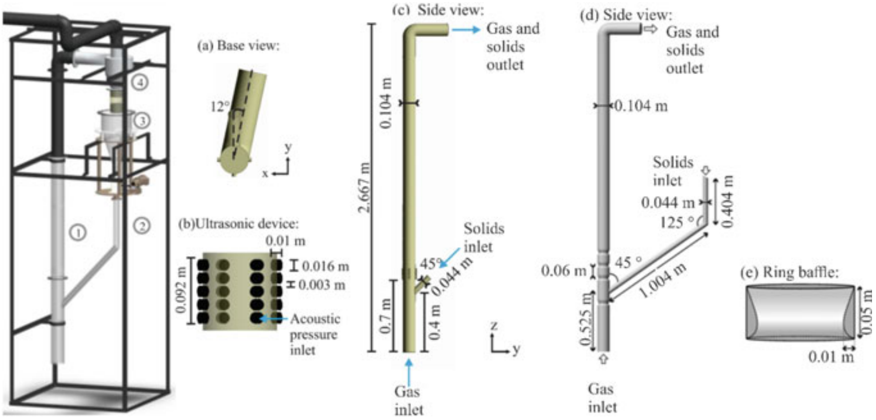

Fig. 1 Geometry of the CFB unit and the experimental devices: **a** base view of the gas and solids outlet; **b** ultrasonic device; **c** side view of the lab-scale CFB riser with the ultrasonic device; **d** side view of the riser with airfoil-shaped ring baffles; **e** geometry of the ring baffles

the internal diameter of the riser, the ratio between this distance and the half of a wavelength results in 24.04 pressure nodes that are formed. As this is not an integer value, the acoustic field produced is slightly non-resonant. However, one must also consider the acoustic field deformation caused by the gas-solid flow transversal to it and the interaction between the acoustic fields of the neighboring transducers.

The ring baffles were manufactured in polypropylene, with the geometrical properties stated in Fig. 1e. Each baffle has a height of 0.05 m and a thickness of 10 mm, resulting in an internal opening area of 80% relative to the duct area. Four baffles were inserted into the riser, the first being below the solids inlet and the others above, with 60 mm from each other, as illustrated in Fig. 1d.

Table 1 describes the operating conditions used in the experiments, both with ring baffles and acoustic waves. The ambient air velocity was varied by 5.7 m/s and 8.3 m/s and the mass flow of solids was varied by 1.60 kg/m^{2}s and 2.93 kg/m^{2}s. These operating conditions are limited by the capacity of the experimental unit and produce solid loadings compatible with the measurement technique used because the PDA technique has limitations in measuring concentrated particulate flows. In this study, we also aim to detect the formation of particle clusters in the inlet region and the core-annulus flow in the riser wall, which occur less frequently in diluted flows (Bi and Grace 1995) such as those adopted. However, these phenomena can be observed even in diluted flows, because of the instabilities generated by the collisions between particles and the high turbulence (Helland et al. 2007). Table 1 shows the solids mass loading and the solids-to-gas ratio corresponding to the 4 operating conditions studied. An analysis using the fluidization diagram of Bi and Grace (1995) shows that conditions 1 and 2 are in the limits of fast fluidization, while conditions 3 and 4 are classified as dilute phase transport. According to Bi and Grace (1995), a fast fluidization regime is characterized by a higher concentration of particles at the base

Table 1 Operating conditions of the experiments

Operating condition	v_g (m/s)	G_s (kg/m^{2}s)	Solids mass loading (kg sol./kg gas)	Solids-to-gas ratio (kg sol./m^3 gas)
1	5.7	1.60	0.23	0.28
2	5.7	2.93	0.43	0.51
3	8.3	2.93	0.29	0.35
4	8.3	1.60	0.16	0.19

and a diluted top region. The diluted phase transport regime may or may not exhibit a core-annular profile.

13.2.2 PDA Measurements

The PDA technique was used to gain experimental data from the gas-solid flow with acoustic waves, with deflector rings, and without solid dispersion devices. The error of this measurement technique is lower than 1% for the velocity and 5% for the particle diameter and concentration (Werther 1999). Dantec Dynamics A/S anemometer was used to perform non-invasive optical measurements of velocity, concentration, and diameter of the solid particles keeping the experimental design proposed in Table 2. An acquisition time of 60 s was adopted, to guarantee that over 2000 particles were measured at each point and that the time average of the measurements was the same at all points. The software BSA Flow was used to determine particle velocity from the Doppler frequency. The concentration and diameter of the particles were measured using a 112 mm PDA probe as a receiver (Rossbach et al. 2020a). The measurements were made at points along the cross section, at a height of 0.80 m from the gas inlet, as shown in Fig. 2. The measurement points were used to plot solid velocity and solid volume fraction profiles on the x and y axes. Mean data was also transformed using polar coordinates to get maps of properties in the cross section.

Table 2 PDA configurations for the experimental measurements of the gas-solid flow in the CFB riser

Acquisition time	60 s
Scattering angle	50°
Focal distance to the transmitter	300 mm
Focal distance to the receptor	310 mm
Polarization direction	Negative
Scattering mode	1st order refraction
Phase-validation ratio	30%
Refraction index	1.51
Laser power	70 mW

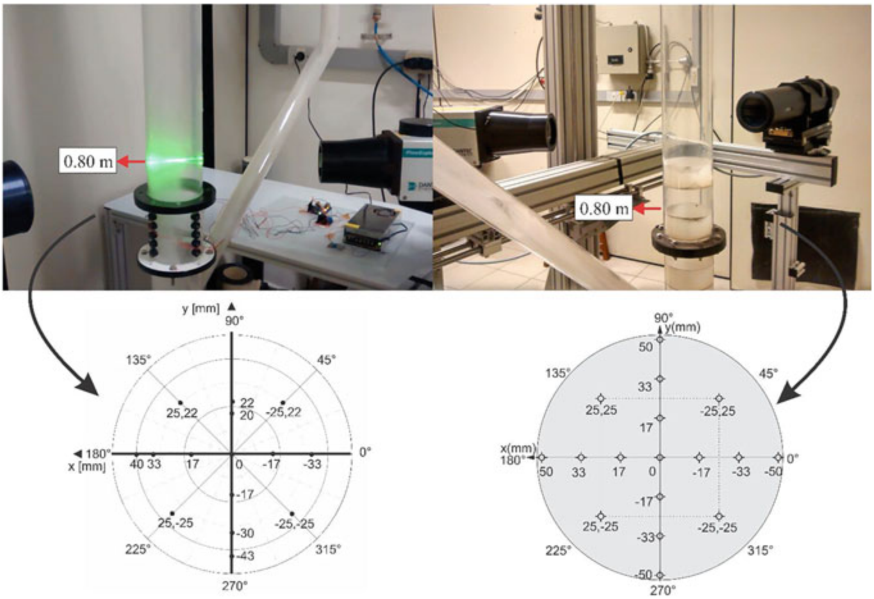

Fig. 2 Illustration of the experimental setup and maps of points measured in the cross section of the riser at 0.80 m height

13.2.3 Solids Dispersion Coefficient

Solids dispersion along the cross section of the riser at a height of 0.80 m was evaluated using the statistical dispersion coefficient as proposed by Rossbach et al. (2019). Gas-solid dispersion was also evaluated, using the correlation for the radial Péclet number proposed by Wei et al. (1998). The solids dispersion coefficient (C_v) was calculated using Eq. (1), where $\tilde{\sigma}_{sd}$ is the standard deviation of the solid volume fraction and $\overline{x}$ is the mean value of the property in the points of the cross section. The radial Péclet number (Pe_{sr}) is given by Eq. (2), where f_s is the mean solid volume fraction at the points and the Reynolds number is calculated using the solid velocity, a particle density of 2450 kg/m^3 and a viscosity of 1.7×10^{-5} PaS.

$$C_v = \frac{\tilde{\sigma}_{sd}}{\overline{x}} \tag{1}$$

$$Pe_{sr} = 225.7(1 - f_s)^{-0.29} Re^{0.43} \tag{2}$$

13.3 Results and Discussion

13.3.1 Solid Velocity

Figure 3 presents a comparison of the solid velocity profiles for the gas-solid flow in the riser with ring baffles, with ultrasonic waves, and without these two methods. The solid velocity profiles presented in Fig. 3a–d are situated in the symmetrical axis of the riser, while the solid velocity profiles illustrated in Fig. 3e–h are situated in the unsymmetrical axis of the riser which is parallel to the solids inlet. These are the transversal lines that go from one wall to the other, passing through $r = 0$. In the unsymmetrical axis, the solid velocity profiles of the three cases are similar and have a minor deviation from the expected axisymmetric profile on the left side, because of the larger solids concentration in these regions. With ring baffles, this deviation is slighter and the velocity profiles are closed to an axisymmetric behavior. Also, solid velocity increases in some regions of the ring-baffled riser concerning the standard case. In the operating conditions C1 and C2, the solids velocity slightly decreases using ultrasound, but if the fluctuations are considered, the velocity profiles are substantially the same. However, the cross-flow generated by the ultrasonic waves regarding the ascendant gas-solid flow produces a contrary effect to the desired one on its dispersion. It can be checked especially in conditions C1 and C2, where the gas velocity of the ascendant flow is smaller. Otherwise, an increase in the solid velocity can be noted near one of the walls of the ring-baffled riser in Fig. 3b, f because of the reduction of the opening area in the region of the rings. In the operating condition C3, the solid velocity increased with respect to the standard case in one of the walls, both with ultrasound and ring baffles. However, the solid velocity profile on the unsymmetrical axis became smoother with ultrasound (Fig. 3g). In the operating condition C4, only the ring baffles changed the solid velocity with respect to the standard case.

The solid velocity was modified in the unsymmetrical axis (Fig. 3e–h) with respect to the standard case using ring baffles and acoustic waves, but not in all the cases. In the operating condition C1, there was no velocity variation in the case with ultrasound relative to the standard case. With ring baffles, the velocity variation was greater on the wall parallel to the solids inlet. However, the velocity increased on the wall opposite to that, where more particles accumulate. In the operating condition C2, there was a decrease in the solid velocity with the use of ring baffles on the wall opposite the solids inlet and an increase in velocity on the other wall. In this operating condition, the solid velocity was not modified with the use of ultrasound; however, its behavior Is similar in both cases—ring baffles and ultrasound—on the wall opposite to the solids inlet. In the operating conditions C3 and C4, the solid velocity profiles are more symmetric because the gas superficial velocity is higher than in the other conditions It causes a more diluted flow and reduces the thickness of the core-annulus profile. The solid velocity profile in condition C3 (Fig. 3g) is more unsymmetrical with ring baffles and a decrease of these values near the wall is observed near the wall. With the use of ultrasound, there is a slight increase in the solid velocity in the same region

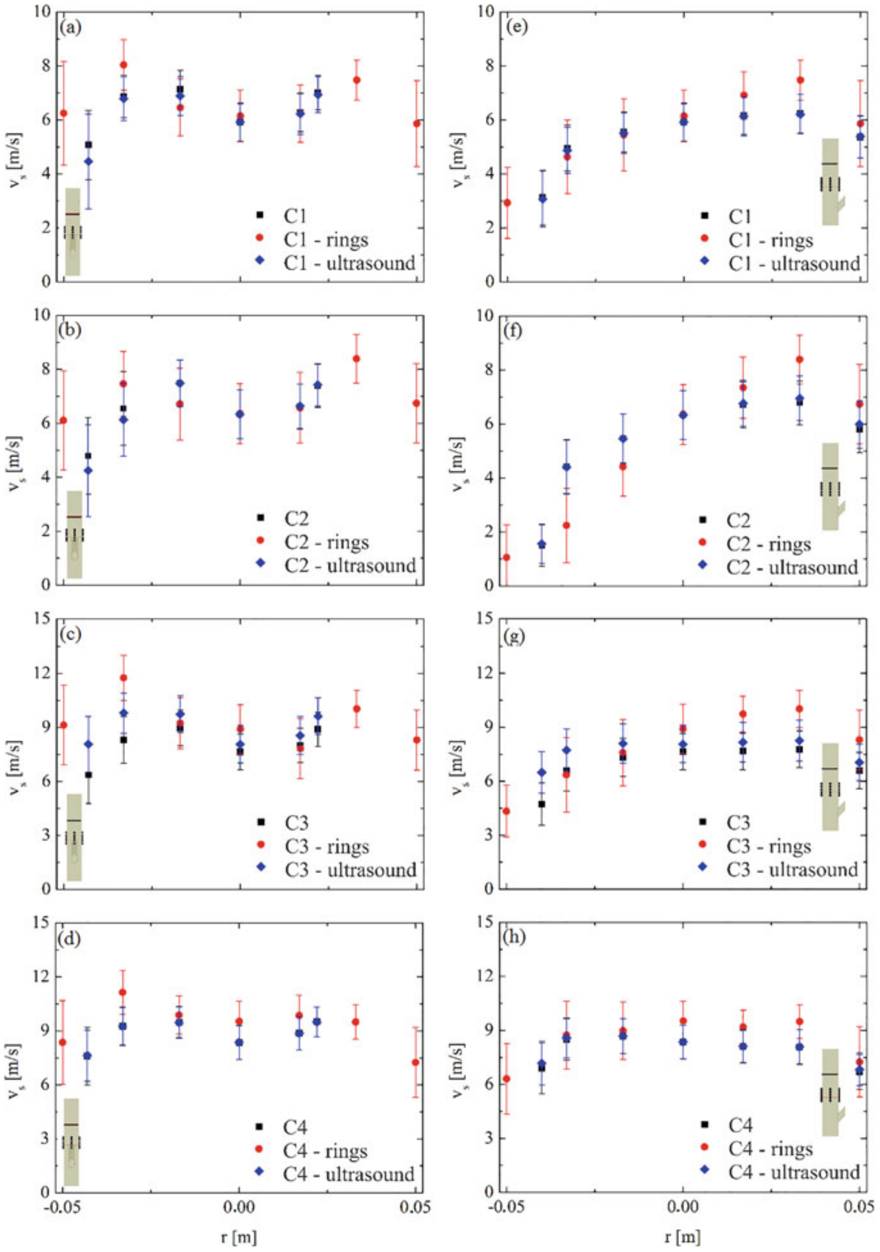

Fig. 3 Solid velocity profiles of the four operating conditions with and without ring baffles and with the influence of the acoustic field. The error bars are the RMS values of the variables

regarding the standard case and uniform distribution of velocities along the axis. In condition C4, the velocity profiles were not modified considering the fluctuation values.

The RMS values in Fig. 3 show the mean solid velocity fluctuation during the acquisition time of the PDA measurements. In the symmetrical axis of the riser, both the ring baffles and the ultrasonic waves increase solid velocity fluctuation near the wall. Otherwise, lower solid velocity fluctuation is observed in the unsymmetrical axis with the use of ultrasonic waves. The lower values of velocity fluctuation are observed near the wall opposite to the solids inlet, where the solids concentration is higher. It suggests that the particle clusters were not broken but increased, as shown in the next results. However, in the operating condition C2, even though particle clusters were not broken, solid velocity became negative near the wall considering the RMS values in the unsymmetrical axis, with the use of ring baffles. At least 10,000 values of solid axial velocity were gathered with PDA at each point, with an error lower than 1%. The raw data showed a normal distribution and some negative values of velocity were observed, which was associated with the fall of particles that, consequently, lead to back mixing.

13.3.2 Solid Volume Fraction

In Fig. 4, the solid volume fraction contours of the three cases are compared at 0.80 m above the base of the riser, calculated using the solids concentration and the average Sauter diameter given by the PDA technique at each measurement point. The standard cases in the four operating conditions (C1, C2, C3, and C4) are in the first line, followed by the cases with ring baffles and with ultrasound. In the operating conditions C1 and C2, the ring baffles contribute to a better solids dispersion, decreasing its concentration in the annular region and improving the distribution of solids along the cross section. In these cases, the use of ultrasound increased the concentration of particles in the annular region and reduced dispersion. In the operating conditions, C3 and C4 both ring baffles and ultrasound contributed to promoting the solids dispersion. In the cases with ring baffles, the particles are redirected to the center of the riser and accumulate in this region. With acoustic waves, there is a slight accumulation of particles in the center and their dispersion along the cross section is similar to that observed with ring baffles. Regarding the core-annulus profile, the ring baffles contributed to breaking it in the measured position. Ultrasound was not able to reduce the concentration of solids near the wall under operating conditions C1 and C2, in which the fast fluidization regime is dominant. One reason for this result may be that the superficial velocity of the flow is low relative to the solids mass loading, causing the pressure drop to be greater and there is a back mixing. Also, it can be noted a large difference in the solid volume fraction distributions in Fig. 4, although the difference in velocity profiles between the 3 cases (standard, ring baffles, and ultrasound) is minimum. The velocity component measured with the PDA technique is the axial component. With ultrasound, the greatest change in velocity takes place

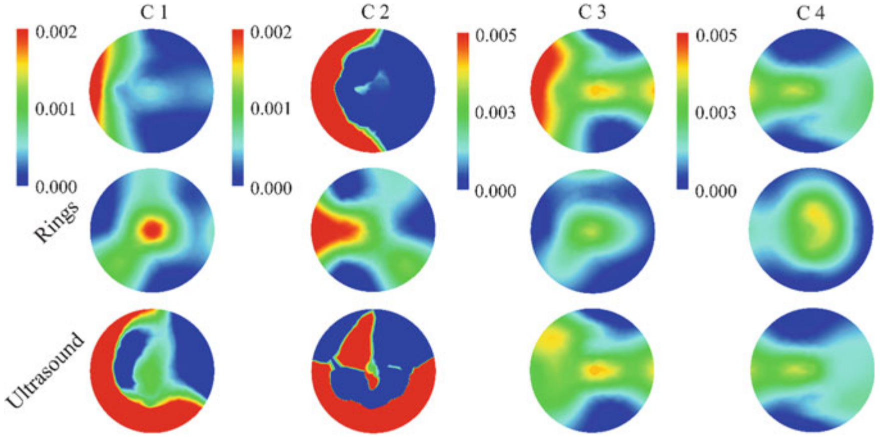

Fig. 4 Solid volume fraction contours in the riser cross section at 0.80 m height in the operating conditions C1, C2, C3, and C4 with and without ring baffles and with the influence of ultrasonic waves

in the radial direction, which is the direction of propagation of the emitted acoustic waves. This difference in the radial velocity causes the significant change observed in the distribution of solid particles in the cross section. Similar behavior can be attributed to the flow with ring baffles since they redirect the particles near the wall toward the center of the riser. In the ring-baffled riser, however, the axial velocity increases in some points because the opening area of the flow decreases near the baffles.

13.3.3 Gas-Solid Dispersion

The gas-solid dispersion was evaluated using the radial Péclet number, which is the product between the Reynolds number and the Schmidt number of the solids flow. The Péclet number is the product between the Reynolds number and the Schmidt number of the gas-solid flow and relates the importance of convective and diffusive effects on the gas-solid dispersion. It is common to use the modified Péclet number to assess the gas-solid dispersion in CFB risers (Breault 2006), as this parameter considers not only the volume fraction but also the velocity of the solid particles, resulting in a more complete analysis than if only the solid volume fraction was considered. Figure 5 shows the contours of these variables in the cross section at a height of 0.80 m. In the first line are the standard cases (C1, C2, C3, and C4) in the four operating conditions studied. The same operating conditions with the use of ring baffles and ultrasonic waves to disperse solid particles are illustrated in the second and third lines. In the operating condition C1, the radial Péclet number increased on the wall with the use of rings, however, the distribution of this variable in the cross section is more homogeneous in the standard case and with ultrasound. In the operating condition C2, both rings and ultrasound increased the Péclet number near to the riser wall. With rings, there are higher Pe_{sr} values on the walls and smaller ones in the center. With ultrasound, the distribution of particles in the center of the riser was not modified and there was an increase in Pe_{sr} in the wall region. In the operating conditions C3 and C4, there was little influence of ultrasound on the Péclet number, but a better distribution is noted in case C3 with ultrasound, in which there an increase in Pe_{sr} was observed in the wall region. With rings, there is an increase in Pe_{sr} values close to the wall and a slight decrease in the center of the duct in the operating condition C3. The lower influence of ultrasound on the gas-solid dispersion in condition C4 is because this condition has a dilute homogeneous flow, with dispersion that is satisfactory even without the use of dispersion techniques. In conditions C1 and C2, which are of fast fluidization regime, there is a higher solids loading and a tendency to develop clusters due to the number of collisions between particles. Visually, the performance of the ultrasound in increasing the gas-solid dispersion was better in the operating condition C3, in which solids concentration and superficial velocity are higher compared to the other conditions. It provides more dispersion of the acoustic energy by the particles and less impact on the pressure drop compared to conditions C1 and C2.

Using ring baffles improves the gas-solid dispersion near the wall because there is an increase in solids velocity in this region that is attributed to the decrease in the opening area. Also, the solid particles are redirected from the wall to the center of the riser, and their momentum increase in the radial direction. When the increase in Pe_{sr} is very large on the walls, its value decreases in the center of the riser, which is

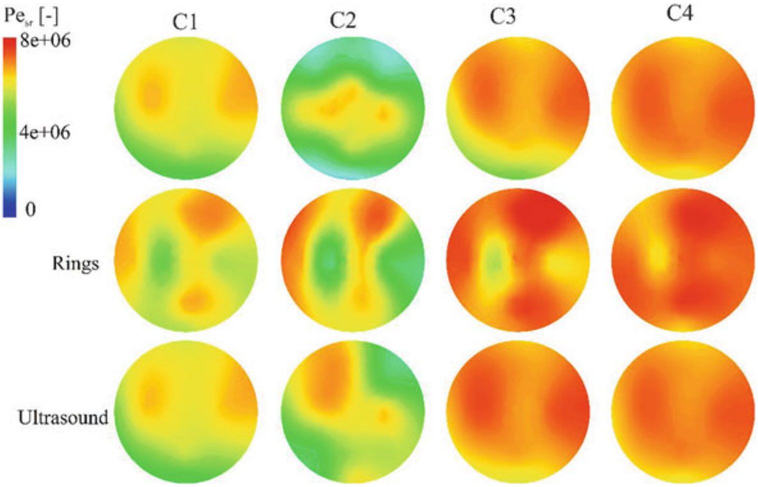

Fig. 5 Radial Péclet number (Pe$_{sr}$) of the four operating conditions with and without ring baffles and under the influence of the acoustic field at 0.80 m height

not desirable. To avoid this behavior, a large increase in the superficial velocity must be avoided, as this can cause the bed dilution and lower gas-solid dispersion.

To quantify the solids dispersion in the cross section of the riser, the solids dispersion coefficient and the radial Péclet were calculated for the cross section in each case, at 0.80 m above the base of the riser, as shown in Fig. 6. In the operating condition C1, the dispersion coefficient decreased by 51% with rings and increased by 60% with ultrasound. In condition C2, there was a decrease of 72% with rings and 24% with ultrasound. In conditions C3 and C4 there was a decrease in the dispersion coefficient in both cases. With rings, the decrease was 5% and 8% with ultrasound. In condition C4, it was 16% with rings and 10% with ultrasound. In the analysis of the radial Péclet number, an increase in the value of the variable compared to the standard case shows that the gas-solid dispersion improved. The greatest Péclet number values were observed in case C2 with acoustic waves and in case C3 with rings. In the operating condition C3, both techniques improve the dispersion of particles, but the rings provide a better result. In operating condition C2, the gas-solid dispersion improves a lot with the use of ultrasound and worsens with the use of ring baffles. This result differs from the analysis of the dispersion coefficient, which shows that the solids dispersion with the use of rings improves in condition C2. It is noteworthy that the Péclet number provides more complete results of the gas-solid dispersion, as it considers the solid velocity and the solid volume fraction. The statistical dispersion coefficient considers only the mean solid volume fraction and its standard deviation in the cross section. In the operating condition C1, it is also noted that the statistical dispersion coefficient shows lower solids dispersion with ultrasound, which is not observed considering the Péclet number. In the operating condition C4, the dispersion coefficient shows that the dispersion worsens with both techniques, but there is an increase in the Péclet number with the use of ring baffles. The best gas-solid dispersion with ultrasound was obtained in the cases where the solids loading is higher and, thus, the acoustic field interacts with a larger number of particles. With the use of ring baffles, the best gas-solid dispersion considering the Péclet number was obtained with the highest solids velocity, equal to 8.3 m/s.

13.4 Conclusions

Considering these results, both dispersion techniques presented are feasible to increase the contact between the solid particles and the gas phase in a CFB riser. Although ultrasound cannot break the core-annulus profile under the conditions of rapid fluidization analyzed, its use increases the gas-solid contact in the radial direction, as verified through the Péclet number. However, it is necessary to test the effect of acoustic waves on the flow under other operating conditions, by applying different sound frequencies and electrical powers in the transducers. Ring baffles are an intrusive way to reduce the core-annulus profile development in the flow and to break particle clusters. Using ring baffles in extended operating campaigns leads to wear and erosion, and that must be analyzed together with the pressure drop generated

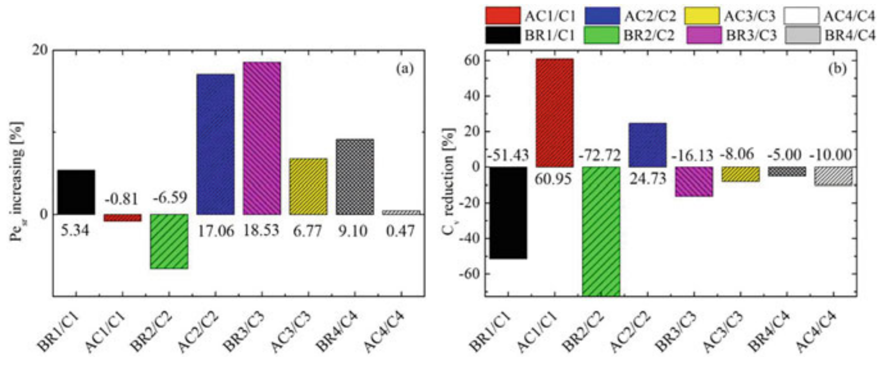

Fig. 6 Increasing in the radial Péclet number (Pe_{sr}) and reduction in the solids dispersion coefficient (C_V) with acoustic waves and ring baffles in comparison with the standard measurements in the four operating conditions (C1, C2, C3, C4). BR refers to the cases with ring baffles and AC, to the cases with ultrasonic waves

because of the reduction of the opening area. Also, it is necessary to assess, for both techniques, in which axial positions new deflectors or transducer sets should be positioned to prevent the core-annulus profile to develop again and reducing the gas-solid contact.

Acknowledgements The authors are grateful for the financial support of this research from Petróleo Brasileiro S.A. (Petrobras), through the cooperation agreements 0050.0070 334.11.9 and 5850.0103010.16.9, and from the National Council for Scientific and Technological Development (CNPq), under process number 308714/2016-4. This study was financed in part by the Coordenação de Aperfeiçoamento de Pessoal de Nível Superior - Brasil (CAPES).

References

Bi HT, Grace JR (1995) Flow regime diagrams for gas-solid fluidization and upward transport. Int J Multiph Flow

Breault RW (2006) A review of gas-solid dispersion and mass transfer coefficient correlations in circulating fluidized beds. Powder Technol

Da Rosa LM, Bastos JCSC, Mori M, Martignoni WP (2008) Simulation of a high-flux riser-reactor flow using CFD techniques. AIChE Annu Meet Conf Proc

Ferschneider G, Mège P (2002) Dilute gas-solid flow in a riser. Chem Eng J 87(1):41–48

Gan J, Yang C, Li C, Zhao H, Liu Y, Luo X (2011) Gas–solid flow patterns in a novel multi-regime riser. Chem Eng J 178:297–305

Helland E, Bournot H, Occelli R, Tadrist L (2007) Drag reduction and cluster formation in a circulating fluidised bed. Chem Eng Sci

Jiang P, Bi H, Jean RH, Fan LS (1991) Baffle effects on performance of catalytic circulating fluidized bed reactor. AIChE J 37(9):1392–1400

Marzo A, Barnes A, Drinkwater BW (2017) TinyLev: a multi-emitter single-axis acoustic levitator. Rev Sci Instrum 88(8)

Namkung W, Kim SD (1998) Gas backmixing in a circulating fluidized bed. Powder Technol

Rossbach V, Padoin N, Meier HF, Soares C (2020) Influence of acoustic waves on the solids dispersion in a gas-solid CFB riser: numerical analysis. Powder Technol 359:292–304

Rossbach V, Utzig J, Decker RK, Meier HF (2016a) Experimental analysis of the gas-solid flow in a ring-baffled CFB riser using Laser Doppler Anemometry (LDA) and Phase-Doppler Anemometry (PDA). In: Proceedings of EPTT 2016a—10th ABCM spring sch transit turbul

Rossbach V, Utzig J, Decker RK, Noriler D, Meier HF (2016b) Numerical gas-solid flow analysis of ring-baffled risers. Powder Technol

Rossbach V, Utzig J, Decker RK, Noriler D, Soares C, Meier HF (2019) Gas-solid flow in a ring-baffled CFB riser: numerical and experimental analysis. Powder Technol 345

Wei F, Cheng Y, Jin Y, Yu Z (1998) Axial and lateral dispersion of fine particles in a binary-solid riser. Can J Chem Eng

Yan WC, Li J, Luo ZH (2012) A CFD-PBM coupled model with polymerization kinetics for multizone circulating polymerization reactors. Powder Technol 231:77–87

Werther J (1999) Measurement techniques in fluidized beds. Powder Technol 102:15–36

Zhou W, Zhao C, Duan L, Liu D, Chen X (2011) CFD modeling of oxy-coal combustion in circulating fluidized bed. Int J Greenh Gas Control 5:1489–1497

Part IV
Instrumentation and Experiments

Chapter 14
Estimation of the Energy Dissipation Rate in a Stirred Tank by 2D PIV Measurements

Lucas Freitas de Lima e Freitas, Helder Lima de Moura,
Rodrigo de Lima Amaral, Paula Trindade da Silva, José Roberto Nunhez,
and Guilherme José de Castilho

Abstract Stirred tanks agitated by impellers are used in a wide range of industries, e.g., chemical, food, pharmaceutical, and petroleum. The tank design, the impellers, and the number and type of baffles are often associated with their application. Thus, the experimental investigation of these parameters in the turbulent flow is crucial for the control and optimization of this equipment. Particle Image Velocimetry (PIV) is a non-intrusive and quantitative technique that allows determining the vector fields of the flow using tracers. The distribution obtained by this method can also assist in the validation of CFD simulations. The objective of this work is to estimate the energy dissipation rate (EDR) of a stirred tank from PIV 2C-2D measurements and its relation with the spatial resolution. The work was conducted in 0.38 m diameter tank (T) with a pitch blade turbine (PBT) impeller of diameter D ($D/T = 1/3$) in water. The angle-resolved PIV enables a number of turbulent features to be identified. Hence, measurements were taken for three angles, 0°, 45°, and 75°. The EDR was estimated using four methodologies: by the assumption of local axisymmetry (AS), by direct estimation (DE), by modified direct estimation (MDE), and by large eddy simulation (LES). For the optimization and reduction of possible errors, different

---

L. F. de Lima e Freitas · H. L. de Moura · P. T. da Silva · J. R. Nunhez · G. J. de Castilho (✉)
Process Engineering Department, School of Chemical Engineering, University of Campinas,
Campinas, Brazil
e-mail: guijcas@unicamp.br

L. F. de Lima e Freitas
e-mail: l192527@dac.unicamp.br

H. L. de Moura
e-mail: h115196@dac.unicamp.br

P. T. da Silva
e-mail: p211778@dac.unicamp.br

J. R. Nunhez
e-mail: nunhez@unicamp.br

R. de Lima Amaral
NDF, Department of Mechanical Engineering, POLI, University of São Paulo, São Paulo, Brazil
e-mail: rodrigoamaral@usp.br

H. F. Meier et al. (eds.), *Advances in Turbulence*, ABCM Series on Mechanical Sciences
and Engineering, https://doi.org/10.1007/978-3-031-25990-6_14

processing strategies were used to decrease the noise level of the PIV measurements. This study showed that values of EDR were found to vary by two orders of magnitude from near the impeller to the circulation region of the tank. Herein, the effect of measuring angle on EDR was analyzed and provided an insight into the anisotropy of the turbulence in the stirred tank. However, EDR estimation is exceptionally challenging due to the lack of knowledge to distinguish its accuracy and the influence of spatial resolution.

Keywords Turbulence flow · EDR · Spatial resolution · Stirred tank · Impeller · PIV

14.1 Introduction

Mechanically agitated mixing tanks are widely used in industrial operations such as in the food, pharmaceutical, oil, chemical, and metallurgical areas. They are used for mixtures of liquids, solid–liquid, dispersion of gas in liquids, reactive flows, and to improve the efficiency of mass and heat transfer (Guida et al. 2010). Impellers (or mechanical stirrers) and baffles (or deflectors) are the essential elements of a mixing tank. Due to the application of the mixing tank in different contexts, its geometry, the design of the impellers, and the number of deflectors are important variables in the optimization of this equipment. Thus, these geometric properties and operating conditions can directly define the fluid dynamics inside the tank (Basavarajappa et al. 2015; Sossa-Echeverria and Taghipour 2015). The flows generated in the agitated tanks are predominantly turbulent due to the high rotor speeds used to achieve the necessary process conditions, such as the mixing time (Basavarajappa et al. 2015). Research to investigate the characteristics of turbulent flow in processes is essential for understanding the industrial operations mentioned above. The energy dissipation rate is widely studied to determine the characteristics of the single-phase and multi-phase mixing process (Joshi et al. 2011; Liu et al. 2016). In the turbulent regime, fluid dynamics are characterized by a wide range of length scales, for example, the Kolmogorov scale (Eq. 1)—η, where turbulent kinetic energy is dissipated by molecular viscosity (Escudié and Liné 2003).

$$\eta = \left(\frac{v^3}{\varepsilon}\right)^{1/4} \tag{1}$$

where v is the kinematic viscosity of the fluid.

Particle image velocimetry (PIV) is one of the most relevant experimental techniques in contributing to many advances in understanding turbulent and complex flow (Westerweel et al. 2013). The PIV technique is a non-intrusive flow measurement method that provides instantaneous velocity fields through tracer particles introduced into the flow (Okamoto et al. 2000; Prasad 2000). According to Hoque et al. (2014), it is possible to calculate important parameters such as velocity gradient, integral length scale, structure functions, and spatial energy spectrum from PIV 2C-2D data. However, there are certain conditions to estimate the energy dissipation rate from the velocity data, and each of them has limitations depending on the theoretical assumptions, such as assuming isotropy.

14.1.1 Energy Dissipation Rate

In a mixing tank, the impeller transmits kinetic energy to the fluid, generating both the mean flow field and the fluctuating velocities associated with it (Guida et al. 2010). The kinetic energy supplied to the fluid by the impeller is eventually converted to heat by viscous dissipation. Shear stresses perform a deformation work that increases the internal energy of the fluid at the expense of the kinetic energy of turbulence (Khan 2005). Direct PIV experimental data are unable to resolve the smallest length scale, resulting in an underestimation of turbulent dissipation (Hlawitschka and Bart 2012). In addition, for the PIV 2C-2D technique, only the axial and radial components of the velocity can be measured in the x–y plane (Unadkat 2009). Thus, several estimation methods have been studied in the past years to decrease the EDR underestimation, and the following methods were performed in this work.

14.1.1.1 Direct Estimation (DE)

Gabriele et al. (2009) determined the EDR using direct estimation. For this method, it is necessary to provide an estimate for the third component (w), in this case, using the statistical isotropy hypothesis (Delafosse et al. 2011; Gabriele et al. 2009; Hoque et al. 2015; Khan 2005; Liu et al. 2016; Sharp and Adrian 2001).

$$\varepsilon_{DE} = v\left[2\overline{\left(\frac{\partial u}{\partial x}\right)^2} + 2\overline{\left(\frac{\partial v}{\partial y}\right)^2} + 3\overline{\left(\frac{\partial u}{\partial y}\right)^2} + 3\overline{\left(\frac{\partial v}{\partial x}\right)^2} + 2\overline{\frac{\partial u}{\partial y}\frac{\partial v}{\partial x}}\right] \tag{2}$$

14.1.1.2 Modified Direct Estimation (MDE)

According to Alekseenko et al. (2007), another method to estimate the EDR is using a correction factor. The proposed correction factor, f_e based on Pao (1965) spectrum for PIV resolutions below the Kolmogorov length scale, as follow:

$$f_e = 1 - e^{\left[-\frac{3}{2}\alpha\left(\frac{\pi}{\Delta}\eta_M\right)^{1/3}\right]} \tag{3}$$

$$\eta_M = \left(\frac{v^3 f_e}{\varepsilon}\right)^{1/4} \tag{4}$$

$$\varepsilon_{MDE} = \varepsilon_{DE}/f_e \tag{5}$$

where α is a constant equal to 1.6, η_M is the modified Kolmogorov length scale and ε_{MDE} was computed iteratively as follows: in the first cycle, f_e was taken as unity, and the value of η_M was estimated from the hypothetical value of ε, where $\varepsilon = max(\varepsilon_{MDE})$. In the second cycle, f_e was calculated from Eq. (3), and η_M was recalculated.

14.1.1.3 Large Eddy Simulation (LES)

The energy dissipation rate can be estimated by the large eddy simulation. Sheng et al. (2000) proposed this method that estimates the EDR by multiplying the sum of terms known by 9/5. Consequently, velocity gradients should be replaced by the sum of the known terms multiplied by 12/6. Thus, the estimation of EDR by the LES method is given by

$$\varepsilon_{LES} = C_s^2 \Delta^2 \left[4\overline{\left(\frac{\partial u}{\partial x}\right)^2} + 4\overline{\left(\frac{\partial v}{\partial y}\right)^2} + 2\overline{\left(\frac{\partial v}{\partial x}\right)^2} + 2\overline{\left(\frac{\partial u}{\partial y}\right)^2} \right]^{1/2} \tag{6}$$

where Δ is the filtered scale corresponding to the size of the interrogation window used in the PIV and C_s is the Smagorinsky constant, which can be assigned a value equal to 0.21 (Meyers and Sagaut 2007).

14.1.1.4 Assumption of Local Axisymmetry (AS)

This method to estimate the EDR is an alternative way, depending only on the measurements in the x–y plane. Once the asymmetric axis is identified, this hypothesis leads to an estimate of the EDR using the four-velocity gradients solved in the 2D Classic PIV (George and Hussein 1991; Xu and Chen 2013). Thus, EDR can then be estimated from the velocity gradients of the measured planes using Eq. (7).

$$\varepsilon_{AS} = v\left[\overline{\left(\frac{\partial u}{\partial x}\right)^2} + 8\overline{\left(\frac{\partial v}{\partial y}\right)^2} + 2\overline{\left(\frac{\partial v}{\partial x}\right)^2} + 2\overline{\left(\frac{\partial u}{\partial y}\right)^2} \right] \tag{7}$$

14.2 Methodology

Experiments were conducted in an acrylic tank with ASME 10% torispherical bottom (width $T = 380$ mm, height $H = 760$ mm (50 L)) equipped with a four-pitched-blade impeller (diameter $D = T/3$ and inclination angle 45°) and four equally spaced baffles ($B = 0.1\,T$), as shown in Fig. 1. The chosen fluid for the experiments was water with the following physical properties density $\rho = 998.2\,\text{kg}\cdot\text{m}^{-3}$, and viscosity $\mu = 1.003\,\text{mPa}\cdot\text{s}$. The impeller was placed, and its rotation speed was maintained at $N = 660$ rpm, providing a Reynolds number $Re = \rho N D^2/\mu$ (1.7×10^5). As shown in Fig. 1a, the PIV 2C-2D system consists of a Nd:YAG laser (emission wavelength 532 nm), a FlowSense EO 8M-21 CCD camera with a resolution of 3312 × 2488 pixels. The seeding particles used were silver coated hollow glass spheres with a mean particle diameter of 10 μm provided by Dantec Dynamics. A shaft encoder was employed to control the camera and laser by impeller position. In the present work, the angle between the impeller blade and the measuring plane was set to 0°, 45°, and 75° to demonstrate the anisotropy of flow in the stirred tank. The angle-resolved (AR) measurements were performed considering a fixed position between two consecutive baffles, and varying the plane relative to the position of the impeller, considering the 0° starting point in this plane. In other words, the tip of the impeller was aligned at 0° relative to the 45° plane between two baffles.

For each experiment, 1,000 pairs of images were recorded in double-frame mode and $100\,\mu s$ interframe time. The initial spatial resolution was defined as 36 × 36 px with a value of the size of the interrogation window (Δ) equal to 1.08 mm and with a final resolution of 5 × 5 px with a window size corresponding to 0.15 mm. In the image processing, the multigrid iterative interrogation window deformation strategy was applied, which was carried out from the adaptation of the spatial resolution (Kim and Sung 2006). In this way, the size of the interrogation window was

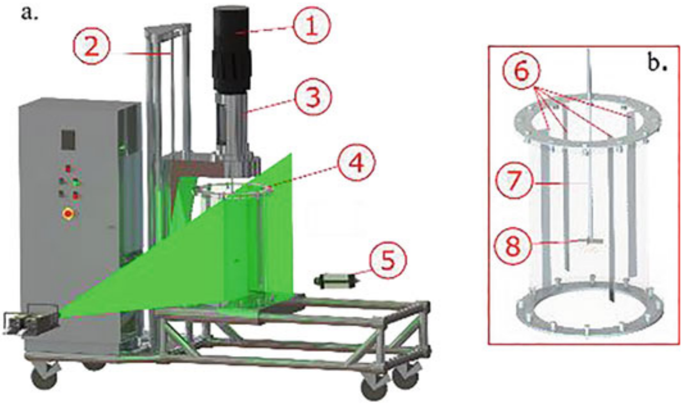

Fig. 1 Experimental set-up for PIV investigation: 1. Motor; 2. Shaft for adjusting the impeller height; 3. Torquemeter; 4. Acrylic tank; 5. Camera; 6. Baffles; 7. Shaft; 8. PBT 45° impeller

reduced progressively in 5 steps, making it possible to obtain 6 different spatial resolutions to analyze the EDR distribution: 36 × 36 px (1.08 mm), 27 × 27 px (0.81 mm), 20 × 20 px (0.6 mm), 15 × 15 px (0.45 mm), 10 × 10 px (0.3 mm) and 5 × 5 px (0.15 mm). Images were processed with standard cross-correlation (SCC) technique and optimized using the signal-to-noise ratio (SNR) metrics. The experiments were carried out with the camera focused on a limited image area to obtain high spatial resolution levels. Thus, the main objective of this study was to analyze the effect of estimating the EDR values from the variation of the spatial resolution for different fixed positions of the impeller in the image plane (0°, 45°, and 75°) in angle-resolved measurements. To observe this effect, four methods of estimating EDR, described above, were studied, namely: local axisymmetry (AS), direct estimation (DE), modified direct estimation (MDE), and large eddy simulation method (LES).

14.3 Results and Discussion

Figure 2 shows the results of the EDR distribution obtained at AR 0° measurements in two spatial resolutions: 36 × 36 px (1.08 mm) and 10 × 10 px (0.3 mm). The EDR distribution was estimated by the four methods described in the introduction, considering the EDR normalized by the rotation speed (N) and tank diameter (D), in the relation: ε/N^3D^2. The results for the 36 × 36 px resolution showed that the normalized EDR values varied in a range from 0 to 0.15 for the AS, DE, and MDE methods, whereas for the LES method, the maximum normalized EDR value was equal to 4. For the EDR distribution obtained for the 10 × 10 px of spatial resolution, the values of the maximum ε/N^3D^2 increased by 85% for the first three methods, with a value equal to $\varepsilon/N^3D^2 = 1$, while for the LES method, the increase in ε/N^3D^2 between the two spatial resolutions was smaller—with 20% variation compared to 36 × 36 px. It is evident the increase of the spatial coherence in the ε/N^3D^2 distributions by varying the spatial resolution from 1.08 mm to 0.3 mm. Also, the turbulent kinetic energy dissipation initialized just above the impeller tip and concentrated in that region for both spatial resolutions at AR 0°. While far from this region, little variation in energy dissipation was observed. This behavior is related to the formation and dissipation of the trailing vortex behind the reference blade, which occurred from this angle in a circulatory movement through the interaction of the impeller blades with the baffles, as described by Schäfer et al. (1998). In other words, a significant change in velocity caused by the movement of the blades occurred in this region close to the impeller, which generated considerable energy dissipation just behind and above the lead blade at AR 0°. Besides, the turbulence treatment was performed using an angle-resolved approach; thus, the periodicity induced by the crossing of the blades was attenuated, so that the dissipation values found have a main random contribution, in other words, the intrinsic turbulence to the flow (Yianneskis 2000).

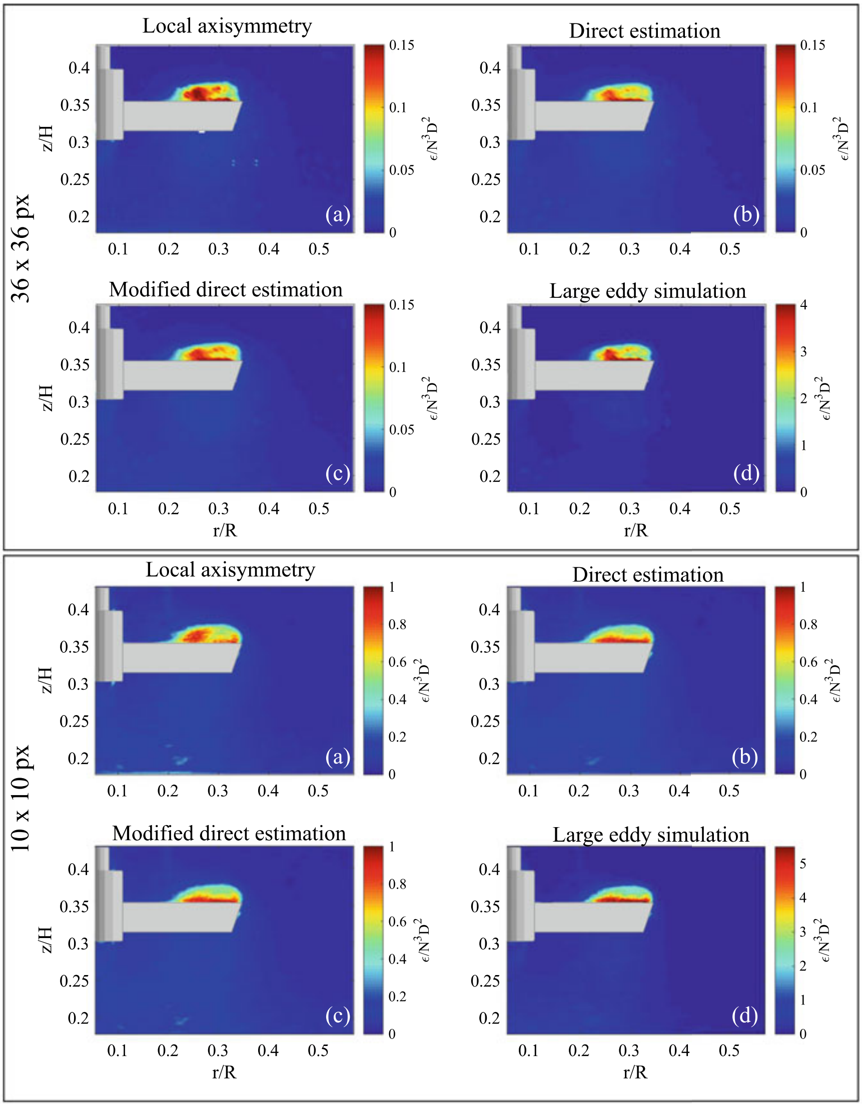

Fig. 2 Angle-resolved EDR distribution of 0° using different estimation methods with 36 × 36 px or 10 × 10 px **a** AS; **b** DE; **c** MDE and **d** LES

Figures 3 and 4 show the distribution of ε/N^3D^2 estimated by the same methods and spatial resolutions, at AR measurements 45° and 75°, respectively. Analyzing Fig. 3 for the 45° AR, it was possible to observe deviations from the maximum values of ε/N^3D^2 related to the effect of increasing the spatial resolution for the AS, DE, and MDE method, whose value was increased by 87.5%, with a local maximum equal to $\varepsilon/N^3D^2 = 0.4$. While for the LES method, the increase in spatial resolution to 0.3 mm implied an increase of 46.67% in the maximum of ε/N^3D^2, with a value equal to $\varepsilon/N^3D^2 = 1.5$. Applying the same analysis to Fig. 4, the deviations from the maximum of ε/N^3D^2 for the three methods were around 90%, with a final value $\varepsilon/N^3D^2 = 0.25$ for AS and DE, while for the MDE method, the final value was equal to $\varepsilon/N^3D^2 = 0.3$. The variation at AR 75° for LES was 50%, with a final value equal to $\varepsilon/N^3D^2 = 0.6$.

It was observed the increase of AR leads to a high deviation between the local maximums of EDR. This may be related to a higher degree of anisotropy for greater angles associated with the effect of magnifying the spatial resolution. Higher spatial resolutions imply a more significant number of velocity vectors computed in the plane optimizing the representativeness of ε/N^3D^2—predominantly anisotropic regions that present different turbulence scales (Micheletti et al. 2004; Liu et al. 2016). This can be evidenced by the points with intense magnitude (in red) of ε/N^3D^2, possibly inadequate in terms of representativeness of the phenomenon, for the 36 × 36 px resolution in the impeller discharge region. These inappropriate points occurred for both 45° and 75° angles in the vortex region of the PBT 45° impeller. This region is characterized by a non-stationary flow, with recirculation, vortices, eddies and pseudo turbulence (periodicity) that can be related to different macro-instability phenomena (Hasal et al. 2008).

Still comparing the dissipation phenomenon for different angles, from a global perspective, it was possible to observe for all ARs, a region of high energy dissipation presented itself close to the impeller tip. Also, it was clear that the maximum point shifted in the measurement plane, as the impeller blade changed its angle, indicating the movement and dissipation of the trailing vortices in the discharge region, suggesting a helical circular shape (Schäfer et al. 1998; Roy et al. 2010). Comparing the 0°, 45°, and 75° angles, the maximum points ε/N^3D^2 reduced proportionally with the increase of the blade angle. This indicated that the dissipation of the vortices occurred in a small region and gradually with the movement of the impeller relative to the baffle. It was also possible to observe that at AR 45°, the maximum point occurred farther from the tip of the impeller, indicating that for this angle, significant axial extension of the dissipated trailing vortices occurred.

At AR 75°, however, it was possible to observe a greater spread of the dissipation in the impeller discharge region, because, at this angle, there was greater interaction between the trailing vortex formed with the bulk flow, with a mixture between high and low ε/N^3D^2. This phenomenon described the dispersion, in which the vortices produced near the impeller blade broke as these structures move from the tip to the region of strong turbulence, where friction with the fluid dissipated most of the energy (Yianneskis 2000; Ducci and Yianneskis 2007). The understanding of this mixing process and the characterization of these macro-instabilities defined by trailing vortices and their effect on the efficiency of the agitation processes are complex and still present study opportunities, as mentioned by Nikiforaki et al. (2003).

According to Saarenrinne et al. (2001), it is possible to obtain 90% accuracy in determining the EDR for $\Delta \approx 2\eta$ and 65% accuracy for $\Delta \approx 9\eta$. In this work, $\eta =$

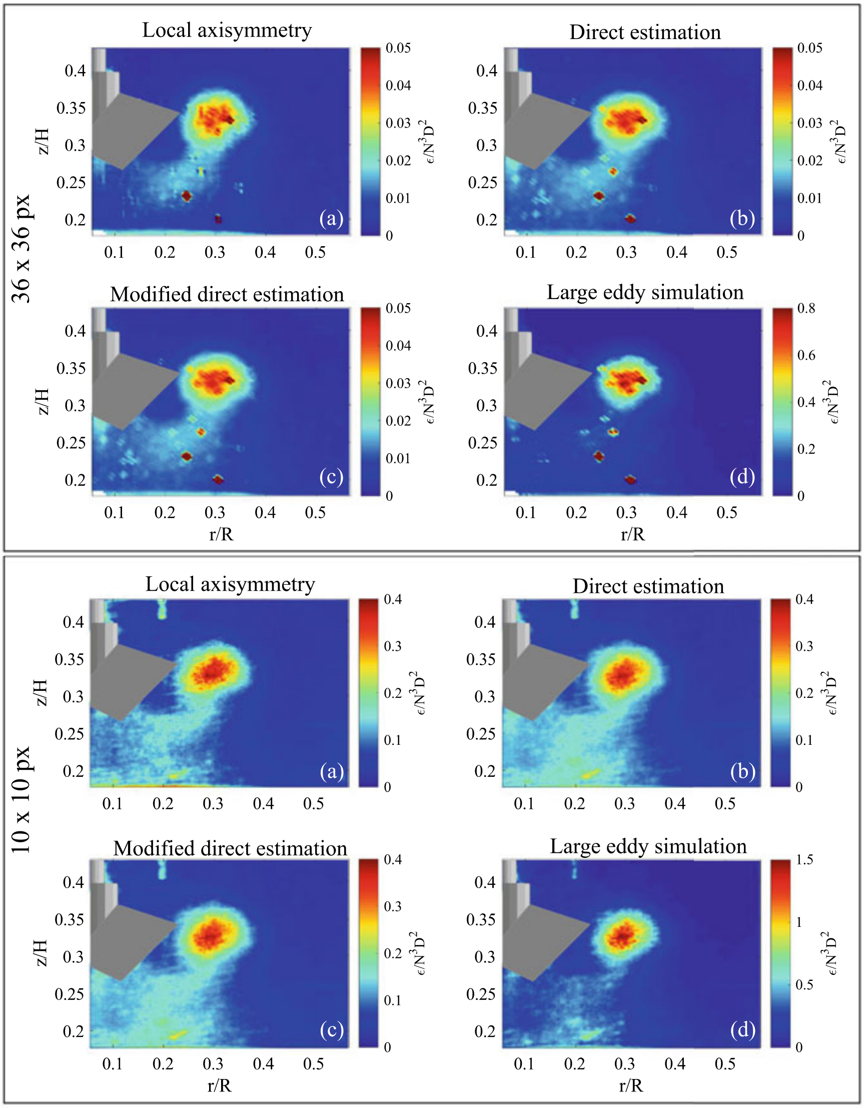

Fig. 3 Angle-resolved EDR distribution of 45° using different estimation methods with 36 × 36 px or 10 × 10 px: **a** AS; **b** DE; **c** MDE and **d** LES

0.029 mm determined by $\eta = \left(\upsilon^3/\overline{\varepsilon}_T\right)^1/4$. The average rate of energy dissipation in the tank was obtained by $\varepsilon = \overline{\varepsilon}_T = P/\rho V$. In this case, P $(P = 2\pi MN)$ is the power, M being the torque (0.98952 N · m), obtained experimentally for 660 rpm, and V the tank volume (0.05 m^3). Thus, for the spatial resolution of 36 × 36 px, we obtained $\Delta \approx 37\eta$, which was equivalent to an accuracy of 8% for EDR. And for the spatial resolution of 10 × 10 px, the calculated value was $\Delta \approx 10\eta$, which was a

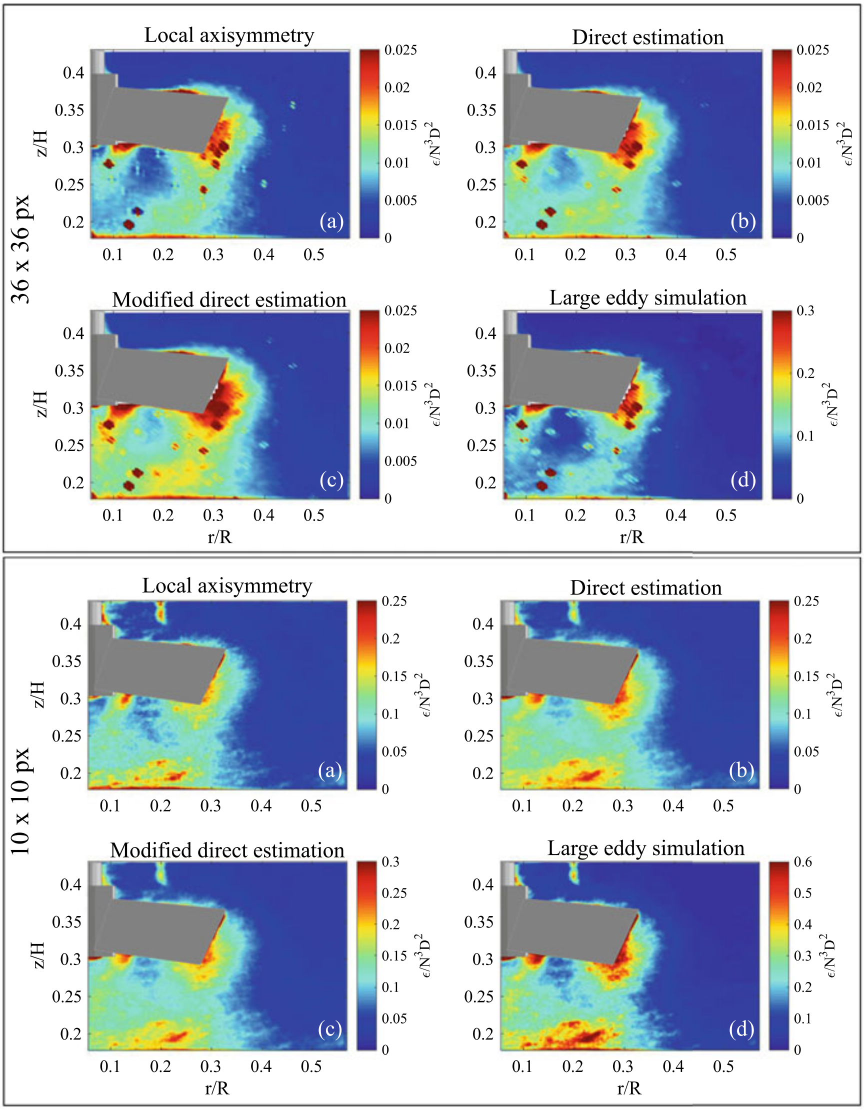

Fig. 4 Angle-resolved EDR distribution of 75° using different estimation methods with 36 × 36 px or 10 × 10 px: **a** AS; **b** DE; **c** MDE and **d** LES

representation close to 50% for the EDR distribution. Figure 5 shows the results for the mean spatial dissipation obtained as a function of the interrogation window for the 0°, 45°, and 75° plane. The results showed an exponential effect of the EDR values with the decrease in Δ that confirms which was already reported in the literature. As shown in Fig. 6, decreasing to a resolution of 5 × 5 px ($\Delta = 0.15$ mm) for AR 45°, the noise interference became predominant due to several factors in PIV

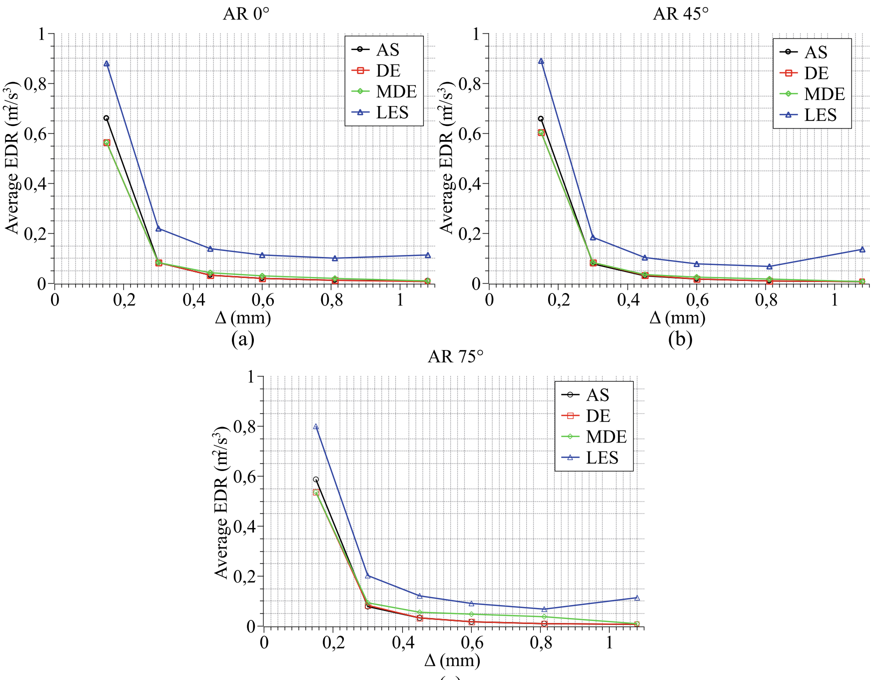

(a)

(b)

(c)

Fig. 5 Turbulence energy dissipation averaged over the impeller stream region, plotted against spatial resolution of the PIV measurements **a** AR 0°, **b** AR 45°, **c** AR 75°

measurements. Some of them can be the possible insufficiency of pairs of images of correlated particles, reflections of the laser light, particle diameter very close to the value of Δ, among others (Tanaka and Eaton 2007). In this way, the values of the EDR distribution were overestimated at this resolution.

Direct estimation of EDR using velocity gradients with the assumption of isotropy (DE), local axisymmetry (AS), or local isotropy (MDE) resulted in a significant underestimation of EDR with the growth of Δ. However, the indirect estimate (LES) showed higher values of EDR compared to the other methods, although it showed the same variation with the increase in Δ. The DE and AS methods showed subtle differences for EDR (Fig. 5), but the values were underestimated due to the hypotheses followed by the methods. For example, the assumption of the isotropy that approximates seven components of the velocity gradient tensor making the precision of the DE method difficult, since the small-scale flow is anisotropic, not only near the impeller tip but throughout the all investigated region (Sharp and Adrian 2001). In addition to the isotropy assumption, the numerical error in the estimation of the velocity gradient from the PIV data increases the susceptibility to the presence of noisy data (Hoque et al. 2015). To apply the AS method, the asymmetric axis must be predetermined, and different selections result in differences in the EDR, and as the DE

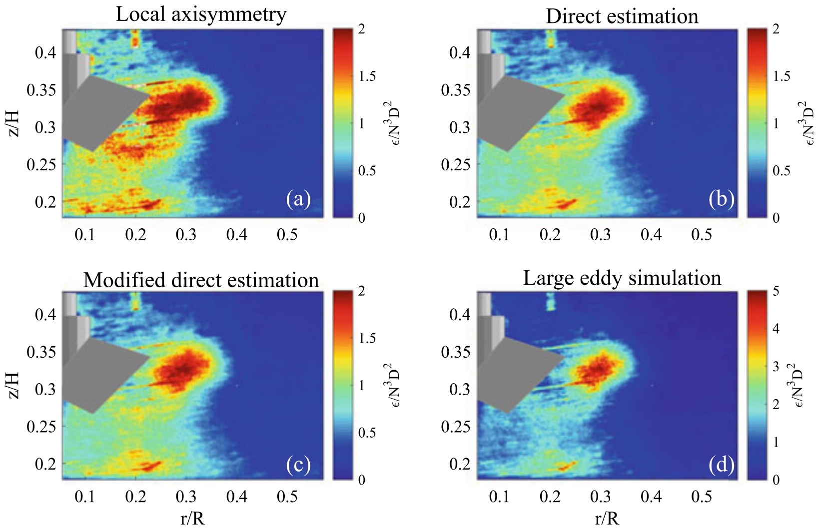

Fig. 6 Angle-resolved EDR distribution of 45° using different estimation methods with 5 × 5 px (0.15 mm): **a** AS; **b** DE; **c** MDE and **d** LES

method, it provides significant underestimated values as the size of the interrogation window increases (Xu and Chen 2013).

Regarding the MDE method, the Pao (1965) model was used to evaluate the results obtained. Figure 7a shows, for example, for AR 45°, that the data obtained from the spatial resolution of 36 × 36 px not fitted the model presented, unlike the data obtained from the spatial resolution of 10 × 10 px (Fig. 7b) that converged reasonably—see region $30 < \Delta/\eta < 250$. Thus, it is possible to assume that the MDE model has little influence to correct the underestimation of EDR.

Based on an LES approach, the EDR captures at least 70% of the real value of the kinetic energy dissipation in the flow using PIV (Sharp and Adrian 2001). The LES method estimates the dissipation rates using a simple turbulent viscosity hypothesis model. As shown in Fig. 2, the values obtained for EDR by the LES method are higher than the DE, MDE, and AS methods. Since the current PIV measurements were not resolved to the Kolmogorov scale, the Smagorinsky model was used to estimate the amount of dissipation contained in the unresolved scales. Thus, this method is dependent on the Smagorinsky constant, and according to Meyers and Sagaut (2007) the theoretical behavior of C_s in many practical simulations is far from being constant. In this work, $C_s = 0.21$ was adopted as previously presented. In the literature, the value of the Smagorinsky constant generally varies between 0.13 (Gabriele et al. 2009), 0.17 (Sheng et al. 2000; Pope 2000), and 0.21 (Meyers and Sagaut 2007; Sharp and Adrian 2001). The implementation of other values for C_s will be discussed in future work.

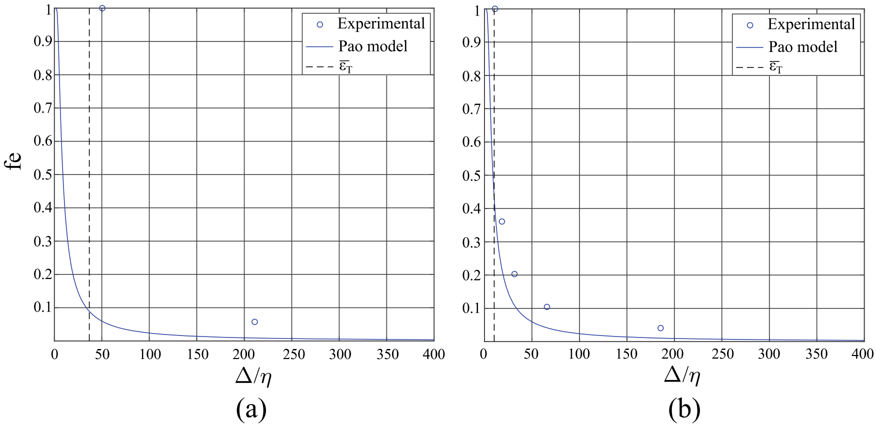

Fig. 7 The underestimation coefficients (f_e) for EDR using MDE with **a** 36 × 36 px (1.08 mm) and **b** 10 × 10 px (0.3 mm)

14.4 Conclusion

Measurements of energy dissipation rate (EDR) were obtained in a tank mechanically agitated with water by a PBT 45° impeller in downward pumping equipped with baffles using PIV (2C-2D) technique. Measurements at angle-resolved were evaluated regarding the respective impeller angles at 0°, 45°, and 75°. Four different methods for calculating the EDR were used: local axisymmetry (AS), direct estimation (DE), modified direct estimation (MDE), and large eddy simulation method (LES). Results of normalized EDR distribution showed a strong influence on the effect of spatial resolution. For the finer spatial resolution, 5 × 5 px, it was observed an overestimation of EDR levels causing loss of coherence of the dissipation phenomenon. For all angles-resolved, the deviations from the maximum values found for normalized EDR were above 80% for the AS, DE, and MDE methods. Only for the LES method, a deviation of less than 50% for the angles of 0°, 45°, and 75° was obtained.

Acknowledgements This research was funded by Petroleo Brasileiro S/A—PETROBRAS (Cenpes) through Grant 2017/00376-1. The authors wish to acknowledge useful assistance and discussions concerning experimental data with the members of the Multiphase Flow Characterization Laboratory (LACEM) at the School of Chemical Engineering, University of Campinas, Brazil.

References

Alekseenko SV, Bilsky AV, Dulin VM, Markovich DM (2007) Experimental study of an impinging jet with different swirl rates. Int J Heat Fluid Flow 28:1340–1359

Basavarajappa M, Draper T, Toth P, Ring TA, Miskovic S (2015) Numerical and experimental investigation of single phase flow characteristics in stirred tank using Rushton turbine and flotation impeller. Miner Eng 83:156–167

Delafosse A, Collignon ML, Crine M, Toye D (2011) Estimation of the turbulent kinetic energy dissipation rate from 2D-PIV measurements in a vessel stirred by an axial Mixel TTP impeller. Chem Eng Sci 66:1728–1737

Ducci A, Yianneskis M (2007) Vortex tracking and mixing enhancement in stirred processes. AIChE J 53:305–315

Escudié R, Liné A (2003) Experimental analysis of hydrodynamics in a radially agitated tank. AIChE J 49(3):585–603

Gabriele A, Nienow AW, Simmons MJH (2009) Use of angle resolved PIV to estimate local specific energy dissipation rates for up- and down-pumping pitched blade agitators in a stirred tank. Chem Eng Sci 64:126–143

George WK, Hussein HJ (1991) Locally axisymmetric turbulence. J Fluid Mech 233:1–23

Guida A, Nienow AW, Barigou M (2010) The effects of the azimuthal position of the measurement plane on the flow parameters determined by PIV within a stirred vessel. Chem Eng Sci 65:2454–2463

Hasal P, Jahoda M, Fořt I (2008) Macro-instability: a chaotic flow component in stirred tanks. Philos Trans R Soc A Math Phys Eng Sci 366:409–418

Hlawitschka MW, Bart H-J (2012) Determination of local velocity, energy dissipation and phase fraction with LIF- and PIV-measurement in a Kuhni miniplant extraction column. Chem Eng Sci 69(1):138–145

Hoque MM, Sathe MJ, Joshi JB, Evans GM (2014) Analysis of turbulence energy spectrum by using particle image velocimetry. Proc Eng 90:320–326

Hoque MM, Sathe MJ, Mitra S, Joshi JB, Evans GM (2015) Comparison of specific energy dissipation rate calculation methodologies utilising 2D PIV velocity measurement. Chem Eng Sci 137:752–767

Joshi JB, Nere NK, Rane CV, Murthy BN, Mathpati CS, Patwardhan AW, Ranade VV (2011) CFD Simulation of stirred tanks: comparison of turbulence models. Part I: Radial flow impellers. Can J Chem Eng 89:23–82

Khan FR (2005) Investigation of turbulent flows and instabilities in a stirred vessel using a particle image velocimetry. PhD thesis, Loughborough University, Loughborough

Kim BJ, Sung HJ (2006) A further assessment of interpolation schemes for window deformation in PIV. Exp Fluids 41:499–511

Liu N, Wang W, Han J, Zhang M, Angeli P, Wu C, Gong J (2016) A PIV investigation of the effect of disperse phase fraction on the turbulence characteristics of liquid-liquid mixing in a stirred tank. Chem Eng Sci 152:528–546

Meyers J, Sagaut P (2007) On the model coefficients for the standard and the variational multi-scale Smagorinsky model. J Fluid Mech 569:287–319

Micheletti M, Baldi S, Yeoh SL, Ducci A, Papadakis G, Lee KC, Yianneskis M (2004) On spatial and temporal variations and estimates of energy dissipation in stirred reactors. Chem Eng Res Des 82:1188–1198

Nikiforaki L, Montante G, Lee KC, Yianneskis M (2003) On the origin, frequency and magnitude of macro-instabilities of the flows in stirred vessels. Chem Eng Sci 58:2937–2949

Okamoto K, Nishio S, Kobayashi T, Saga T, Takehara K (2000) Evaluation of the 3D-PIV standard images (PIV-STD project). J Visualization 3(2):115–123

Pao YH (1965) Structure of turbulent velocity and scalar fields at large wavenumbers. Phys Fluids 8:1063–1075

Pope SB (2000) Turbulent flows. Cambridge University Press, Cambridge, New York

Prasad AK (2000) Particle image velocimetry. Curr Sci 79(1):51–60

Roy S, Acharya S, Cloeter MD (2010) Flow structure and the effect of macro-instabilities in a pitched-blade stirred tank. Chem Eng Sci 65:3009–3024

Saarenrinne P, Piirto M, Eloranta H (2001) Experiences of turbulence measurement with PIV. Meas Sci Technol 12(11):1904–1910

Schäfer M, Yianneskis M, Wächter P, Durst F (1998) Trailing vortices around a 45° pitched-blade impeller. AIChE J 44:1233–1246

Sharp KV, Adrian RJ (2001) PIV study of small-scale flow structure around a Rushton turbine. AIChE J 47:766–778

Sheng J, Meng H, Fox RO (2000) A large eddy PIV method for turbulence dissipation rate estimation. Chem Eng Sci 55(20):4423–4434

Sossa-Echeverria J, Taghipour F (2015) Computational simulation of mixing flow of shear thinning non-Newtonian fluids with various impellers in a stirred tank. Chem Eng Process 93:66–78

Tanaka T, Eaton JK (2007) A correction method for measuring turbulence kinetic energy dissipation rate by PIV. Exp Fluids 42:893–902

Unadkat H (2009) Investigation of turbulence modulation in solid-liquid suspensions using FPIV and micromixing experiments. PhD thesis, Loughborough University, Loughborough

Westerweel J, Elsinga GE, Adrian RJ (2013) Particle image velocimetry for complex and turbulent flows. Annu Rev Fluid Mech 45:409–436

Xu D, Chen J (2013) Accurate estimate of turbulent dissipation rate using PIV data. Exp Thermal Fluid Sci 44:662–672

Yianneskis M (2000) Trailing vortex, mean flow and turbulence modification through impeller blade design in stirred reactors. In Proceedings of the 10th European conference on mixing, Delft, The Netherlands